

**Multinuclear Magnetic Resonance Investigations
of Structure and Order in Borates and Metal
Cyanides.**

By

Pedro M. Aguiar

A thesis

submitted to the Faculty of Graduate Studies

in partial fulfillment of the requirements

for the degree of

Doctor of Philosophy

Copyright © 2007

Table of Contents

List of Figures.....	v
List of Tables.....	xviii
Abstract.....	xix
List of Abbreviations and Symbols.....	xx
Acknowledgements.....	xxiii
1 Introduction	1
2 Interactions in NMR	3
2.1 Zeeman.....	3
2.2 Chemical Shift	4
2.3 Quadrupolar	7
2.4 Direct Dipole-Dipole.....	15
2.5 Indirect Dipole-Dipole	17
2.6 Fermi Contact.....	17
3 Solid-State NMR.....	20
3.1 Non-Spinning	20
3.2 Magic-Angle Spinning (MAS)	21
3.3 Multiple-Quantum MAS	24
3.4 Dipolar Recoupling under MAS	27
4 Theoretical Investigations of MQMAS	30
4.1 Materials & Methods.....	31
4.1.1 Sample Preparation.....	31
4.1.2 NMR	32

4.1.3	Simulations	33
4.2	SIMPSON and Evaluation of Spin Dynamics	34
4.3	MQ off-MAS	35
4.3.1	Amorphous B ₂ O ₃	37
4.3.2	Rubidium Perchlorate (RbClO ₄)	44
4.4	Conclusions.....	46
4.5	Future Work	46
5	Borates	47
5.1	Structure of Glasses.....	48
5.2	Select Techniques for Investigating Glass Structure	52
5.2.1	Diffraction Experiments	52
5.2.1.1	X-ray diffraction.....	53
5.2.1.2	Neutron diffraction.....	53
5.2.1.3	Electron diffraction.....	54
5.2.2	Spectroscopic techniques.....	55
5.2.2.1	EXAFS.....	55
5.2.2.2	XANES.....	56
5.2.2.3	Infrared and Raman vibrational spectroscopy	56
5.2.2.4	NMR spectroscopy.....	58
5.3	Materials & Methods.....	59
5.3.1	Sample Preparation.....	59
5.3.1.1	Glasses.....	59
5.3.1.2	Crystals	60

5.3.2	NMR	61
5.4	Alkali Borate Glasses	65
5.4.1	^{11}B MAS of Glasses	66
5.4.2	Probing Medium-Range Order with $^{11}\text{B}\{^{133}\text{Cs}\}$ REDOR.....	81
5.4.2.1	Cesium Triborate Crystal.....	83
5.4.2.2	Cesium Borate Glasses.....	85
5.4.3	NMR Parameters of Borate Fundamental Building Blocks	90
5.4.3.1	Cesium Triborate (CsB_3O_5)	90
5.4.3.2	Cesium Pentaborate (CsB_5O_8)	94
5.4.3.3	Potassium and Rubidium Diborate ($\text{K}_2\text{B}_4\text{O}_7$ & $\text{Rb}_2\text{B}_4\text{O}_7$).....	96
5.4.3.4	DFT Calculations of FBBs.....	98
5.4.4	^{11}B MAS and Multiple-Quantum MAS of High Alkali-content Glasses	101
5.5	Borosilicates	112
5.6	Conclusions.....	119
5.7	Future Work	120
6	Transition Metal and Main Group Cyanides.....	122
6.1	Materials & Methods.....	124
6.1.1	Synthesis	124
6.1.2	NMR	125
6.1.2.1	Diamagnetic Mercury Cyanides	125
6.1.2.2	Lead Cyanides.....	126
6.1.2.3	Paramagnetic Samples.....	127
6.2	Diamagnetic Systems	128

6.2.1	^{199}Hg and ^{13}C NMR of Mercury Cyanides.....	128
6.2.2	Structural Investigation of a Poorly-Crystalline Lead-Gold Cyanide.....	137
6.2.3	Variable Temperature ^{207}Pb NMR of $\text{Pb}[\text{Au}(\text{CN})_2]_2$	149
6.3	Paramagnetic Systems.....	153
6.3.1	$[\text{Cu}(\text{en})_2][\text{Hg}(\text{CN})_2\text{Cl}]_2$, (1)	154
6.3.2	$[\text{Cu}(\text{en})_2][\text{Ag}_2(\text{CN})_3][\text{Ag}(\text{CN})_2]$, (2).....	157
6.3.3	$[\text{Cu}(\text{dmeda})_2\text{Au}(\text{CN})_4][\text{Au}(\text{CN})_4]$, (3).....	161
6.3.4	$[\text{Cu}(\text{en})_2[\text{Zn}(\text{NC})_4(\text{CuCN})_2]$, (4)	164
6.3.5	$\{(\text{tmeda})\text{NiHg}(\text{CN})_2\}\text{HgBr}_4$, (5) and $\{(\text{tmeda})\text{CuHg}(\text{CN})_2\}\text{HgBr}_4$, (6) ...	171
6.3.6	Trends in ^{13}C NMR Peak Positions	176
6.3.7	$[\text{Cu}(\text{en})_2][\text{Au}(\text{CN})_2]_2$, (7) & $[\text{Zn}(\text{en})_2][\text{Au}(\text{CN})_2]_2$, (8).....	178
6.4	Conclusions.....	185
6.5	Future Work	186
	References.....	188

List of Figures

Figure 2.1: Energy level diagrams for a spin-5/2 nucleus completely unperturbed ($B_0 = 0$) and in the presence of a static field B_0 ($B_0 > 0$).....	4
Figure 2.2: Simulation of the effect chemical shift anisotropy on the observed spectrum. The principal components of the shift tensor δ_{ii} are denoted for the two conventions defined in the text. Simulated using STARS.	7
Figure 2.3: Effects of quadrupolar interaction to first- ($H_Q^{<1>}$) and second-order ($H_Q^{<2>}$) for $I = 5/2$. The symmetric transitions, which are unaffected to first-order are denoted by blue arrows.	10
Figure 2.4: Simulations of the central transition under (a) non-spinning and (b) under magic-angle spinning (see sections 3.1 and 3.2). A reduction of the anisotropic quadrupole shift (broadening) by a factor of ~ 3 is obtained under MAS. However, the isotropic quadrupole shift of the centre-of-gravity from the isotropic chemical shift is identical. Simulated with WSolids. ¹⁵	11
Figure 2.5: Simulated powder pattern lineshapes for an $I = 5/2$ nucleus experiencing an axially symmetric ($\eta = 0$) EFG with a quadrupole coupling, C_Q of 5 MHz. The spectrum consisting of all transitions ($m = 1/2, 3/2, 5/2$), the <i>inner satellites</i> ($m = 3/2$) and the <i>outer satellites</i> ($m = 5/2$) are shown. The widths $\Delta\nu_{TS}$ and $\Delta\nu_{PS}$ (from which C_Q and η may be extracted) are denoted for the $m = 5/2$ transitions. Simulated with STARS.....	13

-
- Figure 2.6: Simulated central-transition lineshapes as a function of the asymmetry parameter, η and ellipsoids representing the electric field gradient tensor for different values of η . Simulated with WSolids.¹⁵ 14
- Figure 2.7: Simulated ^{31}P Pake doublet pattern arising from the coupling to a single proton (1.1 Å, 36.5 kHz). Simulated with WSolids.¹⁵ 16
- Figure 2.8: Simulated spectra of a spin, I, coupled to a spin, S. In the case where S is another nucleus, the +1/2 and -1/2 spin state are nearly equally populated (a), and upon decoupling a single peak at δ_{iso} is observed (b). In the case where S is an electron, (c) a greater population difference between +1/2 and -1/2 states of the electron is reflected in the relative intensities. Decoupling results in a single resonance displaced from δ_{iso} (d). Simulated with STARS. 19
- Figure 3.1: MAS sample rotor oriented at the magic-angle (θ_m) with respect to the static field, B_0 , rotating about its axis with a frequency ν_{rot} 22
- Figure 3.2: The effect of MAS on a spin experiencing CSA. Higher resolution spectra are obtained by spinning faster at the cost of accurate extraction of tensor principal components. Simulated with WSolids.¹⁵ 23
- Figure 3.3: Basic pulse sequence for a shifted-echo MQMAS²⁹ along with the coherence-order (p) pathways for the 3QMAS of an I = 3/2 nucleus. The coherence order pathway for a shifted anti-echo is also shown. 25
- Figure 3.4: Simulated 3QMAS spectra for I=3/2 nucleus after 2D FT (a), resulting in anisotropic projections along both orthogonal axes. A high-resolution axis is denoted by the dashed line. After phase correction (b), the isotropic dimension is orthogonal to the directly detected 3Q-filtered MAS dimension. Simulated with SIMPSON.³² 26

Figure 3.5: The application of a 180° (π) pulse inverts the net magnetization of a nucleus S, changing the sign of the net dipolar field experienced by spin I at a distance r_{IS} .	28
Figure 3.6: Schematic of the REDOR pulse sequence. ³⁷ Application of pulses on the recouple channel modulate the populations of the spin-states, disrupting the spatial averaging of the dipolar interaction.....	29
Figure 4.1: Simulations of the 2-dimensional MQMAS spectra (^{11}B at 14.1 T, $C_Q = 2.6$ MHz, $\eta = 0.2$) showing the effects of shielding anisotropy, upon deviation from the magic angle.....	39
Figure 4.2: Isotropic projections of the $\delta_{\text{CSA}} = 10$ ppm simulated MQMAS spectra (a) at the magic-angle and (b) off-angle by + 1.0 degree. The centre-of-gravity is unchanged, however, the off-angle spectrum displays an anisotropic lineshape.	40
Figure 4.3: ^{11}B NMR T_2^{CT} relaxation data acquired using a Hahn-echo for B_2O_3 . Single-exponential fits yield average spin-spin relaxation time constants of <i>ca.</i> 4.9 and 6.9 ms for on and off-angle (+ 0.45°) experiments, respectively.	41
Figure 4.4: Skyline projections of the magnitude-mode echo spectra. The increased T_2^{CT} and T_2^{3Q} with increasing deviation from the magic angle results in increased echo intensity.	43
Figure 4.5: Projection of the isotropic dimension (F1) of ^{11}B MQMAS spectra of B_2O_3 acquired on-angle, $+0.25^\circ$ and $+0.45^\circ$	43
Figure 4.6: F1 projections on- and off-angle (55.516°) obtained from (a) experiment and (b) numerical simulations.	45

-
- Figure 5.1: Enthalpy (or viscosity) of a material as a function of temperature, showing the formation of crystalline or glassy products by cooling at different rates. The melting point (T_m) and glass transition temperatures (T_g) are shown..... 48
- Figure 5.2: Addition of alkali cations to a borate (in the form of alkali oxide) requires formation of anionic borate species. The two possibilities are $^{[4]B}$ sites or $^{[3]B}$ species with non-bridging oxygens. The B-O-B bonds to additional B are shown cutoff for clarity. 51
- Figure 5.3: Raman spectra (incident radiation, $\lambda = 1064$ nm) of a series of potassium borate glasses of composition R ($R = K_2O/B_2O_3$) from 0 to 0.48. Assignment of resonances to rings with zero (boroxol), one and multiple $^{[4]B}$ centres based on work by Kamitsos.^{89,90} 58
- Figure 5.4: A typical ^{11}B MAS spectrum at 14.1 T of a borate glass. The $^{[3]B}$ and $^{[4]B}$ signals are readily identified and the resolution allows straightforward integration of signals. 66
- Figure 5.5: The evolution of the $^{[4]B}$ fraction, \mathcal{N}_4 ($\mathcal{N}_4 = [^{[4]B}] / \{^{[3]B} + ^{[4]B}\}$) for lithium borate glasses of different composition. A linear increase (with slope=1) in \mathcal{N}_4 is observed until $R = 0.4$, where the rate of $^{[4]B}$ formation changes, requiring another charge-balancing mechanism. 67
- Figure 5.6: Comparison of the lithium and cesium borate glasses of different composition. The cesium borates are very similar to lithium until $R = 0.4$. Beyond $R = 0.4$, the fraction of $^{[4]B}$ begins to decrease for cesium, requiring a larger number of NBOs ($\# \text{NBOs} = R - \mathcal{N}_4$). Errors in \mathcal{N}_4 are on the scale of the points (± 0.01). 68

- Figure 5.7: ^{11}B MAS spectrum of amorphous B_2O_3 acquired using the 2.5 mm double-resonance probe at 21.1 T. The background signal arising from the boron nitride probe components (shaded magenta) significantly hinders quantification. 71
- Figure 5.8: ^{11}B MAS spectrum of the $R = 0.1$ cesium borate glass at 14.1 T. The ^{41}B signal (centred about 1 ppm) exhibits a clear inflection point..... 72
- Figure 5.9: Structures of the more common FBBs in borates with varying numbers of ^{41}B atoms: non-ring ^{31}B (a), boroxol ring (b), non-ring ^{41}B (c), triborate (d), di-triborate (e), diborate (f) and pentaborate (g). Filled circles represent boron, open circles oxygen. 74
- Figure 5.10: ^{11}B MAS spectra of $R = 0.1$, lithium, potassium and cesium borate glasses. Only the potassium and the cesium exhibit multiple ^{41}B signals. 75
- Figure 5.11: ^{11}B MAS spectra of the CsB-20 glass acquired at 11.7, 14.1 and 21.1 T (corresponding to ^1H frequencies of 500, 600 and 900 MHz respectively). No significant change in the ^{41}B signal is observed, unlike the ^{31}B signal, at varying static field, B_0 76
- Figure 5.12: The evolution of the ^{41}B signals for the cesium borate case. The intensities of the two signals (0.5 and 1.5 ppm) along with their sum (Total) are shown as a function of R . Similar evolutions were observed for K and Rb. 78
- Figure 5.13: ^{11}B MAS of the $R = 0.1$ lithium (LiB-10) and cesium (CsB-10) borate glasses at 21.1 T. No evidence of multiple ^{41}B sites is observed for the lithium borate. The spectrum of the cesium glass of analogous composition is shown below for comparison. 79

- Figure 5.14: Relative peak widths (see text) for a series of alkali borate glasses. The heavy alkali (K, Rb and Cs) exhibit nearly constant ^{41}B linewidth, whereas the Li and Na linewidths increase with increased alkali loading. The error bars denote the estimated errors.80
- Figure 5.15: The borate fundamental building blocks (a) diborate and (b) triborate. The alkali cations are shown in teal, boron in blue and oxygen atoms in yellow.....82
- Figure 5.16: ^{11}B MAS spectrum (a) of the cesium triborate (CsB_3O_5) crystal. The results of the $^{11}\text{B}\{^{133}\text{Cs}\}$ REDOR experiments (b) for BO_3 and BO_4 signals along with the results of two-site numerical simulation with $R_{\text{DD}}(^{11}\text{B},^{133}\text{Cs}) = 120 \text{ Hz}$ (3.49 \AA).85
- Figure 5.17: The ^{133}Cs MAS spectrum of the $R = 0.6$ (CsB-60 glass). The width of the centre band is $\sim 10,000 \text{ Hz}$, whereas the second-order broadening is calculated to be $\sim 10 \text{ Hz}$86
- Figure 5.18: ^{11}B MAS spectra of the CsB-10 (a) and CsB-54 (b) glasses. The results of the $^{11}\text{B}\{^{133}\text{Cs}\}$ REDOR experiments for these glasses along with best-fit numerical simulations.....87
- Figure 5.19: $^{11}\text{B}\{^{133}\text{Cs}\}$ REDOR dephasing data for the high (1.5 ppm) and low (0.5 ppm) frequency ^{41}B signals in the CsB-10 glass.89
- Figure 5.20: ^{133}Cs MAS spectrum of the cesium triborate crystal. The central transition is displayed off scale and a minor impurity (*ca.* 2%) is marked with an asterisk.....91
- Figure 5.21: The central-transition of a non-spinning ^{133}Cs spectrum of the cesium triborate crystal along with a simulation of the chemical shielding anisotropy.93

- Figure 5.22: ^{11}B NMR spectra of CsB_5O_8 ; The MAS spectrum (a) is shown for comparison with the F2 projection of the (b) 3QMAS spectrum. An expansion of the ^{13}B region is shown inset.....95
- Figure 5.23: The ^{11}B MAS spectrum of the potassium diborate crystal. The four ^{13}B signals (two from the diborate ring, the other two from the di-triborate ring) appear between 3 and -1 ppm. Fits to the ^{13}B lineshape allowed extraction of those parameters (see Table 5.3). The rubidium diborate yielded an identical spectrum..97
- Figure 5.24: Correlation of the observed ^{11}B isotropic chemical shifts for the ^{13}B sites with those calculated using DFT. Line of best-fit and R^2 shown on graph.....98
- Figure 5.25: Depiction of the calculated four-coordinated boron ^{11}B isotropic chemical shifts.101
- Figure 5.26: ^{11}B MAS spectra of the $R = 2.5$ lithium borate glass at 14.1 and 21.1 T along with simulations of the ^{13}B sites. Simulations were constrained by the NMR parameters (δ_{iso} , C_Q and η) obtained from the ^{11}B 3Q-MAS acquired at 14.1 T.... 104
- Figure 5.27: Contour plot of ^{11}B MQMAS spectrum of $R = 2.5$ lithium borate glass. Distinct signals are observed for the T^1 (87 ppm) and T^0 (95 ppm) sites..... 105
- Figure 5.28: Experimental slices from the MQMAS of $R = 2.5$ lithium borate glass (expt.) along with simulated lineshapes under ideal conditions (MAS) and full 3Q-filtered (3QF) simulation. Note that both simulations yield identical parameters (δ_{iso} , C_Q , η), however, the 3Q-filtered simulations better reproduce the experimental lineshape distortions. 107
- Figure 5.29: Isotropic projections of the $R = 0.7$ cesium (solid) and lithium (dashed) borate glasses. 108

- Figure 5.30: ^{11}B MQMAS spectra for the lithium and cesium borate glasses investigated. The stacked plots are displayed showing every 5th slice (digital resolution = 0.44 ppm/pt) in the indirect (isotropic) dimension. 110
- Figure 5.31: ^{11}B MQMAS isotropic projections for $R = 0.7, 0.9$ and 1.4 cesium borate glasses. Despite the lack of site resolution, the predicted trend to higher shifts with alkali loading is observed..... 111
- Figure 5.32: $\text{Na}_2\text{O}-\text{B}_2\text{O}_3-\text{SiO}_2$ ternary phase diagram showing the *corrected* (see text) compositions of real and other model wastefrom-glass compositions. An extended compositional range partially accounting for errors in *corrections* is also shown (green dashed line)..... 113
- Figure 5.33: ^{29}Si MAS spectrum of datolite ($\nu_{\text{rot}} = 1109 \pm 10$ Hz) along with best-fit simulation. The simulation is based on integrated spinning sideband intensities, rather than peak heights, due to inconsistency of spinning rate. The isotropic peak is marked by an asterisk..... 115
- Figure 5.34: $^{11}\text{B}\{^1\text{H}\}$ CPMAS spectrum of datolite ($\nu_{\text{rot}} = 5000$ Hz). The central transition is shown cutoff..... 115
- Figure 5.35: Proton NMR spectra of datolite. Spectrum observed via $^1\text{H}\{^{11}\text{B}\}$ CPMAS (a) and direct polarization (b). The isotropic peak is shown inset..... 117
- Figure 5.36: REDOR dephasing curve for $^{29}\text{Si}\{^{11}\text{B}\}$ experiment on datolite. The line is drawn as a guide to the eye showing the modulations expected from REDOR..... 118
- Figure 6.1: ^{13}C MAS of HgCN_4 at 14.1 T. The $^1\mathcal{J}(^{199}\text{Hg}, ^{13}\text{C})$ satellites are clearly evident at the base of the peaks. Shown inset is the +1 spinning sideband showing the resolution the sites..... 132

Figure 6.2: ^{199}Hg MAS of HgCN_4 along with two-site (2:1 intensity) simulation to account for the three crystallographically-distinct sites.	135
Figure 6.3: ^1H MAS spectra of (a) the hydrated sample (b) after dehydration and (c) the empty rotor. The loss of signals arising from the sample upon dehydration is clearly evident.	138
Figure 6.4: ^{207}Pb non-spinning NMR spectra for (a) PbAu1 and (b) PbAu2 showing the principal components ($\delta_{11} \geq \delta_{22} \geq \delta_{33}$) of the chemical shift tensors.	139
Figure 6.5: ^{15}N MAS NMR of (a) PbAu1 and (b) PbAu2 spinning at 18 and 17 kHz respectively.	140
Figure 6.6: Relative orientation of a dipolar coupled spin system (separated by a distance, r_{IS}) with respect to the shielding tensor of the observed spin.	141
Figure 6.7: $^{15}\text{N}\{^1\text{H}\}$ CP non-spinning spectrum of PbAu1. The high-frequency edge of the pattern is shown inset, and the splittings due to the effective dipolar couplings for sites one and two (R_{eff}^1 and R_{eff}^2 , respectively) are designated.	142
Figure 6.8: ^{13}C MAS (a) and simulation (b) of the hydrated compound. The isotropic chemical shift is marked by an asterisk.	144
Figure 6.9: ^{13}C MAS (a) and simulation (b) of the dehydrated compound. The isotropic chemical shift is marked by an asterisk.	145
Figure 6.10: Formation of square prisms in PbAu2 (b) upon dehydration of PbAu1 (a) via adjacent slabs, including proposed chemical shift tensor orientations. View down b-axis, with δ_{33} directed out of the plane of the page. Lead in purple, oxygen in red, gold in yellow.	147

- Figure 6.11: The proposed structure based on the combination of solid-state NMR and powder x-ray diffraction. The “square” arrangement of the gold atoms can be seen in (a), and in (b) the distortion from square anti-prismatic geometry can be seen. Lead in purple, gold in yellow, nitrogen in blue and carbon in white..... 148
- Figure 6.12: Variable-temperature non-spinning ^{207}Pb NMR of PbAu_2 . The positions of the perpendicular and parallel components are denoted on the 298 K spectrum.. 151
- Figure 6.13: A plot of the temperature dependence of the ^{207}Pb shielding tensor principal components (and isotropic shifts calculated from them) for PbAu_2 reveals a decreased shielding with increasing temperature. The rate of change of the parallel component is greater than that of the perpendicular component, resulting in a decrease in the observed span. 152
- Figure 6.14: Structure of compound (1). The CN1-Cu distance is the shortest contact (2.77 Å). Mercury shown dark blue, carbon grey, nitrogen light blue, chlorine in green and hydrogen atoms have been omitted. 154
- Figure 6.15: ^{13}C MAS spectrum of $[\text{Cu}(\text{en})_2][\text{Hg}(\text{CN})_2\text{Cl}]_2$, with the inset figure showing the region around -300 ppm as acquired using a single-pulse experiment. Two cyanide signals are present, and the presence of satellite peaks are observed at the base of the peaks arising from the $^{17}\mathcal{J}(^{199}\text{Hg}, ^{13}\text{C})$ coupling..... 155
- Figure 6.16: The structure of compound (2), exhibiting a Jahn-Teller distorted geometry about the copper with contacts to the “axial” CN21 ligands of 2.66 Å. The copper atom is shown in red, carbon in grey, nitrogen in blue, silver in yellow and hydrogen atoms have been omitted. 158

Figure 6.17: ^{15}N MAS spectrum of sample (2). The observation of four resonances confirms the presence of head-to-tail cyanide orientational disorder in the structure.	158
Figure 6.18: ^{13}C MAS spectrum of compound (2) with inset showing the presence of four cyanide signals in the isotropic region.	159
Figure 6.19: Observed chemical shifts for the ethylenediamine ($-\text{CH}_2-$) and for CN21 of compound (2). An expansion of CN21 region (shown inset) reveals the temperature dependence more clearly.	160
Figure 6.20: The structure of compound (3). In (a) the copper-bearing chain, in (b) the copper-free chain. Reprinted from Shorrock <i>et al.</i> ¹⁶⁸ Copyright (2003) American Chemical Society.	162
Figure 6.21: Isotropic region of the ^{13}C MAS spectrum of compound (3).	162
Figure 6.22: Depiction of known cyanide coordination modes. For cases with multiple metals, M, it need not be the same metal.	164
Figure 6.23: The structure of compound (4). The overall network structure (a) with the $\text{Cu}(\text{en})_2$ outside the cyanide framework. In (b), a more detailed view of the Zn/Cu(I) cyanide bonding is shown.	165
Figure 6.24: ^{15}N MAS spectrum of sample (4). Four signals in <i>ca.</i> 1:2:2:1 intensity are observed.	166
Figure 6.25: ^{13}C MAS spectrum of compound (4). The isotropic shifts are marked and other peaks are spinning sidebands.	167

- Figure 6.26: ^{13}C spin-spin relaxation data for compound (4), along with single-exponential fits. The fit to the 122 ppm signal was performed using only the first four points due to poor S/N at long evolution times. 169
- Figure 6.27: Isotropic region of ^{13}C MAS spectrum of (4), acquired at 12.5 kHz spinning. 170
- Figure 6.28: The structure of compound (6). That of compound (5) is identical, but with nickel replacing the copper. Reprinted in part from Draper *et al.*¹⁵² Copyright (2003) American Chemical Society. 171
- Figure 6.29: ^{13}C MAS spectrum of sample 5. The isotropic cyanide peak is denoted by an asterisk. 174
- Figure 6.30: ^1H Bloch decay and Hahn-echo spectra of (5), showing the disappearance of the broad peak ($\delta_{\text{iso}} = 80$ ppm) due to short T_2 (marked with an asterisk). 176
- Figure 6.31: Observed trends in the ^{13}CN chemical shifts for a series of paramagnetic metal cyanides. Assigned (solid) and unassigned (dashed) peaks are included for completeness. 178
- Figure 6.32: ^{13}C CPMAS (a) of sample (8), along with (b) the ^{13}C MAS of sample (7). The highlighted region denotes the isotropic cyanide shifts. 180
- Figure 6.33: The observed temperature dependence of the two ^{13}C cyanide signals for sample 7. Extrapolation to infinite temperature provides diamagnetic shifts of 152 ppm for both signals. 181
- Figure 6.34: The $^{15}\text{N}\{^1\text{H}\}$ CPMAS spectrum of (8) (a) yields no signal after 50 hours of acquisition (121 mg). The ^{15}N MAS of (7) (b) exhibits two clear signals after 17 hours (32 mg). 183

Figure 6.35: The structure of compound (7). That of (8) is identical, only with Zn replacing Cu. Reprinted with permission from Leznoff *et al.*²²² Copyright (2001) American Chemical Society..... 184

List of Tables

Table 5.1: The N_4 values for all alkali borates up to $R = 0.8$ acquired at 14.1 T. Uncertainty in values is ± 0.01	69
Table 5.2: ^{11}B and ^{133}Cs NMR parameters for cesium triborate (CsB_3O_5) crystal obtained via simulation of the experimental spectra.....	91
Table 5.3: Calculated and experimental ^{11}B NMR parameters.....	99
Table 5.4: ^{11}B NMR parameters for various ^{11}B sites.....	103
Table 5.5: ^{11}B NMR parameters for the $R = 2.5$ lithium borate glass, from MAS and MQMAS NMR.....	106
Table 5.6: NMR parameters obtained for datolite from MAS NMR, along with select previously published parameters.	116
Table 6.1: ^{13}C MAS NMR Parameters.....	133
Table 6.2: ^{199}Hg MAS NMR Parameters.	136
Table 6.3: NMR parameters for the hydrated (PbAu1) and dehydrated (PbAu2) samples.	144

Abstract

The local information provided by nuclear magnetic resonance (NMR) makes it an ideal method for the structural investigations of materials lacking extended long-range ordering. This work focuses on investigations of two types of materials possessing very different types of disorder. The first section involves investigations of alkali borate glasses and the application of solid-state NMR techniques to probe short- and medium-range ordering in such glasses. Differences between the various alkali borates over a wide compositional range are probed using one and two-dimensional techniques. The use of double-resonance dipolar recoupling techniques to investigate cesium-boron distances is investigated. The second section probes a series of transition-metal cyanide coordination polymers. The bidentate nature of the cyanide ligand allows for the possibility of forming numerous isomers. Information about the isomer(s) present is gained via the various NMR parameters available, such as the chemical shifts, shift anisotropies and \mathcal{J} -couplings. This is then extended to the characterization of paramagnetic transition-metal cyanides, where strong electron-nuclear interactions are shown to significantly increase spin-lattice relaxation rates allowing the acquisition of spectra without the need of typically employed enhancement techniques, yet often yielding spectra of better quality. Variable temperature experiments allow a measure of the electron-nuclear interaction, which can be related to spatial proximity, and provide “diamagnetic” chemical shifts allowing comparison with other cyanides. \mathcal{J} -couplings and chemical shift anisotropies are shown to be applicable in much the same fashion as with diamagnetic systems.

List of Abbreviations and Symbols

3Q	triple-quantum
5Q	quintuple-quantum
CP	cross-polarization
CSA	chemical shift (or shielding) anisotropy
CT	central transition
CW	continuous wave
DFT	density functional theory
dmeda	N,N'-dimethylethylenediamine
EFG	electric field gradient
en	ethylenediamine
Et	ethyl
FAM	fast amplitude modulation
FBB	fundamental building block
FT	Fourier transform
FWHM	full-width at half-maximum
GIAO	gauge-invariant atomic orbitals
ⁱ Pr	isopropyl
MAS	magic-angle spinning
MQ	multiple quantum
MQMAS	multiple-quantum magic-angle spinning

MQ-OMAS	multiple-quantum off-magic-angle spinning
NMR	nuclear magnetic resonance
NQR	nuclear quadrupole resonance
PAS	principal axis system
ppm	parts per million
PPN	bis(triphenylphosphoranylidene)amine
QCPMG	quadrupolar Carr Purcell Meiboom Gill
REAPDOR	rotational-echo adiabatic passage double-resonance
REDOR	rotational-echo double resonance
rf	radiofrequency
ST	satellite transition
STMAS	satellite transition magic-angle spinning
TEDOR	transferred echo double-resonance
tmeda	N,N,N',N'-tetramethylethylenediamine
TRAPDOR	transfer of populations in double-resonance
xrd	x-ray diffraction
HgCN1	[PPN][Hg(CN) ₂ Cl]·H ₂ O
HgCN2	[ⁿ Bu ₄ N][Hg(CN) ₂ Cl]·0.5H ₂ O
HgCN3	[Co(en) ₂][Hg(CN) ₂ Cl ₂]{[Hg(CN) ₂] ₂ Cl}
HgCN4	[Co(NH ₃) ₆] ₂ [Hg(CN) ₂] ₅ Cl ₆ ·2H ₂ O
PbAu1	Pb(H ₂ O)[Au(CN) ₂] ₂
PbAu2	Pb[Au(CN) ₂] ₂

- (1) $[\text{Cu}(\text{en})_2][\text{Hg}(\text{CN})_2\text{Cl}]_2$
- (2) $[\text{Cu}(\text{en})_2][\text{Ag}_2(\text{CN})_3][\text{Ag}(\text{CN})_2]$
- (3) $[\text{Cu}(\text{dmeda})_2\text{Au}(\text{CN})_4][\text{Au}(\text{CN})_4]$
- (4) $[\text{Cu}(\text{en})_2[\text{Zn}(\text{NC})_4(\text{CuCN})_2]$
- (5) $\{(\text{tmeda})\text{NiHg}(\text{CN})_2\}\text{HgBr}_4$
- (6) $\{(\text{tmeda})\text{CuHg}(\text{CN})_2\}\text{HgBr}_4$
- (7) $[\text{Cu}(\text{en})_2][\text{Au}(\text{CN})_2]_2$
- (8) $[\text{Zn}(\text{en})_2][\text{Au}(\text{CN})_2]_2$

Acknowledgements

I am most grateful to my supervisor Scott Kroeker for his guidance, patience (and/or perhaps tolerance) as I have gone about this - sometimes - arduous task. From Scott I have learned much, including a little about NMR spectroscopy and science in general. His meticulous nature in everything he does especially in crafting of a manuscript has helped me to become a much better writer, although I prefer not to be *two* meticulous.

In addition to Scott, I have been lucky enough to have additional support and guidance from two other very talented NMR spectroscopists. Prof. Joseph O'Neil who, in addition to being on my advisory and examining committees, introduced me to the Bloch equations and taught me the about the density matrix. Many of the practical aspects of NMR I was lucky enough to learn from Dr. Kirk Marat. From the basics of arcing (why, where etc.) to the nuances of zero-filling, Kirk almost always had the answers, plus often a few extra questions just to keep me thinking.

I am also grateful for the efforts of our collaborators. Danny Leznoff's group at Simon Fraser University provided me with several interesting metal-cyanide samples, often at a rate I struggled to keep up with. In fact, there may still be some samples to be run....

The ability of the group of Steven Feller and Mario Affatigato to make glasses at very challenging compositions was crucial for my work at very-high alkali content glasses, especially the work on the lithium borate invert glass.

I would like to thank the other members of the Kroeker group who put up with me over the years: Vlad, Christine, Paul, Amy, Anthony, Erin, Kenan, Joy and Carolyn. All of you provided interesting conversation and made the work seem less so.

In addition to the students in the Kroeker group I have been lucky enough to spend my time at the University of Manitoba with some truly gifted graduate students. I wish to thank in particular Jason, Richard, Sergei, Laina.

1 Introduction

Many nuclei have a non-zero spin angular momentum $I\hbar/2\pi$, and an associated co-linear dipolar magnetic moment, μ . The existence of nuclear spin paramagnetism, present as a net magnetization of the sample, allows a measure of μ (in analogy to electron paramagnetism). However, nuclear magnetic moments are generally much smaller than electron magnetic moments, with typical values on the order of 10^{-3} to 10^{-5} Bohr magnetons, μ_B . Many techniques have been developed or theorized to probe this nuclear paramagnetism.¹ However, the technique that has gained the most widespread use is that of nuclear magnetic resonance. The nuclear magnetic resonance (NMR) spectroscopy experiment was simultaneously developed in the labs of Bloch² and Purcell.³ Since the initial experiments by Bloch and Purcell, NMR (and its daughter technique MRI) has become invaluable in numerous areas of chemistry, physics and medicine. The ability of NMR to measure nuclear spin magnetic moments (thus the magnetogyric ratio) accurately, although useful, would not have made NMR the important tool it is today. It is the other interactions present which have allowed NMR to provide crucial structural information.

Although one of the first experimental observations of an NMR signal was in the solid-state (^1H signal of paraffin wax),³ it was liquid-state NMR which first flourished; fueled by the observation of the chemical shift⁴⁻⁶ and spin-spin coupling^{7,8} in these higher resolution spectra. For decades, the ability to obtain high-resolution spectra in liquids has made it the standard for structural characterization in chemistry. This has left the development of solid-state NMR methods largely in the realm of physics rather than

chemistry. This has led to some interesting research in areas such as spin-temperatures and even required the modification of some classical thermodynamic descriptions of heat and temperature.¹ The advent of high-resolution methods such as magic-angle spinning (MAS)^{9,10} and other techniques have allowed for the tremendous expansion of solid-state NMR techniques to much more complex systems than the one and two-spin systems often studied up to that point. The lack of mobility in solids results in different relaxation behaviour in solids than in liquids, in various systems this can actually result in higher resolution spectra in the solid-state; the standard example is that of quadrupolar nuclei, which in solution can possess such broad lines as to be *invisible*. More recently, studies on nanocrystalline biological molecules have been shown to exhibit even narrower signals in the solid-state than in solution.^{11,12}

The work within this thesis attempts to touch upon both theoretical aspects of performing solid-state NMR experiments involving quadrupolar nuclei (e.g., homonuclear correlation and double-resonance dipolar recoupling experiments). As well, more practical will be covered issues such as the structural characterization of various materials with solid-state NMR.

2 Interactions in NMR

The prominence of NMR spectroscopy for the characterization of structure and dynamics is due completely to the presence of the numerous internal and external interactions, which together allow the construction of a single coherent picture. Interactions of the nuclei with external magnetic fields permit the observation of a signal while the internal interactions of the nuclei with one another and with the electrons provide crucial information about the local nuclear environment.

2.1 Zeeman

The Zeeman interaction arises from the coupling of a spin's intrinsic angular momentum with a static magnetic field. This lifts the degeneracy of the, $2I + 1$ nuclear spin-states to energies, E_m .

$$E_m = -\gamma B_0 m \quad \text{Equation 2.1}$$

The effect on the energy levels upon placing a nucleus of spin-5/2 in a magnetic field is represented in Figure 2.1. The field removes the degeneracy of the nuclear spin states, m , and an energy difference between each $(m, m-1)$ pair of $-\gamma B_0$ results. This relation and the realization that NMR could be used to determine the magnetogyric ratios of nuclei and in turn the nuclear g-factors, initially drove physics research in NMR.

$$g_N = \frac{\gamma}{2\pi u_0} \quad \text{Equation 2.2}$$

The observation of a pesky “chemical interference” would be the impetus which piqued the interest of chemists.

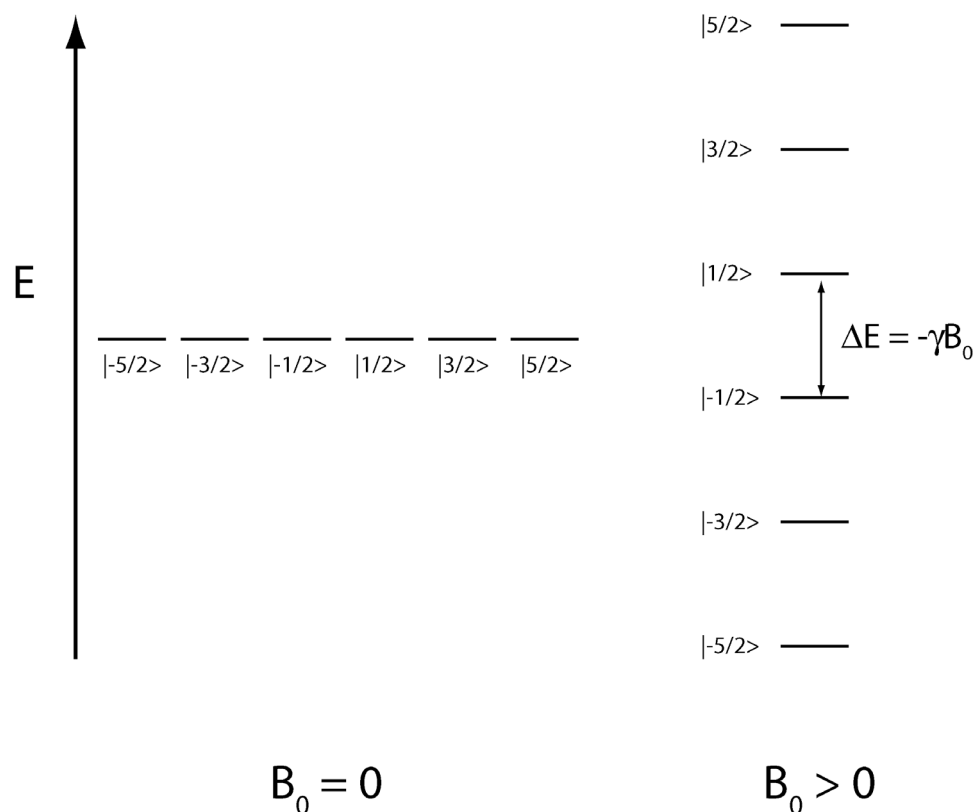


Figure 2.1: Energy level diagrams for a spin-5/2 nucleus completely unperturbed ($B_0 = 0$) and in the presence of a static field B_0 ($B_0 > 0$).

2.2 Chemical Shift

Despite the dismay at the observation of multiple resonance lines in the spectrum of Proctor and Yu,⁸ it is in fact this chemical shift which has made NMR spectroscopy and, to some extent its cousin MRI, such valuable tools. The observed displacement of the resonances from their simple Zeeman-predicted frequencies is due to small perturbations of the local magnetic field each nucleus experiences. The electrons in molecules cause fluctuations in the local fields throughout a molecule, resulting in slightly different resonance frequencies for different parts or groups in the molecule. A “classic” example is the ^1H spectrum of ethanol ($\text{CH}_3\text{-CH}_2\text{-OH}$), which consists of three signals

arising from the methyl, methylene and hydroxyl sites. The chemical shift is largely an intramolecular effect, however, intermolecular interactions can play a role. The mechanism may be broken down into two basic steps. Initially the static field, B_0 induces current flow within the orbitals, this current flow then creates a small local field, B_{loc} . By virtue of the direct proportionalities between B_{loc} and the current flow and the current flow and B_0 , the chemical shift is itself proportional to B_0 .

The chemical shift Hamiltonian is defined by $\hat{H}_{CS} = -\sigma\gamma B_0$, where σ is a second-rank tensor possessing a non-zero trace that describes the shielding in Cartesian space. As a tensor of second rank, it may be denoted as follows,

$$\sigma = \begin{pmatrix} \sigma_{11} & \sigma_{12} & \sigma_{13} \\ \sigma_{21} & \sigma_{22} & \sigma_{23} \\ \sigma_{31} & \sigma_{32} & \sigma_{33} \end{pmatrix} \quad \text{Equation 2.3}$$

In the secular approximation, only the symmetric portion of the tensor affects the spectrum. Being a second-rank symmetric tensor with a non-zero trace, 6 unique components are required to fully describe it. Diagonalization of this matrix transforms it into its principal axis system (PAS).

$$\sigma = \begin{pmatrix} \sigma_{11} & 0 & 0 \\ 0 & \sigma_{22} & 0 \\ 0 & 0 & \sigma_{33} \end{pmatrix} \quad \text{Equation 2.4}$$

We may define the principal components such that $\sigma_{33} > \sigma_{22} > \sigma_{11}$. The other three components needed to fully describe the tensor in the molecular frame are thus the three Euler angles relating the PAS to the molecular frame. As all experiments will measure

relative shifts as opposed to absolute shieldings, conversion to shifts may be done using the following relation:

$$\delta = \left(\frac{\sigma_{ref} - \sigma_{11}}{1 - \sigma_{ref}} \right) * 10^{-6} \approx \sigma_{ref} - \sigma_{11} \quad \text{Equation 2.5}$$

The approximation is generally valid for many nuclei investigated. However, for nuclei such as ^{199}Hg , ^{207}Pb , and ^{59}Co , which possess chemical shift ranges of many thousands of parts-per-million,¹³ this may result in significant errors. In terms of shifts, we then have the principal components, $\delta_{11} \geq \delta_{22} \geq \delta_{33}$ to describe the tensor. The isotropic shift is given by the average of the three components $\delta_{iso} = (\delta_{11} + \delta_{22} + \delta_{33})/3$. It is often more convenient to ascribe some other parameters to describe the extent of the anisotropy and the symmetry of the shielding tensor. One method (most commonly used herein) is that of the span, Ω ($\Omega = \delta_{11} - \delta_{33}$) and the skew, κ ($\kappa = 3(\delta_{22} - \delta_{iso})/\Omega$). The span is always positive, and skew is defined from +1 to -1. Both $\kappa = +1$ and -1 correspond to tensors with two identical components; $\kappa = +1$ has $\delta_{11} = \delta_{22}$, while $\kappa = -1$ implies that $\delta_{22} = \delta_{33}$. A spectrum showing the relative position of these frequencies is shown in Figure 2.2. Another convention less often used in this work defines the principal components with respect to the isotropic chemical shift, such that $|\delta_{ZZ} - \delta_{iso}| \geq |\delta_{XX} - \delta_{iso}| \geq |\delta_{YY} - \delta_{iso}|$. The anisotropy, δ_{CSA} , is derived such that $\delta_{CSA} = \delta_{ZZ} - \delta_{iso}$, and an asymmetry parameter, η , is defined as follows: $\eta = (\delta_{YY} - \delta_{XX})/\delta_{CSA}$. Under this system, the asymmetry parameter varies between 0 and 1, and the anisotropy may be either positive or negative valued.

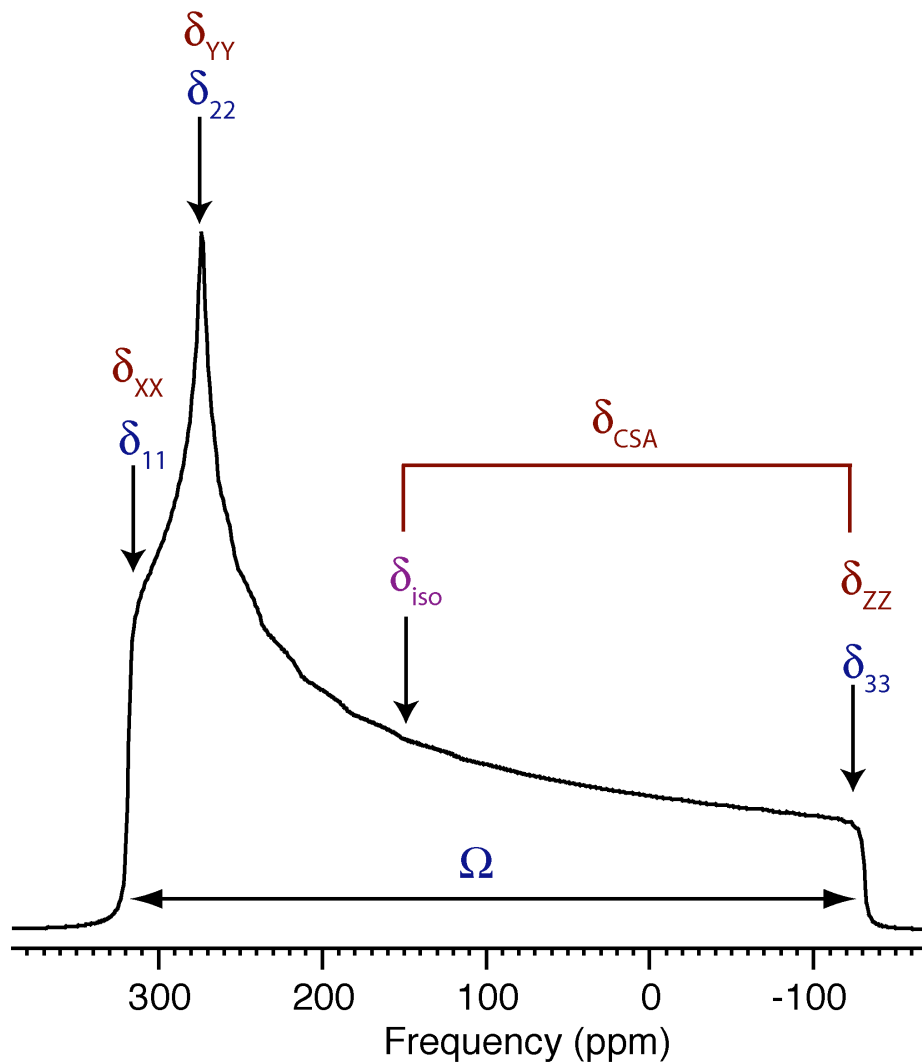


Figure 2.2: Simulation of the effect chemical shift anisotropy on the observed spectrum. The principal components of the shift tensor δ_{ii} are denoted for the two conventions defined in the text. Simulated using STARS.

2.3 *Quadrupolar*

For spins with nuclear spin quantum number greater than $1/2$, there exists a nuclear electric quadrupole moment, Q . The nuclear electric quadrupole moment can couple with a local electric field gradient (EFG) tensor, \mathbf{V} , at the nucleus, resulting in

additional perturbation of the nuclear energies. The EFG tensor is of second-rank, symmetric and of vanishing trace. The principal components are defined such that $|V_{ZZ}| \geq |V_{YY}| \geq |V_{XX}|$. Within the PAS of the EFG tensor, only two components are required to fully describe it: the largest component and an asymmetry parameter, η .

$$\eta = \frac{V_{XX} - V_{YY}}{V_{ZZ}} \quad \text{Equation 2.6}$$

The quadrupole Hamiltonian is given by the following:

$$\hat{H}_Q = \frac{C_Q h}{4I(2I-1)} \left[3\hat{I}_z^2 - \hat{I}^2 + \frac{\eta}{2} (\hat{I}_+ + \hat{I}_-) \right] \quad \text{Equation 2.7}$$

$$C_Q = \frac{e^2 Q V_{ZZ}}{h} \quad \text{Equation 2.8}$$

C_Q is the quadrupole coupling constant and is the more common method of describing V_{ZZ} .

The often very large quadrupole interactions present result in a breakdown of the secular approximation. Thus the total quadrupolar Hamiltonian is generally taken to include both 1st and 2nd order terms such that,

$$\hat{H}_Q = \hat{H}_Q^1 + \hat{H}_Q^2$$

where \hat{H}_Q^1 and \hat{H}_Q^2 are the first- and second-order quadrupole interactions, respectively, and their explicit formalisms are¹⁴

$$\hat{H}_Q^1 = \frac{eQ}{4I(2I-1)} \sqrt{\frac{3}{2}} [3\hat{I}_z^2 - \hat{I}^2] V_0 \quad \text{Equation 2.9}$$

and

$$\hat{H}_Q^2 = -\frac{2}{\nu_0} \left(\frac{eQ}{4I(2I-1)} \right)^2 \left\{ V_1 V_{-1} \hat{I}_Z (4\hat{I}^2 - 8\hat{I}_Z^2 - 1) + V_2 V_{-2} \hat{I}_Z (2\hat{I}^2 - 2\hat{I}_Z^2 - 1) \right\} \quad \text{Equation 2.10}$$

where e is the elementary charge, Q is the nuclear electric quadrupole moment, I is the spin quantum number. $V_0 = \sqrt{3/2}eq$ (eq is the largest component of the EFG tensor), ν_0 is the Larmor Frequency, $V_{\pm 1} = 0$ and $V_{\pm 2} = eq\eta/2$.

The energy of the $-1/2, 1/2$ transition (i.e., the central transition) is not affected by the quadrupole interaction to first order. All other $m-1, m$ transitions are affected by the first-order quadrupole interaction, which results in a large anisotropic broadening of the resonance. In fact, none of the symmetric transitions ($m, -m$) are affected by the quadrupole interaction to first-order (see Figure 2.3). Despite the absence of a first-order quadrupole interaction, the central transition is affected by the second-order quadrupole interaction and the resonance is anisotropically broadened, although, to a much lesser extent than the first-order anisotropic broadening of the satellite transitions. There is also an isotropic quadrupole shift, which displaces the centre-of-gravity of the central transition response signal from the isotropic chemical shift. The effect of the second-order quadrupole interaction on the observed spectrum of the central transition is shown in Figure 2.4.

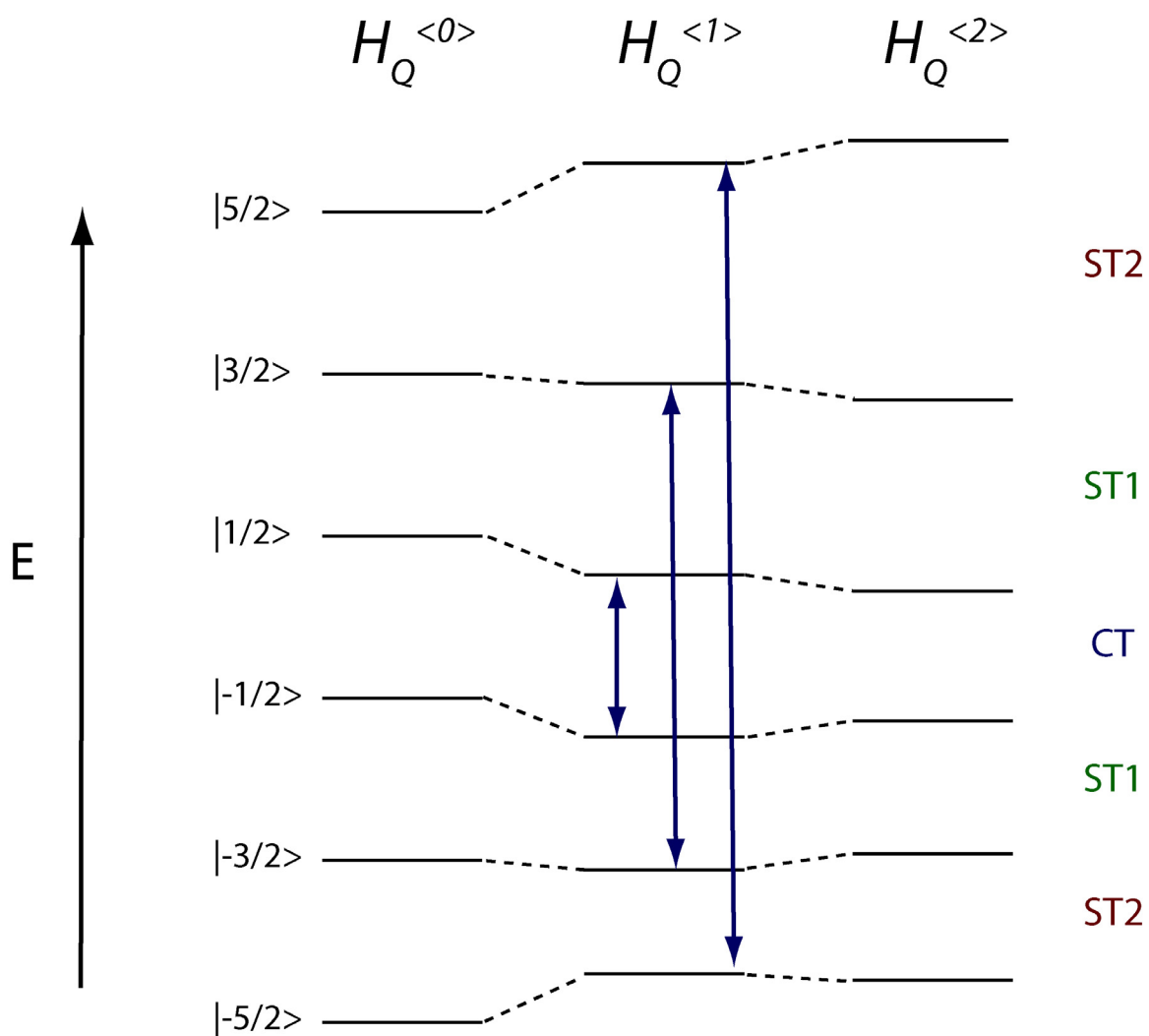


Figure 2.3: Effects of quadrupolar interaction to first- ($H_Q^{<1>}$) and second-order ($H_Q^{<2>}$) for $I = 5/2$. The symmetric transitions, which are unaffected to first-order are denoted by blue arrows.

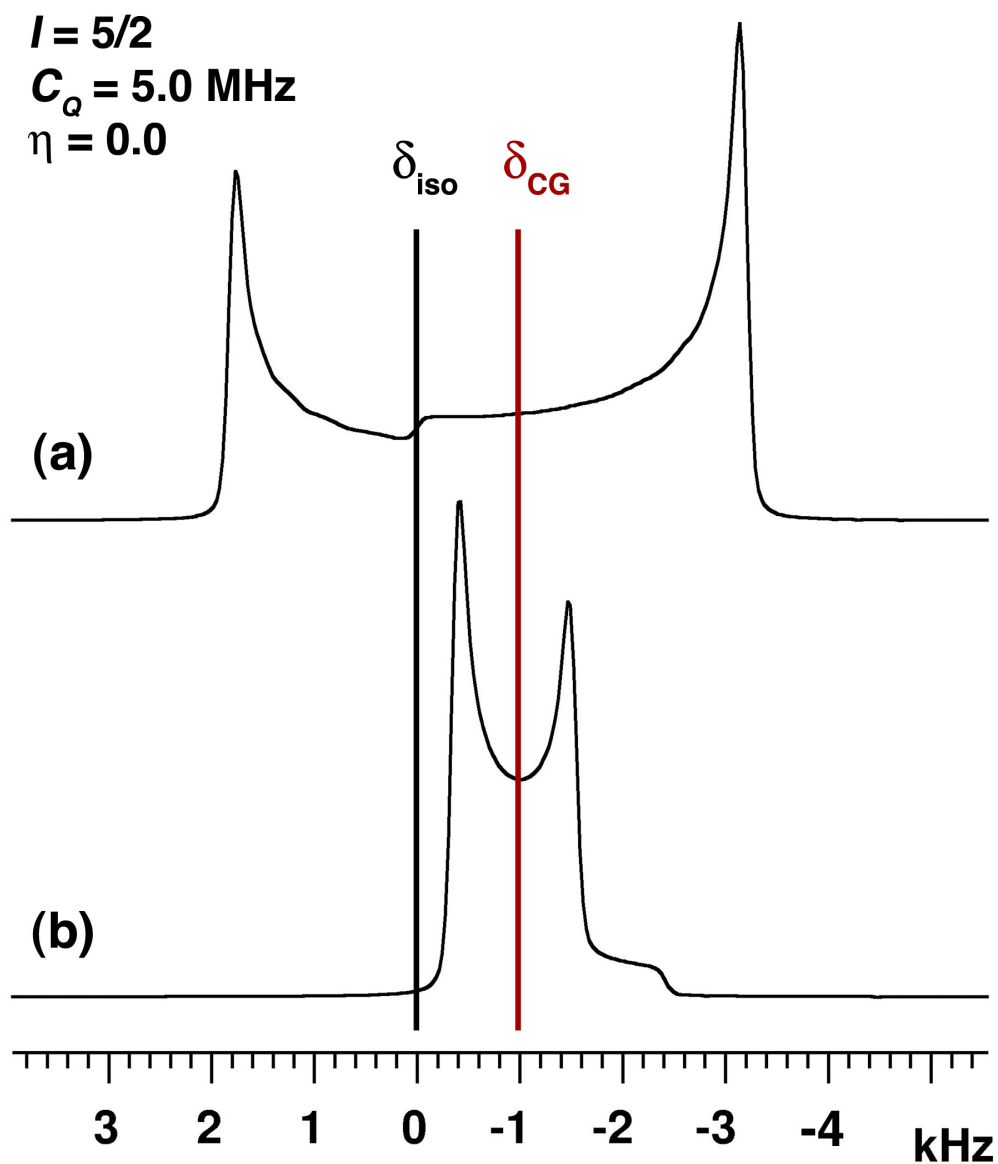


Figure 2.4: Simulations of the central transition under (a) non-spinning and (b) under magic-angle spinning (see sections 3.1 and 3.2). A reduction of the anisotropic quadrupole shift (broadening) by a factor of ~ 3 is obtained under MAS. However, the isotropic quadrupole shift of the centre-of-gravity from the isotropic chemical shift is identical. Simulated with WSolids.¹⁵

The practical extraction of information about the EFG tensor (magnitude of the quadrupole interaction and asymmetry) from experimental spectra may be accomplished by direct measurement of the position of the discontinuities and/or computer simulation. From the discontinuities and inflection points of the satellite transition signals, estimates of the C_Q and η may be made. From the total breadth, $\Delta\nu_{TS}$, (measured at the base) of the outer edges of a transition pair (e.g., $m=5/2$, Figure 2.5), the C_Q can be obtained using the relation¹⁶

$$\Delta\nu_{TS} = |1 - 2m|\nu_Q = |1 - 2m|\frac{3C_Q}{2I(2I - 1)} \quad \text{Equation 2.11}$$

The asymmetry parameter can then be obtained from the frequency difference of the discontinuities, $\Delta\nu_{PS}$, using the following:¹⁶

$$\Delta\nu_{PS} = \Delta\nu_{TS} \frac{(1 - \eta)}{2} \quad \text{Equation 2.12}$$

For spins $> 3/2$, the other transitions (e.g., the $m=3/2$ of the $I = 5/2$ in Figure 2.5) can also be used to further constrain the values of C_Q and η .

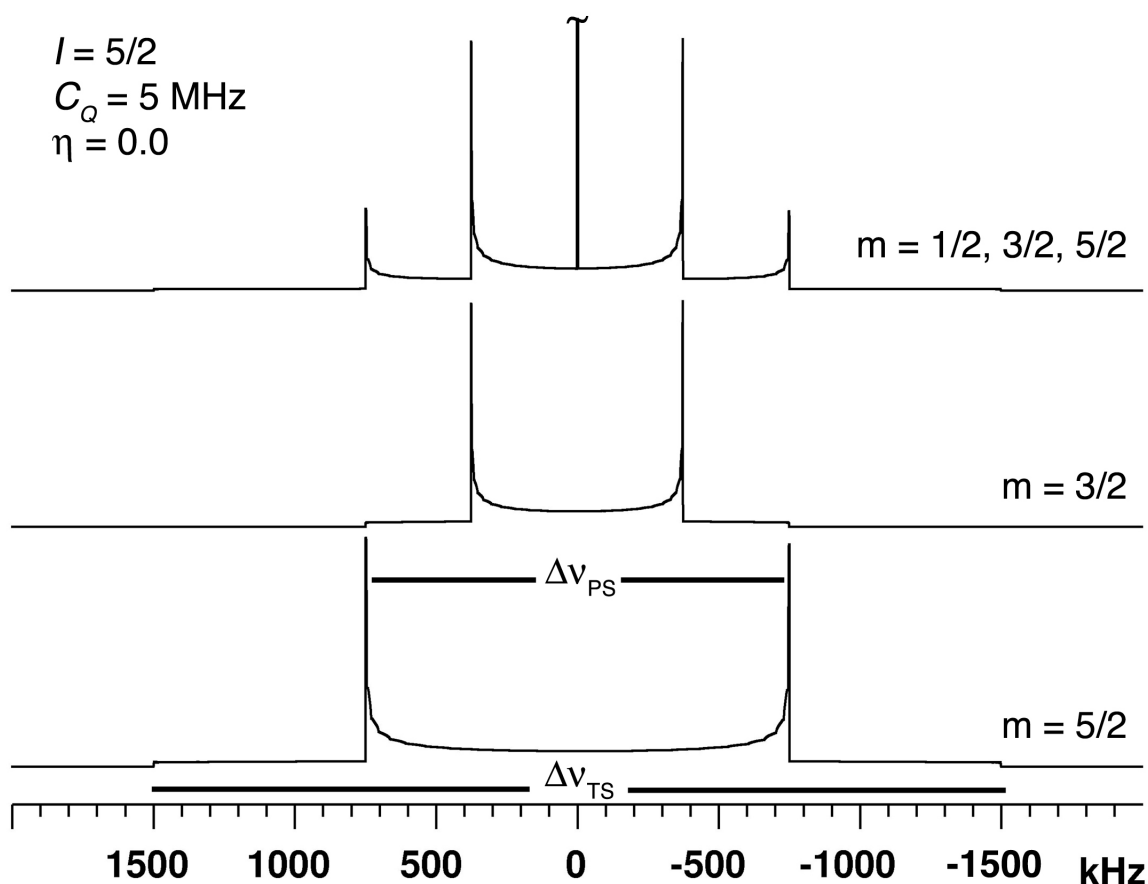


Figure 2.5: Simulated powder pattern lineshapes for an $I = 5/2$ nucleus experiencing an axially symmetric ($\eta = 0$) EFG with a quadrupole coupling, C_Q of 5 MHz. The spectrum consisting of all transitions ($m = 1/2, 3/2, 5/2$), the *inner satellites* ($m = 3/2$) and the *outer satellites* ($m = 5/2$) are shown. The widths Δv_{TS} and Δv_{PS} (from which C_Q and η may be extracted) are denoted for the $m = 5/2$ transitions. Simulated with STARS.

Difficulties in obtaining significant signal from the first-order broadened satellite transitions limits this analysis, and more commonly the second-order lineshape of the central transition is used to extract these parameters. It should be noted that for quadrupolar nuclei of integer spin ($I = N$), there is no central transition. As a result, all

single-quantum transitions are subject to first-order broadening, and correspondingly the vast majority of work on quadrupolar nuclei has focused on half-integer ($I = N/2$) quadrupoles or on integer quadrupoles with small quadrupole interactions (e.g., ^2H).

Simulations of the central transition lineshape for a series of asymmetry parameters are depicted in Figure 2.6. Cartoons of the electric-field gradient ellipsoids for the $\eta = 0$, $\eta = 1$ and $0 < \eta < 1$ cases are also shown.

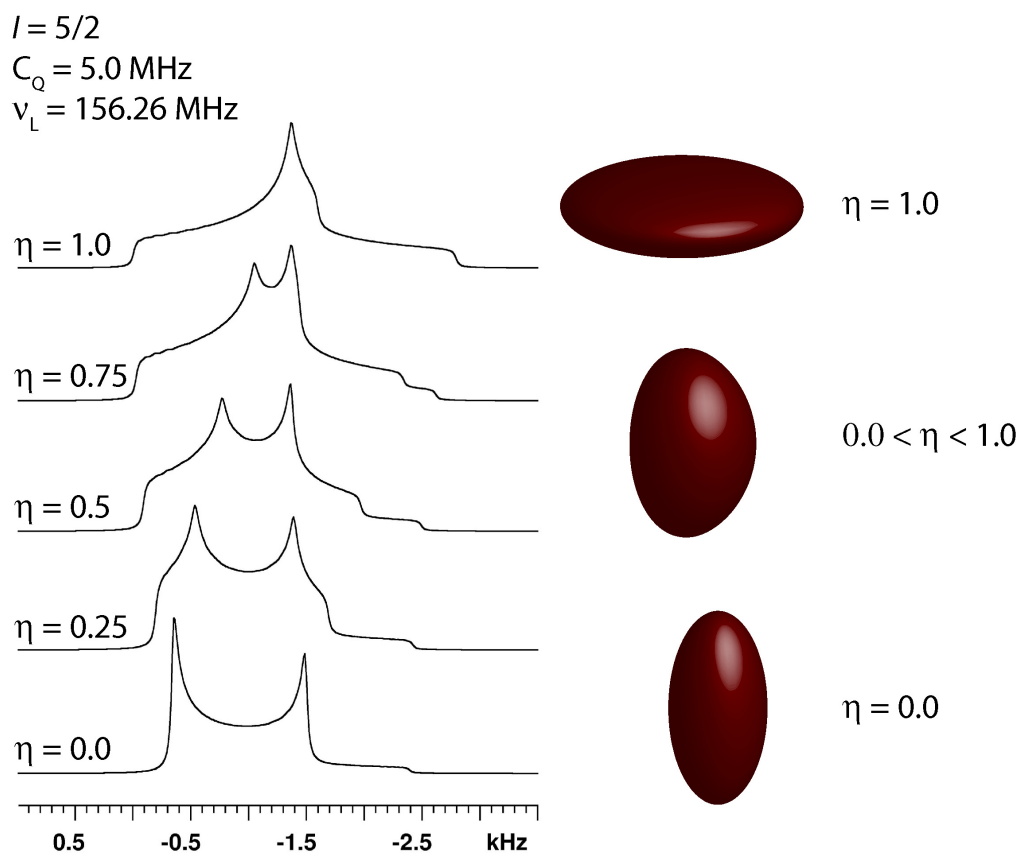


Figure 2.6: Simulated central-transition lineshapes as a function of the asymmetry parameter, η and ellipsoids representing the electric field gradient tensor for different values of η . Simulated with WSolids.¹⁵

2.4 Direct Dipole-Dipole

The direct dipole-dipole interaction arises from the coupling of two magnetic dipoles. The classical interaction energy for two magnetic dipoles, μ_1 and μ_2 , separated by a distance r is given by¹

$$E_D = \frac{\mu_0}{4\pi} \left[\frac{\mu_1 \cdot \mu_2}{r^3} - \frac{3(\mu_1 \cdot r)(\mu_2 \cdot r)}{r^5} \right] \quad \text{Equation 2.13}$$

Substituting $\mu_1 = \gamma \hbar I_1$ and $\mu_2 = \gamma \hbar I_2$ and converting into Cartesian coordinates, the well-known dipolar Hamiltonian is obtained:¹⁴

$$\begin{aligned} \hat{H}_D &= \frac{\gamma_I \gamma_S \hbar \mu_0}{4\pi r^3} [A + B + C + D + E + F] \\ A &= I_{1Z} I_{2Z} (1 - 3 \cos^2 \theta) \\ B &= \frac{-1}{4} [I_{1+} I_{2-} + I_{1-} I_{2+}] (1 - 3 \cos^2 \theta) \\ C &= \frac{-3}{2} [I_{1Z} I_{2+} + I_{1+} I_{2Z}] \sin \theta \cos \theta e^{(-i\phi)} \\ D &= \frac{-3}{2} [I_{1Z} I_{2-} + I_{1-} I_{2Z}] \sin \theta \cos \theta e^{(i\phi)} \\ E &= \frac{-3}{4} I_{1+} I_{2+} \sin \theta \cos \theta e^{(-2i\phi)} \\ F &= \frac{-3}{4} I_{1-} I_{2-} \sin \theta \cos \theta e^{(2i\phi)} \end{aligned} \quad \text{Equation 2.14}$$

The angles θ and ϕ denote the polar and azimuthal angles, respectively, which relate the dipolar vector and the static field, B_0 . The dipole-dipole coupling constant, R_{DD} , is

$$R_{DD} = \frac{\gamma_I \gamma_S \hbar \mu_0}{4\pi r^3} \quad \text{Equation 2.15}$$

Only the terms B through F of the dipole-dipole interaction energy cause any mixing of the Zeeman energy states. With the exception of very low fields, $\hat{H}_Z \gg \hat{H}_D$, they are dropped in the secular approximation for heteronuclear interactions.¹ For homonuclear interactions, the spin states $\alpha\beta$ and $\beta\alpha$ are degenerate and thus the B term

remains in the secular approximation. The relation between dipole-dipole coupling and the internuclear distance allows an accurate measure of the through-space proximity of nuclei in a molecule or extended structure.

In the solid-state, the “classic” experiment is that of Pake,¹⁷ who observed a “Pake-doublet” for an isolated spin pair (spin-1/2) (see Figure 2.7), as opposed to the simple gaussian response signal expected of an non-coupled spin. Using the frequencies of the discontinuities and inflection points, the dipole-dipole couplings may be extracted. In more general terms, for interaction with any spin, I, of any number of spins, N (all of N being identical), the resonance is split into $2NI + 1$ bands, each of which is broadened to first-order.

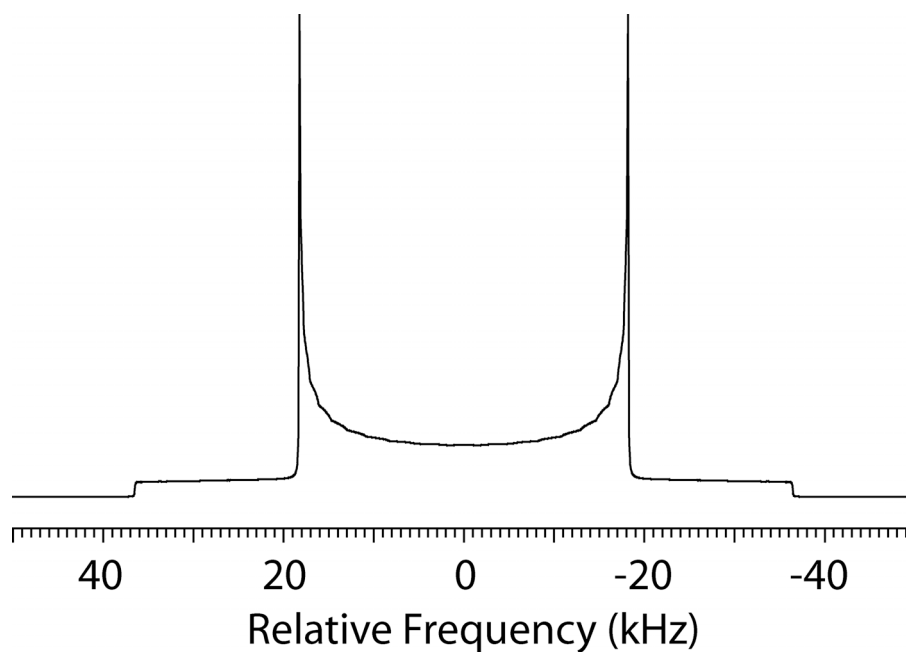


Figure 2.7: Simulated ³¹P Pake doublet pattern arising from the coupling to a single proton (1.1 Å, 36.5 kHz). Simulated with WSolids.¹⁵

2.5 *Indirect Dipole-Dipole*

The indirect dipole-dipole coupling is also widely referred to as \mathcal{J} -coupling or scalar coupling; however, the term “indirect dipole-dipole coupling” better conveys information about the mechanism. The interaction is mediated by coupling of the nuclei with the intervening electrons (thus indirectly). As a result, it provides direct spectroscopic evidence of chemical bonds. Two spins will generally only exhibit \mathcal{J} -coupling if they are linked by chemical bonds, including hydrogen bonds. However, there are many exceptions where so-called “through-space” \mathcal{J} -coupling has been observed.^{18,19} The \mathcal{J} -coupling interaction may be defined by a second-rank tensor of non-zero trace. In isotropic solutions only the average or trace impacts the spectrum. In solids, the anisotropy of the \mathcal{J} -coupling, $\Delta\mathcal{J}$ is also present. However, its angular dependence is identical to that of R_{DD} , which can make separating these two components challenging.²⁰ The effect on the observed spectrum of a spin, S, induced by \mathcal{J} -coupling to a spin, I, is a splitting of the resonance into a $2NI + 1$ multiplet, where N is the number of chemically identical I spins present.

2.6 *Fermi Contact*

The Fermi contact interaction arises from the presence of unpaired electron spin density, $\rho_{\alpha\beta}$, at the nucleus. The only orbitals with non-zero probabilities at the nucleus are *s*-orbitals; as a result, the Fermi contact shift is an isotropic shift of the resonance frequency. The shift of the resonance is temperature dependent.

The presence of the shift, and its temperature dependence, can be understood as a two-site exchange problem. In the case of two coupled spin-1/2 nuclei (Figure 2.8 a and

b), the net polarization of the coupled spin (S) is very small ($N_\alpha \sim N_\beta$ at room temperature), and thus the I spin doublet is of equal intensity. The centre-of-gravity of the resonances is halfway between the two, which also corresponds to the isotropic chemical shift. In the case where the spin S is an electron, the magnetogyric ratio is nearly 1000 times larger than any nucleus, resulting in a much larger net polarization ($N_\alpha > N_\beta$) at room temperature, and the doublet exhibits very different intensities. As with the case of a nucleus, any decoupling results in a single resonance at the centre-of-gravity. However, now because of the large difference in the populations of the two electron states, the centre-of-gravity is not at the true isotropic shift. Since in the high-temperature regime, the relative populations of the two states follow a Boltzmann distribution, following the observed shift over various temperatures should allow extraction of the coupling constant and the isotropic shift. The observed shift of the resonance from the value expected for the “same” species in a diamagnetic system is given by $\Delta\nu/\nu_0$,²¹

$$\frac{\Delta\nu}{\nu_0} = -\frac{A}{\hbar\gamma_I B_0} \langle S_Z \rangle \quad \text{Equation 2.16}$$

where A is the isotropic Fermi contact coupling constant, γ_I is the magnetogyric ratio of the observed nucleus, \hbar is Planck’s constant in hertz and B_0 is the static field. $\langle S_Z \rangle$ is the mean electron spin given by,²¹

$$\langle S_Z \rangle = -\frac{g_e \mu_\beta S(S+1)}{3kT} \quad \text{Equation 2.17}$$

where g_e is the g-factor of an electron (generally taken as -2.0023), μ_β is the Bohr magneton, S is the electronic spin of the paramagnetic centre, k the Boltzmann constant and T the temperature.

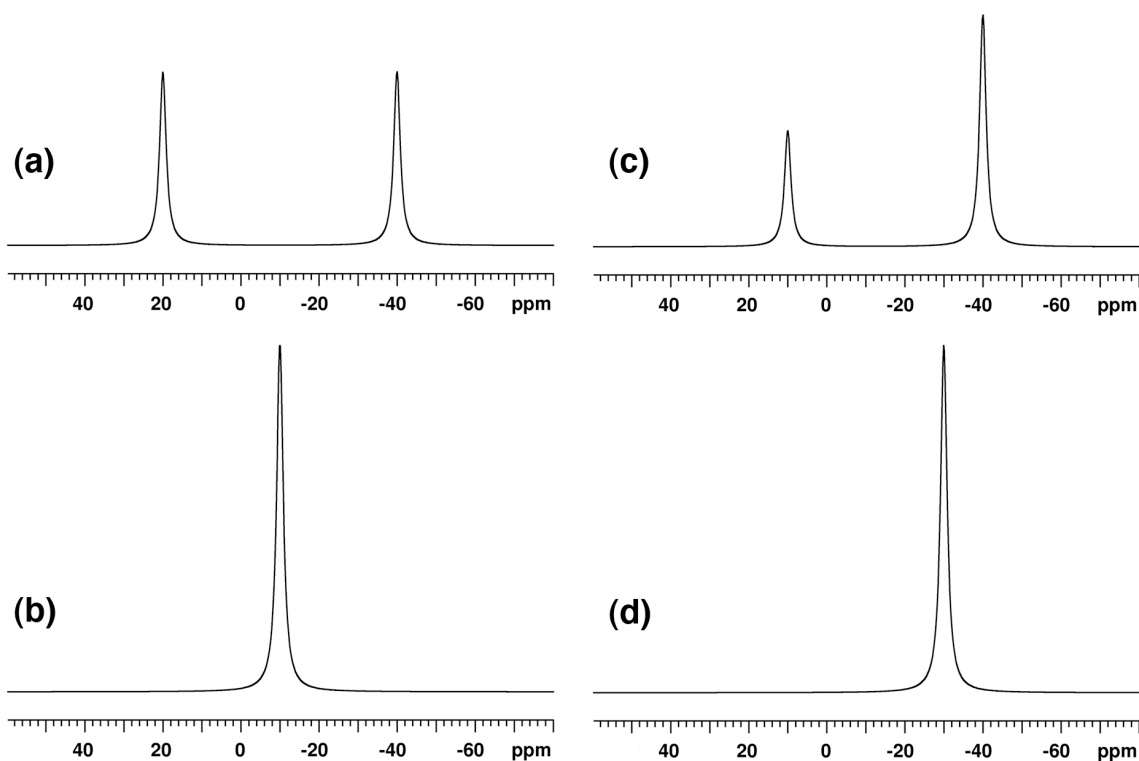


Figure 2.8: Simulated spectra of a spin, I, coupled to a spin, S. In the case where S is another nucleus, the $+1/2$ and $-1/2$ spin state are nearly equally populated (a), and upon decoupling a single peak at δ_{iso} is observed (b). In the case where S is an electron, (c) a greater population difference between $+1/2$ and $-1/2$ states of the electron is reflected in the relative intensities. Decoupling results in a single resonance displaced from δ_{iso} (d). Simulated with STARS.

3 Solid-State NMR

3.1 *Non-Spinning*

Traditionally, all solid-state spectra were collected on stationary samples, either powders or single crystals. The combination of the two allowed for the discovery and confirmation of the orientation dependencies (with respect to the magnetic field direction) of various anisotropic interactions. A single crystal in a particular orientation will give rise to a spectrum consisting of a single line (per transition) with its position dependent upon the typical NMR parameters (e.g., δ_{iso}) and its relative orientation with respect to the field. Thus by rotating the single crystal one can map out the total anisotropy of the interactions to which the nucleus is subject to. A powder may be considered as a very large collection of small crystals (crystallites), which are orientated arbitrarily. The result is a spectrum which is the sum of the spectra of a large number of single crystals covering all orientations of the unit sphere, and is sometimes called a powder pattern. The anisotropy of these interactions in NMR can result in very broad spectra of stationary samples, as can be seen from Figure 2.2 and Figure 2.5. Although these powder patterns can provide vital information about the spin system, when the number of interactions is more than one or two, the fitting of these lineshapes to extract the vital information about the anisotropic interactions can be more challenging. The presence of multiple sites in a sample also complicates analysis due to overlap, putting severe limitations on the complexity of samples amenable to analysis by such solid state NMR experiments. Experiments to enhance resolution of solid-state spectra have thus garnered much attention. The dipole-dipole interactions were the first anisotropic interactions to be

tackled (both heteronuclear and homonuclear) via more complex pulse sequences. Their removal allowed more accurate analysis of shielding tensors and identification of multiple sites. The removal of shielding anisotropy and quadrupole interactions required development of new hardware to modulate the sample (and its interactions) with respect to the static field, as well as novel methods of modulating the spins in spin space.

3.2 *Magic-Angle Spinning (MAS)*

Although Andrew⁹ and Lowe¹⁰ first independently developed the requisite hardware to rapidly rotate a solid sample about a fixed axis with respect to the magnetic field in the late 1950's, it was not until nearly twenty years later that magic-angle spinning (MAS) would become a staple of solid-state NMR. MAS relies on the presence of a $P_2(\cos\theta)$ ($P_2(\cos\theta) = \frac{3}{2}\cos^2\theta - \frac{1}{2}$) spatial relation between many of the anisotropic interactions relative to the static field B_0 . The solutions for the roots of $P_2(\cos\theta)$ are $\tan^{-1}(\sqrt{2})$ and $\pi - \tan^{-1}(\sqrt{2})$, or 54.7356° and 125.2644° , which are of course identical (see Figure 3.1).

By spinning a sample at the magic-angle at a rate faster than the extent of the anisotropy, it can be completely removed. For example, a non-spinning ^{13}C spectrum with a span, Ω of 80 kHz (at a particular field), would require spinning rates of at least 80 kHz to provide a completely isotropic spectrum. However, typically obtainable spinning rates (until very recently) have not exceeded 35 kHz.

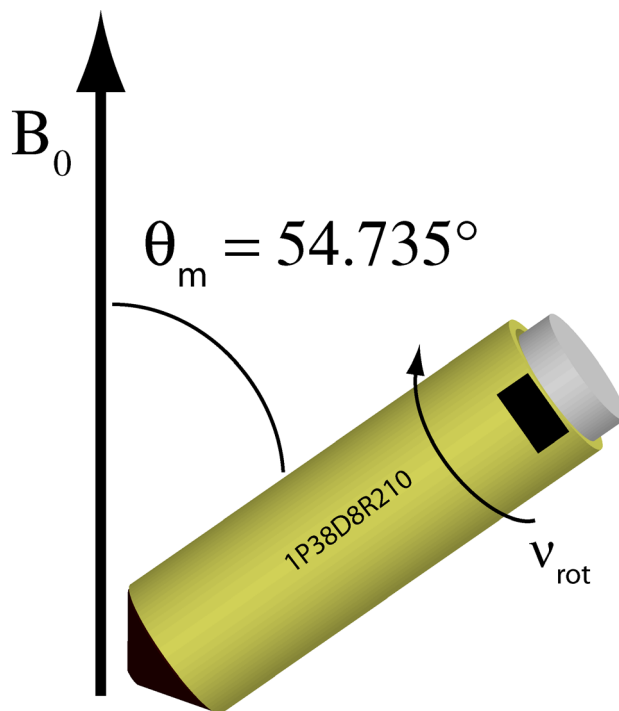


Figure 3.1: MAS sample rotor oriented at the magic-angle (θ_m) with respect to the static field, B_0 , rotating about its axis with a frequency ν_{rot} .

The result of this incomplete averaging on the observed spectrum is the appearance of spinning sidebands which are separated from the peak at the isotropic chemical shift (i.e., the isotropic peak) by an integer multiple of the rotation frequency. Their extent and intensities are governed by the anisotropic interactions the nucleus is subject to. Although fast spinning at the magic angle is capable of providing high-resolution spectra and facilitating the investigation of materials possessing multiple sites, it can come at the sacrifice of crucial information from the non-spinning spectrum such as chemical shielding anisotropy. The non-spinning spectrum along with a series of MAS spectra at various spinning rates, denoted with respect to the span, Ω , of the shielding tensor, are shown in Figure 3.2. At the fastest spinning rates ($\nu_{rot}/\Omega = 2$), a *liquid-like*

isotropic spectrum is obtained, and no information about the anisotropy can be extracted. Of the two slower spinning spectra ($\nu_{\text{rot}}/\Omega = 0.25$ and 0.05 , respectively), only from the latter can one extract a reasonably accurate estimate of all the tensor components.^{22,23} Therefore the acquisition of spectra at different spinning rates can be used to extract different pieces of information (e.g., isotropic shifts *versus* full CSA tensor)

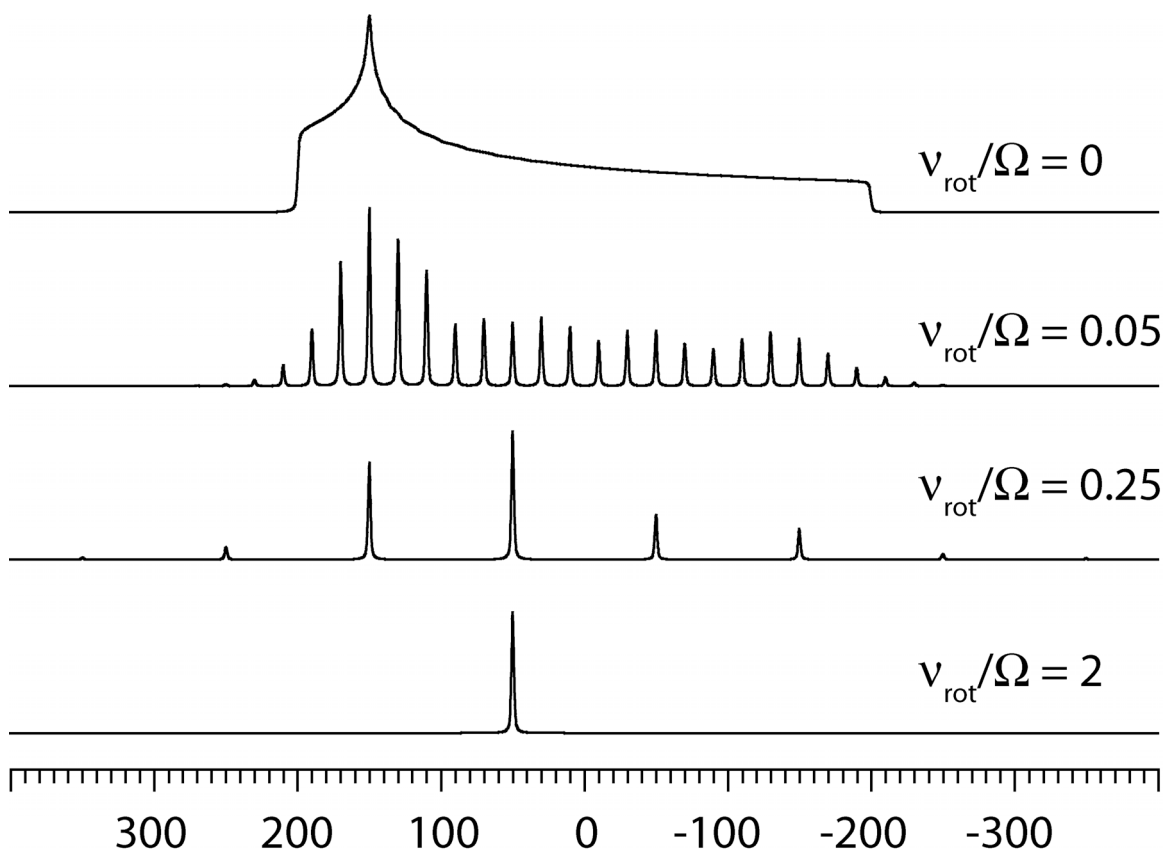


Figure 3.2: The effect of MAS on a spin experiencing CSA. Higher resolution spectra are obtained by spinning faster at the cost of accurate extraction of tensor principal components. Simulated with WSolids.¹⁵

3.3 *Multiple-Quantum MAS*

It was established by Ernst that an n-quantum (nQ) to m-quantum (mQ) coherence transfer-echo can be created which will refocus at some time $k\tau_1$, where k is a constant relating the evolution of the system during the evolution times (τ_1 and τ_2) such that τ_1 and τ_2 are the evolution times before and after the coherence transfer.²⁴ The most well-known and widely used coherence transfer echo is the Hahn-echo, where the coherence transfer involved is the ± 1 to ∓ 1 . In the case where m is the $| -1/2 \rangle, | 1/2 \rangle$ transition and n is any of the other available symmetric MQ transitions (3Q for $I = 3/2$, 3Q or 5Q for $I = 5/2$ etc.), the refocusing time of the echo is a function of the anisotropic quadrupole shift (i.e., the quadrupole broadening observed by MAS). The ratio of this interaction during the two “detection” periods define the slope of the high-resolution axis (see Figure 3.4a).^{25,26}

By collecting a series of experiments varying the initial evolution times of the MQ coherence, t_1 (see Figure 3.3), a 2D interferogram can be constructed which, upon Fourier transformation along both dimensions, yields a 2D spectrum with anisotropically broadened lineshapes in both dimensions (see Figure 3.4a). However, a dimension along the slope defined by the refocusing condition for the given nQ to mQ coherence transfer (i.e., k) possesses resonances completely free of any anisotropic broadening. The time constants, k, for various multiple quantum transitions and for nuclei of varying spin quantum number, I, are well known.^{25,27,28} A t_1 -dependent first-order phase correction in F2 (or t_2) results in a spectrum where the isotropic axis is orthogonal to the directly observed axis, simplifying analysis of spectra with standard NMR processing software.

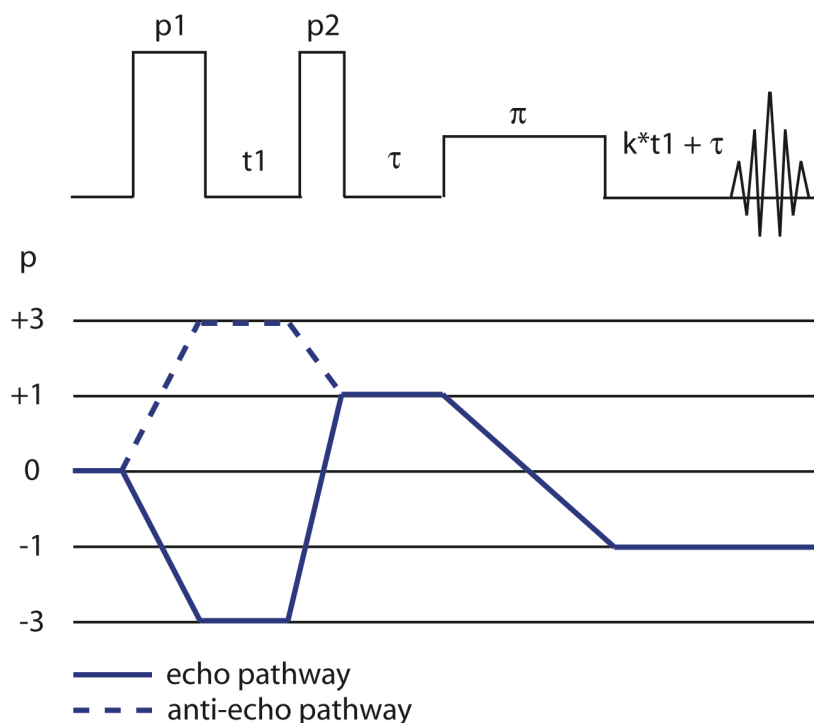


Figure 3.3: Basic pulse sequence for a shifted-echo MQMAS²⁹ along with the coherence-order (p) pathways for the 3QMAS of an $I = 3/2$ nucleus. The coherence order pathway for a shifted anti-echo is also shown.

Although this results in high-resolution spectra of half-integer nuclei for well-ordered crystalline materials, in disordered and/or amorphous systems, inherent distributions in the chemical shielding and quadrupolar parameters result in distributions along both dimensions. The effects of distributions in either the chemical or quadrupole shifts are well-defined for any nucleus of given spin-quantum number, I , and the MQ coherence investigated. In systems with sufficient resolution of different site-types, or with only a *single site*, the distribution of these parameters can provide insight into the distributions of key structural parameters such as bond lengths and bond angles. This has

been used to gain insight into the structural distributions of amorphous SiO₂ using an experiment analogous to MQMAS, dynamic angle spinning (DAS).^{30,31}

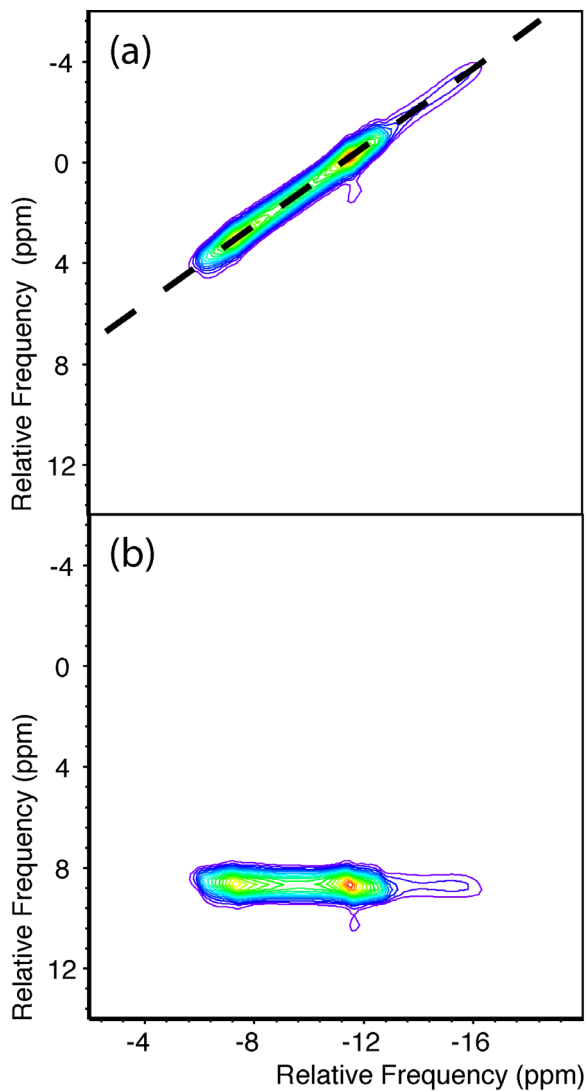


Figure 3.4: Simulated 3QMAS spectra for $I=3/2$ nucleus after 2D FT (a), resulting in anisotropic projections along both orthogonal axes. A high-resolution axis is denoted by the dashed line. After phase correction (b), the isotropic dimension is orthogonal to the directly detected 3Q-filtered MAS dimension. Simulated with SIMPSON.³²

3.4 Dipolar Recoupling under MAS

MAS removes the effects of direct dipole-dipole coupling on the observed spectra. Although this allows acquisition of higher-resolution spectra in solids, it results in the loss of vital internuclear distance information (see equation 2.12). As a result, numerous techniques such as REDOR,³³ REAPDOR,³⁴ TRAPDOR³⁵ and select C, R and S sequences developed by Malcolm Levitt³⁶ have been developed for the controlled re-introduction of the dipole-dipole coupling. These all allow acquisition of high-resolution spectra without loss of the information in the dipole-dipole coupling.

Rotational echo double-resonance (REDOR) and its numerous cousins, REAPDOR, TEDOR, TRAPDOR etc., have become the most widely used methods for the re-introduction of heteronuclear dipole-dipole interactions in the solid state. At their heart, all of these methods rely on modulation of the populations of the spin eigenstates of one (or more) of the spins of interest, in combination with MAS to decrease the efficiency of the spatial averaging of the dipole-dipole coupling over some integer number of rotor periods ($N\tau_r$). One of the simplest ways of doing this is by the application of a 180° pulse. This has the effect of inverting the net macroscopic spin of the nuclei. The dipole field experienced by a spin I near a spin S is depicted in Figure 3.5. For simplicity, the spin, S, is assumed to be of spin-1/2. The argument is still valid in terms of state populations of other spin values; however, a breakdown in the simple spatial vector model occurs for quadrupolar nuclei. The application of the 180° pulse inverts the populations of spin, S (shown as a flipping of the direction of the magnetization vector), which results in a change in sign of the field at spin, I.

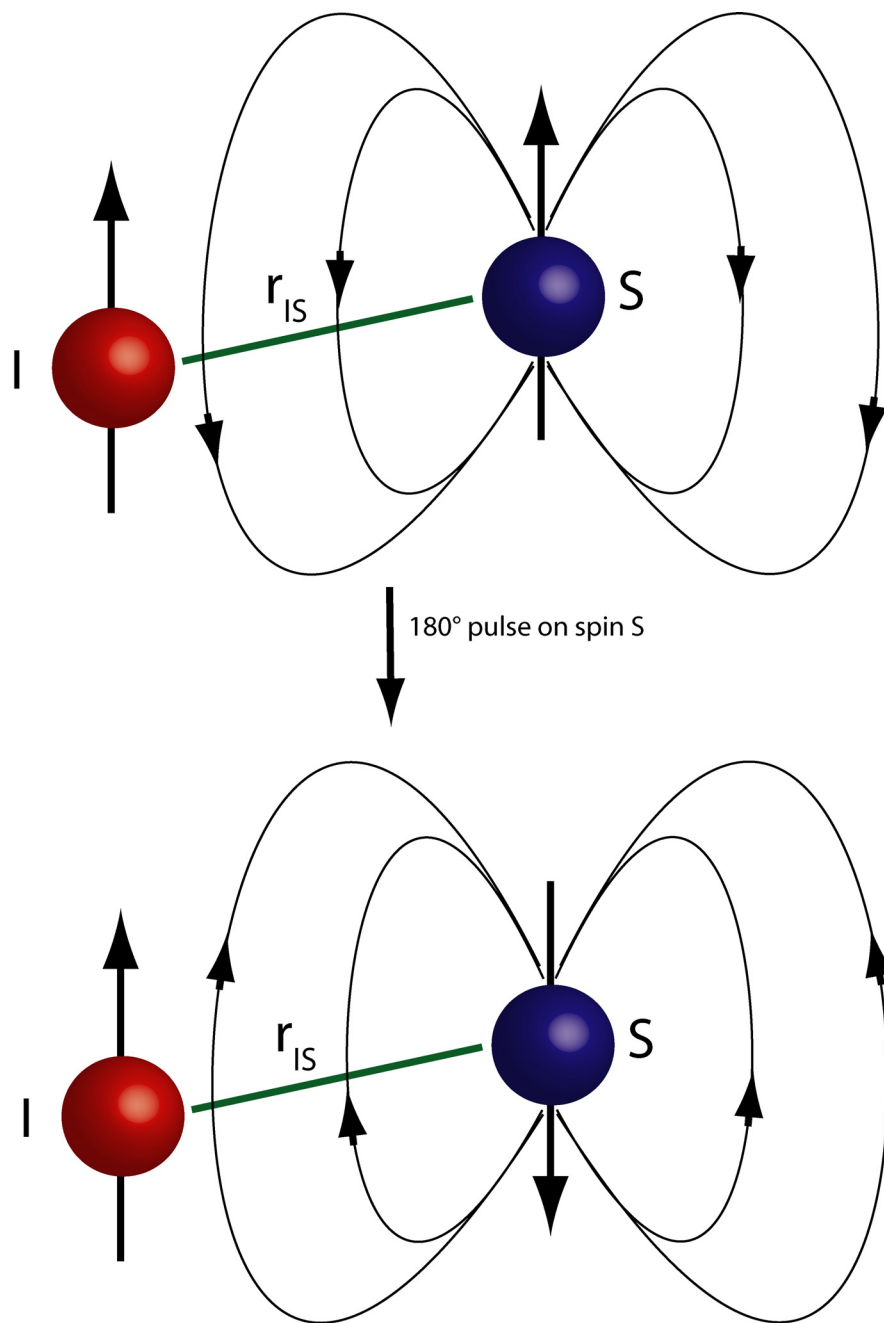


Figure 3.5: The application of a 180° (π) pulse inverts the net magnetization of a nucleus S, changing the sign of the net dipolar field experienced by spin I at a distance r_{IS} .

The most general case of REDOR is where the inversion of the spin state occurs at the mid-point of the rotor cycle (Figure 3.6) over a total number of m , rotor cycles. This simultaneous inversion of the spatial and spin components effectively cancels the effect of MAS, leading to the most effective re-coupling of the dipole-dipole interaction. It should be noted that distance information may be extracted even when the interference with the spatial averaging of the dipole-dipole is not maximal, as long as the experimental conditions are well known.

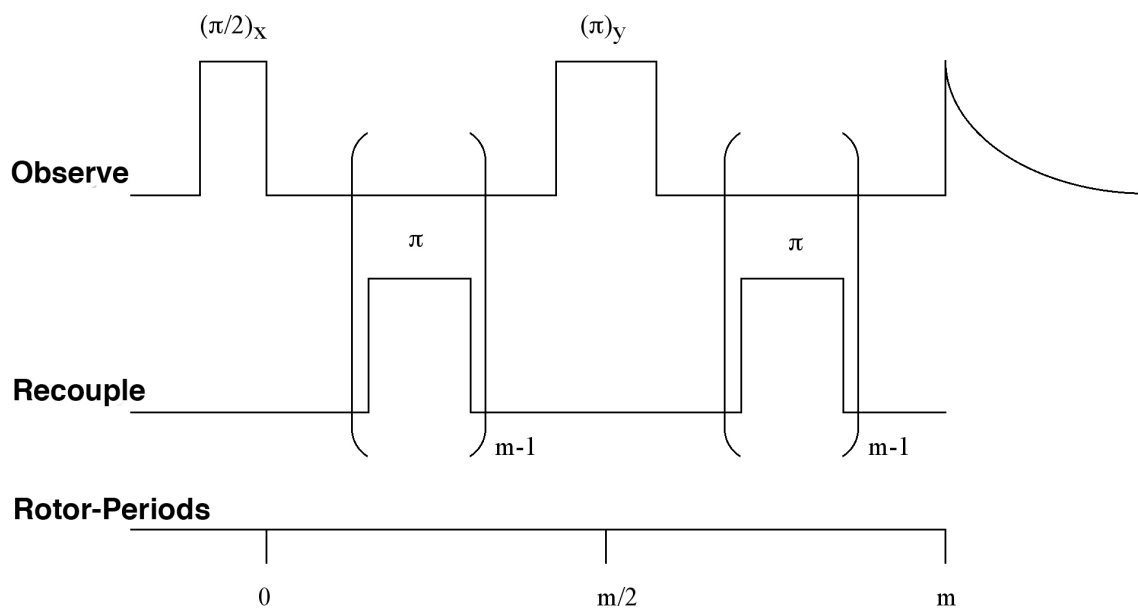


Figure 3.6: Schematic of the REDOR pulse sequence.³⁷ Application of pulses on the recouple channel modulate the populations of the spin-states, disrupting the spatial averaging of the dipolar interaction.

4 Theoretical Investigations of MQMAS

MQMAS has become a crucial tool in the investigation of materials possessing half-integer nuclei.³⁸⁻⁴⁰ However, the intrinsic low sensitivity of the technique has attracted much attention over the decade since its initial development. Two recent methods relying on “special” resonance conditions between the resonance frequencies or rf frequencies with the rotor spinning frequency (rotational resonance and rotary resonance, respectively) have been demonstrated to increase signal-to-noise.^{41,42}

The effect of chemical shielding anisotropy on the intensities of spinning sidebands in MQMAS spectra has been studied previously in systems with smaller quadrupole frequencies, ν_Q .⁴³⁻⁴⁵ From these studies the quadrupole parameters, CSA and the relative tensor orientations (note: a single unique solution is not always possible), could be acquired. The applicability of MQ-variable angle spinning (MQVAS) was investigated by Frydman,⁴⁶ and the greatest dependence of the observed 2D-lineshapes was found for the case of sample rotation at 0° relative to the static field, B_0 . Given that this condition is identical to that of non-spinning, but requires the use of probe/coil designs less efficient than solenoids due to the necessary requirements of the relative orientations of the B_0 and B_1 fields, without any significant benefit over non-spinning, they employed an ideal non-spinning set-up. Experiments (3Q-, 5Q- and 7Q-, where available) under non-spinning conditions for a series of compounds of varying spin quantum number did exhibit lineshapes which could be used to extract the various tensor components and the relative orientations of the respective tensors.

There are however, certain drawbacks to the proposed experiment, arising from its non-spinning nature. The anisotropic quadrupolar broadening under non-spinning conditions is approximately three times that under MAS, significantly reducing any resolution of multiple sites. Dipole-dipole couplings (homo and heteronuclear) are completely unaveraged, resulting in broadening of the resonances, possibly to the point of completely obscuring the information of interest. The efficient excitation and conversion of MQ-coherence can be less efficient than under MAS⁴² and, if it is not equal for all crystallite orientations, can lead to highly distorted lineshapes.

In this chapter, these dependencies are investigated theoretically and experimentally in order to determine the general utility of off-magic-angle experiments to obtain higher resolution and/or more information (e.g., EFG and CSA tensors) than from experiments done at the magic-angle. The ⁸⁷Rb of rubidium perchlorate is often used as a model compound to test novel high-resolution techniques, and the EFG and CSA tensors are well known, allowing comparison of calculated and experimental spectra, without the need to make approximations for relative tensor orientations. The applicability to amorphous systems is probed using the ¹¹B signal of amorphous B₂O₃.

4.1 Materials & Methods

4.1.1 Sample Preparation

RbClO₄ was purchased from Alfa Aesar and used without further purification. Amorphous B₂O₃ was obtained by dehydration of H₃BO₃ in a platinum crucible over a meaker burner. The melt was left for approximately 1 h, after which the escape of water

vapour was no longer observed. This molten B_2O_3 was subsequently quenched by immersion of the bottom of the crucible in de-ionized water at room temperature.

4.1.2 NMR

All experiments were acquired on a Varian Inova 600 spectrometer ($B_0 = 14.1$ T) equipped with a 3.2 mm double-resonance T3-probe (Varian-Chemagnetics). The rotor angle was set by recording the ^{23}Na (158.625 MHz) spectrum of sodium nitrate ($NaNO_3$), and simulation of the spectra with the STARS® software as implemented within the VnmrJ environment.

^{11}B MAS spectra and T_2 measurements were acquired at 192.404 MHz employing an rf nutation frequency of 50 kHz and a Hahn-echo sequence.⁴⁷ MQMAS spectra were acquired using a shifted echo pulse sequence as per Massiot *et al.*,²⁹ employing rf nutation frequencies of 155 kHz for the first (4.2 μs) and second pulses (1.2 μs), and 15.6 kHz (16 μs) for the soft central-transition selective π -pulse. The nutation frequencies (as measured with 0.1 M H_3BO_3) were found not to change with the increasing angle, and thus any increase in S/N is assumed not to be due to the coil sitting in a position closer to the most efficient orientation of 90° with respect to B_0 *.

^{87}Rb MQMAS spectra of rubidium perchlorate were acquired using a shifted-echo sequence, but with FAM-1⁴⁸ conversion pulse train replacing the second pulse in the standard sequence (Figure 3.3, page 25) to enhance sensitivity. The accuracy of the

* The field produced in a solenoid coil is directed along the wind axis, yet the field B_1 affecting the nutation is only that component orthogonal to B_0 . Thus, the maximum field at the same input voltage is achieved when oriented at 90° to B_0 .

magic angle was verified using a 2D satellite transition MAS (STMAS) experiment of the sample, performed without modifying the parameters determining the mean angle of rotation.⁴⁹

4.1.3 Simulations

MQMAS simulations were done using the SIMPSON program,³² and a shifted-echo sequence. Filtering and detection of the appropriate matrix elements allowed for selection of the desired coherence pathways (i.e., echo or anti-echo). Spectra were processed using the program Risonanza Magnetica Nucleare (RMN),⁵⁰ with 100 Hz of Gaussian broadening applied in both dimensions. The apodization function in the directly detected dimension had a t_1 -dependent shift of its maximum so as to coincide with the top of the echo in the time-domain for all increments. A t_1 -dependent first-order phase correction (i.e., shearing) was also applied. Calculations were done using hard-pulse excitation and conversion pulses of 4.2 and 1.0 μs in duration ($\nu_{\text{rf}} = 160$ kHz), respectively, followed by a soft π -pulse of 10 μs ($\nu_{\text{rf}} = 25$ kHz). Spectral widths in both dimensions were synchronized with the MAS frequency of 10 kHz.

¹¹B MQMAS simulations were done for a pseudo-^{[3]B} site ($C_Q = 2.6$, $\eta = 0.2$). The simulations were done varying the anisotropy, $\delta_{\text{CSA}} = 0, 5$ and 10 ppm, which is in line with experimental results.⁴³ The rotor angle was varied from 54.73561° to 55.73561° in steps of $+ 0.5^\circ$.

Simulations for RbClO_4 were done using the known quadrupolar and CSA principal components reported previously:⁵¹⁻⁵³ $C_Q = 3.29$ MHz, $\eta = 0.21$, $\delta_{\text{CSA}} = 13.8$ ppm and $\eta_{\text{CSA}} = 0.6$. The Euler angles relating the relative tensor orientations (ψ, χ, ξ) in

the ‘‘Haerberlen-Mehring’’ convention (i.e., δ_{CSA} and η_{CSA}) were set to those obtained from single-crystal studies, (94, 28, 87).⁵³

4.2 SIMPSON and Evaluation of Spin Dynamics

The SIMPSON (SIMulation Program for SOLid-state Nmr spectroscopy) program³² is a tool which allows full numerical evaluation of the Liouville-von-Neumann equation of motion,⁵⁴

$$\frac{d}{dt}\rho(t) = -i[H(t),\rho(t)] \quad \text{Equation 4.1}$$

where $\rho(t)$ is the reduced density matrix operator and $H(t)$ is the time-dependent Hamiltonian to which the spin(s) is(are) subject. The formal solution to $d\rho(t)/dt$ is given by

$$\rho(t) = U(t,0)\rho(0)U^\dagger(t,0) \quad \text{Equation 4.2}$$

where $\rho(0)$ is some initial density operator (this can be for example at thermal equilibrium, or after some given preparation), $U(t,0)$ is the operator responsible for the evolution of the spins from time zero to time t . $U(t,0)$ is related to the Hamiltonian by the exponential of its integral over the time, $t=0$ to $t=t$, the numerical calculation of which may be obtained from the time-ordered product,

$$U(t,0) = \prod_{j=0}^{n-1} e\{-H(j\Delta t)\Delta t\} \quad \text{Equation 4.3}$$

where n is the number of time intervals and Δt is the time interval over which the Hamiltonian is considered to be time-independent. For each time interval, exponentiation is done by diagonalization of the matrix representation of the Hamiltonian. For simulation of time-dependent experiments, it is important to verify that the time-interval chosen is small enough to provide a reasonable approximation for the time-dependence.

All of the Hamiltonians (internal and external) are described by their high-field components in the Zeeman interaction frame. As a result, certain conditions incompatible with this approximation will lead to erroneous results; for example, the evaluation of the effects of quadrupolar or dipolar coupling fields on the order of or larger than the Zeeman frequency. These approximations make calculations more efficient, although, the user must take care to keep them in mind before starting and in interpreting results.

4.3 MQ off-MAS

Refocusing of the coherence transfer echo occurs at a time $k \cdot t_1$, where k is the ratio of the evolution effect of the interaction(s) to be removed in the two evolution periods. Typically for MQMAS, this is the anisotropic quadrupole shift (or broadening). Other interactions which may lead to anisotropic broadening, such as the chemical shift anisotropy and dipole-dipole coupling, are removed by virtue of carrying out the experiment at the magic angle. It should be noted that the homonuclear multiple-quantum single-quantum correlation experiment does not need to be done at the magic-angle, this is simply convenient because of the removal of interactions having $P_2(\cos\theta)$ spatial dependence.

Recently, it has been shown that acquisition of spectra of half-integer quadrupolar nuclei at angles off the magic-angle by up to 2° can have significant impact on both the spin-lattice and the spin-spin relaxation time-constants.⁵⁵ The former often limits the rate at which experiments may be repeated for co-addition, and thus the total acquisition time of the experiments. The latter relaxation has a significant impact on the natural linewidths of the resonances, and under the condition that inhomogeneous broadenings are small with respect to homogeneous broadenings, it can significantly impact the observed linewidths.

Experiments investigating the effect of the spin-spin relaxation for the coherence order, p (T_2^p) for MQMAS (3Q and 5Q) or satellite transition (T_2^{ST}) for STMAS (ST1 and ST2), have recently been carried out for the ^{27}Al site in AlPO_4 (berlinite).⁴¹ Their results confirm the previous results reported by Kwak and co-workers⁵⁵ for the enhancement of the central transition spin-spin relaxation. They develop a pulse sequence for direct measurement of the spin-spin relaxation of the MQ coherence: simply, a coherence transfer-echo between the two evolving coherences (e.g., ± 3 to ∓ 3) in analogy to the well-known Hahn-echo used for the measurement of T_2^{1Q} . By varying the initial evolution time, the relaxation of this coherence arising solely from homogeneous interactions can be obtained by a fit of the echo intensities *versus* the total evolution time (twice the initial evolution time). They found that the homogeneous linewidth for the $p=3$ coherence decreases, and because of the lack of any significant inhomogeneous broadening of signal, a decrease in the isotropic dimension linewidth is also observed. This has significant benefits because the increased spin-spin relaxation

time-constants (T_2^{CT} and T_2^{3Q}) result in enhancements of signal-to-noise and resolution in the isotropic dimension.

Although in this case, off-MAS MQ experiments show significant benefit, the authors underemphasize the fact that their selected model system is virtually free of significant additional anisotropic interactions. The nearest Al-P distance is 3.097 Å leading to dipole couplings, R_{DD} , of 430 Hz. When spinning off the magic-angle by $\pm 1^\circ$, a residual dipole coupling of only *ca.* 10 Hz thus remains. Aluminum-27 generally possesses fairly small shielding anisotropies ($\Omega > 50$ ppm), although some exceptions have been observed.⁵⁶⁻⁵⁸ In this particular case, however, the high local symmetry of the aluminum site (nearly tetrahedral, T_d) precludes the presence of any significant anisotropy of the shielding.

In order to investigate the *real-world* applicability of MQ off-MAS experiments for nuclei experiencing non-zero shielding anisotropies, and for samples where the observed linewidths are dominated by inhomogeneous broadenings, a series of calculations and experiments were done. Theoretical calculations/simulations of quadrupolar spins also subject to shielding anisotropy were undertaken to investigate the impact on the expected lineshapes and resolution for the case of “small” deviations ($< 2^\circ$) from the magic-angle.

4.3.1 Amorphous B_2O_3

As a test of the MQ-OMAS experiment for a non-ideal system, ^{11}B 3QMAS was chosen. Boron is well known to possess an anisotropic shielding (albeit small in most cases)^{43,59} and due to its high natural abundance (80.1%), even under MAS the efficient averaging of homonuclear dipole-dipole couplings can require fast spinning, and should

be an even greater challenge when off the magic-angle. MQMAS spectra for a typical three-coordinate boron site in borates ($C_Q = 2.6$ MHz, $\eta = 0.2$) were calculated at angles deviating from the magic-angle by 0, +0.5 and +1.0 degrees with shielding anisotropies, δ_{CSA} , of 0, 5 and 10 ppm. The sheared spectra are shown in Figure 4.1. The simulations exhibit a clear change in the observed lineshape with increasing shielding anisotropy and increased deviation from the magic angle. It is worth noting that even in the absence of shielding anisotropy, the acquisition of MQMAS off the magic angle by 1° (and even at 0.5°) shows some distortion which will increase the observed linewidth of the signal in the isotropic dimension. Projections of the isotropic dimensions (Figure 4.2) show no change in the centre-of-gravity in the isotropic dimension (necessary for extraction of NMR parameters). However, a pronounced change in the lineshape is observed. Without careful analysis of the whole 2D lineshape, distortions of this type could potentially be misinterpreted as arising from multiple sites.

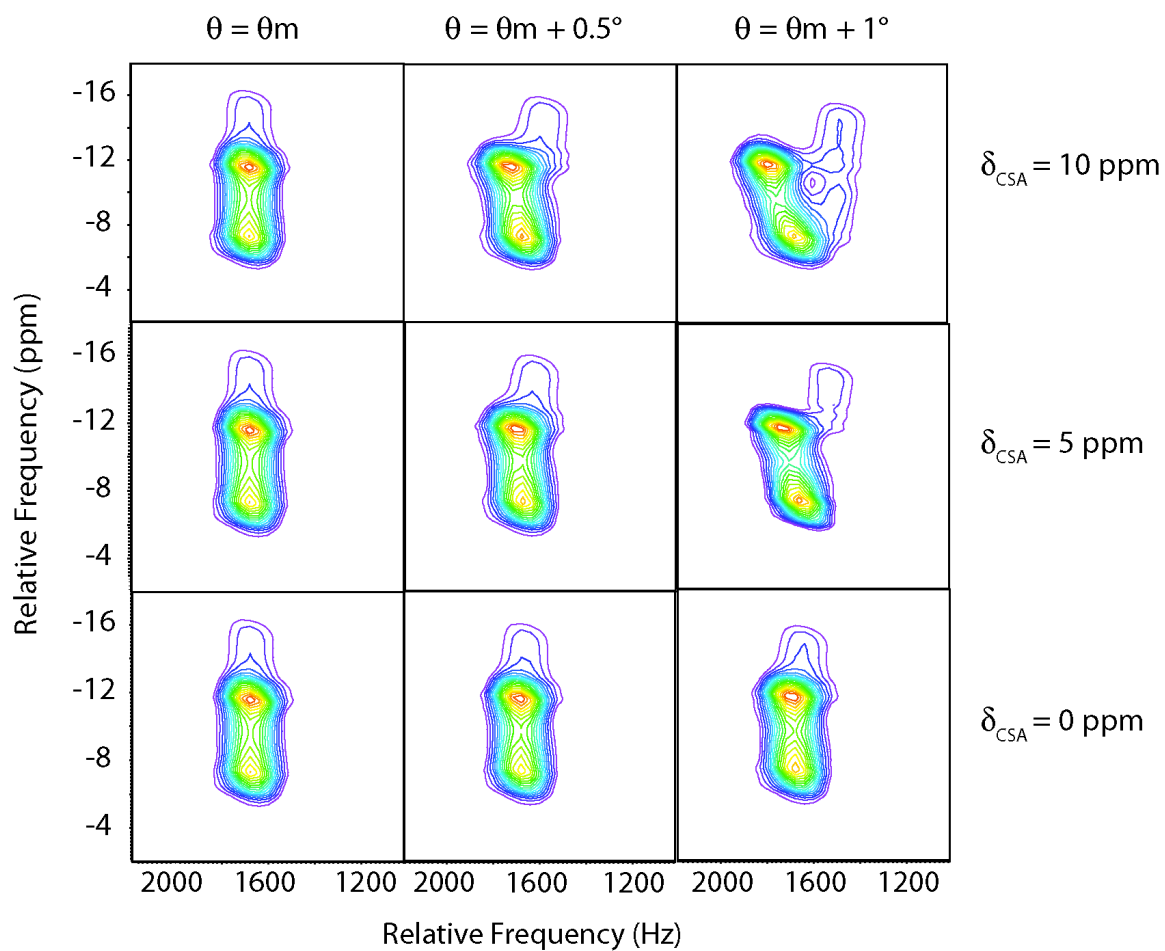


Figure 4.1: Simulations of the 2-dimensional MQMAS spectra (^{11}B at 14.1 T, $C_Q = 2.6 \text{ MHz}$, $\eta = 0.2$) showing the effects of shielding anisotropy, upon deviation from the magic angle.

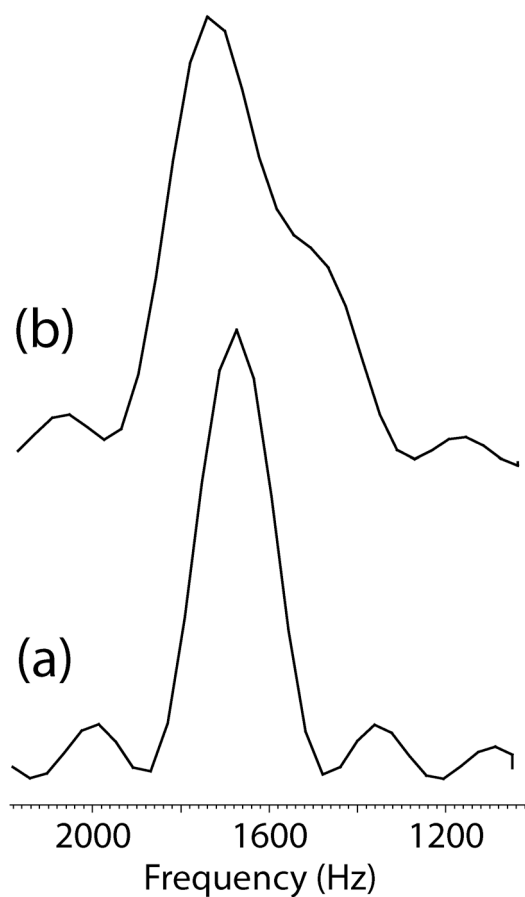


Figure 4.2: Isotropic projections of the $\delta_{\text{CSA}} = 10$ ppm simulated MQMAS spectra (a) at the magic-angle and (b) off-angle by + 1.0 degree. The centre-of-gravity is unchanged, however, the off-angle spectrum displays an anisotropic lineshape.

In addition to the effects of shielding anisotropy probed via simulations of the spin-system, the impact of MQ-OMAS on samples subject to inhomogeneous broadenings due to structural disorder and stronger homonuclear dipole-dipole couplings was investigated using amorphous B_2O_3 . Spin-spin relaxation measurements of the central transition revealed an increase in the relaxation time constant, T_2 , from 4.9 to 6.4 ms (as fit to a single-exponential decay) when off the magic-angle. This corresponds to significant narrowing of the intrinsic (homogeneous) linewidth from *ca.* 204 Hz to 156 Hz.

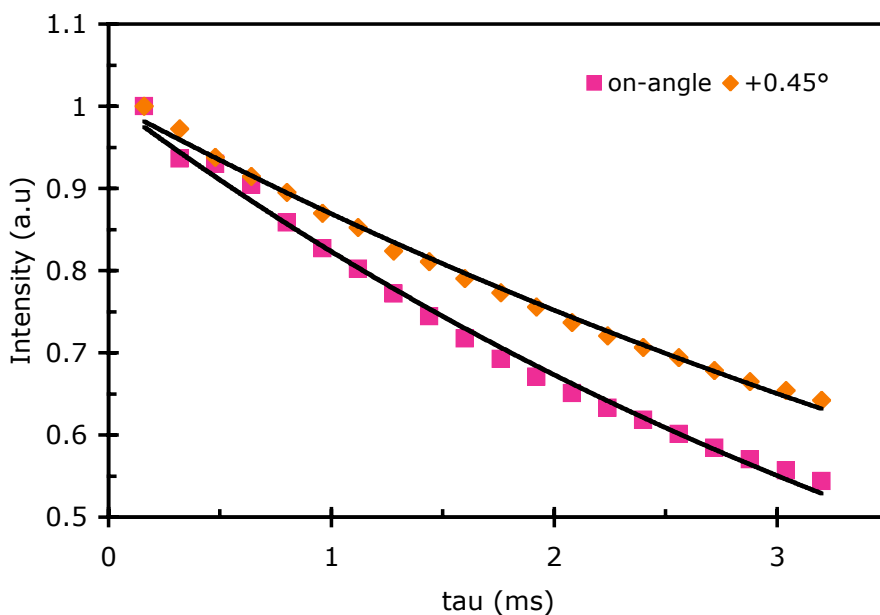


Figure 4.3: ^{11}B NMR T_2^{CT} relaxation data acquired using a Hahn-echo for B_2O_3 . Single-exponential fits yield average spin-spin relaxation time constants of *ca.* 4.9 and 6.9 ms for on and off-angle ($+0.45^\circ$) experiments, respectively.

For AlPO_4 , Amoureux and Trebosc observed an increase in T_2^{CT} of 30%, and of 79% in $T_2^{3\text{Q}}$. With the observation of an increased relaxation time constant for the ^{11}B central transition signals in B_2O_3 , the effect of an increase in $T_2^{3\text{Q}}$ on the observed 3QMAS spectrum was probed. As a shifted-echo 3QMAS sequence was used, the intensity of the echo observed is determined by $T_2^{3\text{Q}}$ during the evolution period t_1 , and by T_2^{CT} during the central-transition evolution periods, τ and t_2 . Increases in either/both of these would result in increased echo intensity over the t_1 values arrayed. A plot of the skyline (maxima) projection of the magnitude-mode echo spectrum (effectively the magnitude-mode time-domain data in t_1), Figure 4.4 shows increased echo intensity upon increased deviation from the magic-angle. In order to gauge any possible enhancement in

resolution in the isotropic dimension, Fourier transformation along the second-dimension is required. The isotropic projections of three spectra are shown in Figure 4.5. Upon slight deviation of the rotor angle ($+ 0.25^\circ$), an increase in the intensity of the boroxol-ring site (-1 kHz) is observed, together with a negligible decrease in the linewidth. The signal corresponding to non-ring BO_3 (~ 2.2 kHz) seems to decrease in intensity relative to the boroxol signal. Further deviation of the angle results in a significantly broadened non-ring signal, a slight broadening of the boroxol resonance, and decreases in peak height. The amorphous nature of the sample obfuscates any characteristics in the two-dimensional lineshape, which would allow a more confident assessment of these observations. However, in light of the simulations using quadrupole and CSA parameters in line with those expected for this system, it would not be unreasonable to assume that the increased linewidths in the isotropic dimension are largely a result of shielding anisotropy. The effects of homonuclear dipole-dipole interactions, however, cannot completely be dismissed as making at minimum some contribution to the increased linewidth.

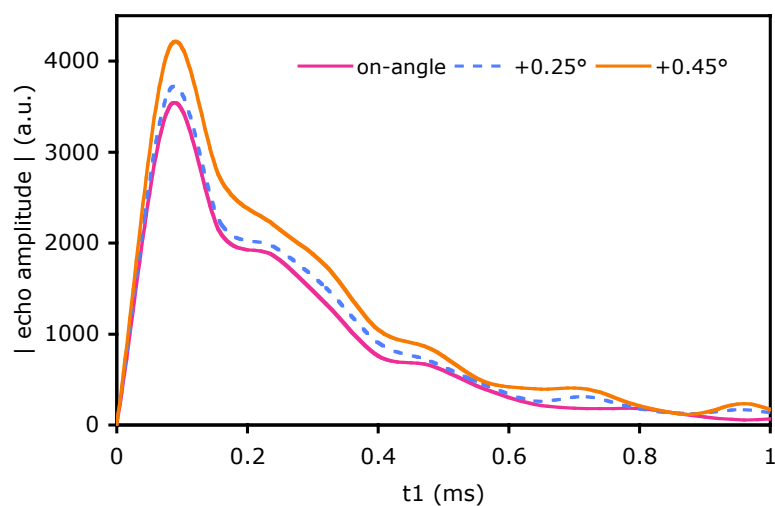


Figure 4.4: Skyline projections of the magnitude-mode echo spectra. The increased T_2^{CT} and T_2^{3Q} with increasing deviation from the magic angle results in increased echo intensity.

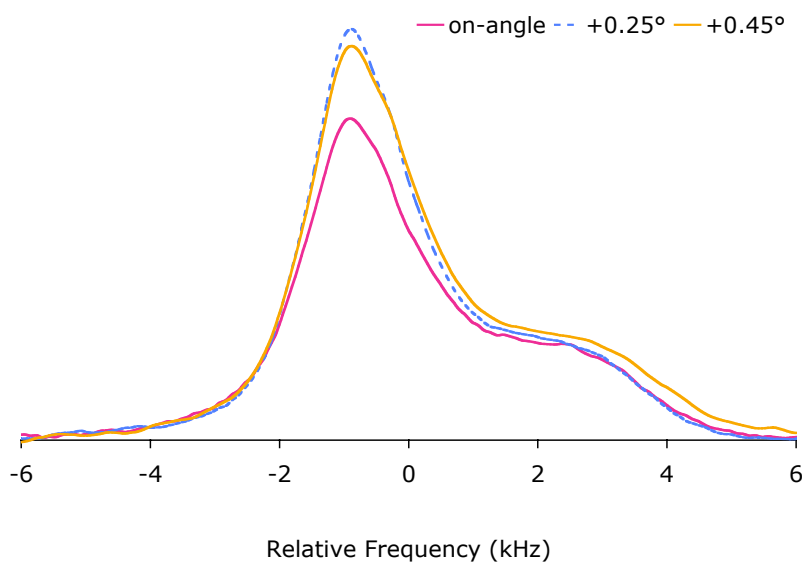


Figure 4.5: Projection of the isotropic dimension (F1) of ^{11}B MQMAS spectra of B_2O_3 acquired on-angle, $+0.25^\circ$ and $+0.45^\circ$.

4.3.2 Rubidium Perchlorate (RbClO_4)

Rubidium perchlorate does not suffer from the significant inhomogeneous broadenings due to the structural disorder of the amorphous boron trioxide; however, it is known to possess a non-zero shielding anisotropy.⁵³ The isotropic projection of the ^{87}Rb 3QMAS (Figure 4.6) clearly shows an increase in the linewidth for the off-angle experiment (from 400 to 510 Hz). The simulated MQMAS results predict a 100 Hz increase in the linewidth for the system (220 vs. 320 Hz). It is worth noting that although neither the central-transition spin-spin relaxation rate (T_2^{CT}) nor that of the triple-quantum coherence ($T_2^{3\text{Q}}$) were measured, an increase in the echo intensity of *ca.* 13% off the magic-angle was observed; thus one or both must be enhanced. As these simulations ignore the effects of relaxation completely, the increased linewidth is dominated by the presence of shielding anisotropy, and given the agreement with the simulations, it seems that in this case, $T_2^{3\text{Q}}$ is only slightly modified by spinning off the magic-angle, and thus the enhancement observed for berlinite⁴¹ may not be the rule.

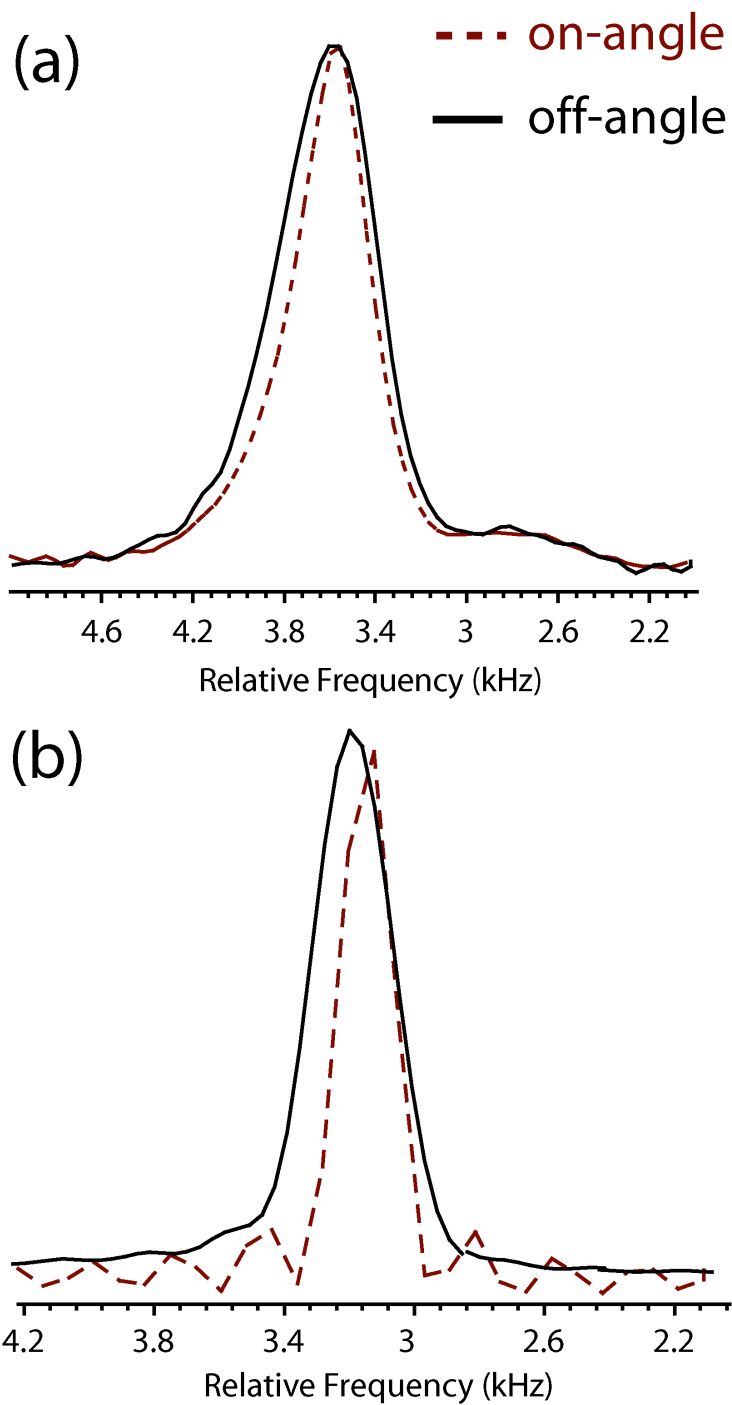


Figure 4.6: F1 projections on- and off-angle (55.516°) obtained from (a) experiment and (b) numerical simulations.

4.4 Conclusions

Despite the observation of decreased relaxation rates and thus the potential for increased resolution by performing MQMAS experiments off the magic-angle, the presence of even fairly small shielding anisotropies ($\delta_{\text{CSA}} = 5\text{-}15$ ppm) can easily offset any potential enhancement. In fact, for systems with larger anisotropies, the potential of obtaining spectra with misleading lineshapes is significant.

In systems with sizeable CSA (with respect to the second-order linewidth of the central-transition), the 2D lineshapes should be characteristic of the magnitudes of the components of the two tensors and their relative orientation in principle allowing extraction of all the parameters by a single experiment.

4.5 Future Work

Although an argument has been proposed to explain the observation of differences in the spin-lattice and spin-spin relaxation time constants for half-integer quadrupolar nuclei at angles deviating from the magic-angle based on rotational resonance, no definitive theoretical treatment has been shown to completely explain all the observed phenomena. In addition, it has been noted that the relaxation of spin-1/2 nuclei also exhibit angle-dependent relaxation.⁶⁰ A better understanding of the origins of this phenomenon, and a method by which to predict the effect could be beneficial in the acquisition of spectra with very-long spin-lattice relaxation times such as ^{29}Si and $^{107/109}\text{Ag}$. Such a model may also allow for a simple method by which to obtain decoupling of other nuclei by reducing their spin-lattice relaxation times, thus negating the need for any additional rf.

5 Borates

Boron containing glasses and crystals have various applications such as the everyday Pyrex® used in laboratory and kitchen glassware. Barium borate crystals have also been exploited for their non-linear optical properties.⁶¹⁻⁶³ Another application of glassy materials is for the storage of radioactive byproducts from the production of nuclear power. Glasses such as the French R7T7 glass are largely composed of SiO₂ and B₂O₃ (although many more components are also present in these glasses).⁶⁴⁻⁶⁸ These glasses must be capable of containing radioisotopes for upwards of a thousand years, and thus their long-term stability must be examined. The ability of the sodium borosilicate glass system to produce inhomogeneous glasses is well-known.^{69,70} Glasses in this system can separate into silicate-rich and borate-rich phases, the latter being susceptible to dissolution by acidic solutions. Clearly a readily dissolved glass would be a poor containment material. It has been shown that this immiscibility varies with alkali type. In this section, NMR of a series of simpler alkali-borate glasses is used in an attempt to better understand what (if any) possible structural differences can be ascribed to the observed differences in bulk properties. Differences in the degree of network depolymerization of the glasses, which can affect their solubility, with different alkali cations are probed using high-field MAS and MQMAS experiments. In addition, the use of double-resonance dipolar recoupling methods are investigated to probe alkali-boron interactions, and as a possible method of detecting phase separation in more complex systems.

5.1 Structure of Glasses

Glasses are materials which lack long-range periodic translational order and exhibit “glass-transition behaviour”.⁷⁰ This so-called glass-transition behaviour is typically observed over a region, under which an endothermic release of energy is observed by calorimetric measurements, such as differential scanning calorimetry. Figure 5.1 shows a typical diagram⁷⁰ illustrating the formation of a glassy-state from an initial liquid. Rapid, or “super-cooling” allows insufficient time for crystallization, yet increases the viscosity until a solid is formed at the glass-transition temperature, T_g .

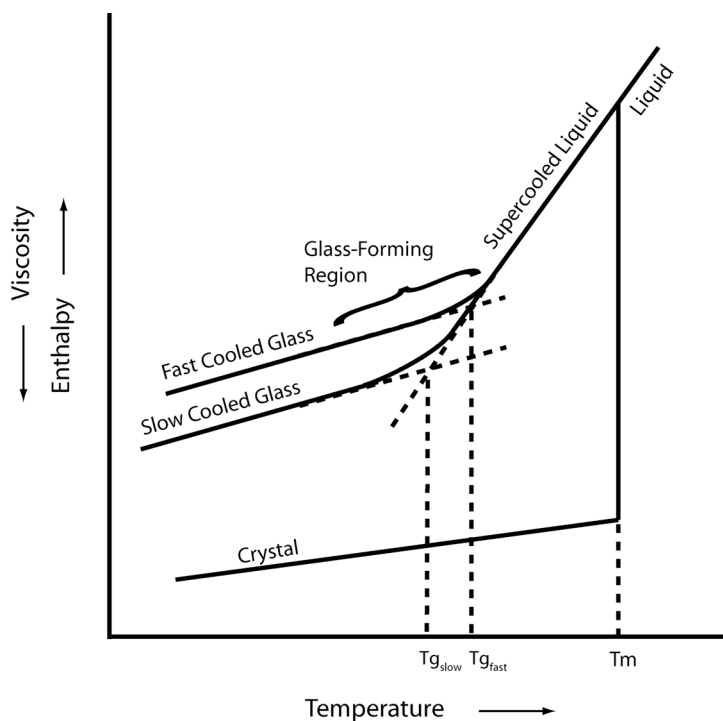


Figure 5.1: Enthalpy (or viscosity) of a material as a function of temperature, showing the formation of crystalline or glassy products by cooling at different rates. The melting point (T_m) and glass transition temperatures (T_g) are shown.

Most structural models of oxide glasses are based on extensions of models devised to describe silicate glasses. The most widely used model of glassy oxide structures is the continuous random network model, which is built upon the rules proposed by Zachariasen.⁷¹ The continuous random network model relies on a series of rules for any glass structure:

- 1) Each oxygen may be linked to no more than 2 cations.
- 2) The oxygen coordination of the network forming cation must be small (generally less than 5). Higher coordination numbers would make the cation:oxygen ratio too small to have a continuous network.
- 3) Oxygen polyhedra share only corners. No edges or faces are shared. This ensures that the network is an open structure.
- 4) At least 3 corners of any oxygen polyhedra must be shared in order to form a three-dimensional network

In borate glasses the network forming cation is boron (boron and silicon in borosilicates) since it possesses an electronegativity similar to that of oxygen and forms a relatively covalent bond.⁷² The electronegativity difference between alkali and alkaline earth metals and oxygen is much greater, thus the interactions are more ionic in nature. As a result, they generally do not form part of the network, rather they act to modify the network. In silicates, the addition of network modifiers often result in breaking a Si-O-Si bond, creating Si-O---Mⁿ⁺ interactions.^{70,73,74} Another change which may be brought about by network modifiers is a change in coordination number of the network former. This is a common characteristic of many glass forming materials; P₂O₅,⁷⁵ B₂O₃,⁷⁶ TeO₂^{77,78} and is believed to occur in GeO₂^{79,80} glasses. While a glass lacks the basic

symmetry operations and periodic translational order of crystalline counterparts, the local site symmetry is very similar between the two (coordination numbers, bond lengths and bond angles etc.).

Amorphous boron trioxide is composed solely of three-coordinated boron ($^{[3]}\text{B}$) species and oxygen. All of the oxygen atoms are two coordinate and bridge adjacent boron atoms, and are referred to as bridging oxygens (BOs). The addition of alkali cations (in the form of the alkali oxide) to B_2O_3 requires the conversion of the neutral boron units to an anionic unit. There are two possible mechanisms for this on borates (see Figure 5.2). The first mechanism is by increasing the coordination number of boron from three to four ($^{[4]}\text{B}$). This results in increasing network connectivity and creates a species possessing a -1 charge with which to balance the $+1$ charge of the alkali cation. The second mechanism, in contrast, involves the breaking of B-O-B bonds and reduces network connectivity. This forms a non-bridging oxygen (NBO), which possess a localized charge of -1 (per NBO, the maximum number of NBOs per boron atom being 3). $^{[4]}\text{B}$ species always have all bridging oxygens and thus only a *single* type exists. For $^{[3]}\text{B}$ species, the number of NBOs provides initial distinction between sites. For this reason, a method for further delineating the type of $^{[3]}\text{B}$ species is helpful. One method extends from the commonly used Q^n naming scheme used for silicates; in this case, it is the T^n system. The T standing for trigonal (or ternary) and the superscript n denoting the number of bridging oxygens directly bonded to the boron atom in question. Thus for example in amorphous B_2O_3 where all oxygens are BOs, all of the boron atoms are of the T^3 variety. In Figure 5.2, the hypothetical formation of a $^{[3]}\text{B}$ species with a single NBO is depicted; such a boron atom would be termed a T^2 . The formation of $^{[4]}\text{B}$ species precedes the formation

of NBO-bearing species at low alkali concentrations (< 30 mol % alkali oxide). Beyond this concentration, NBOs are expected to form in addition to (or possibly in place of) $^{[4]}\text{B}$ species.⁸¹⁻⁸³

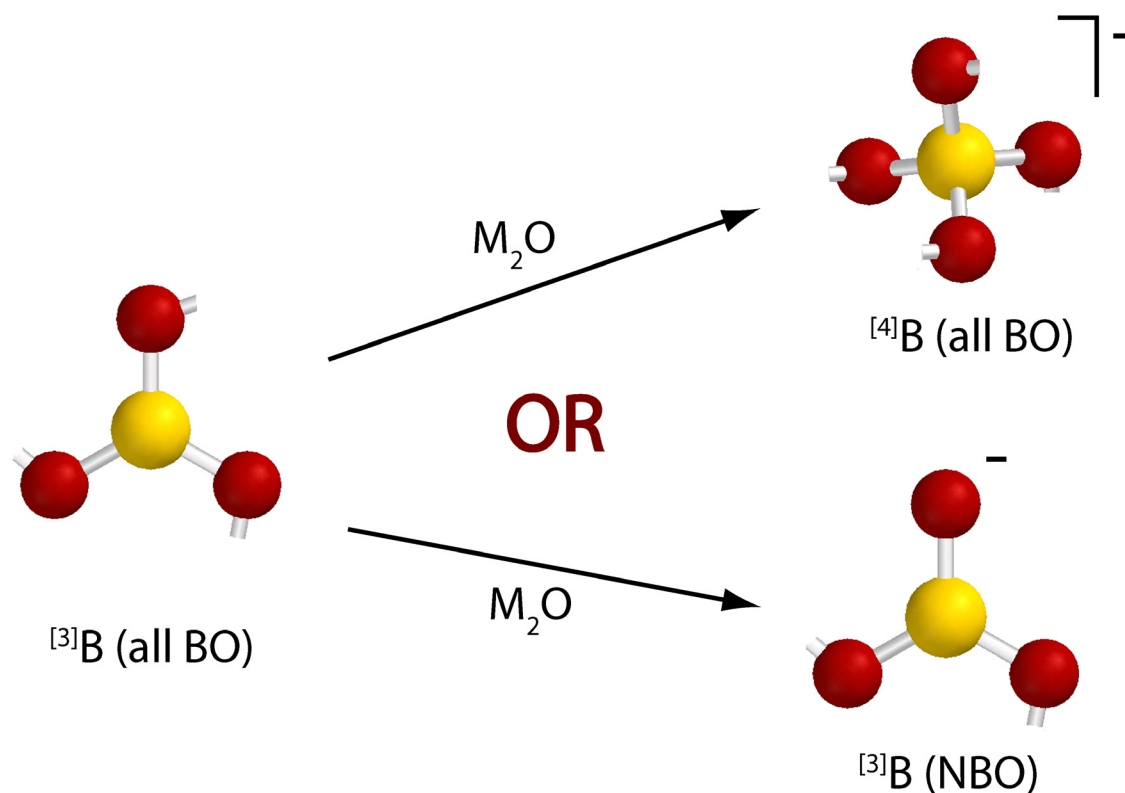


Figure 5.2: Addition of alkali cations to a borate (in the form of alkali oxide) requires formation of anionic borate species. The two possibilities are $^{[4]}\text{B}$ sites or $^{[3]}\text{B}$ species with non-bridging oxygens. The B-O-B bonds to additional B are shown cutoff for clarity.

In this chapter, boron-11 NMR is used to probe the mechanism(s) of charge compensation in alkali borate glasses. Exploratory ^{11}B MAS experiments reveal good agreement with models of borate evolution for the lithium borates. However, discrepancies for the heavier alkalis are discovered. In order to probe the extent of these

differences further and to attempt to shed light on their possible structural origins, additional experiments such as $^{11}\text{B}\{^{133}\text{Cs}\}$ REDOR and ^{11}B MQMAS are used.

5.2 *Select Techniques for Investigating Glass Structure*

Due to the intrinsic disorder present in glasses, a precise description of their structure is quite challenging. In order to provide the most complete overall picture of a glass's structure a multi-pronged approach is ideal. Numerous techniques exist which can provide individual pieces required to solve the puzzle. These techniques include various diffraction-based methods as well as some other spectroscopic techniques. A brief description of some of these additional methods is given below.

5.2.1 Diffraction Experiments

The complex structure of glasses makes a complete description of the 3-dimensional structure with the same precision of a crystal impossible. The structure of amorphous solids may, however, be discussed using an averaged one-dimensional description, through the use of radial (pair) distribution functions (RDF), ($G(r) = 4\pi r^2 \rho(r)$).^{84,85} The radial density function, $\rho(r)$, gives the number of atoms lying between r and $r+dr$. These functions provide an average description of the local environment, defined by a given radius, r , about a given nucleus. This 1D approximation works well in glasses because they are isotropic in nature, with respect to both their structure and physical properties.⁸⁴

5.2.1.1 X-ray diffraction

The x-ray diffraction experiment for a glass is carried out in a fashion identical to that employed for a crystalline sample. The scattering intensity is collected in k-space (i.e., as a function of k), which can be related back to a radial distribution function. Typical lab instruments use either Cu $K\alpha$ or Mo $K\alpha$ radiation for the generation of x-rays. These provide x-rays with wavelengths of 1.54 and 0.71 Å, respectively. These wavelengths place a limit on the maximum range in k-space collectable (8.2 and 17.7 Å⁻¹ for Cu and Mo, respectively). Since the Fourier transform relation between k-space and real space assumes infinite data collection in k-space, truncation of the data is inevitable. This is analogous to the issue of time-domain data truncation in NMR, and as with NMR, this problem may be alleviated by an artificial smoothing of the data at $k = k_{\max}$. However, this results in a reduction of the resolution in real-space.

The solution of the radial distribution function for a multi-component glass is generally quite complicated and the deconvolution of the contribution of all pairs cannot be obtained from a single x-ray experiment (i.e., a single wavelength).^{84,85} X-ray diffraction techniques are also limited by the origin of the scattering phenomenon itself: since the x-rays are scattered by the electrons, the scattering describes the position in space of the electron density, a significant fraction of which is associated with the bonds *between* nuclei as opposed to being centred about the atom, in the case of light atoms.

5.2.1.2 Neutron diffraction

Neutron diffraction deals with much smaller wavelengths than x-ray diffraction, ranging from 0.1 to 1 Å. Neutrons are scattered by the nuclei, not the electrons, thus

more precise nuclear locations can be obtained. The scattering depends on the scattering length, b , of the isotopes.⁸⁴ The differences in b - especially differences in the sign - can allow for deconvolution of the multiple pair distribution functions more easily than with x-ray diffraction. This is especially true with the use of multiple samples which have been selectively isotopically enriched. Although isotopic enrichment adds to the overall cost of the technique, it remains a small fraction of the cost associated with the construction and upkeep of the requisite nuclear reactor. In addition to the cost factor, the requirement of multiple samples (for optimal ease of characterization) effectively rules out neutron diffraction as a routine technique for structural characterization.

5.2.1.3 Electron diffraction

The wavelengths available for electron diffraction are even smaller than those of neutrons, with wavelengths as small as 0.05 Å being typical. Scattering is due to both the electrons and the nuclei. Unlike x-rays or neutrons which bear no charge, an electron is negatively charged and thus coulombic interactions become an issue. Both the repulsive interaction with the electrons and the attractive interactions with the nuclei affect the electron scattering factor. The result is that there is significant inelastic scattering of the electrons and may also be multiple scattering of the incident electron. In order to minimize these issues, very thin samples are generally employed.⁸⁵

The main limitation of all diffraction techniques is that they can only provide a pair distribution function. For a single-component system such as Fe or Si, the fit to the total function is straightforward as there are only Fe-Fe (or Si-Si) pairs. However, for

multicomponent systems (and even the most basic oxide glasses involve two components) it is not so simple. For a sample with n different atom types, the total pair correlation function is a convolution of $n(n-1)/2$ individual pair distribution functions.

5.2.2 Spectroscopic techniques

5.2.2.1 EXAFS

Extended x-ray absorption fine structure (EXAFS) relies on the absorption of an x-ray by the sample. An x-ray of energy commensurate with that of an inner-shell electron is absorbed, ejecting an electron, which is scattered by adjacent electrons and nuclei. As the energy of these inner-shell electrons will vary from atom to atom, EXAFS is element and site-specific. EXAFS requires the use of radiation over a range of energies (thus, wavelengths) and thus a synchrotron source is employed.⁸⁶ If one considers the transmitted intensity, I_T , detected at some detector after impinging upon a sample as a function of the energy of the incoming radiation, there will be distinct minima where the absorption occurs. Directly preceding this minimum (in the energy dimension) there appears a series of “wiggles” in the intensity. These are a result of the interference (altering both phase and intensity of detected radiation) from the ejected inner-shell electron as it is scattered. Fitting of these undulations provides information about the nearest neighbour atoms (type and spatial orientation) with respect to the probe atom. Thus by probing all the atoms, and even multiple electron shells of the same atom a coherent picture may be constructed about the average structural arrangement.

A limitation of this technique is that the phase component to the undulation cannot be determined independently for an amorphous structure, and thus a crystalline system of

similar composition and with a structure similar to that of the glass must be used to constrain the phase component of the scattering.^{84,86} Since the data analysis requires assumptions about the structural units, some level of indeterminacy is inevitable.

5.2.2.2 XANES

X-ray absorption near edge structure (XANES), is simply the structure of the absorption at the low-energy edge of the x-ray absorption. These so-called “pre-edge features” arise from electron transitions involving the particular shell being probed. For example, a 1s-2p transition may be observed for the K-edge (1s) absorption spectrum of an atom. The allowed transitions and therefore the nature of this “fine structure” are dependent upon the coordination environment (number and coordinating species) of the probed atom. Because of this, XANES has been used to quantify the fraction of ^[4]B present in borates.^{87,88} The identification of species with the same coordination numbers, but different ligands or ligand arrangements (i.e., isomers) can be challenging by XANES. As such, the identification of different types of ^[3]B or ^[4]B in the structure would be more challenging.

5.2.2.3 Infrared and Raman vibrational spectroscopy

The resonance frequencies of molecular vibrations occur in the infrared region of the spectrum. Both infrared (IR) and Raman spectroscopy probe this region, but in different manners. The former technique relies on direct absorption of radiation, whereas the latter technique involves scattered radiation. Differences in the local structure, such as the identities of the nearest and next-nearest neighbours, in particular their relative

arrangement, have a significant impact on the exact resonance frequencies observed, and thus can be diagnostic of particular arrangements. A significant shortcoming of vibrational spectroscopy is that the peak intensities cannot be simply related to the populations giving rise to them.

IR and Raman spectroscopy have both been used to probe the structure of glasses. In borates the “ring-breathing” mode (a concerted B-O stretch) allows for the identification of boroxol rings in B_2O_3 glass. In alkali borate glasses the presence of fundamental building blocks possessing differing numbers of four-coordinated borons may also be identified by IR and/or Raman.⁸⁹⁻⁹² The spectra obtained for a series of potassium borates are shown in figure 5.3, where a progression from boroxol rings (808 cm^{-1}) in B_2O_3 to rings containing one or more ^{11}B can be seen. These Raman results together with the ^{11}B MAS NMR results (section 5.4) reveal that the identity of the species giving rise to the two ^{11}B NMR signals are not the same throughout the compositional range.

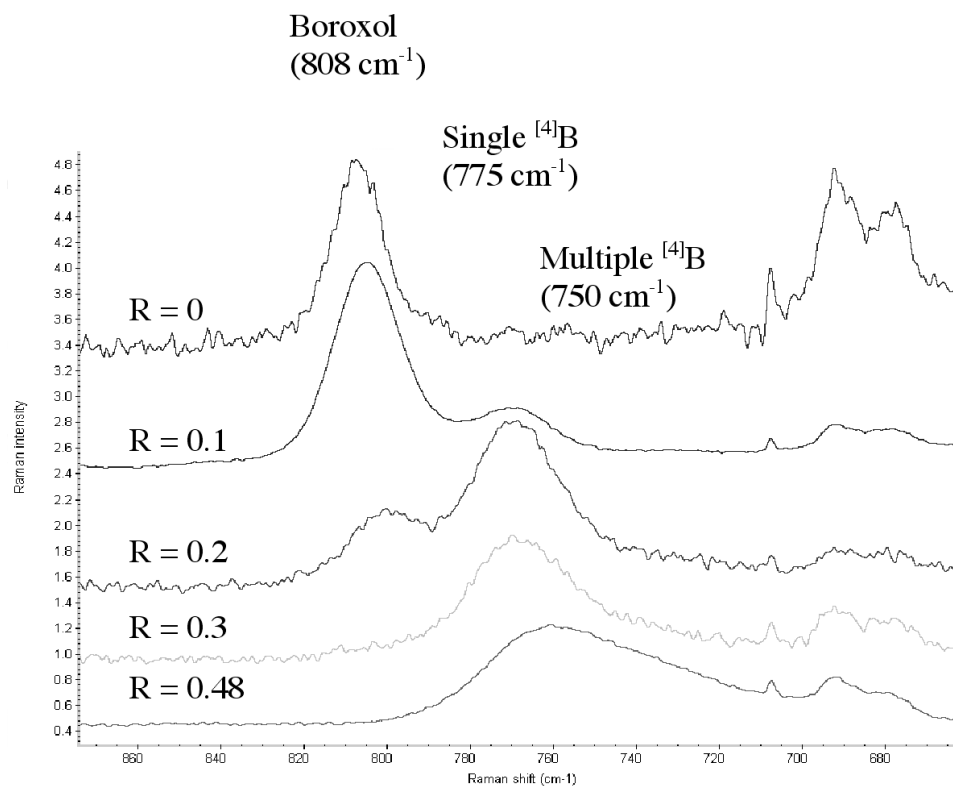


Figure 5.3: Raman spectra (incident radiation, 1064 nm) of a series of potassium borate glasses of composition R ($R = \text{K}_2\text{O}/\text{B}_2\text{O}_3$) from 0 to 0.48. Assignment of resonances to rings with zero (boroxol), one and multiple $^{[4]}\text{B}$ centres based on work by Kamitsos.^{89,90}

5.2.2.4 NMR spectroscopy

The details of high-field NMR have been discussed previously in the introductory sections, however the application of NMR in zero static field has not. The particular variant of that technique discussed here is nuclear quadrupole resonance (NQR). In NQR, the degeneracy of the nuclear spin states is removed not by the Zeeman interaction (which requires $B_0 > 0$), but rather by the local electric field gradient at the

nucleus. This is only possible for quadrupolar nuclei. As with NMR, the application of radiation of energy commensurate with the energy-gap of the magnetic-dipole-allowed transition (dependent on C_Q) creates a coherence which may be detected in the same fashion as an NMR signal of similar frequency. Both NMR and NQR have been extensively used in the study of glasses,⁷⁶ providing information about the types of boron species present, though not necessarily the relative amounts.

5.3 *Materials & Methods*

5.3.1 Sample Preparation

5.3.1.1 Glasses

Alkali borate glasses were synthesized from boron trioxide and the appropriate alkali carbonate. Starting materials were ground together in an agate mortar and pestle, placed in a platinum (or Pt/5%Au) crucible then heated in a Thermolyne 1300 box furnace at 400-700 °C, with the temperature increased gradually and held for 1-15 h as necessary to allow complete de-carbonation. Once a constant weight consistent with that expected based on the batch stoichiometry was achieved, a melt was obtained by heating to 900-950°C for approximately 15 minutes to allow mixing in the liquid state. The melt was quenched by immersing the bottom of the crucible in de-ionized water (25°C or ~0°C). In select cases, small amounts (< 0.2 mol %) of paramagnetic oxides such as Co_2O_3 or CrO_6 were added to increase relaxation rates.

Some glasses investigated were provided by collaborators Steven A. Feller and Mario Affatigato (Department of Physics, Coe college, Cedar Rapids, Iowa) and were synthesized either in a fashion similar to that described above, or by the *solution-method*.^{93,94} The solution method involves initial dissolution of the alkali carbonate and boron trioxide in water. This solution is stirred with heating, to yield a crystalline material (of varying hydration level), which is first dehydrated at 120-170°C, then finally melted at 900-950°C before quenching in a fashion similar to the other glasses. The more intimate mixing provided by this method than by mechanical grinding has been shown to allow access to glass compositions not attainable otherwise.^{93,94}

5.3.1.2 Crystals

The cesium triborate crystal (CsB_3O_5) used in the $^{11}\text{B}\{^{133}\text{Cs}\}$ REDOR experiments was synthesized by slow annealing from the glass of the same composition at 800 °C, as described previously⁹⁵ by Ms. Carolyn Robertson. The structure was confirmed by powder x-ray diffraction.

The cesium enneaborate crystal ($\text{CsB}_9\text{O}_{14}$) was obtained from Adrian Wright (Department of Physics, University of Reading, UK). Due to its hygroscopic nature, the sample was crushed and packed under a N_2 atmosphere in a bench-top glovebox.

Cesium pentaborate was made following the previously outlined procedure.⁹⁶ The hydrated pentaborate crystal was prepared by dissolution of freshly prepared B_2O_3 and

dry cesium carbonate in water*. This mixture was stirred while heating until a white material precipitated. The hydrated crystalline material (known to exist as one of or a mixture of two structures) was not structurally analyzed, but annealed at 490°C for four days to yield the anhydrous pentaborate crystals. Comparison of the experimental powder x-ray diffraction (xrd) with one simulated using the FullProf package⁹⁷ confirmed the successful synthesis (xrd performed by Rylan Lundgren, in the Group of Mario Bieringer, Department of Chemistry, University of Manitoba).

Potassium and rubidium diborate crystals were provided by Steven Feller (Department of Physics, Coe College, Iowa). Both were annealed for three days at 600°C (below the melting point) to improve the crystallinity of the samples. The improved crystallinity was determined by the enhanced resolution of the four-coordinated boron signals in the ¹¹B MAS spectrum. A sample of datolite, CaBSiO₄(OH), was obtained from Frank Hawthorne (Department of Geological Sciences, University of Manitoba).

5.3.2 NMR

Boron-11 MAS spectra at 14.1 T were acquired on a Varian UNITYInova 600 spectrometer operating at 192.4 MHz and equipped with 3.2 mm double- or triple-resonance probes (Varian-Chemagnetics). In order to minimize errors in population analysis of sites due to different quadrupole couplings, excitation was effected by the use of short (i.e., small tip-angle) pulses of 0.5-0.8 μs duration at rf nutation frequencies of 45-

* The published procedure used boric acid (H₃BO₃). However, there may exist an uncertainty in the exact level of hydration of boric acid, imparting an uncertainty in the relative stoichiometry. To overcome this, freshly prepared anhydrous B₂O₃ was substituted.

60 kHz and under moderately-fast MAS spinning (typically $16,000 \pm 2$ Hz). Boron-11 MAS spectra at 21.1 T were acquired on a Bruker Avance II 900 spectrometer (NRC, Ottawa ON) with a 2.5 mm double-resonance probe (Bruker). MAS spinning rates of 20 kHz were used in combination with $0.3 \mu\text{s}$ pulses ($\nu_{\text{rf}} = 83$ kHz). Due to the presence of a significant background signal arising from the boron nitride components in the Bruker MAS probe (see Figure 5.6) rotor-synchronized Hahn-echo ($90\text{-}\tau\text{-}180\text{-}\tau\text{-acq}$) spectra were also acquired to investigate the lineshapes, despite the fact that use of the Hahn-echo rules out quantification of sites. All ^{11}B chemical shifts are given with respect to $\text{BF}_3\cdot\text{OEt}_2$, using $0.1\text{M H}_3\text{BO}_3$ (+19.6 ppm) as a secondary external reference.

^{133}Cs (78.7 MHz) MAS spectra of glasses were acquired with a rotor-synchronized echo experiment at spinning rates of 18-22 kHz to ensure that the first point of the FID is at $t = 0$ before Fourier transformation, thus eliminating the need for first-order (frequency dependent) phase correction.

^{133}Cs MAS spectra of the crystalline materials were acquired at spinning rates of 5-20 kHz. To ensure effective excitation over the entire spinning sideband manifold, pulses of $0.5\text{-}2 \mu\text{s}$ duration ($9\text{-}36^\circ$ tip-angle) were used. The use of a less-than 90° pulse significantly alleviates the need to wait $5xT_1$ between co-added experiments (which can be quite long for ^{133}Cs , especially in well-ordered systems). Despite this, the required recycle delays necessary for complete relaxation were found to be very long (> 2 min). The cesium triborate and pentaborate crystals possess a single cesium site, and are thus less affected by saturation. However, the cesium enneaborate ($\text{CsB}_9\text{O}_{14}$) possesses two crystallographically inequivalent cesium sites. Since the use of recycle delays in excess of 60 minutes were necessary with a 36° pulse the relative intensities of the isotropic peaks of

the two sites were analyzed for experiments from 0.01-3600 s. Beyond 240 s, the increase in intensity was identical for both signals, providing reasonable assurances of the ability to quantify the spectra, under steady state conditions and a d1 of 300s. Non-spinning ^{133}Cs spectra were acquired with an echo (pentaborate) and with a single-pulse experiment (triborate).

$^{11}\text{B}\{^{133}\text{Cs}\}$ REDOR spectra were acquired at 14.1 T using a 3.2 mm triple-resonance probe simultaneously tuned to 192.4 MHz (^{11}B) and 78.6 MHz (^{133}Cs). The REDOR pulse sequence used was the *Hahn-echo* variant initially proposed by Gullion³⁷ and shown in Figure 3.6. The observe channel Hahn-echo used the extended phase-cycling scheme of Oldfield,⁹⁸ and xy-8⁹⁹ was used for the re-coupling channel pulse train. Spinning rates of 6250 ± 1 Hz ($\tau_r = 160 \mu\text{s}$) were used. Rf nutation frequencies of 50 kHz were used on both channels. The large difference in 90° pulse lengths between the ^{31}B and ^{41}B sites necessitated separate experiments with pulse lengths optimized for each site. Initial setting of the ^{133}Cs π -pulse was done via a nutation experiment and fine calibration of the π -pulse length on the re-coupling channel was achieved by maximizing the signal loss for an eight rotor-cycle experiment.

^{11}B 3QMAS spectra were acquired using a 3.2 mm double-resonance probe at spinning rates of 20-22 kHz. A shifted-echo pulse-sequence as described by Massiot²⁹ and shown in Figure 3.3 with hard excitation (3.4-4.2 μs) and conversion pulses (0.9-1.0 μs) at 160-165 kHz and a soft central-transition selective π -pulse (12 μs) at 21 kHz were used. Indirect dimension spectral widths were synchronized with the rotation frequency, eliminating the added complication of spinning sidebands in F1 while additionally providing a small increase in signal.¹⁰⁰ Spectra were processed including a shearing

transform using RMN.⁵⁰ The indirectly detected (F1) dimension is referenced using the C_z convention.^{25,28}

$^{11}\text{B}\{^1\text{H}\}$ cross-polarization experiments on datolite were acquired on a 3.2 mm double-resonance probe tuned to 599.68 (^1H) and 192.40 MHz (^{11}B). At a sample spinning rate of 5000 ± 2 Hz, maximum polarization transfer was effected over a time of 3 ms during which the ^{11}B rf frequency was varied linearly from 57 to 70 kHz and the ^1H field held constant at 67 kHz. The signal was acquired for 16 ms (2 μs dwell time), over which continuous-wave ^1H decoupling was employed (47 kHz)*.

$^1\text{H}\{^{11}\text{B}\}$ cross-polarization experiments were conducted on the same probe as the $^{11}\text{B}\{^1\text{H}\}$ experiments. The sample was spun at 12 kHz. Polarization transfer was based on the parameters used for the reverse experiment.

^{29}Si MAS spectra of datolite were acquired on the same 3.2 mm triple-resonance probe. A spectrum acquired at 5 kHz spinning yields a nearly isotropic spectrum, allowing straightforward identification of the isotropic chemical shift. In addition, a spectrum acquired at $\nu_{\text{rot}} = 1109 \pm 10$ Hz was acquired, allowing extraction of the anisotropy of the chemical shift.

Density functional theory (DFT) calculations were done on a SunFire6800 cluster, running Solaris 9 with the Gaussian 98 and 03 programs. Geometries were optimized at HF/6-31G* and the convergence to a stationary point verified by calculation of vibrational frequencies. Calculation of the shieldings and electric field gradients were

* As has been established for the common $^{13}\text{C}\{^1\text{H}\}$ cw-decoupling example, the use of rf nutation frequency incommensurate with the rotation frequency improves the efficiency of the decoupling.

done at B3LYP/cc-pVTZ using the GIAO¹⁰¹ method for the shieldings. Lacking a known absolute shielding scale for boron, the geometry was optimized for H₃BO₃ (C_{3h} symmetry) and the shieldings calculated at the same levels of theory as other borate models. Using this calculated shielding and the known experimental shift of +19.6 ppm (relative to BF₃·OEt₂), all of the calculated shieldings were converted to shifts.

5.4 Alkali Borate Glasses

Borate glasses have been studied extensively by NMR, beginning with early wide-line (i.e., non-spinning) experiments by Bray.^{76,102-104} In these early experiments, the distinction between three-coordinate (³B) and four-coordinate (⁴B) sites was based on the vast differences in the quadrupole coupling constants. The quadrupole coupling constants of the ⁴B sites are generally less than 600 kHz, whereas those of ³B sites fall between 2.3 and 2.8 MHz in borates. With the development of MAS and ready availability of higher field magnets, the ¹¹B chemical shifts can also distinguish between sites. The ³B sites have chemical shifts, δ_{iso} , in the range of 14-24 ppm, and ⁴B sites fall between -2 and 4 ppm in borates.⁷⁶ A typical ¹¹B MAS spectrum of an alkali borate glass is shown in Figure 5.4. The signals arising from the ³B and ⁴B species are highlighted. The combination of the chemical shifts and quadrupole interactions (the main contributor to the ³B signal width) makes their identification simple. At static fields, $B_0 \geq 14$ T, the resolution of the sites is generally sufficient to allow extraction of site population information via peak areas. At lower applied fields, the isotropic quadrupole shift and the anisotropic quadrupole broadening of the ³B site both increase, resulting in overlap of the ³B and ⁴B signals.

^{11}B MAS at 14.1 T

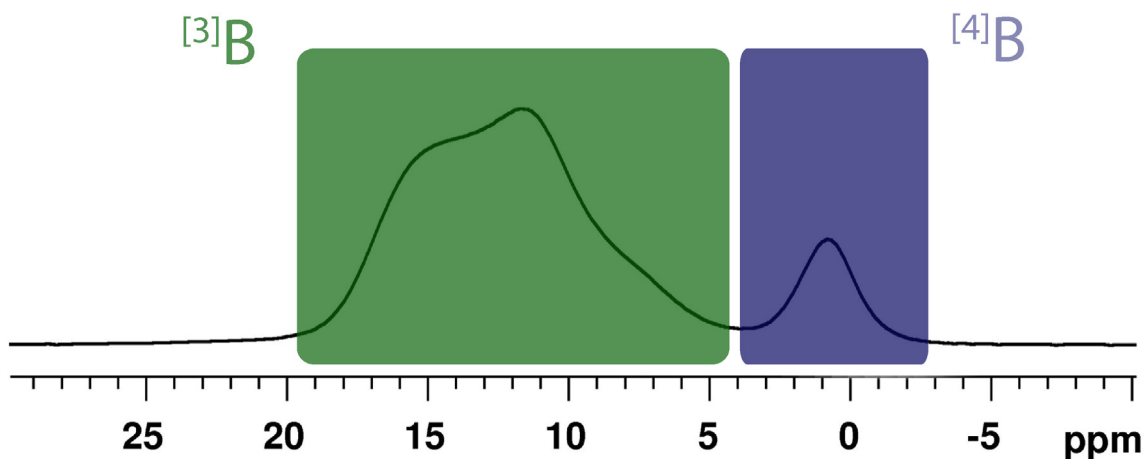


Figure 5.4: A typical ^{11}B MAS spectrum at 14.1 T of a borate glass. The $^{[3]}\text{B}$ and $^{[4]}\text{B}$ signals are readily identified and the resolution allows straightforward integration of signals.

5.4.1 ^{11}B MAS of Glasses

Initial Boron-11 MAS experiments of the alkali borates were carried out for glasses ranging in composition from 3 to 45 mol % alkali oxide. Another method of describing the composition of these glasses is by their R ratio, where R denotes the ratio of alkali oxide to boron trioxide. As expected, initial addition of alkali oxide to the glass resulted in the formation of $^{[4]}\text{B}$ species. A plot of the $^{[4]}\text{B}$ fraction, \mathcal{N}_4 ($\mathcal{N}_4 = [^{[4]}\text{B}]/[^{[3]}\text{B}] + [^{[4]}\text{B}]$), is shown in Figure 5.5 for the lithium borate glasses. Initial addition of alkali oxide is accompanied by an increase in the $^{[4]}\text{B}$ population, until $R = 0.4$ (ca. 29 mol %).

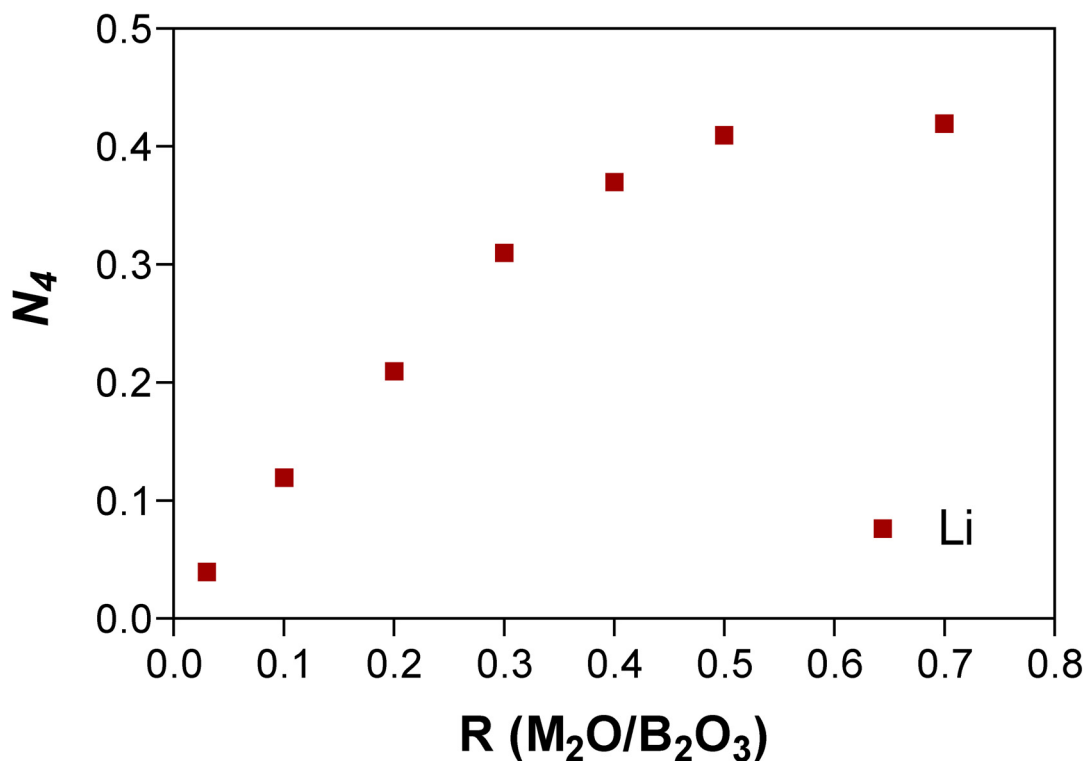


Figure 5.5: The evolution of the ${}^{[4]}\text{B}$ fraction, N_4 ($N_4 = {}^{[4]}\text{B}/\{{}^{[3]}\text{B}+{}^{[4]}\text{B}\}$) for lithium borate glasses of different composition. A linear increase (with slope=1) in N_4 is observed until $R = 0.4$, where the rate of ${}^{[4]}\text{B}$ formation changes, requiring another charge-balancing mechanism.

The lithium borate glasses (and in fact all alkali borate glasses) show a marked decrease in the rate of formation of ${}^{[4]}\text{B}$ upon alkali addition. The reason for this has been ascribed to the avoidance of the energetically unfavourable bonding of two anionic ${}^{[4]}\text{B}$ species. The increased addition of alkali oxide must however, be tempered in some fashion and it is at this point ($R = 0.4$, or 29 mol% alkali oxide) where the formation of NBOs begins.

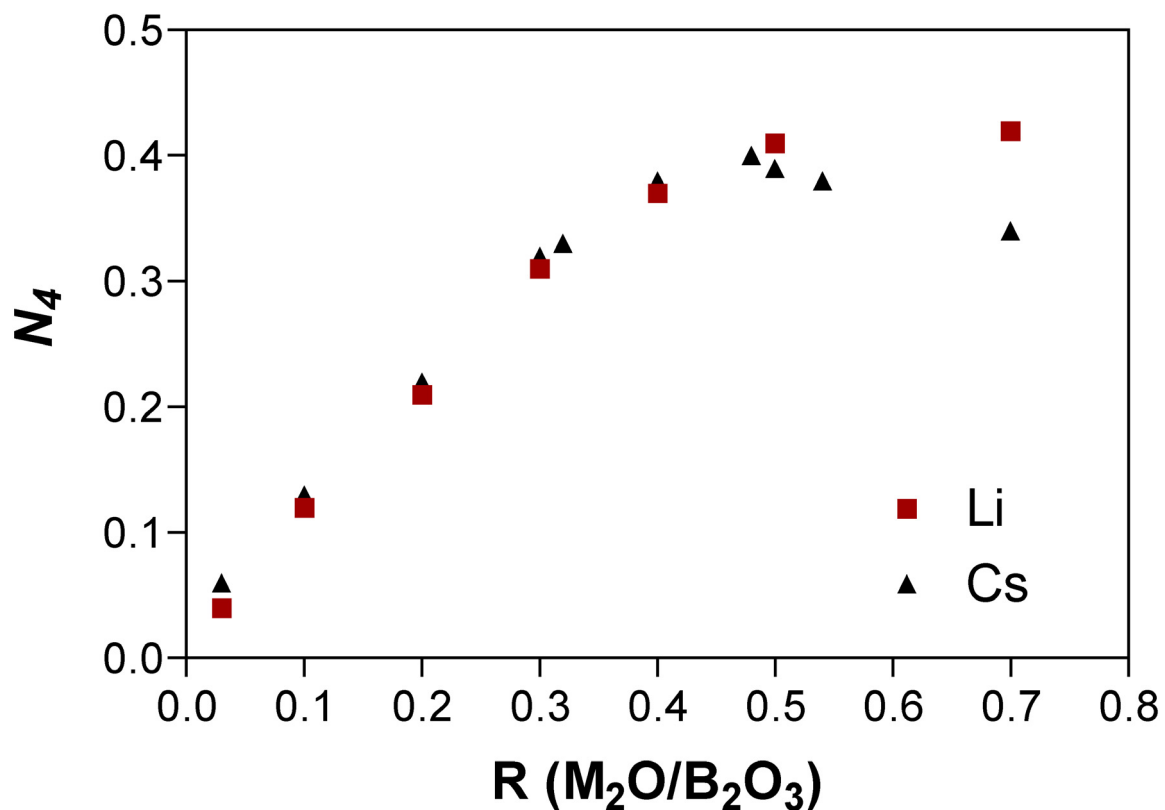


Figure 5.6: Comparison of the lithium and cesium borate glasses of different composition. The cesium borates are very similar to lithium until $R = 0.4$. Beyond $R = 0.4$, the fraction of [4]B begins to decrease for cesium, requiring a larger number of NBOs ($\# \text{ NBOs} = R - N_4$). Errors in N_4 are on the scale of the points (± 0.01).

Table 5.1: The N_4 values for all alkali borates up to $R = 0.8$ acquired at 14.1 T.**Uncertainty in values is ± 0.01 .**

R	N_4										
	Li	Na	K		Rb			Cs			
	<i>Total</i>	<i>Total</i>	<i>Low</i>	<i>High</i>	<i>Total</i>	<i>Low</i>	<i>High</i>	<i>Total</i>	<i>Low</i>	<i>High</i>	<i>Total</i>
0.03	0.04	-	0.03	0.02	0.05	0.03	0.02	0.05	0.03	0.03	0.06
0.10	0.12	0.12	0.09	0.05	0.14	0.09	0.06	0.15	0.07	0.06	0.13
0.20	0.21	0.22	0.11	0.11	0.22	0.13	0.08	0.21	0.11	0.11	0.22
0.30	0.31	0.31	0.22	0.10	0.32	0.16	0.17	0.33	0.19	0.13	0.32
0.32	-	-	0.22	0.13	0.35	0.12	0.24	0.36	0.20	0.13	0.33
0.40	0.37	0.38	0.20	0.18	0.38	-	-	-	0.19	0.19	0.38
0.48	-	-	0.23	0.20	0.43	0.19	0.23	0.42	0.16	0.24	0.40
0.50	0.41	0.42	0.22	0.21	0.43	0.19	0.22	0.41	0.12	0.27	0.39
0.54	-	-	0.18	0.25	0.43	0.18	0.25	0.43	0.13	0.25	0.38
0.60	-	-	-	-	-			0.37			0.36
0.70	0.42	0.39			0.31	0.11	0.23	0.34	0.11	0.23	0.34
0.80	-	-	-	-	-	-	-	-			0.33

^a The low frequency signal corresponds to the signal with centre-of-mass at *ca.* 0.5 ppm, the high frequency signal is that at *ca.* 1.5 ppm.

Until this point ($R = 0.4$) all of the alkali oxides exhibit identical behaviour with respect to the total ^{14}B signal. However, at higher alkali loadings, the heavy alkali (K, Rb and Cs) exhibit different changes in N_4 . For the heavier alkali, the fraction of ^{14}B not only deviates from one-to-one, but begins to decrease as the alkali oxide concentration

increases. A plot comparing the lithium and cesium borates (Figure 5.6) clearly shows the differences between the two. The other alkali exhibit a similar trend to that of cesium (see Table 5.1). Attempts to verify the N_4 values obtained at 14 T using spectra acquired at 21.1 T, where the baseline resolution of the two sites from the glasses is unquestioned, was unfortunately hindered by the baseline itself; the presence of boron nitride components within the probe result in a large baseline hump which could not be removed without loss of accuracy in integration. A ^{11}B MAS spectrum at 21.1 T of B_2O_3 is shown in Figure 5.6 and the large signal arising from the probe is shaded in magenta. The lineshapes at the higher field do however provide valuable information (*vide infra*).

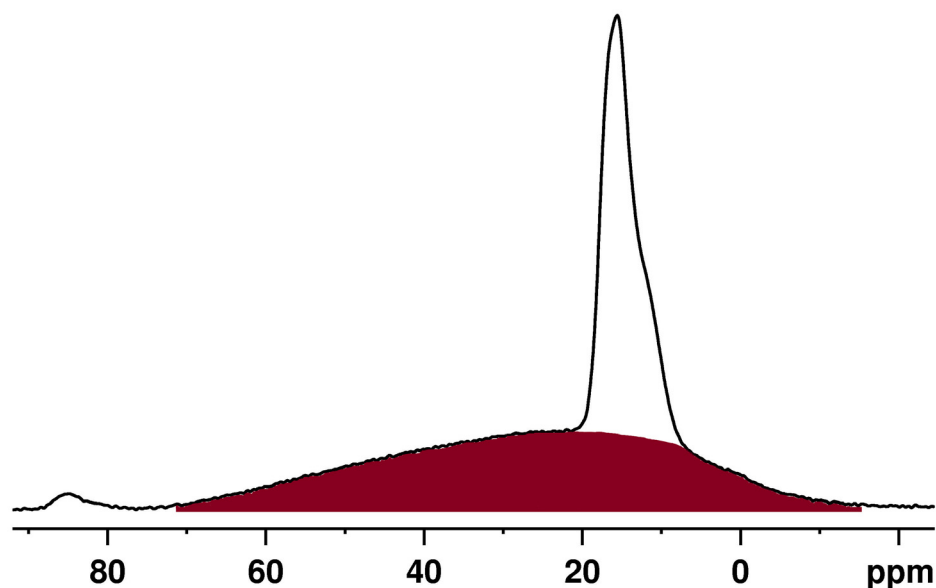


Figure 5.7: ^{11}B MAS spectrum of amorphous B_2O_3 acquired using the 2.5 mm double-resonance probe at 21.1 T. The background signal arising from the boron nitride probe components (shaded magenta) significantly hinders quantification.

In addition to the differences in the total integrated intensity of the ^{11}B signals for the cesium borate glasses, one significant difference in the spectra of the heavy alkali (K, Rb and Cs) borate glasses is the presence of multiple signals in the ^{11}B region (see Figure 5.8). The presence of such signals has been shown to span the compositional range $R = 0.03\text{-}0.54$.^{105,106} This is in contrast to previous studies of binary borate glasses.^{104,107} The presence of multiple sites implies an additional mode of site differentiation, but the identity of the different four-coordinated peaks is unknown.

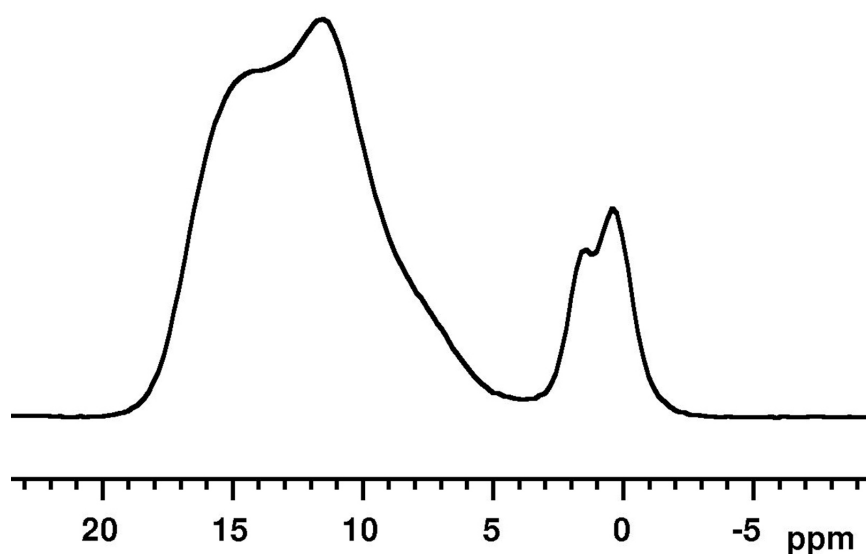


Figure 5.8: ^{11}B MAS spectrum of the $R = 0.1$ cesium borate glass at 14.1 T. The ^{11}B signal (centred about 1 ppm) exhibits a clear inflection point.

Unlike three-coordinate boron where NBO species are well known, the formation of NBOs (each bearing an additional negative charge) on ^{11}B is highly unlikely, given that the boron in a $\text{BO}_{4/2}$ unit already possesses a formal charge of -1 (although it is more likely to be distributed over the more electronegative oxygens). To the best knowledge of the author, no reports of four-coordinated boron possessing a non-bridging oxygen have been confirmed in the literature. However, indications of the potential formation of such species comes from some molecular dynamics studies.¹⁰⁸

In addition to the degree of polymerization (i.e., number of NBOs) of ^{11}B sites, it is well-established that medium-range order can result in differences in the local shielding of nuclei. The archetypal B_2O_3 glass consists solely of ^{11}B species in a three-dimensional network. Vibrational spectroscopic methods such as infrared¹⁰⁹⁻¹¹¹ and Raman^{90,92} as well as numerous NMR reports¹¹²⁻¹¹⁴ show clear evidence of multiple sites. These sites have

been assigned to boron in three-membered rings (boroxol rings), and those not in rings. Numerous ab initio and DFT studies of vibrational frequencies¹¹⁵ and chemical shieldings and nuclear electric field gradients¹¹⁶⁻¹¹⁸ confirm these assignments. Further evidence of medium range order comes from investigations of numerous borate crystals which show the propensity to form rings of different sizes.^{119,120} Some common examples of these fundamental building blocks are shown in Figure 5.9. If present in glasses, as widely thought, such species could potentially account for the observation of multiple ¹¹B signals.

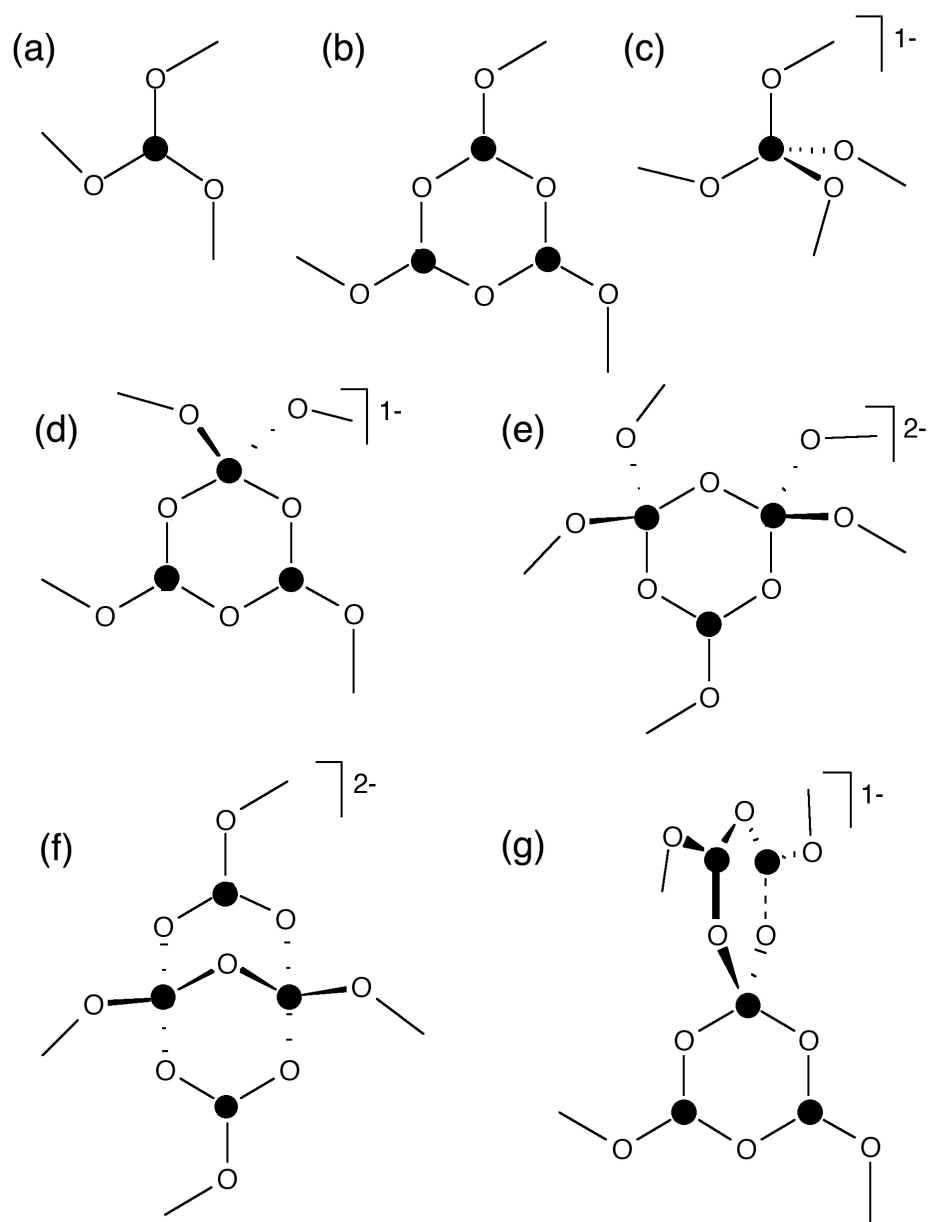


Figure 5.9: Structures of the more common FBBs in borates with varying numbers of $[4]B$ atoms: non-ring $[3]B$ (a), boroxol ring (b), non-ring $[4]B$ (c), triborate (d), dtriborate (e), diborate (f) and pentaborate (g). Filled circles represent boron, open circles oxygen.

Given that the cesium borate glasses exhibit multiple ^{11}B sites at static fields exceeding 11.7 T, the ^{11}B MAS spectra were acquired for all alkali borate glasses (except francium) at the same (and some additional) compositions as those reported previously.¹⁰⁵ The ^{11}B MAS of all the heavy alkali (K, Rb, and Cs) borate glasses showed evidence of multiple ^{11}B sites.

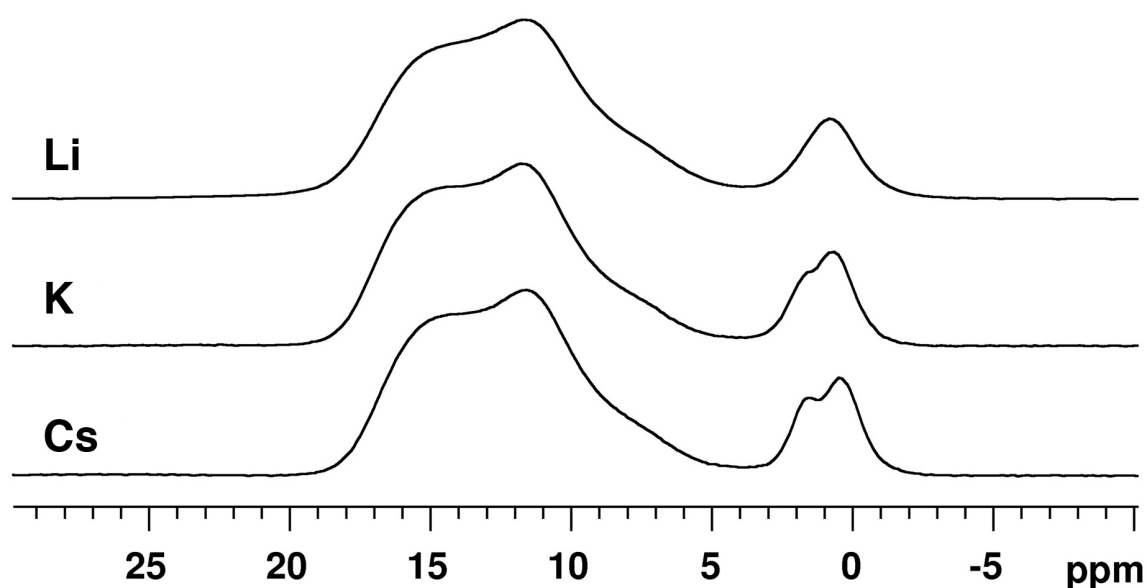


Figure 5.10: ^{11}B MAS spectra of $R = 0.1$, lithium, potassium and cesium borate glasses. Only the potassium and the cesium exhibit multiple ^{11}B signals.

Although the ^{11}B signal in Figure 5.10 of the cesium and potassium borate glasses may appear to be due to the anisotropic second-order quadrupolar broadening, several different rationales rule out this possibility. The acquisition of spectra at multiple fields (11.7 to 21.1 T) for the CsB-20 glass (Figure 5.11) very clearly show the predicted behaviour of a second-order broadened signal for the ^{11}B peak: narrowing and shifting to higher frequency (i.e., towards the isotropic shift) with increasing field. The ^{11}B region

displays none of this and in fact is relatively unchanged, with perhaps a very small enhancement in resolution with increasing field strength.

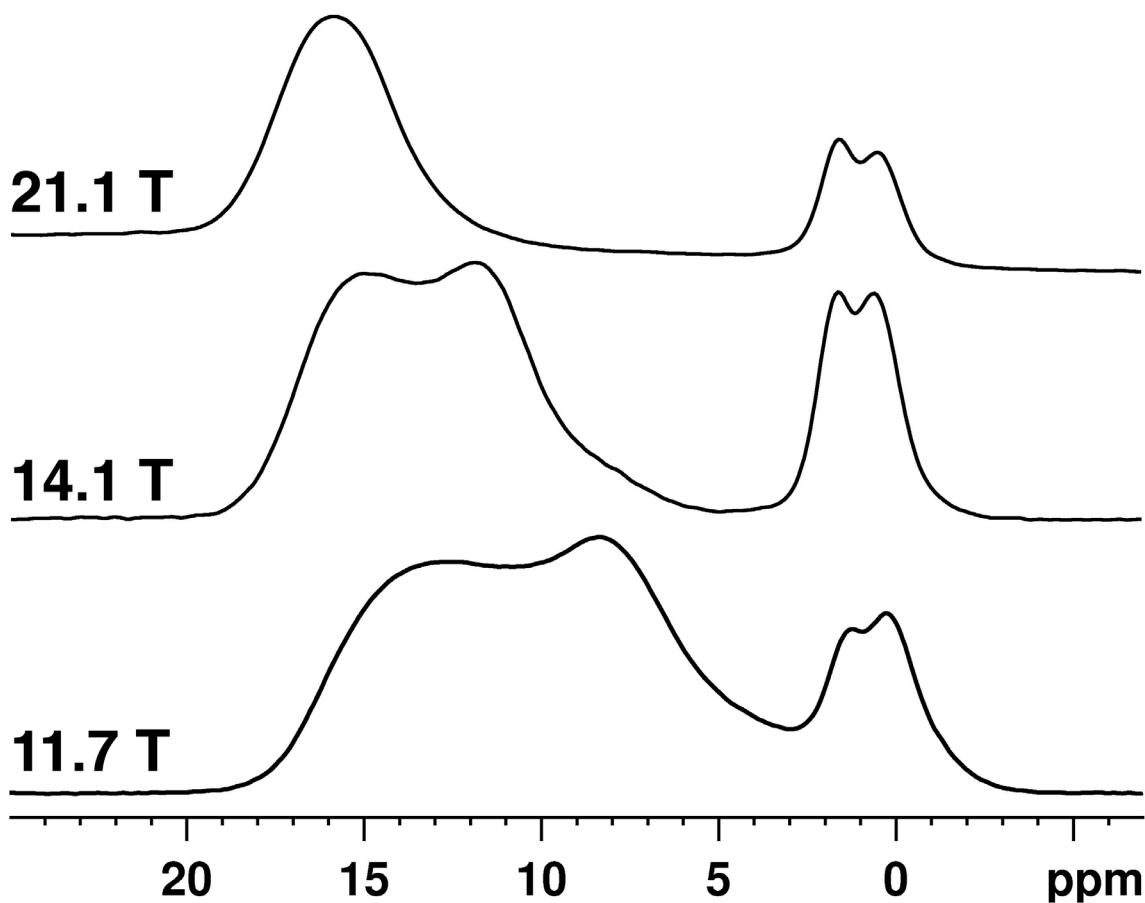


Figure 5.11: ^{11}B MAS spectra of the CsB-20 glass acquired at 11.7, 14.1 and 21.1 T (corresponding to ^1H frequencies of 500, 600 and 900 MHz respectively). No significant change in the ^{11}B signal is observed, unlike the ^{13}B signal, at varying static field, B_0 .

Another possibility to explain the double peaks is poor shimming (i.e. inhomogeneity of the static field within the volume of the sample). The presence of identical observations at multiple fields rules this out completely, as one would require not only all three magnets to be poorly shimmed, but for the field gradients to be very similar

if not identical*. The potassium and rubidium borates exhibit a less pronounced resolution of the sites than the cesium borates, although, sufficient lineshape character (e.g., an inflection point) existed to allow fitting to two sites. Cases with insufficient resolution (i.e., a single peak was observed) are reported as such (see Table 5.1).

Examining Figure 5.12, it can be seen that at low R values (< 0.3), the two sites increase in intensity together. Above $R = 0.2$, the evolution changes. The intensity of the low frequency signal (*ca.* 0.5 ppm) continues to increase, whereas that of the high-frequency signal (*ca.* 1.5 ppm) remains roughly constant. Beyond $R = 0.4$, the intensities of the two signals diverge, with the low-frequency component decreasing in intensity and that of the high-frequency signal increasing. The sodium glasses exhibit a small shoulder to the high frequency side of the ^{14}B signal for the $R = 0.2$ glass only. The presence of this shoulder has been further shown by another student in the lab to be reproducible, and only for compositions near $R = 0.2$; neither the $R = 0.1$ nor the 0.3 glass show any evidence of this site.¹²¹ The lithium borates all exhibit a single symmetric peak. Lineshape fitting of selected samples showed that a single line (with some Lorentzian character) provides a good description of the experimental response signal.

* As an added note, the probes used at 14.1 T were verified by the author on a regular basis to provide ^{13}C FWHM for adamantane of < 0.03 ppm, width at 10% of ≤ 0.1 ppm and maximum symmetry of the peak below 5 %.

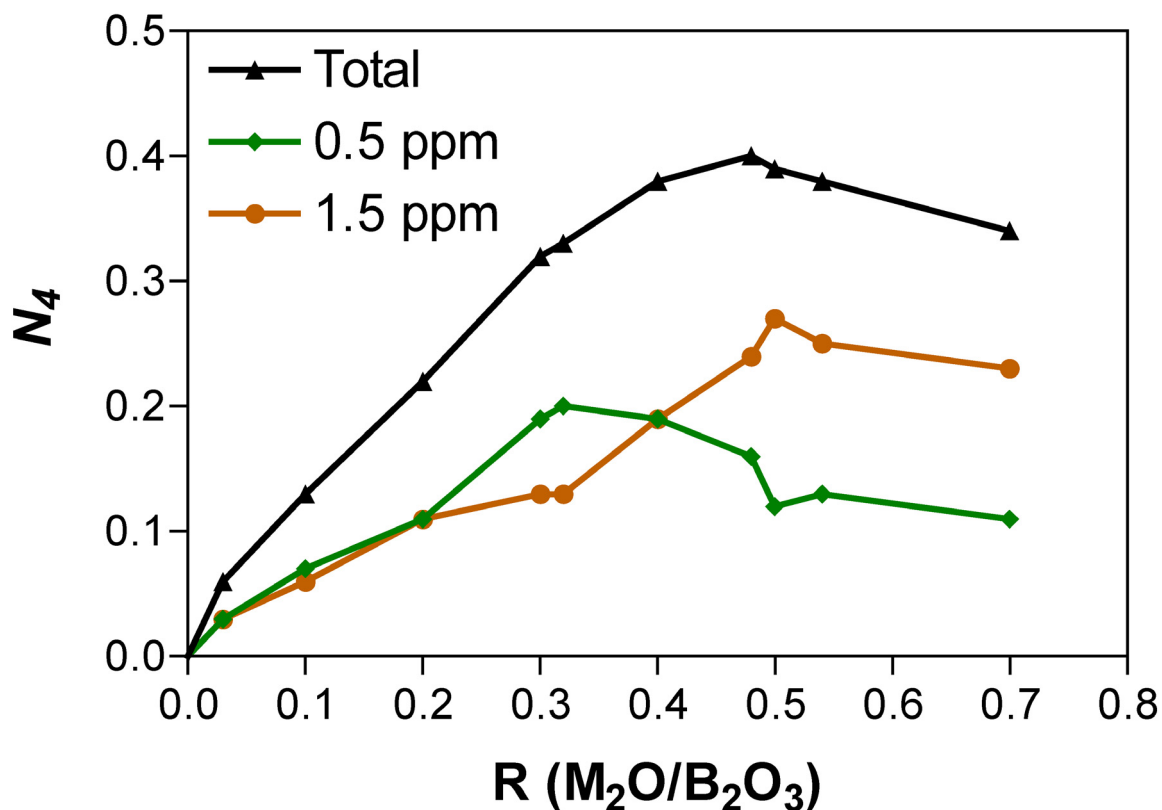


Figure 5.12: The evolution of the ^{11}B signals for the cesium borate case. The intensities of the two signals (0.5 and 1.5 ppm) along with their sum (Total) are shown as a function of R. Similar evolutions were observed for K and Rb.

Given that the two peaks of the cesium and other heavy-alkali glasses are only present in static fields of 11.7 T and greater, ^{11}B MAS of the lithium borates were acquired at the highest currently available field of 21.1 T, and still no asymmetry in the lineshape or splitting of the peak was observed (Figure 5.13).

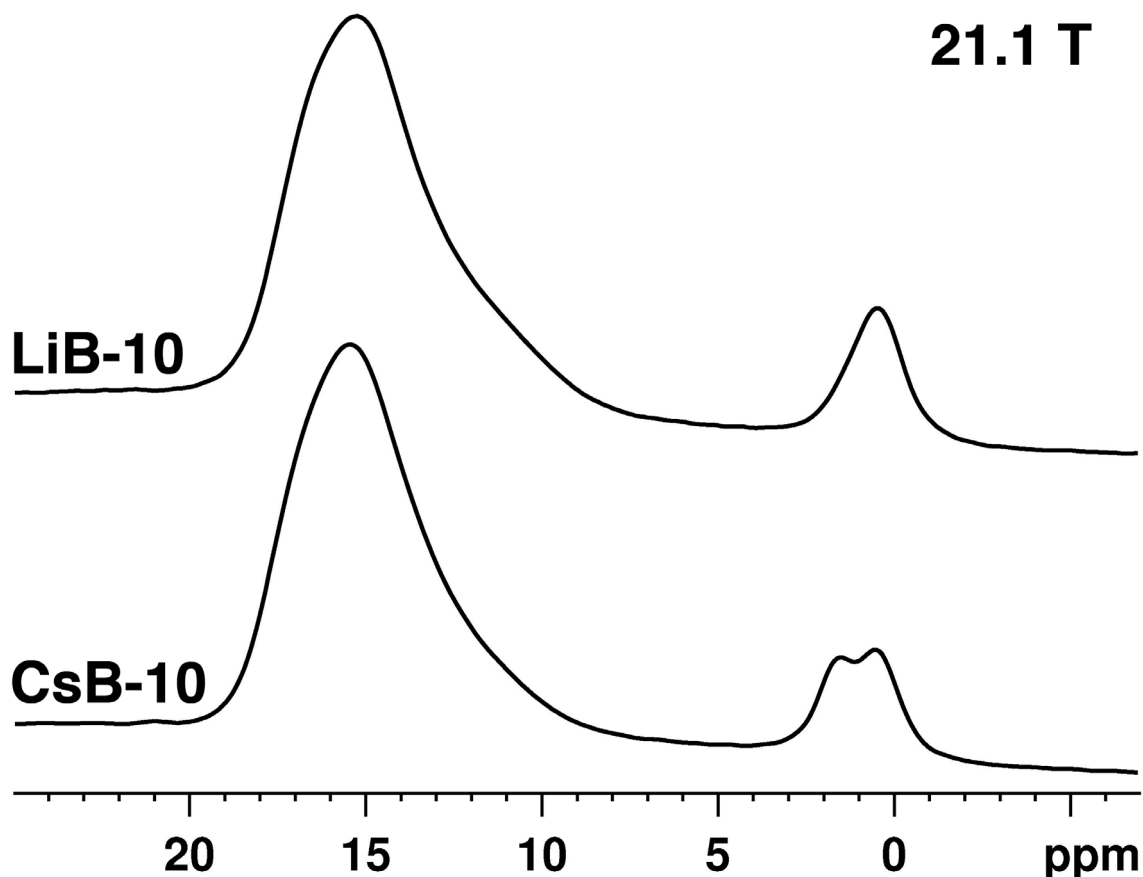


Figure 5.13: ^{11}B MAS of the $R = 0.1$ lithium (LiB-10) and cesium (CsB-10) borate glasses at 21.1 T. No evidence of multiple ^{11}B sites is observed for the lithium borate. The spectrum of the cesium glass of analogous composition is shown below for comparison.

It has been shown that the ^{11}B chemical shift is quite sensitive to the B-O-B angles,¹¹⁶ and to dihedral angles (see section 5.4.3.4). The ^{11}B lineshapes of the lithium and sodium borates generally exhibit a greater “broadening out” of the lineshape relative to the cesium borate glass, indicating less uniform bond lengths and angles for the ^{11}B species. The presence of more extensive medium-range ordering in these heavier glasses might be expected to reduce the ranges of angles and lengths, and thus yield more distinct

^{13}B lineshapes. The ^{14}B linewidths (FWHM) were measured for a series of glasses to probe if the absence of multiple ^{14}B sites for the Li and Na borates is merely a result of lack of resolution of the two sites. The observed linewidths (normalized to the $R = 0.2$ glass) as a function of R-value are plotted in Figure 5.14.

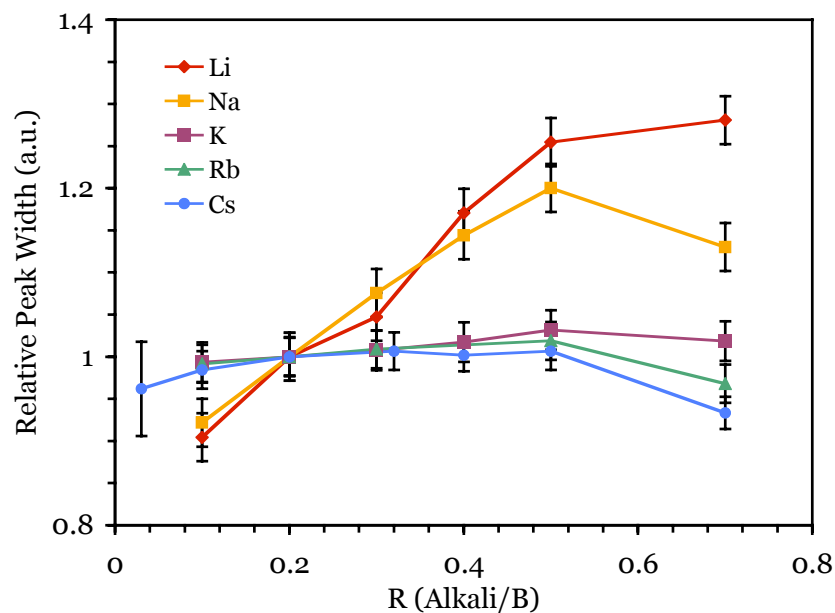


Figure 5.14: Relative peak widths (see text) for a series of alkali borate glasses. The heavy alkali (K, Rb and Cs) exhibit nearly constant ^{14}B linewidth, whereas the Li and Na linewidths increase with increased alkali loading. The error bars denote the estimated errors.

It can be seen that for the heavier alkalis, the total breadth of the ^{14}B signals remains fairly constant over the entire range ($0.03 \leq R \leq 0.7$). That the total width is relatively constant is consistent with the idea - although not the sole possibility- that in these glasses, there are two major ^{14}B -containing FBBs whose relative populations vary with alkali loading. However, the lithium and sodium borates exhibit a relatively steady

increase in linewidth with alkali loading. This may indicate that for the borate glasses of these lighter alkalis, there exists less of a predilection for the presence of specific FBBs; as with the ^{14}B sites, a larger distribution in the structural parameters of the borons would be expected to yield a greater distribution in the observed chemical shifts (i.e., broader linewidths).

5.4.2 Probing Medium-Range Order with $^{11}\text{B}\{^{133}\text{Cs}\}$ REDOR

One significant difference among the common FBBs of Figure 5.9 is the number of anionic ^{14}B sites and thus the overall charge of the particular species. The presence of multiple ^{14}B sites, for example in the diborate and di-triborate groups, require additional nearby cations to ensure local charge balance. In particular, the oxygen bridging the ^{14}B sites might be expected to possess a slightly higher partial negative charge than the other oxygens, requiring more and/or closer Cs^+ contacts in order to fulfill bond-valence requirements (see Figure 5.15). In order to probe this possibility, REDOR was used to recouple the ^{11}B - ^{133}Cs dipolar interaction (the strength of which is proportional to the inverse cube of the internuclear distance), and gain insight into the possible types of FBBs present in these borate glasses.

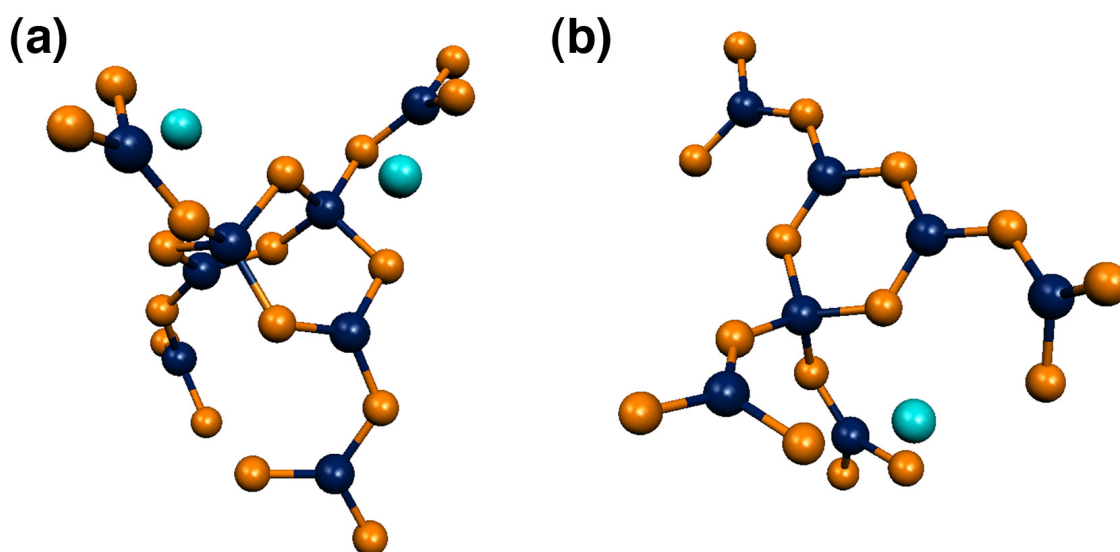


Figure 5.15: The borate fundamental building blocks (a) diborate and (b) triborate. The alkali cations are shown in teal, boron in blue and oxygen atoms in yellow.

Although REDOR was originally designed for spin-1/2 nuclei (as are the typical arguments used to describe its mechanism of recoupling),^{33,122} the extension to spins greater than 1/2 and to glasses has been reported.^{99,123-125} Many of these studies have involved sodium-23, which generally possesses a much larger C_Q and thus ν_Q ($\nu_Q = 3C_Q/2I(2I-1)$),^{14,121,124} making the complete inversion of all populations more challenging. Given the success with sodium-23, the cesium-133 case -with its very small quadrupole couplings- would be expected to work equally well. In order to ensure that the experiment worked, and that we could extract mean dipole-dipole couplings (and therefore distances), the experiment was first tested on a crystalline sample with well-established internuclear distances.

5.4.2.1 Cesium Triborate Crystal

The cesium triborate crystal (CsB_3O_5) consists of a borate network structure made entirely of triborate groups (see Figure 5.9d or Figure 5.15b).⁹⁵ There are three distinct boron sites: two $^{[3]}\text{B}$ and one $^{[4]}\text{B}$, and a single crystallographically unique cesium atom. The nearest-neighbour boron-cesium distances for the two $^{[3]}\text{B}$ sites are 3.53 and 3.62 Å and $^{[4]}\text{B}$ is 3.56 Å. These distances yield an average ^{11}B - ^{133}Cs dipole-dipole coupling of 112 ± 4 Hz. The next-nearest cesium interactions for all three boron sites range between 3.68 and 4.12 Å, corresponding to dipole-dipole couplings of 102 and 73 Hz, respectively. Given the relative sizes of these couplings and the large dependence of the net dipolar field experienced by a nucleus on the relative orientations as well as the magnitudes of the dipolar couplings,^{99,123,126} the nearest-neighbour interaction would be expected to dominate the observed coupling. However, the next-nearest neighbour interactions will be non-negligible. Thus the expected behaviour might be that resulting from a dipolar field slightly greater than that due solely to the nearest cesium-133 nucleus. The REDOR data for the triborate crystal are shown in Figure 5.15 and show very similar dephasing behaviour for the $^{[3]}\text{B}$ and $^{[4]}\text{B}$ sites. Comparison of the $^{[3]}\text{B}$ lineshapes for different dephasing (or evolution) periods showed no significant change in the lineshapes, indicating similar behaviour of the two $^{[3]}\text{B}$ sites, and therefore the entire $^{[3]}\text{B}$ region was treated as a single signal. The similar dephasing behaviour of the $^{[3]}\text{B}$ and $^{[4]}\text{B}$ regions is consistent with the atomic distances from the x-ray diffraction data.⁹⁵ Fits to the experimental data were done using calculated REDOR dephasing curves, employing an isolated ^{11}B - ^{133}Cs spin-pair model (density matrix 32×32 elements) to minimize computation time. Calculations for a three-spin system (one ^{11}B and two ^{133}Cs nuclei)

necessitating a density matrix of 256×256 (64 times larger!) were attempted, and initial results (averaging over 200 instead of 320 crystallite orientations) showed similar dephasing behaviour, especially at shorter dephasing times (which are expected to be dominated by nearest-neighbour interactions and to be less sensitive to the various relative tensor orientations). This lack of differentiation provides additional confidence in the simple two-spin model to extract mean dipolar fields (couplings) and thus mean distances. Analysis of the dephasing data for the triborate crystal revealed that the boron nuclei experience a mean cesium dipolar field of 120 ± 10 Hz, corresponding to 3.49 ± 0.1 Å. This is only slightly stronger than would be expected from just the nearest neighbour interactions (112 Hz), indicating some -although small- contribution from the next-nearest cesium.

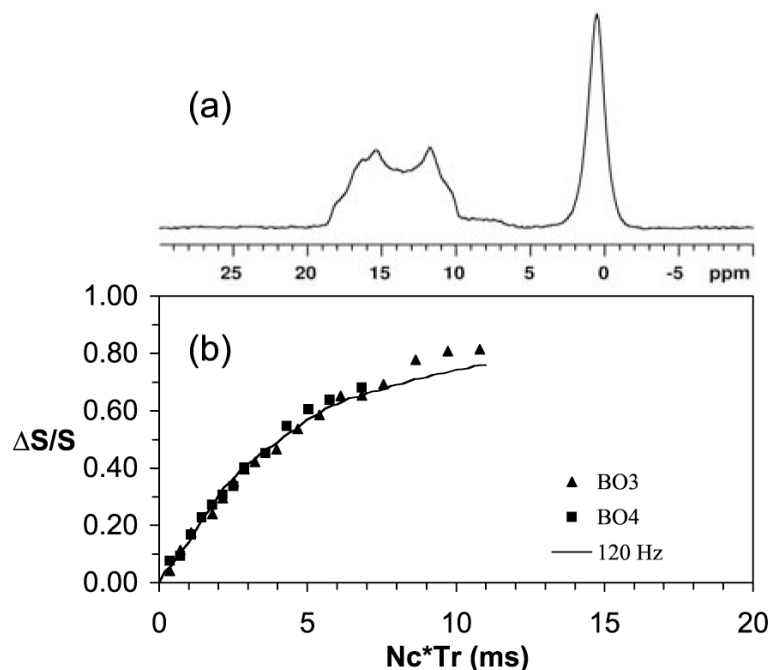


Figure 5.16: ^{11}B MAS spectrum (a) of the cesium triborate (CsB_3O_5) crystal. The results of the $^{11}\text{B}\{^{133}\text{Cs}\}$ REDOR experiments (b) for BO_3 and BO_4 signals along with the results of two-site numerical simulation with $R_{DD}(^{11}\text{B}, ^{133}\text{Cs}) = 120 \text{ Hz}$ (3.49 \AA).

5.4.2.2 Cesium Borate Glasses

Having shown with the well-characterized triborate crystal that $^{11}\text{B}\{^{133}\text{Cs}\}$ REDOR experiments work (the inversion of the cesium spin-state populations results in a re-coupling of the dipole-dipole interaction) and that simulation allows extraction of the mean dipolar field (and thus a mean internuclear distance), experiments were attempted on glassy systems. Two systems with very different cesium content ($R = 0.1$ and 0.54) were chosen. The sole charge-balancing mechanism for the $R = 0.1$ glass is the formation of $^{[4]}\text{B}$ sites, whilst for the $R = 0.54$ glass some NBO-bearing $^{[3]}\text{B}$ sites are expected at this composition. Both glasses also possess two $^{[4]}\text{B}$ signals.

The cesium-133 MAS spectra of both glasses have spinning sideband manifolds extending approximately 220 kHz, which corresponds to C_Q of ~ 500 kHz. An exact measure of the quadrupole coupling is hindered by the large distribution of chemical environments and thus NMR parameters in these disordered systems. This distribution in the chemical shift is evident from the width of the isotropic peak (Figure 5.17). A cesium-133 quadrupole coupling of 500 kHz was thus used in the numerical simulations used to fit the experimental data.

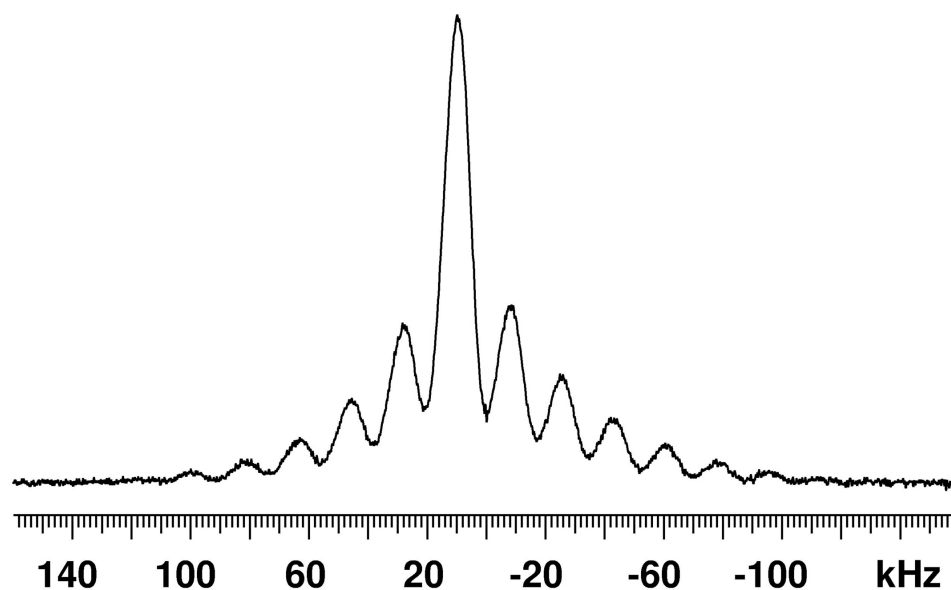


Figure 5.17: The ^{133}Cs MAS spectrum of the $R = 0.6$ (CsB-60 glass). The width of the centre band is $\sim 10,000$ Hz, whereas the second-order broadening is calculated to be ~ 10 Hz.

The REDOR results for the $R = 0.1$ and 0.54 glasses are depicted in Figure 5.18c. At low alkali concentrations, the ^{14}B signals dephase at a greater rate than the ^{13}B signal. This result is consistent with the expectation that alkali cations will preferentially interact with the anionic ^{14}B species; or more specifically with the oxygens about such

boron sites as they would be expected to bear a greater partial negative charge than those linking two neutral $^{[3]}\text{B}$ sites. The dephasing of the $^{[3]}\text{B}$ in addition to the $^{[4]}\text{B}$ indicates that the cesium cations are coordinated to oxygens on both $^{[3]}\text{B}$ and $^{[4]}\text{B}$ sites. This would be expected if the $^{[4]}\text{B}$ sites were distributed evenly throughout the glassy network, as opposed to being clustered together.

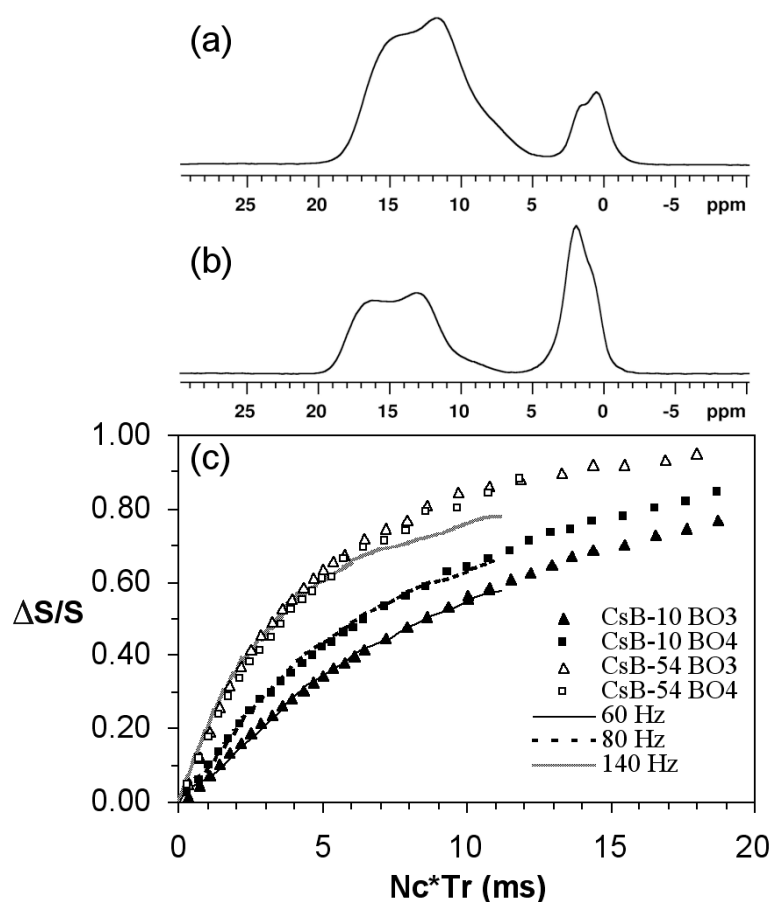


Figure 5.18: ^{11}B MAS spectra of the CsB-10 (a) and CsB-54 (b) glasses. The results of the $^{11}\text{B}\{^{133}\text{Cs}\}$ REDOR experiments for these glasses along with best-fit numerical simulations.

A two-spin simulation allows an approximation of the mean dipole-fields experienced by the nuclei. The results of these simulations are shown in Figure 5.18c. For

the low-alkali glass, the ^{14}B sites are best fit to a mean dipolar field of 80 Hz (3.99 Å) and the ^{13}B site to 60 Hz (4.40 Å). This confirms the assumption that the cesium cations are preferentially associated with the ^{14}B sites within the glass. This is in contrast to what was observed for $^{11}\text{B}\{^{23}\text{Na}\}$ REDOR experiments of sodium borate glasses, where the ^{13}B and ^{14}B exhibit very similar dephasing.¹²⁵ The exact cause of this difference between sodium and cesium is still unclear. However, it may be due to interference of the first-order quadrupole interaction on the efficient inversion of populations of the re-coupling nucleus: Na-23 has been shown to possess C_Q 's of 1.5-2.3 MHz.^{121,124} Such large quadrupole couplings would make complete inversion (especially of the satellite transitions) challenging. Another possibility could be the effect of ion mobility in the glasses. It is well documented that the smallest alkali cation, lithium (excluding H^+), exhibits significant mobility in lithium borate glasses. The larger alkali cations generally exhibit less mobility than lithium.¹²⁷ The $R = 0.54$ glass exhibited greater cesium dipole fields for both ^{13}B and ^{14}B sites, which could be fit to a coupling of approximately 120 Hz (3.49 Å). Such a result may be expected due solely to the much higher cesium content of the glass. In addition, at such high alkali-loadings, the ^{14}B fraction, \mathcal{N}_4 (0.38) is not sufficient to charge-balance the network modifying cesium cations, and thus non-bridging oxygens form on ^{13}B . These oxygen's in contrast to those bonded to ^{14}B atoms should possess a formal charge of -1 , not just a partial negative charge, and hence a shorter Cs-O bond length (i.e., greater Cs-O interaction) would be expected. Inspection of the REDOR dephasing data does in fact show that the ^{13}B signal is dephasing to a greater extent for every point (experiment), than the ^{14}B signal. However, the difference is within

the experimental error for the measurement, thus limiting any information obtainable about the interaction of the cesium with NBOs.

A more detailed analysis of the ^{14}B region was done in order to investigate the relative cesium-boron interactions of the two signals. It was found that for neither the $R = 0.1$ nor $R = 0.54$ glass was there any significant difference in the dephasing of the two ^{14}B signals (see Figure 5.19). Given that FBBs possessing multiple ^{14}B sites (e.g., diborate, di-triborate) would require either more and/or closer cesium contacts (see Figure 5.15) due to the increased localization of negative charge, it can be assumed that in both these cases, the species (FBBs) giving rise to the observed signals likely both contain either a single or two ^{14}B sites in these glasses.

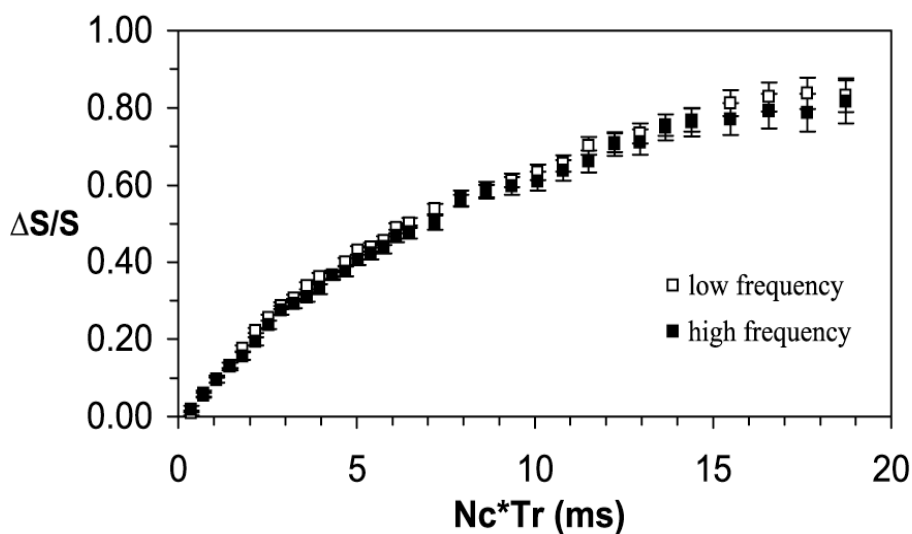


Figure 5.19: $^{11}\text{B}\{^{133}\text{Cs}\}$ REDOR dephasing data for the high (1.5 ppm) and low (0.5 ppm) frequency ^{14}B signals in the CsB-10 glass.

5.4.3 NMR Parameters of Borate Fundamental Building Blocks

In order to better understand the effects of different fundamental building blocks on the observed NMR spectra, the NMR parameters of a series of FBBs were probed. Several FBBs present in anhydrous crystalline borates are known and cover the range of FBBs outlined in Figure 5.9 reasonably well.¹²⁸ Spectra of a series of these crystalline borates were acquired in order to determine the NMR parameters characteristic of given borate fundamental building blocks (if any). DFT calculations of isolated clusters were also utilized to account for any other effects in the crystals arising from the presence of different cations, bonding arrangements and in cases where crystals with a particular FBB could not be found and/or synthesized.

5.4.3.1 Cesium Triborate (CsB_3O_5)

The cesium triborate crystal (CsB_3O_5) consists of a borate network structure made entirely of triborate groups (see Figure 5.9d and Figure 5.15b).⁹⁵ The NMR data are consistent with two ^{13}B and one ^{11}B , and a single crystallographically unique cesium atom. The boron-11 MAS spectrum is consistent with the diffraction data (Figure 5.15a). The isotropic chemical shifts obtained via simulation are 19.1 and 17.8 ppm for the two ^{13}B sites and 0.5 ppm for the ^{11}B site. Other NMR parameters obtained along with errors are given in Table 5.2.

The cesium-133 MAS spectrum (Figure 5.20) indicates the presence of a single cesium site. A small impurity was detected (<2 %) the identity of which is unknown beyond identification as arising from a crystalline impurity due to its narrow peak width. The isotropic chemical shift and an estimate of the quadrupole parameters for the cesium

site may be extracted from the MAS spectrum. The extent of the spinning sideband manifold (from $m = 7/2$ transitions) of 161 ± 5 kHz yields a C_Q of 375 ± 12 kHz, which would impart an isotropic second-order shift of the central transition of less than 9 Hz (~ 0.1 ppm at 14.1 T). This quadrupole coupling was used for the simulation of the $^{11}\text{B}\{^{133}\text{Cs}\}$ REDOR data for this system. As a result the centre-of-gravity of the isotropic band, provides a reasonable estimate of the true isotropic chemical shift ($\delta_{\text{iso}} = 54.5$ ppm).

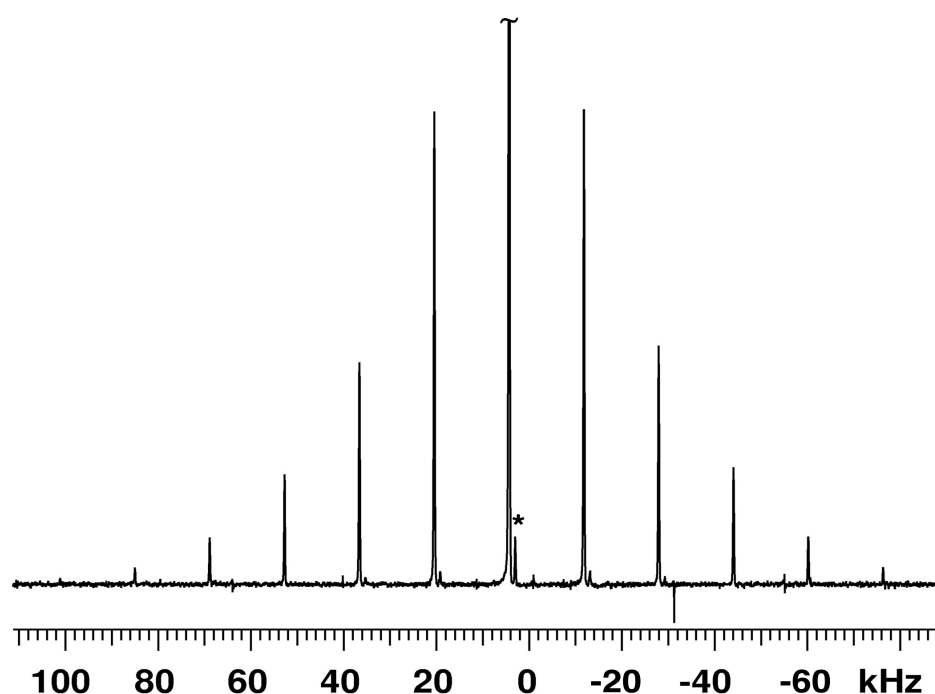


Figure 5.20: ^{133}Cs MAS spectrum of the cesium triborate crystal. The central transition is displayed off scale and a minor impurity (*ca.* 2%) is marked with an asterisk.

Table 5.2: ^{11}B and ^{133}Cs NMR parameters for cesium triborate (CsB_3O_5) crystal obtained via simulation of the experimental spectra.

Nucleus/Site	δ_{iso} (ppm)	C_Q (MHz)	η	Ω (ppm)	κ
¹¹ B					
Site 1 (¹³ B)	19.1 ± 0.5	2.75 ± 0.05	0.27 ± 0.05	n.d.	n.d.
Site 2 (¹³ B)	17.8 ± 0.5	2.55 ± 0.05	0.30 ± 0.05	n.d.	n.d.
Site 3 (¹⁴ B)	0.5 ± 0.5	0.170 ± 0.05	0.5 ± 0.1	n.d. ^a	n.d.
¹³³ Cs	54.5 ± 0.5	0.38 ± 0.01	n.d.	120 ± 3	0.0 ± 0.2

^a An asymmetry in the intensity of the ± 1 order spinning sidebands was observed, indicating a non-zero CSA. However, no definitive estimate could be obtained without knowledge of the relative tensor orientations.

Cesium is highly polarizable, and as a result is known to be subject to substantial shielding anisotropy.¹²⁹ The extent of shielding anisotropy of the cesium was probed by analysis of the central-transition lineshape from a non-spinning spectrum. The non-spinning ¹³³Cs spectrum (Figure 5.21) exhibits a lineshape characteristic solely of shielding anisotropy.¹³⁰ From the C_Q obtained from the MAS spectrum, the breadth of the central transition due solely to the quadrupolar interaction would be 46 Hz (<0.6 ppm at 14.1 T). This miniscule broadening, attributable to the quadrupole coupling with respect to the observed breadth, indicates that the lineshape may be fit, accounting only for the CSA. As a result, the added complication of defining the relative orientation of the two tensors can be avoided. Simulation provides a span of 120 ± 3 ppm and a skew of 0.0 ± 0.06. Simulations of the lineshapes including the quadrupole interaction, resulted in no change in the lineshape.

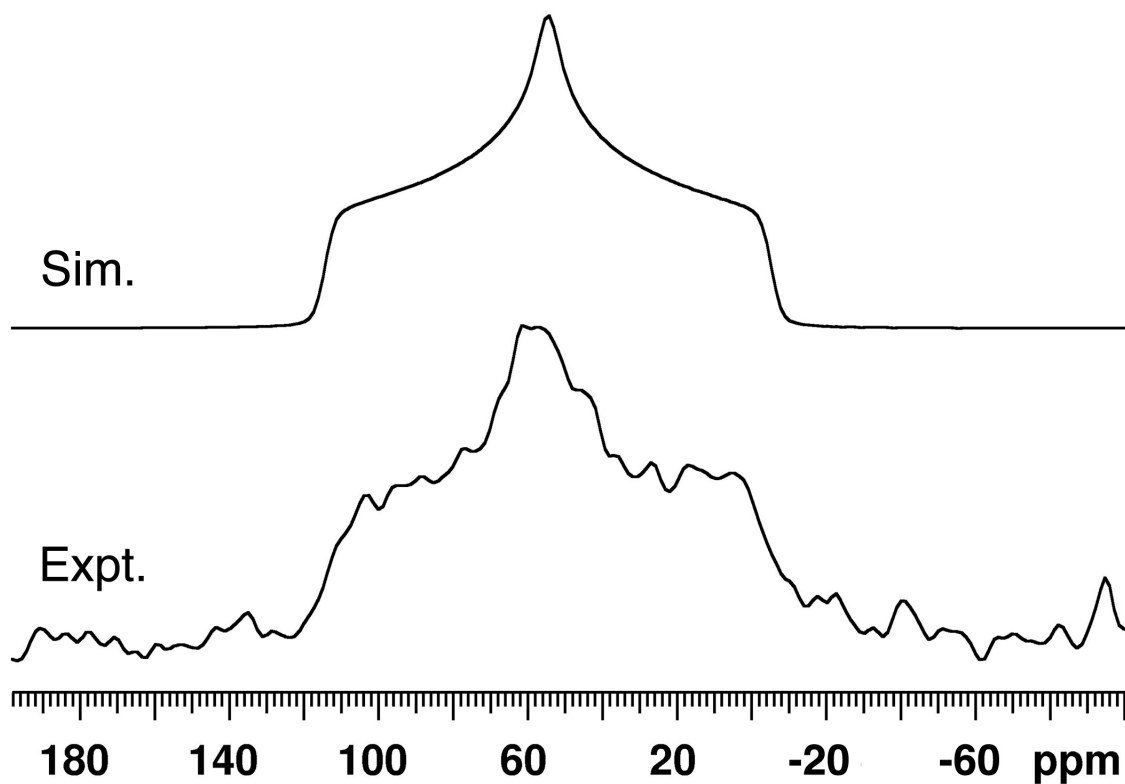


Figure 5.21: The central-transition of a non-spinning ^{133}Cs spectrum of the cesium triborate crystal along with a simulation of the chemical shielding anisotropy.

5.4.3.2 Cesium Pentaborate (CsB_5O_8)

The cesium pentaborate crystal consists solely of pentaborate groups (Figure 5.9g). There is a single ^{11}B site in the asymmetric unit and four distinct ^{10}B sites. The ^{11}B MAS spectrum is shown in Figure 5.22a. A single sharp signal arising from ^{11}B is observed at 2.62 ppm. The ^{10}B region, however, consists of a more complex signal due to the overlap of the signals. Initial attempts at fitting the MAS spectrum revealed that more than one unique combination of parameters (δ_{iso} , C_Q and η) for the four sites could be found which yielded an adequate representation of the lineshape. ^{11}B 3QMAS (see Figure 5.22b) was used to further constrain the fits. The 3QMAS resolves the single overlapping signal into three signals with relative intensities of *ca.* 2:2:3. This deviates somewhat from the total of four sites, however, this may be accounted for by two factors. Firstly, 3QMAS excitation is sensitive to many parameters including the chemical shift in the rotating frame (which differs by ~ 570 Hz in this case). Secondly, the spectrum was truncated slightly in the indirect dimension, thus some intensity must be lost and it need not be the same loss for all sites.

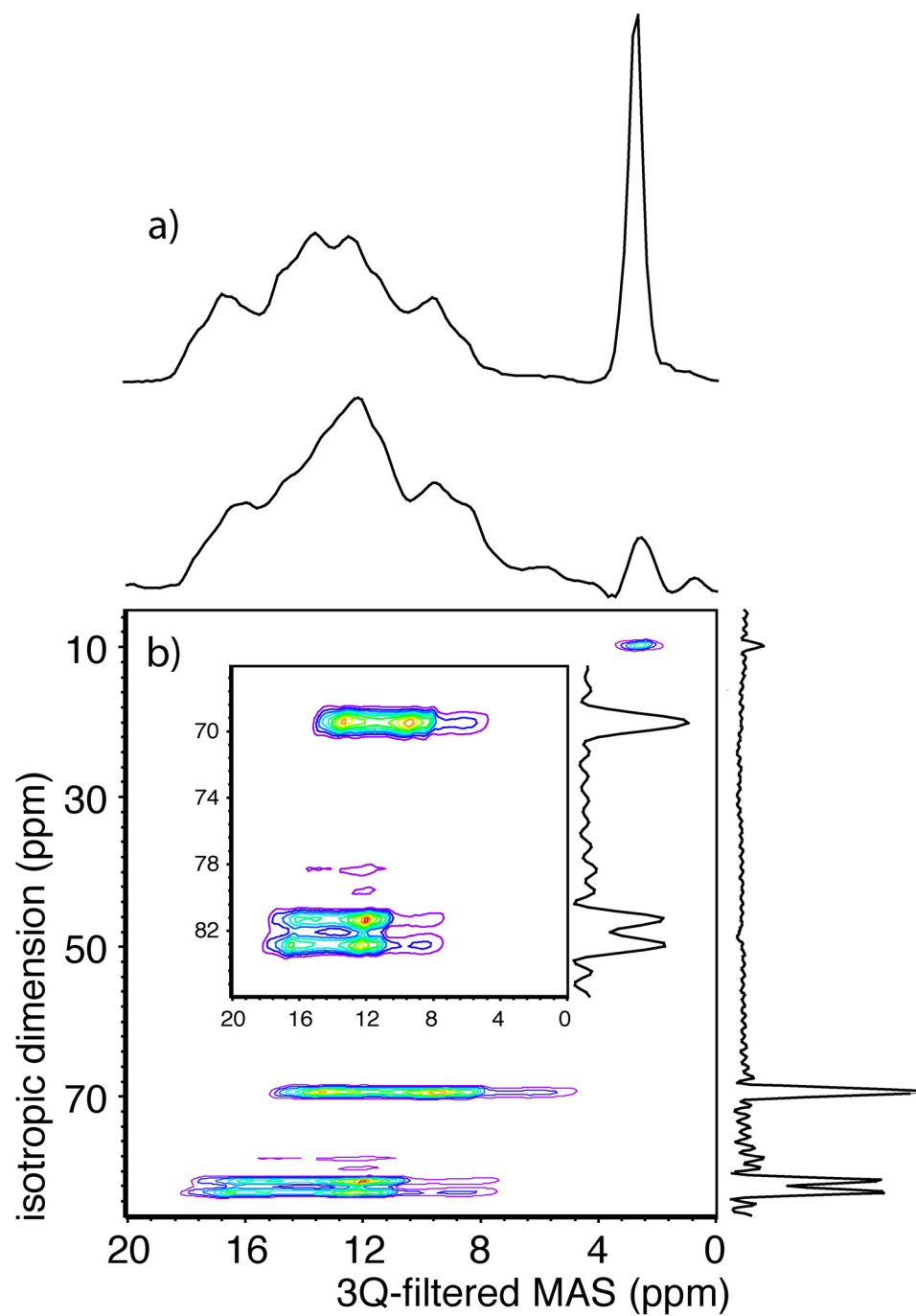


Figure 5.22: ^{11}B NMR spectra of CsB_5O_8 ; The MAS spectrum (a) is shown for comparison with the F2 projection of the (b) 3QMAS spectrum. An expansion of the ^{11}B region is shown inset.

5.4.3.3 Potassium and Rubidium Diborate ($\text{K}_2\text{B}_4\text{O}_7$ & $\text{Rb}_2\text{B}_4\text{O}_7$)

The potassium and rubidium diborate crystals ($\text{K}_2\text{B}_4\text{O}_7$ and $\text{Rb}_2\text{B}_4\text{O}_7$) each possess a diborate group (Figure 5.9f), a di-triborate group (Figure 5.9e), and a non-ring ^{13}B site (Figure 5.9a). The result is a total of eight distinct sites; four three-coordinate and four four-coordinate. The ^{11}B MAS spectrum (Figure 5.23) does in fact exhibit four distinct signals in the ^{14}B region of the spectrum (2.25, 1.70, 0.85 and 0.34 ppm). In contrast to the pentaborate spectrum, deconvolution of the ^{13}B region for the diborate was fairly straightforward and MQMAS was not required; however, it could potentially be used to clear up minor assignment issues (effectively reducing errors in parameter values).

K-39 (QCPMG-MAS) and Rb-87 (QCPMG) NMR spectra (data not shown) were acquired for both of these samples; however, the presence the four distinct alkali cation sites in each crystal could not be resolved by these simple one-dimensional techniques.

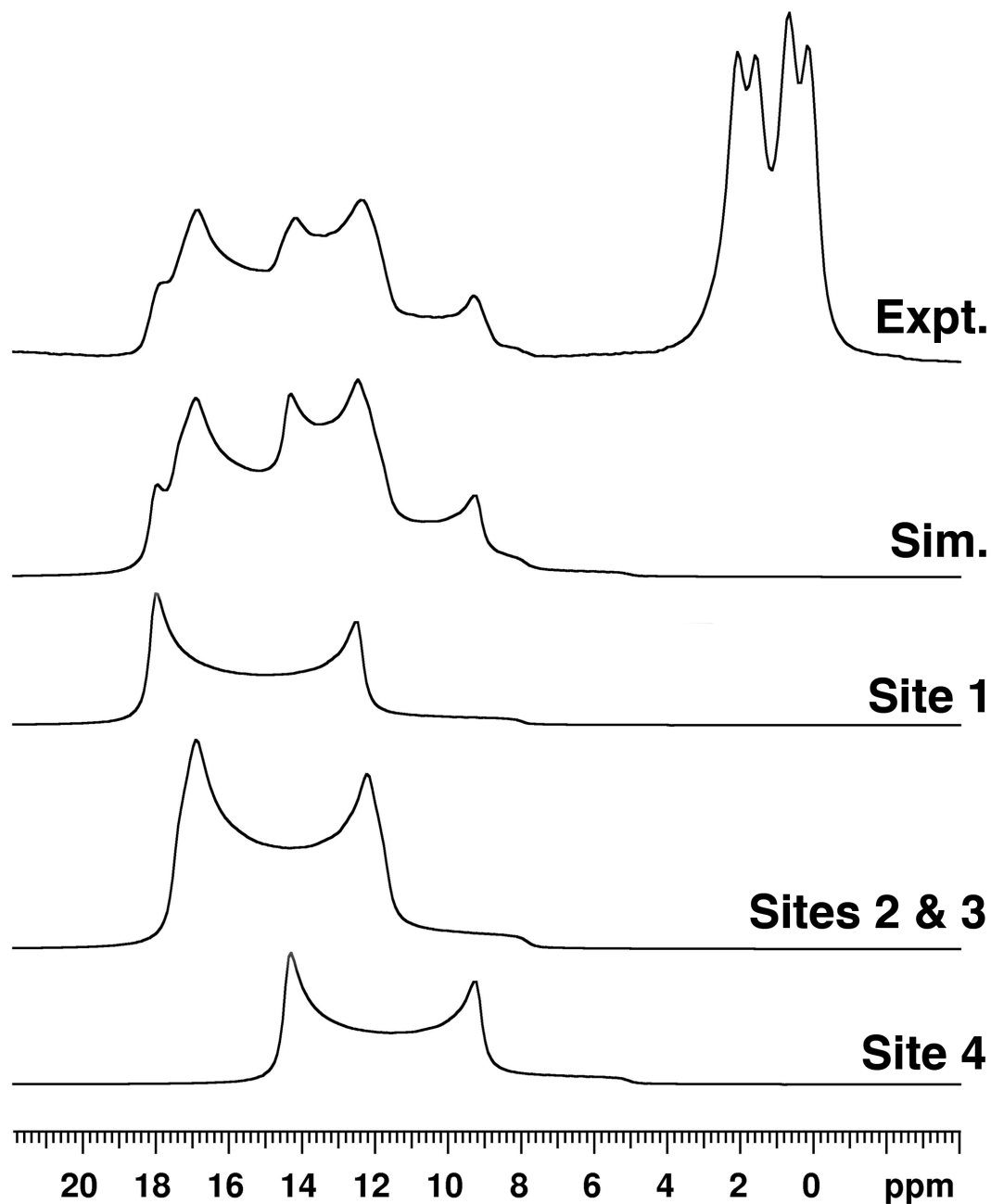


Figure 5.23: The ^{11}B MAS spectrum of the potassium diborate crystal. The four ^{4}B signals (two from the diborate ring, the other two from the di-triborate ring) appear between 3 and -1 ppm. Fits to the ^{3}B lineshape allowed extraction of those parameters (see Table 5.3). The rubidium diborate yielded an identical spectrum.

5.4.3.4 DFT Calculations of FBBs

The calculated parameters for the various FBBs (Table 5.3) are in reasonably good agreement with those obtained experimentally and with those expected of borates in general. The correlation of the experimentally determined and the calculated shifts, although not outstanding, can be seen in Figure 5.24.

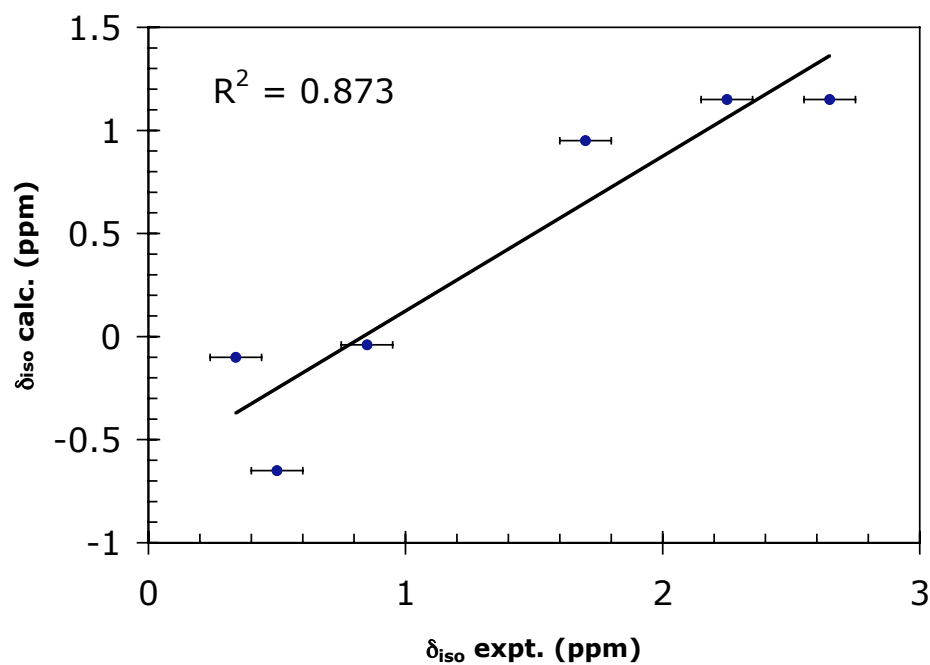


Figure 5.24: Correlation of the observed ^{11}B isotropic chemical shifts for the $[\text{4}]\text{B}$ sites with those calculated using DFT. Line of best-fit and R^2 shown on graph.

Table 5.3: Calculated and experimental ^{11}B NMR parameters.

Structural Unit	Center	δ_{iso} (ppm)	C_Q (MHz)	η
DFT				
Non-ring ^{11}B (dihedral $\neq 180^\circ$)	^{11}B	17.61 (15.45)	2.85 (2.84)	0.00 (0.13)
Boroxol	^{11}B	17.99	2.88	0.32
	^{11}B	18.70	2.88	0.33
	^{11}B	18.12	2.88	0.28
Pentaborate	^{11}B	17.68	2.90	0.15
	^{11}B	17.00	2.84	0.19
	^{11}B	16.44	2.84	0.20
	^{11}B	18.39	2.93	0.17
	^{11}B	1.15	0.70	0.70
Triborate	^{11}B	16.93	2.80	0.16
	^{11}B	16.75	2.82	0.17
	^{11}B	-0.65	0.63	0.64
Di-triborate	^{11}B	16.09	2.82	0.16
	^{11}B	-0.10	0.28	0.52
	^{11}B	-0.04	0.48	0.46
Diborate	^{11}B	18.06	2.70	0.03
	^{11}B	21.02	2.86	0.08
	^{11}B	0.95	0.47	0.49
	^{11}B	1.15	0.23	0.80
Experimental				
Non-ring ^{11}B (B_2O_3 glass) ^a	^{11}B	14.5	2.6	0.2
Non-ring ^{11}B (B_2O_3 crystal) ^b	^{11}B	14.6	2.69	0.05
Non-ring ^{11}B ($\text{K}_2\text{B}_4\text{O}_7$)	^{11}B	16.5	2.55	0.1
Boroxol (B_2O_3 glass)	^{11}B	18.5	2.6	0.3
Triborate (CsB_3O_5)	^{11}B	17.8	2.55	0.3
	^{11}B	19.1	2.75	0.28
	^{11}B	0.5	0.168	0.5
Diborate & Di-triborate ($2\text{B}_2\text{O}_3$) ($\text{K}_2\text{B}_4\text{O}_7$)	^{11}B	18.8	2.55	0.1
	^{11}B	18.8	2.55	0.1
	^{11}B	0.85	0.5	> 0.5
	^{11}B	0.34	0.5	> 0.5
	^{11}B	19.8	2.65	0
	^{11}B	2.25	0.5	> 0.5
	^{11}B	1.70	0.5	> 0.5
Pentaborate (CsB_5O_8)	^{11}B	19.0	2.62	0.21
	^{11}B	18.7	2.62	0.20
	^{11}B x 2	16.0	2.55	0.22
	^{11}B	2.62	0.29	0.55

^a Values reported by Youngmann *et al.*¹⁰⁷

^b Values reported by Kroeker *et al.*¹³¹

A depiction of the isotropic shifts of the ^{11}B signals for various FBBs is shown in Figure 5.25, which provides a clearer picture of the structural impact on the isotropic

chemical shifts. We see that those ^{14}B sites which are part of two rings (pentaborate and diborate) are shifted to the highest frequencies. Those within a single ring (triborate and di-triborate) are slightly more shielded (i.e., appear at lower frequency) and the non-ring ^{14}B signal appears at the lowest frequency (most shielded). This is exactly what is observed for the ^{13}B site ($^{13}\text{B}_{\text{ring}} \sim 18$ ppm, $^{13}\text{B}_{\text{non-ring}} \sim 14$ ppm). This difference in the shielding has been attributed to differences in the B-O-B bond angle.¹¹⁶ However, I have also found that the dihedrals may play a role in the increased shielding (see Table 5.3). The isotropic chemical shift for the non-ring BO_3 model where the B-O-B-O dihedral angle deviates from 180° (or 0°) was calculated to be more shielded by 2.16 ppm than a model where this dihedral angle is 180° (or 0°).

It is worth noting that the observed chemical shift difference of ~ 1 ppm between the two signals experimentally is very closely matched by the shift differences between the “two-ring” and “one-ring” species. Using the correlation of the experimental and calculated ^{14}B shifts, the isotropic chemical shift of the non-ring ^{14}B species would be expected to appear at a resonance frequency of -1.4 ppm. Since the lowest frequency signal in these glasses is $\sim +0.5$ ppm, the hypothesis of non-ring ^{14}B in alkali borate models¹⁰⁷ is likely incorrect.

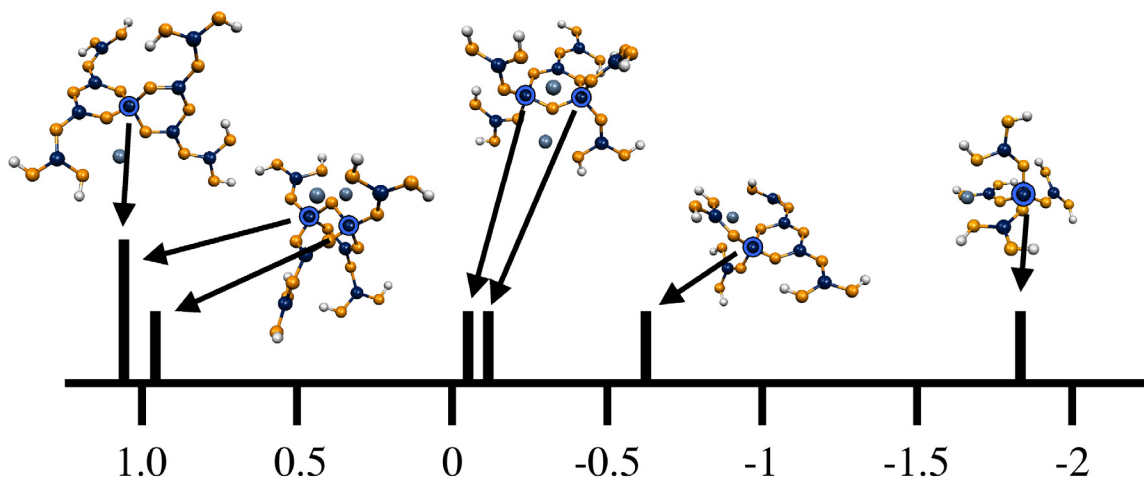


Figure 5.25: Depiction of the calculated four-coordinated boron ^{11}B isotropic chemical shifts.

5.4.4 ^{11}B MAS and Multiple-Quantum MAS of High Alkali-content Glasses

The N_4 values observed for the various alkali borate glasses above $R = 0.4$ are different for cesium and lithium borates (see section 5.4.1). This implies that the cesium borates preferentially form NBOs at higher alkali content. The most direct method of investigating the presence of non-bridging oxygens would be oxygen-17 NMR. However, this approach, is marred by difficulties. Oxygen-17 is present in only 0.035% naturally, and thus usually necessitates costly isotopic enrichment of glasses. It is a spin-5/2 nucleus, possesses a lower Larmor frequency (frequency ratio, $\Xi = 13.556457$) and a moderate-high nuclear electric quadrupole moment ($Q = -2.558 \text{ fm}^2$). Although systems with large C_Q 's are known,¹³² in typical oxide systems, C_Q 's lie between 2 and 7 MHz,^{79,133-135} which at higher fields ($B_0 > 11.7 \text{ T}$), result in little second-order lineshape to the central-

transition. In glasses, the distribution of NMR parameters typically results in broader resonances, precluding direct identification of distinct sites from a 1D MAS spectrum. As a result, techniques such as ^{17}O MQMAS,¹³⁶⁻¹³⁸ DAS^{30,134} or STMAS¹³⁹⁻¹⁴¹ are often required to obtain resolution of sites. The inherent insensitivities of MQMAS and STMAS, in particular, require isotopic enrichment to levels much higher than that needed simply to acquire a 1D MAS spectrum. Because of this, ^{17}O NMR is not the most practical technique for the study of NBOs in borate glasses. A more viable approach is to use ^{11}B MQMAS.

It has been demonstrated previously that in crystalline systems, an increase in the ^{11}B isotropic chemical shift is observed with increasing depolymerization of the borate network.^{103,131} Some typical NMR parameters for ^{11}B sites with zero (T^3), one (T^2), two (T^1) and three (T^0) non-bridging oxygens are given in Table 5.4. Given this known range of NMR parameters, the expected shift ranges in the isotropic dimension of 3QMAS spectra at 14.1 T may be calculated. The expected ranges are dominated by the evolution of the chemical shift; however, the systematic differences in C_Q and η also contribute to the enhanced resolution. Thus using ^{11}B MQMAS it may be possible to resolve peaks due to ^{11}B possessing different numbers of NBOs, allowing a quantification of the depolymerization of the borate network.

The boron-11 MAS spectrum (Figure 5.26) of a very high lithium content borate glass ($R = 2.5$) exhibits an interesting lineshape in comparison to glasses at much lower lithium content and a very small ^{10}B signal (3%). Although the ^{11}B lineshape possesses features indicative of ^{11}B sites bearing NBO's (e.g., site with $\eta = 0.4 - 0.7$), a single satisfactory fit could not be obtained.

Table 5.4: ^{11}B NMR parameters for various ^{13}B sites.

Site	δ_{iso} (ppm)	C_Q (MHz)	η	δ_{MQ} (ppm) ^a
T³	14.5 – 18.0	2.6 ± 0.1	0.05 ± 0.05	65 – 78
T²	16.0 – 19.0	2.5 ± 0.1	0.65 ± 0.1	72 – 83
T¹	18.0 – 22.0	2.7 ± 0.1	0.5 ± 0.1	80 – 95
T⁰	20.0 – 23.0	2.8 ± 0.1	0.05 ± 0.05	87 – 99

^a Frequency in MQ (isotropic) dimension calculated at 14.1 T as per the “ C_z ” convention as described by Millot and Man.²⁸

3QMAS of this glass at 14 T revealed that the ^{13}B signal is dominated by two species in an approximately 3:2 ratio (Figure 5.27). The NMR parameters (δ_{iso} , C_Q and η) indicate that these signals belong to T⁰ and T¹ sites, respectively. Using the isotropic chemical shift values and quadrupole couplings from the 3QMAS, fits to the MAS spectra at 14 T and 21 T were done to further constrain the intensities of the signals from the two sites.

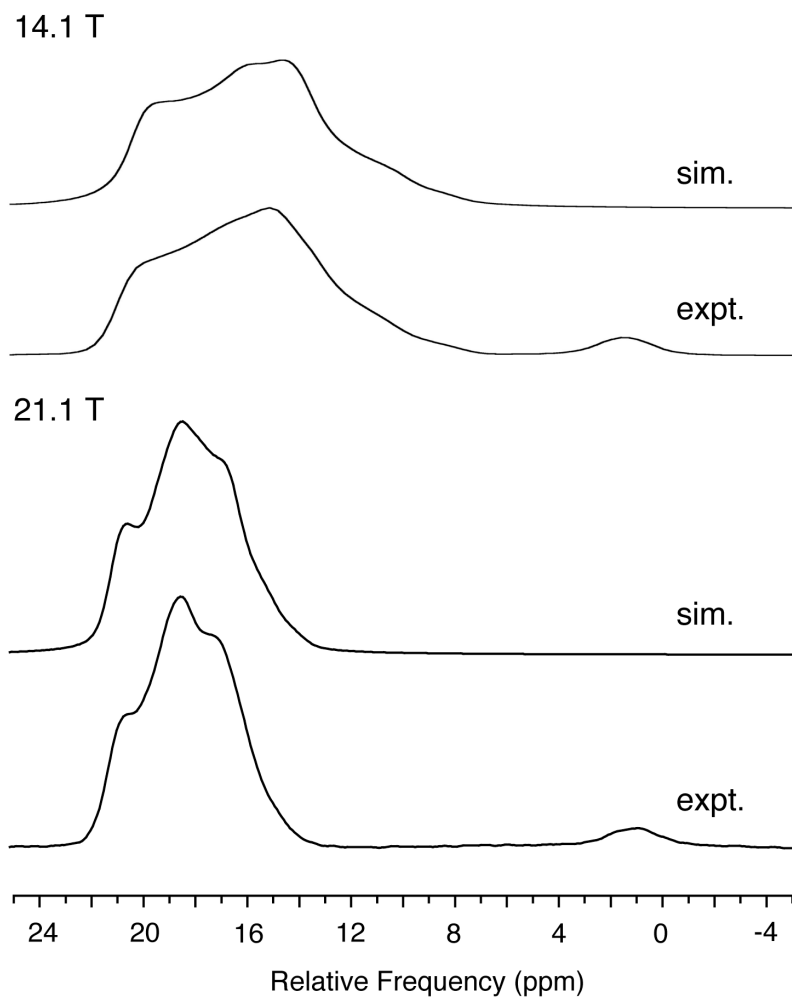


Figure 5.26: ^{11}B MAS spectra of the $R = 2.5$ lithium borate glass at 14.1 and 21.1 T along with simulations of the ^{11}B sites. Simulations were constrained by the NMR parameters (δ_{iso} , C_Q and η) obtained from the ^{11}B 3Q-MAS acquired at 14.1 T.

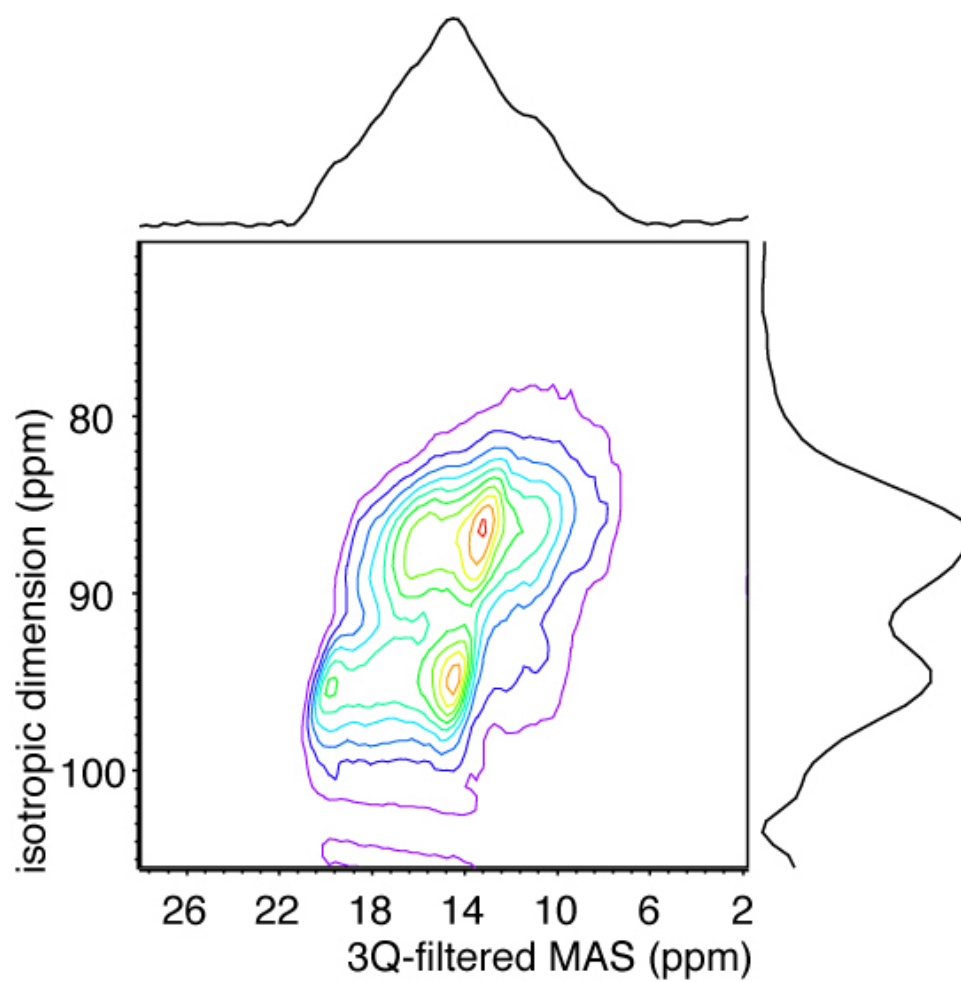


Figure 5.27: Contour plot of ^{11}B MQMAS spectrum of R = 2.5 lithium borate glass.

Distinct signals are observed for the T^1 (87 ppm) and T^0 (95 ppm) sites.

Table 5.5: ^{11}B NMR parameters for the $R = 2.5$ lithium borate glass, from MAS and MQMAS NMR.

Site	δ_{iso} (ppm)	C_Q (MHz)	η	Pop. (%)
T ⁰	22.1 ± 0.4	2.70 ± 0.05	0.06 ± 0.06	38 ± 2
T ¹	20.3 ± 0.4	2.65 ± 0.05	0.57 ± 0.05	58 ± 2
[⁴ B]	0.3 ± 0.2	n.d	n.d	4 ± 0.5

The centre-of-gravity of the observed peaks in both two dimensions allows the extraction of the isotropic chemical shift and the quadrupole parameter, P_Q ($P_Q = C_Q(1 + \eta^2/3)^{0.5}$). Extraction of the quadrupole coupling constant and the asymmetry of the EFG require analysis of the 3Q-filtered (3QF) MAS lineshape. Simulations of the observed lineshapes for the T¹ and T⁰ sites are shown in Figure 5.28. It well known that although the observed lineshape should be identical to that obtained from a MAS experiment, differences in the efficiency of the MQ-excitation and conversion for different crystallite orientations in a powder result in lineshapes which deviate from this ideal lineshape. Such deviations are clearly evident in the spectra of the $R = 2.5$ lithium borate glass; however, the positions of the discontinuities and inflection points are generally still reliable. To ensure that these distortions are not giving rise to deceiving lineshapes, full numerical simulations were done using the same conditions as the experimental spectrum. It should be noted that of particular importance is the shift with respect to the transmitter frequency, as it was found that this can affect the observed lineshape. These simulations (labeled 3QF) show lineshape distortions closely resembling

the experimental lineshapes. The C_Q and η parameters (Table 5.5) are found to be identical within error to those obtained using an ideal MAS lineshape.

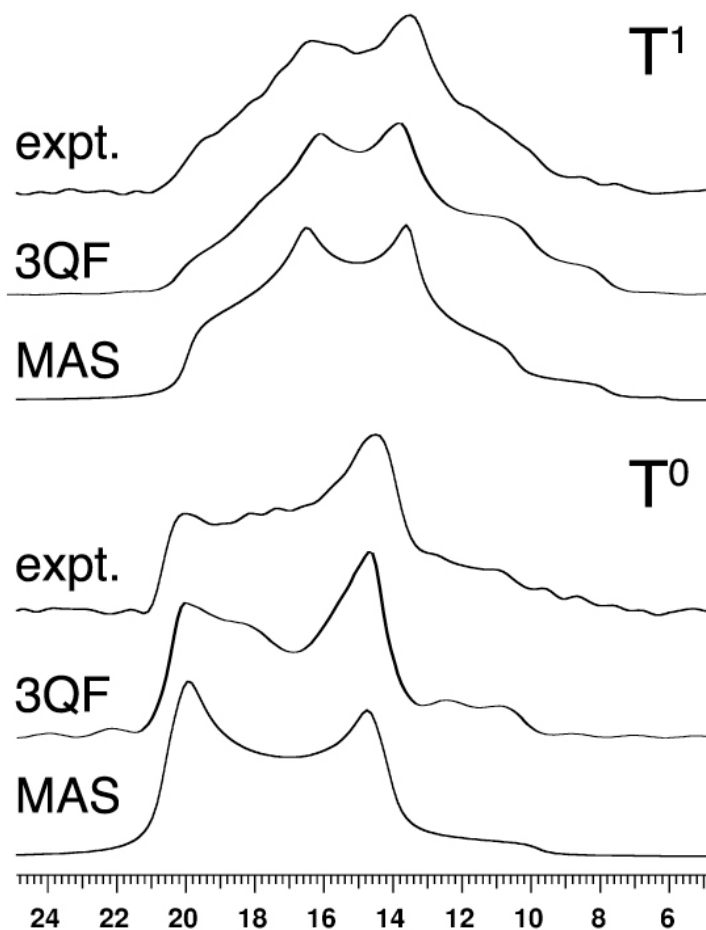


Figure 5.28: Experimental slices from the MQMAS of $R = 2.5$ lithium borate glass (expt.) along with simulated lineshapes under ideal conditions (MAS) and full 3Q-filtered (3QF) simulation. Note that both simulations yield identical parameters (δ_{iso} , C_Q , η), however, the 3Q-filtered simulations better reproduce the experimental lineshape distortions.

In order to further investigate the observed differences in the MAS lineshapes of the ^{13}B region of the lithium versus the cesium borate glasses, 3QMAS experiments were

done for different parallel compositions. Cesium and lithium borate MQMAS spectra exhibit very different lineshapes in both the directly (“MAS”) and indirectly (“isotropic”) detected dimensions. The lineshapes in the isotropic dimension for the cesium borate glasses are generally narrower than those for the corresponding lithium borate glass, and they tend to exhibit some degree of asymmetry to the lineshape (Figure 5.29). This is consistent with the observation of the ^{11}B MAS spectra where lineshapes and linewidths for the lithium borates tend to suggest a greater degree of disorder and the absence of the multiple ^{11}B signals associated with medium-range ordering of the glass.

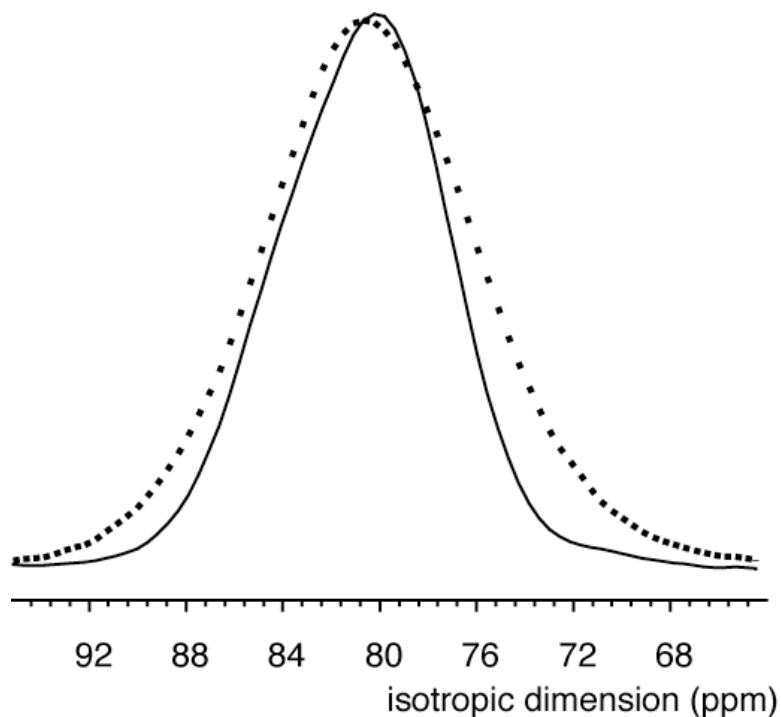


Figure 5.29: Isotropic projections of the R = 0.7 cesium (solid) and lithium (dashed) borate glasses.

The individual slices in the directly detected dimension display very different lineshapes (Figure 5.30). However, the presence of multiple sites (T^3 , T^2 , etc.) and their

quantification cannot be determined reliably due to lack of resolution. Despite this inability to quantify the boron species present in the glass, the observed shift to higher frequency of the resonance in the isotropic dimension conforms well to the predicted shifts based on the work on crystalline materials.

Although the inhomogeneous broadening due to the distributions of NMR parameters precluded the acquisition of spectra with sufficient resolution to quantify the different T^n sites (except in one case), the general trends predicted were observed. An increase in the chemical shift of the resonance in the isotropic dimension with increasing alkali content is observed. In addition, the observed lineshapes in the slices of the MQMAS spectra (Figure 5.30) are indicative of sites with asymmetry parameters in the range of 0.3-0.8 as expected for T^2 and T^1 sites (see Table 5.4).

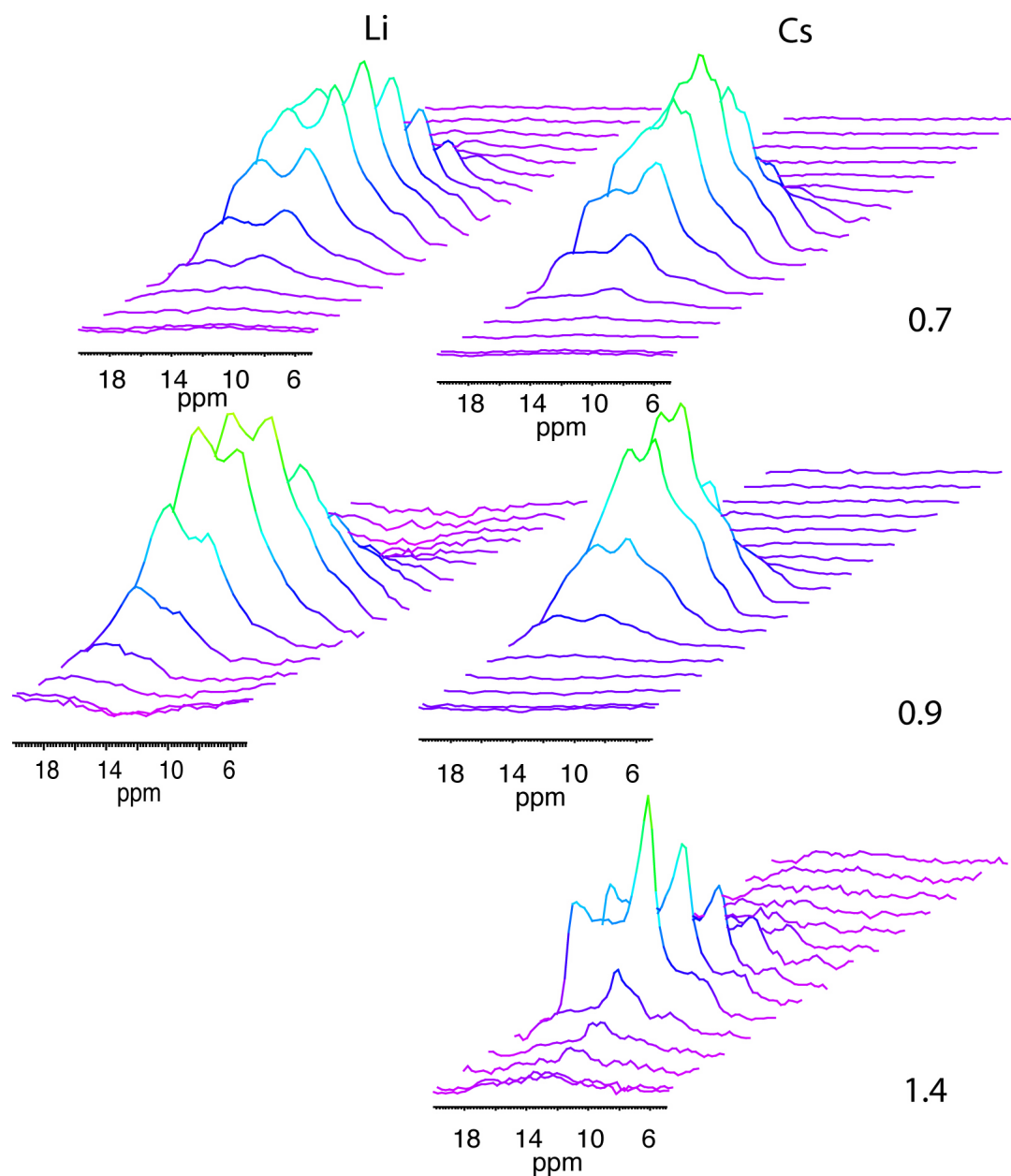


Figure 5.30: ^{11}B MQMAS spectra for the lithium and cesium borate glasses investigated. The stacked plots are displayed showing every 5th slice (digital resolution = 0.44 ppm/pt) in the indirect (isotropic) dimension.

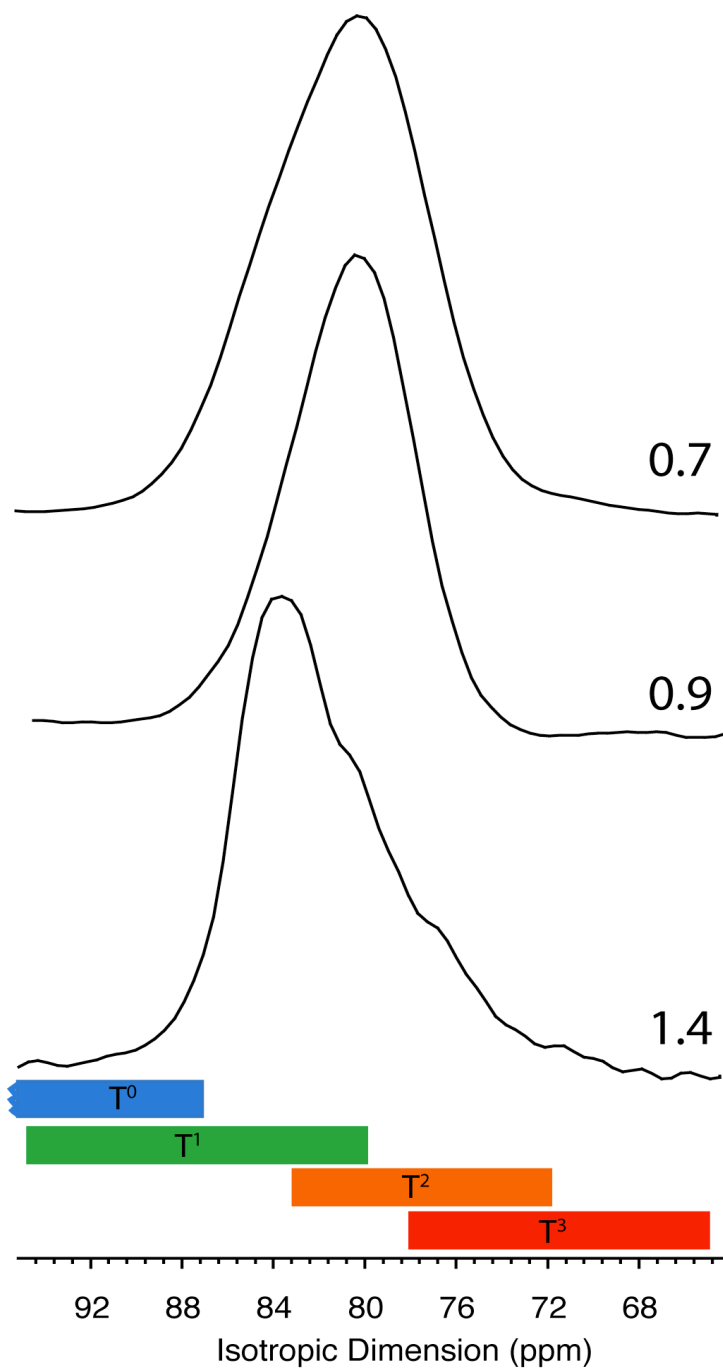


Figure 5.31: ^{11}B MQMAS isotropic projections for $R = 0.7$, 0.9 and 1.4 cesium borate glasses. Despite the lack of site resolution, the predicted trend to higher shifts with alkali loading is observed.

5.5 *Borosilicates*

Given that the $^{133}\text{Cs}\{^{11}\text{B}\}$ dipolar recoupling in cesium borate glasses was successful, the next step was to move to a ternary system more closely resembling the compositions used for radioactive-waste encapsulation. The system chosen was the cesium borosilicate system. The choice of relevant compositions is complicated somewhat as *real* wasteform glasses tend to possess many more components, and even some other model systems investigated possess 7-12 major components,⁶⁴⁻⁶⁸ in addition to the waste oxides (which can have over a dozen different cations). Taking these glass compositions and effectively contracting the phase dimensionality to three was achieved using the following constraints.

- 1) All typical network-modifying cations (e.g., Na^+ , Li^+ , Ca^{2+} , Mg^{2+} etc.) were assumed to play the same role in the glass, and were considered as a single modifier (with appropriate accounting for differences in cation charge).
- 2) Accounting for the presence of additional network formers was done by associating them as either more SiO_2 - or more B_2O_3 -like. Due to the difficulty in assigning this SiO_2 - or B_2O_3 -like quality, switching the designation was used to calculate the error (shown in Figure 5.32).
- 3) The effect of minor components (< 1 wt %) was not considered. Generally, the sum of these components was less than 10 wt % of the glass.

A model ternary cesium borosilicate system was devised according to these constraints, where typical compositions were found in the same region. Other alkali borosilicates (Li and Na) are prone to phase separation into silicon-rich and boron-rich phases. These boron-rich phases are more susceptible to acid catalyzed hydrolysis and dissolution,

allowing for leaching of the radioactive waste that these glasses are expected to encapsulate. One method of probing the homogeneity of such glasses is via ^{17}O MQMAS NMR (the difficulties of which were discussed in the previous section). The use of REDOR NMR ($^{11}\text{B}\{^{133}\text{Cs}\}$, $^{133}\text{Cs}\{^{11}\text{B}\}$, $^{29}\text{Si}\{^{11}\text{B}\}$ and $^{29}\text{Si}\{^{133}\text{Cs}\}$ etc.) could potentially provide the same information without the need for any isotopic labeling.

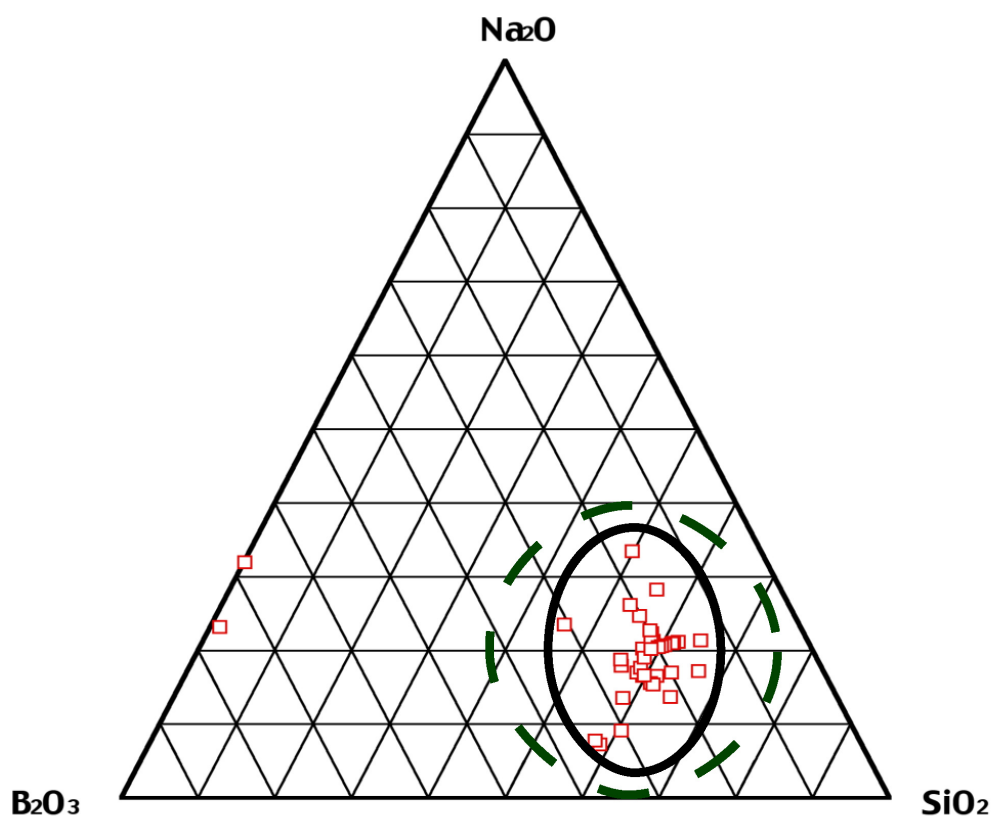


Figure 5.32: $\text{Na}_2\text{O}-\text{B}_2\text{O}_3-\text{SiO}_2$ ternary phase diagram showing the *corrected* (see text) compositions of real and other model wasteform-glass compositions. An extended compositional range partially accounting for errors in *corrections* is also shown (green dashed line)

As with the cesium borates, where the cesium triborate crystal (CsB_3O_5) was used to set-up and test the $^{133}\text{Cs}\{^{11}\text{B}\}$ dipolar recoupling experiments, a crystalline borosilicate

was necessary to test initial Si-B experiments. Datolite, $\text{CaBSiO}_4(\text{OH})$, was selected to test the $^{29}\text{Si}\{^{11}\text{B}\}$ REDOR experiment. Datolite is of fairly low symmetry (monoclinic, $\text{P}_{21/c}$).¹⁴² Neither boron nor silicon lie on a special position and as such, no specific requirements for the magnitude or orientations for the various NMR interaction tensors (e.g., CSA, EFG) exist for either nucleus. The silicon atoms are Q^3 , thus possessing three bridging oxygen bonds (to boron) and a single non-bridging oxygen. The three nearest silicon-boron distances are at 2.745, 2.749 and 2.804 Å ($R_{DD} = -347.6$ to -370.5 Hz), and in a nearly planar T-shaped arrangement. The next-nearest boron nuclei are at much greater distances (4.786-5.425 Å) and thus impart very small additional dipolar fields of -48.0 to -69.9 Hz.

The silicon-29 MAS (Figure 5.33) and the boron-11 MAS spectra (Figure 5.34) are both consistent with previously published results (see Table 5.6).^{43,143} In addition to the ^{29}Si isotropic chemical shift, a slow spinning spectrum allowed estimates of the shielding anisotropy, which could be necessary for proper fitting of REDOR data.

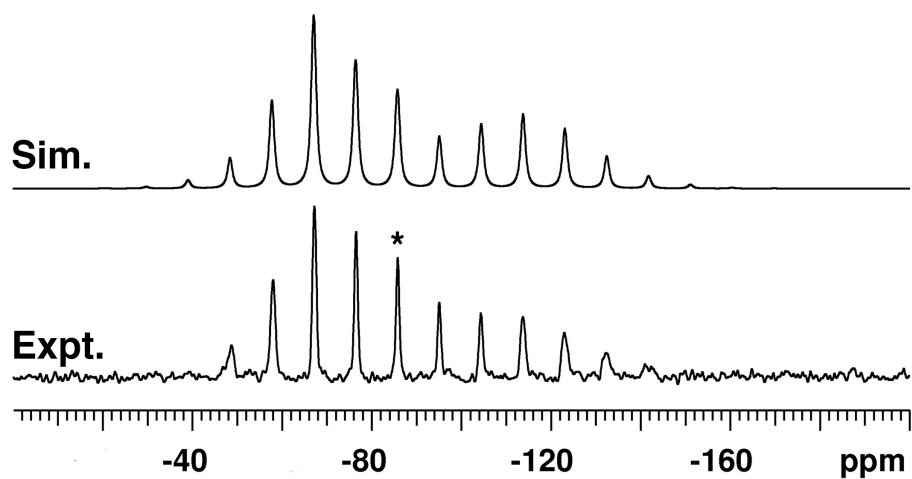


Figure 5.33: ^{29}Si MAS spectrum of datolite ($\nu_{\text{rot}} = 1109 \pm 10$ Hz) along with best-fit simulation. The simulation is based on integrated spinning sideband intensities, rather than peak heights, due to inconsistency of spinning rate. The isotropic peak is marked by an asterisk.

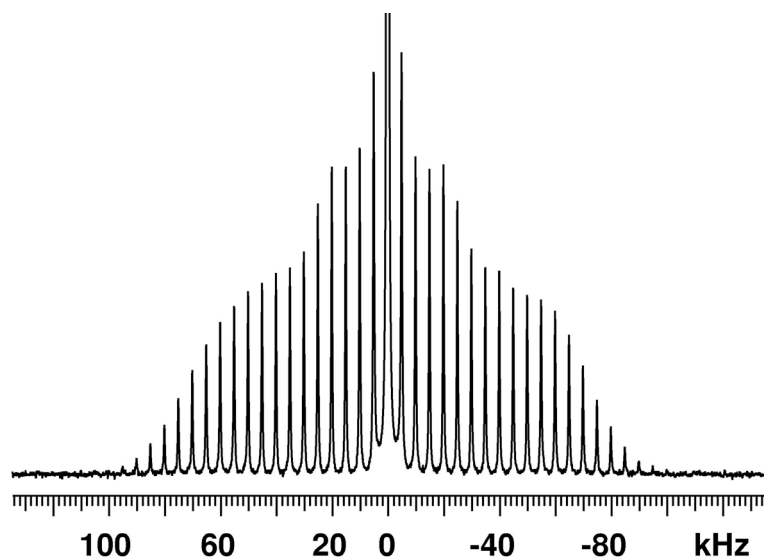


Figure 5.34: $^{11}\text{B}\{^1\text{H}\}$ CPMAS spectrum of datolite ($\nu_{\text{rot}} = 5000$ Hz). The central transition is shown cutoff.

Table 5.6: NMR parameters obtained for datolite from MAS NMR, along with select previously published parameters.

Nucleus	δ_{iso} (ppm)	Ω (ppm)	κ	C_Q (MHz)	η
²⁹ Si	-85 ± 1	54 ± 8	0.5 ± 0.1	-	-
	-83^{a}	n.d.	n.d.	-	-
¹¹ B	0.8 ± 0.5	n.d.	n.d.	0.17 ± 0.01	0.6 ± 0.2
	0.2^{b}	7.8^{b}	0.53^{b}	0.172^{b}	0.647^{b}
¹ H	3.9 ± 0.5	n.d.	n.d.	-	-

^aValue obtained by Sherriff *et al.*¹⁴³

^bValues from single-crystal experiments.⁴³

The set-up for the boron-11 and silicon-29 and the ²⁹Si{¹¹B} REDOR spectra necessitated acquisition of the ¹H MAS spectrum. A single hydroxyl site is expected. In fact, two signals are observed in Figure 5.35b. One of these arises from the rotor components and is often a source of annoyance as it may mask signals (depending on intensity) and imparts a significant frequency-dependent phase to the spectrum (often seen as a baseline roll). Given the properties of the polarization enhancement technique, a ¹H{¹¹B} experiment should yield a spectrum consisting solely of protons within the vicinity of boron-11. The spectrum of Figure 5.35a is clearly of better quality than that of Figure 5.35b. Although unaveraged dipole-dipole couplings may be contributing to the presence and extent of spinning sidebands, the difference in the intensity of the +1 and -1 order spinning sidebands can only be attributed to shielding anisotropy of the ¹H nucleus. No evidence of CSA is observed in the directly detected spectrum, likely a result of the combination of overlapping signals (and their anisotropy) and distortions in signal

intensities arising from the poor baseline. This demonstrates a potentially useful method of overcoming the issue of overlap of signals arising from areas external to the sample.

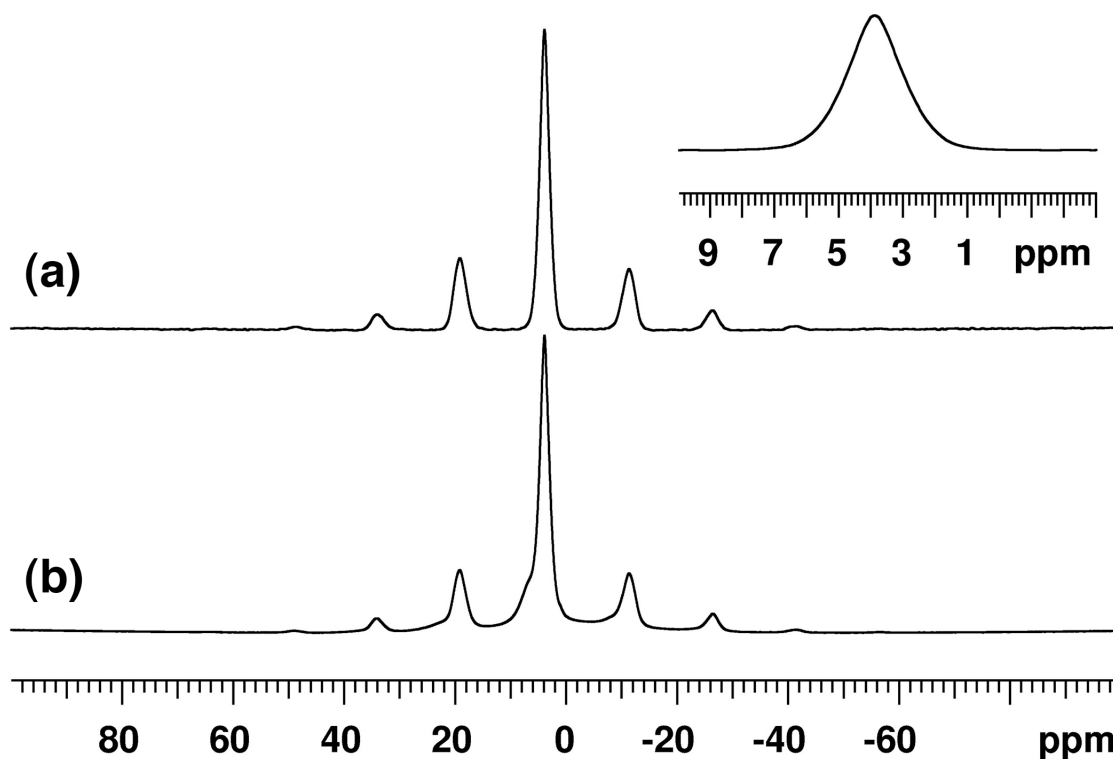


Figure 5.35: Proton NMR spectra of datolite. Spectrum observed via $^1\text{H}\{^{11}\text{B}\}$ CPMAS (a) and direct polarization (b). The isotropic peak is shown inset.

The maximum extent of REDOR dephasing observed is a function of the abundance of the recouple-channel nucleus; thus acquisition of $^{11}\text{B}\{^{29}\text{Si}\}$ is hampered by the low natural abundance of silicon-29 (4.7%). As a result, the better choice is to observe silicon and recouple boron-11 (natural abundance of 81%). A REDOR pulse sequence with only one π -pulse in the middle of the sequence on the boron channel, and multiple

π -pulses on the observe silicon-29 channels was employed due to the greater ease with which one can *perfectly* invert the spin-populations for spin-1/2 nuclei.

Results for an initial attempt at $^{29}\text{Si}\{^{11}\text{B}\}$ REDOR experiment are shown in Figure 5.36. Simulation of this data set has thus far not provided reasonable values. This may be due to the application of ^1H decoupling during the REDOR experiment. Decoupling during the non-REDOR (echo) experiment rules out the possibility that the dephasing is solely (or even largely) due to the ^1H being recoupled on its own. However, interference between the rf at the two frequencies could result in anomalous behaviour.

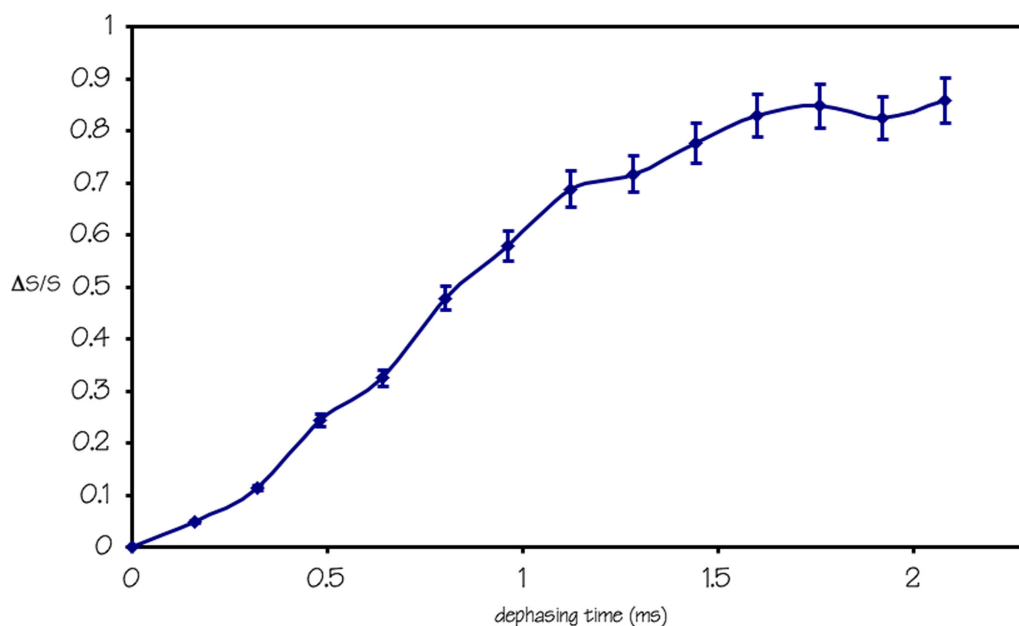


Figure 5.36: REDOR dephasing curve for $^{29}\text{Si}\{^{11}\text{B}\}$ experiment on datolite. The line is drawn as a guide to the eye showing the modulations expected from REDOR.

This preliminary data on a mineral of known structure indicates that reliable REDOR data in glasses may be difficult to obtain, and further optimization is required in order to fully understand the results.

5.6 Conclusions

In contrast to the common assumption that all alkali cations exhibit identical behaviour with respect to determining the structure of the final borate network in alkali borate glasses, clear differences amongst the alkalis are observed.

^{11}B MAS NMR spectroscopy of a series of alkali-borate glasses reveals the presence of multiple four-coordinated boron signals in all the heavy (K, Rb and Cs) alkali borates, whereas only a single ^{11}B signal is observed in the lithium and sodium borate glasses over the same compositional range. The combination of DFT calculations of various species, known to be prevalent in borate crystals, along with ^{11}B NMR of selected crystals was used to probe the structural origins of the multiple ^{11}B signals observed in the ^{11}B MAS spectra. Together they indicate that the presence of non-ring ^{11}B species in alkali borates is highly unlikely. $^{11}\text{B}\{^{133}\text{Cs}\}$ REDOR experiments indicate that the multiple ^{11}B signals arise from FBBs with the same number of ^{11}B species for a given glass composition. Since the presence of rings with multiple ^{11}B sites at low alkali-content is less likely, the two observed signals must be due to more than two fundamental building blocks over the range investigated, despite not showing much variation in the chemical shifts. A precise model of the borate speciation and evolution of fundamental building blocks is limited by the number of constraints provided by the available experimental data.

The trends previously observed in the ^{11}B isotropic chemical shift with network depolymerization for crystalline borates are found to hold in the alkali borate glasses. ^{11}B MQMAS of a lithium borate invert glass allows identification of T^0 and T^1 sites within the glass. The NMR parameters obtained from the high-resolution spectra allow for

fitting of the more-quantitative MAS spectra at 14.1 and 21.1 T, which indicate a structure possessing an anionic charge on the network commensurate with the batch composition.

^{11}B MQMAS of high-alkali borate glasses reveal slightly greater disorder in lithium than cesium borates. A shift of the signal arising from ^{11}B to higher frequency, as predicted from work on crystalline systems, is observed in the glasses.

A regime in the $\text{Cs}_2\text{O-B}_2\text{O}_3\text{-SiO}_2$ system compositionally similar to the much more complex glasses actually used for nuclear waste remediation has been determined by a contraction of the phase dimensionality. A well-characterized model borosilicate crystalline phase (datolite) was investigated by NMR to test the reliability of $^{29}\text{Si}\{^{11}\text{B}\}$ REDOR prior to launching a full-scale study of the ternary glasses; however, there are still difficulties in simulation of the data.

5.7 Future Work

The reason for the observed increase in the ^{11}B resonance frequency with increasing depolymerization is not known. In fact, one might expect that the presence of increased electron density localized at the non-bridging oxygen directly bonded to the boron might increase the shielding, thus decreasing the isotropic shift. A better understanding of the mechanism of the observed decrease in shielding of the boron nucleus may be obtained by the use of quantum chemical calculations.

The synthesis and characterization (boron, cesium and silicon NMR) of cesium borosilicate compositions near those proposed as models for nuclear waste encapsulation could be done. A crystalline material, ideally possessing all of the same nuclei as the

glasses of interest, should be selected/synthesized in order to verify any recoupling experiments to be used for investigations of glasses in order to verify (in)homogeneity.

This would allow a test of the feasibility of using the combination of dipolar fields experienced by the NMR-active nuclei present to probe homogeneity of glasses which could be compared to the results obtained from ^{17}O NMR experiments.

6 Transition Metal and Main Group Cyanides

Research into metal-organic coordination polymers has grown rapidly in recent years, with an emphasis on self-assembled synthesis and functional materials.^{144,145} This has to a great extent been driven by the demand for tunable functional materials exhibiting non-linear optical (NLO),^{146,147} semiconducting^{148,149} and other properties. Metal-organic polymers allow for the tuning of properties via modification of parameters such as the coordination number, oxidation state, ligand size and ligand flexibility.¹⁵⁰ The ability of cyanide to bridge metal centres has been widely used in the construction of such frameworks and related materials.¹⁵¹⁻¹⁵⁴

Structural characterization of these materials using x-ray diffraction methods faces difficulties in distinguishing between carbon and nitrogen due to their similar electron densities. The application of neutron diffraction to some metal cyanides has allowed the distinction of C and N sites,^{155,156} but the large sample-size requirements and the limited availability of neutron sources restricts the widespread use of this technique.

Solid-state multinuclear magnetic resonance experiments of some archetypal metal cyanides such as CuCN,¹⁵⁷ AgCN¹⁵⁸ and AuCN¹⁵⁹ have revealed clear evidence for cyanide orientational disorder of bridging cyanide ligands, and have allowed for improved models of the structures. The presence of cyanide disorder in the copper-zinc cyanide coordination polymer $[\text{N}(\text{Me})_4][\text{Cu}(\text{I})\text{Zn}(\text{CN})_4]$ could only be resolved by NMR.¹⁶⁰

Self-assembly of simple molecular building blocks containing organic ligands and inorganic cations provides a reliable and efficient approach to the design of such

materials, with both components playing crucial roles in the final structural motifs available.¹⁶¹ The steric effects of the organic ligand may provide the driving force(s) for particular arrangements. The presence of hydrogen bonds between adjacent ligands or to the nitrogen of terminal cyanide moieties can also stabilize a particular organization of the constituents.¹⁶² Under certain circumstances, the presence of π - π interactions between aromatic ligands can also impart a directing effect on the final structure. Modification of the metal can drastically alter the electronic arrangement of cyanometallate frameworks. Of course, a change in the electronic arrangement can result in structural changes locally at the metal centre, which then impact the overall one, two or three-dimensional nature of the polymer. Typical metal-cyanide building blocks include systems of varying coordination number. Two-coordinate $M(+X)(CN)_2^{X-2}$, four coordinate (tetrahedral or square planar) $M(+X)(CN)_4^{X-4}$ and six-coordinate $M(+X)(CN)_6^{X-6}$ are some of the more common starting materials and allow a wide-range of structural motifs.

The use of multinuclear magnetic resonance is applied to a wide-range of metal cyanides, providing information about the impact of covalent versus ionic ligands in determining shieldings, determining the structure of a poorly crystalline cyanide and investigating the feasibility of solid-state NMR for structural characterization of paramagnetic systems.

6.1 *Materials & Methods*

6.1.1 *Synthesis*

Mercury cyanide samples [PPN][Hg(CN)₂Cl]·H₂O, [nBu₄N][Hg(CN)₂Cl]·0.5H₂O, [Co(en)₂][Hg(CN)₂Cl₂]{[Hg(CN)₂]₂Cl} and [Co(NH₃)₆]₂[Hg(CN)₂]₅Cl₆·2H₂O (from here on referred to as HgCN1 through HgCN4, respectively) were provided by the research group of Prof. Daniel B. Leznoff (Department of Chemistry, Simon Fraser University, BC) and details about their syntheses are published elsewhere.¹⁶³

The Pb(H₂O)[Au(CN)₂]₂ and Pb(H₂O)[Au(¹³C¹⁵N)₂]₂ samples were synthesized as previously published and provided by Danny Leznoff (Department of Chemistry, Simon Fraser University).¹⁶⁴ The addition of 0.5 mL of an aqueous K[Au(CN)₂] (58 mg, 0.2 mmol) solution to 0.5 mL of a Pb(NO₃)₂ (33 mg, 0.1 mmol) solution, resulted in the immediate precipitation of product. The dehydrated samples (Pb[Au(CN)₂]₂ and Pb[Au(¹³C¹⁵N)₂]₂) were formed by heating the hydrated samples overnight at 170°C.¹⁶⁵ Complete dehydration was initially determined by visual inspection to ensure that the colour change (pale to bright yellow upon dehydration) was homogeneous. The loss of fluorescence when excited with UV radiation was also checked using a UV lamp (λ = 254 nm). Finally, ¹H MAS spectra were acquired to confirm the loss of the signal arising from the water ligands.

All of the paramagnetic samples (1-8) were provided by Danny Leznoff's group. The syntheses of some of the compounds are published elsewhere; [Cu(en)₂][Hg(CN)₂Cl]₂,¹⁶³ [Cu(en)₂][Au(CN)₂]₂, [Cu(en)₂][Zn(NC)₄(CuCN)₂],¹⁶⁶ Cu(en)₂[Ag₂(CN)₃][Ag(CN)₂],¹⁶⁷ and [Cu(dmeda)₂Au(CN)₄][Au(CN)₄].¹⁶⁸ The synthesis

of the HgCl₂ versions of {(tmeda)NiHg(CN)₂}HgBr₄ and {(tmeda)CuHg(CN)₂}HgBr₄ have been previously published.¹⁵² The synthesis of [Zn(en)₂][Au(CN)₂]₂ is unpublished.

6.1.2 NMR

6.1.2.1 Diamagnetic Mercury Cyanides

¹³C{¹H} CPMAS¹⁶⁹ spectra were acquired on a Bruker AMX 500 (11.7 T) spectrometer with a 5 mm double-resonance probe (Doty Scientific). Recycle delays of 25 s were employed and polarization transfer contact times were 4-7 ms. Sample spinning rates of 6-8 kHz were used and isotropic chemical shifts were determined by acquisition of spectra at multiple spinning rates. Selected samples were also run at 14.1 T using a 5 mm double-resonance probe. Chemical shifts are reported relative to TMS and were calibrated using adamantane (+29.5 and +38.6 ppm) as a secondary reference.

¹⁹⁹Hg (107.4 MHz) MAS spectra were acquired at 14.1 T using 5 mm double-resonance probe. A short pulse (0.5 μs, 15° tip-angle) maximizing excitation bandwidth, and recycle delays of 4 s. Spinning rate of 6-8 kHz were used*. Attempts at ¹⁹⁹Hg{¹H} CPMAS experiments were unsuccessful, likely due to inefficient spin-locking of the

* A spurious signal centered about 107.1 MHz covering a range of 50 kHz was observed and required removal by backwards linear prediction of the first few data points of the time-domain data. Given the frequency and breadth, its most likely source is a local radio station operating at 107.1 MHz.

mercury due to the very large CSA. Mercury shifts in ppm are with respect to dimethyl mercury, and calibrated using the secondary reference, $\text{NEt}_4\text{Na}[\text{Hg}(\text{CN})_4]$ (-494 ppm).¹⁷⁰

6.1.2.2 Lead Cyanides

^{207}Pb (125.08 MHz) spectra were acquired using a single-pulse experiment for the MAS spectra with a 1 μs pulse (18° tip angle), recycle delays of 5 and 10 s for $\text{Pb}(\text{H}_2\text{O})[\text{Au}(\text{CN})_2]_2$ (PbAu1) and $\text{Pb}[\text{Au}(\text{CN})_2]_2$ (PbAu2), respectively. Non-spinning experiments were acquired using a Hahn-echo, with pulse lengths of 5 and 10 μs , and recycle delays of 10 and 25 s for PbAu1 and PbAu2, respectively. Chemical shifts are reported with respect to $\text{Pb}(\text{CH}_3)_4$ using 1.0 M lead nitrate at 25°C (-2961.2 ppm) as a secondary reference.¹⁷¹ To ensure that the measured chemical shifts are reliable, the effects of sample heating due to fast spinning were measured for spinning rates up to 11 kHz. The chemical shifts under MAS were found to vary < 0.1 ppm/K, as calibrated by $\text{Pb}(\text{NO}_3)_2$.^{172,173} The small peak shift and symmetric lineshape verify that the temperature dependence is too small to significantly impact the data presented here.

Hydrogen-1 MAS spectra (599.684 MHz) were acquired using 1 μs pulse lengths ($B_1 = 71.4$ kHz), spinning speeds of 5 and 9 kHz, and 20 s recycle delays. ^1H chemical shifts are relative to TMS, using water (+4.8 ppm) as a secondary reference.

$^{13}\text{C}\{^1\text{H}\}$ cross-polarization was employed for the MAS and non-spinning spectra of PbAu1, with recycle delays of 30 s. For PbAu2, a Bloch-decay sequence with 1 μs pulse (18° tip angle) and 60 s recycle delay was used. Non-spinning experiments were done with an echo pulse sequence to eliminate baseline distortions. ^{13}C chemical shifts are relative to TMS, using adamantane (29.5 and 38.6 ppm) as a secondary reference.

Nitrogen-15 spectra were acquired with single-pulse experiments using 2 μ s pulse lengths (35° tip angle) and recycle delays of 720 s for PbAu1. Spectra of PbAu2 were acquired with a 1 μ s pulse length (18° tip angle), and a 120 s recycle delay. ^{15}N chemical shifts are relative to $\text{NH}_3(\text{l})$, using $^{15}\text{NH}_4^{15}\text{NO}_3$ (23.8 ppm, $^{15}\text{NH}_4$).

6.1.2.3 Paramagnetic Samples

All spectra were acquired on a Varian Inova 600 MHz (14.1T) spectrometer. The effect of frictional heating under fast MAS was calibrated using solid lead(II) nitrate,¹⁷⁴⁻¹⁷⁶ and these corrected temperatures were used in determination of the temperature dependence of the chemical shifts.

Carbon-13 MAS spectra of the paramagnetic samples were acquired using 3.2mm double- or triple-resonance probes (Varian-Chemagnetics) with spinning rates of 10-22 kHz. Experiments were collected with a Hahn-echo at B_1 field strengths of 50-83 kHz or single-pulse (Bloch-decay) experiment with 1-2 μ s pulses, with recycle delays of 0.1-2 s. Rotor-synchronized Hahn-echo experiments allowed acquisition of these spectra at natural isotopic abundances despite the considerable ^{13}C background signal from the spinning modules. $^{13}\text{C}\{^1\text{H}\}$ CPMAS spectra of the diamagnetic sample $[\text{Zn}(\text{en})_2][\text{Au}(\text{CN})_2]_2$ (8) were acquired with a 5mm double-resonance probe (Varian-Chemagnetics) at spinning rates of 6-10 kHz, with a recycle delay of 30-60 s and a contact time of 8 ms. T_1 measurements were done using an inversion-recovery experiment, T_2 measurements were done using a Hahn-echo experiment.⁴⁷ Chemical shifts are reported relative to tetramethylsilane (TMS), using adamantane (+29.5 and +36.5 ppm) as a secondary reference.

Nitrogen-15 MAS spectra of the paramagnetic samples were acquired using 3.2mm double- or triple-resonance probes (Varian-Chemagnetics) with spinning rates of 6-22 kHz. Chemical shifts are reported with respect to liquid ammonia at 20°C, using $^{15}\text{NH}_4^{15}\text{NO}_3$ (+23.8 ppm) as a secondary reference. $^{15}\text{N}\{^1\text{H}\}$ CPMAS spectra of sample 8 were acquired with a recycle delay of 60 s and a contact time of 8 ms (ramped linearly on the observe channel) at a spinning rate 8 kHz.

Hydrogen-1 MAS spectra of the paramagnetic samples were acquired using the 3.2mm triple-resonance probe due to the significantly reduced ^1H background from the Kel-F (poly(trifluorochloro-ethylene)) spinning module. Chemical shifts are relative to tetramethylsilane, using deionized water (+4.80 ppm) as a secondary reference.

6.2 *Diamagnetic Systems*

6.2.1 ^{199}Hg and ^{13}C NMR of Mercury Cyanides

The incorporation of the linear HgCN_2 into cyanide coordination polymers has been explored to a lesser extent than other linear cyanide systems such as CuCN and AgCN .^{151,153,177-179} It is known that HgCN_2 can react with simple salts MX (for example where, $\text{M} = \text{Na}, \text{K}, \text{Rb}$ and Cs , and $\text{X} = \text{NCO}^-, \text{NCS}^-, \text{CN}^-, \text{Cl}^-$ etc.) to yield so-called “double-salts”.^{180,181} As the mercury is coordinatively unsaturated in the starting material, it can accept donor ligands during “polymerization”, resulting in mercury centres of higher coordination number. A series of such mercury cyanide/chloride “double salt” coordination compounds all possessing the $\text{Hg}(\text{CN})_2$ moiety were synthesized with different cations and found to yield very different structures. Significant diversity in the mercury coordination numbers was found.

The known chemical shift range for mercury is tens of thousands of parts-per-million.¹³ This is much larger than more common nuclei such as ^1H (*ca.* 15 ppm) and ^{13}C (*ca.* 300 ppm), and makes mercury chemical shifts very sensitive to their local environment. There are two spin-active mercury nuclei present naturally; ^{199}Hg (N.A. = 16.87%, $I = 1/2$, $\Xi = 17.910822$) and ^{201}Hg (N.A. = 13.18, $I = 3/2$, $\Xi = 6.611583$, $Q = 38.6 \text{ fm}^2$).¹⁸² Although the natural abundances are similar, the absence of a quadrupole interaction and a Larmor frequency almost three times larger for ^{199}Hg makes it much more amenable to investigation by NMR. The combination of low Larmor frequency and large nuclear electric quadrupole moment makes direct observation of ^{201}Hg extremely challenging whenever the mercury exists in a site deviating from tetrahedral or octahedral symmetry. In fact, to the best knowledge of the author, the only reported solid-state ^{201}Hg spectrum reported is that by Wu and Wasylshen for the tetrahedral $\text{K}_2\text{Hg}(\text{CN})_4$ complex.¹⁸³

The carbon-13 NMR of cyanide systems also provides information about the local structure. Of course, information about the number of distinct sites may be obtained, given sufficient resolution. In addition, the indirect dipole-dipole coupling to other spin-active nuclei provides information about connectivity (cyanide *versus* isocyanide binding), which may not always be evident from x-ray diffraction due to the similar electron densities of carbon and nitrogen. Nitrogen-15 NMR may be used to distinguish terminal cyanides from those which bridge to another metal center due to differences in the shifts.^{157,160,184,185} However, ^{15}N generally requires costly isotopic labeling of samples in order to obtain sufficient signal-to-noise, even with polarization enhancement techniques such as cross-polarization from abundant spins (e.g., ^1H).

The ^{13}C MAS spectra of the mercury cyanides exhibit a large range of chemical shifts (144.4 to 169.0 ppm), effectively spanning the range of chemical shifts for cyanides in diamagnetic complexes.^{157,158,160,184-186} The overlap of signals, combined with the faster spinning rates used, preclude accurate analysis of the full shielding tensors. However, the observed spans fall between 320 and 380 ppm, typical of metal cyanides. The skews are positive, and generally close to 1, indicating axial symmetry of the shielding tensor, as generally observed for such systems. The $^{13}\text{C}\{^1\text{H}\}$ CPMAS spectrum of HgCN_4 is shown in Figure 6.1, and is typical of the spectra generally acquired for these samples. Two overlapping signals are observed at 150 and 151 ppm, despite the presence of three crystallographic cyanide sites. Complete resolution of the sites is not observed at either field (11.7 or 14.1 T). The resolution of the sites is also hindered slightly by additional broadening of the ^{13}C signals from their neighbouring ^{14}N nuclei via residual dipolar coupling, which is predicted to add an additional 5-10 Hz to the linewidth at these fields, and will impart a slight asymmetry to the peak shape.¹⁸⁷ Also evident in this spectrum is the presence of satellite peaks arising from the one-bond \mathcal{J} -coupling to ^{199}Hg . The magnitude of \mathcal{J} -coupling confirms that the cyanides are in fact carbon-bound to the mercury and not N-bound. The measured coupling constants of 3420 ± 40 Hz are consistent with those observed for linear mercury species. $^1\mathcal{J}(^{199}\text{Hg}, ^{13}\text{C})$ in $\text{Hg}(\text{CN})_2$ is 3158 Hz,¹⁸⁸ whereas $^1\mathcal{J}$ for the tetrahedral $\text{K}_2\text{Hg}(\text{CN})_4$ is substantially smaller at only 1540 Hz.¹⁸⁹

The ^{13}C chemical shifts for some of the other compounds exhibit a greater differentiation of the cyanide signals (see Table 6.1). For HgCN_2 , the two signals vary by nearly 2 ± 0.5 ppm. Although the Hg-C bond distances are similar for the two sites in this

compound, the C-Hg-C bond angles vary significantly: for CN(1) the angle is 150.7°, whereas for CN(2) the bond angle is 160.1°. This might be expected to alter the δ_{11} and δ_{22} components more than the δ_{33} component, as the latter would be expected to lie effectively co-linear with the CN bond. Thus the signal possessing the more axially symmetric tensor (k closer to +1) would arise from the cyanide with the Hg-C-N bond angle closer to 180°. Without an accurate measure of the shielding tensors, the possibility exists that the correct assignments are the opposite of those given in Table 6.1. The ^{13}C MAS spectrum of HgCN1 yielded a single peak at 144 ppm. This is not inconsistent with the structure which has very similar Hg-C bond lengths for the two sites (2.054 and 2.058 Å) and identical Hg-C-N bond angles of 175.9°.

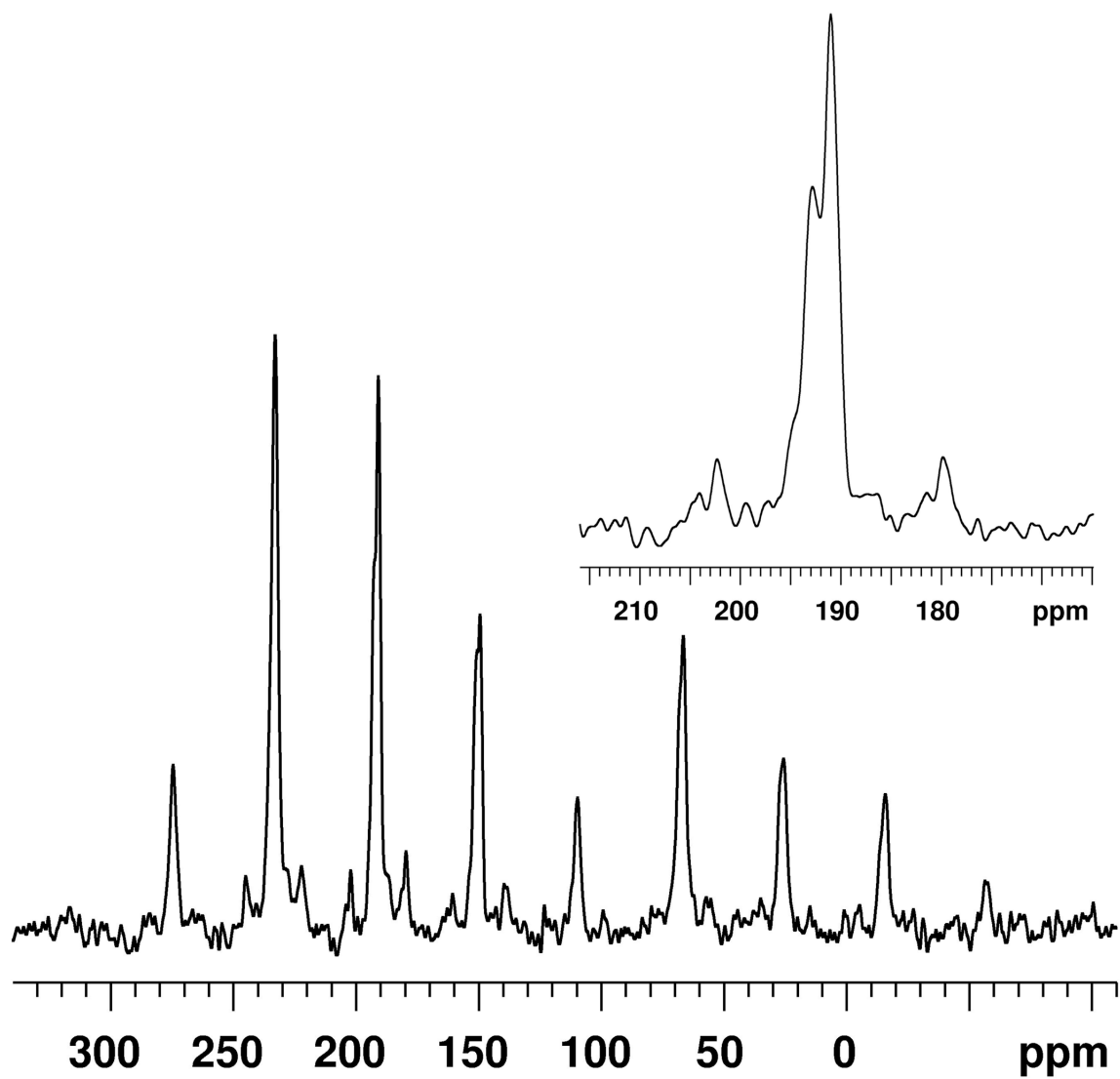


Figure 6.1: ^{13}C MAS of HgCN_4 at 14.1 T. The $1J(^{199}\text{Hg},^{13}\text{C})$ satellites are clearly evident at the base of the peaks. Shown inset is the +1 spinning sideband showing the resolution the sites.

Table 6.1: ^{13}C MAS NMR Parameters.

Compound/sites	δ_{iso} (ppm)	$^1J(^{13}\text{C},^{199}\text{Hg})$ (Hz)
HgCN1		
CN(11)	144.4 ± 0.5	-
CN(12)		
HgCN2		
CN(1)	166.5 ± 0.5	-
CN(2)	169.0 ± 0.5	-
HgCN3		
CN(11)	148.5 ± 0.5	3250 ± 50
CN(12)		
CN(21)	&	&
CN(22)		
CN(31)	150.6 ± 0.5	3250 ± 50
CN(32)		
HgCN4		
CN(1)	150.0 ± 0.5	3420 ± 40
CN(2)	&	&
CN(3)	151.0 ± 0.5	3420 ± 40

Attempts to obtain mercury-199 MAS spectra for all four samples were successful only for samples HgCN3 and HgCN4. Initial attempts with $^{199}\text{Hg}\{^1\text{H}\}$ cross-polarization provided no signal for any samples. However, simple Bloch-decay experiments did yield spectra for HgCN3 and HgCN4 after sufficient signal averaging (2-4 days). The ^{199}Hg

MAS spectrum of HgCN₄ is shown in Figure 6.2. The spectrum exhibits a very large shielding anisotropy (spans of 2700 and 2300 ppm, see Table 6.2), despite the mercury existing in a six-coordinate distorted octahedral geometry. Three mercury centres are present in the structure; however, Hg(1) and Hg(2) are quite similar and a two-site fit (intensity 2:1) reproduces the experimental spectrum to some degree (Figure 6.2). The mercury-199 MAS spectrum of HgCN₃ allowed only an estimate of the shielding tensor components and it was found to exhibit an even larger span of 3400 ± 300 ppm for this four-coordinate mercury centre. No resolution of the sites was detectable. These very large anisotropies are initially in conflict with that expected, based on previous work, which shows a much greater decrease in the anisotropy of the shielding tensor upon increased coordination number.¹⁹⁰ The shielding anisotropy is generally greatest for linear mercury centres and decreases with increasing coordination number; the spans of the linear Hg(CN)₂ and HgCl₂ are ~ 3700 ppm.^{186,191} The trigonal planar mercury centre of [NMe₄][Hg(SiPr)₃] has a span of only 1000 ppm.¹⁹² It thus appears that in these complexes, the mercury shielding is dominated by the arrangement of the cyanide ligands, which are trans in all complexes, and the C-Hg-C bond angles range from 167 to 180°.

It seems that when the combination of covalent and ionic ligands are present, these empirical relations between coordination number and anisotropy of the shielding do not work as well. However, good agreement is observed with the coordination environment of the more covalent ligands alone. A better approach may be to use both ¹⁹⁹Hg and ²⁰¹Hg. Although the shieldings appear to be dominated by the covalent ligands, the electric field gradient should better reflect the total coordination number. Using both

nuclei (^{199}Hg and ^{201}Hg) along with spectra at multiple fields, a better picture of the total environment (including isomerization) could potentially be obtained.

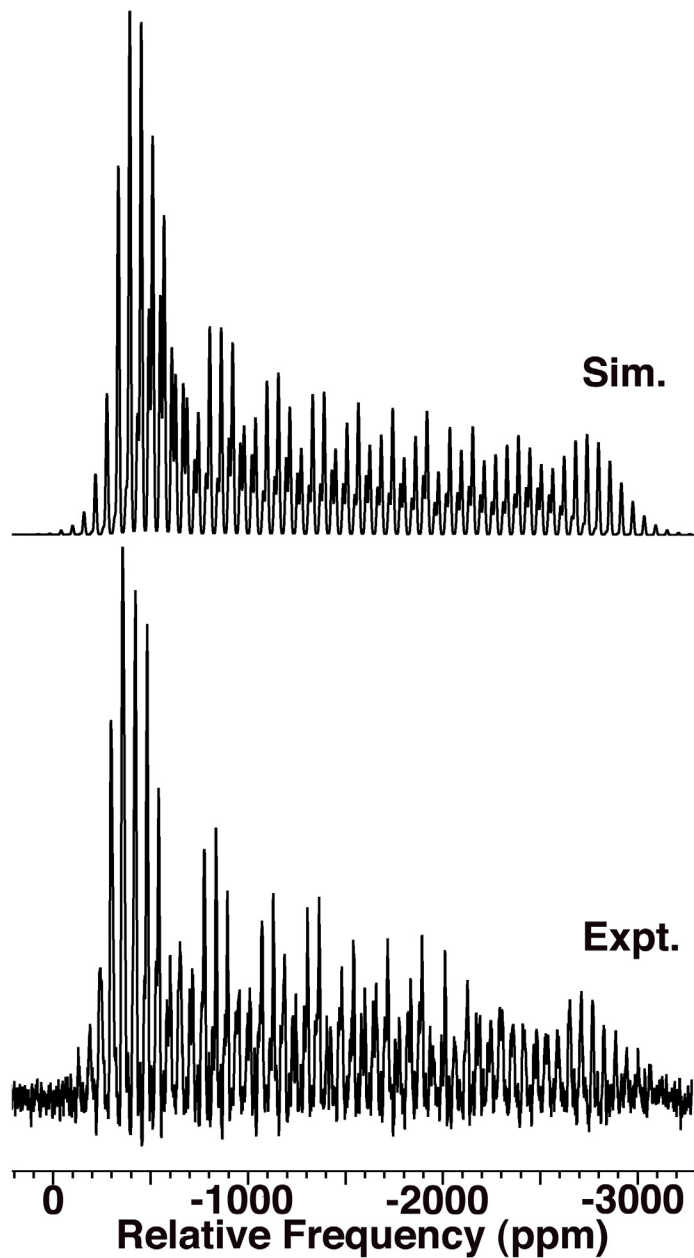


Figure 6.2: ^{199}Hg MAS of HgCN_4 along with two-site (2:1 intensity) simulation to account for the three crystallographically-distinct sites.

Table 6.2: ^{199}Hg MAS NMR Parameters.

Compound/sites	δ_{11} (ppm)	δ_{22} (ppm)	δ_{33} (ppm)	δ_{iso} (ppm)	Ω (ppm)	κ
HgCN1						
$\text{Hg}^{\text{c}}(1)$						
HgCN2						
$\text{Hg}^{\text{c}}(1)$						
HgCN3						
$\text{Hg}^{\text{c}}(1)$						
$\text{Hg}^{\text{c}}(2)$	98 ± 50	98 ± 50	-3301 ± 200	-1035 ± 90	$3400 \pm 300^{\text{a}}$	+1
$\text{Hg}^{\text{c}}(3)$						
HgCN4						
$\text{Hg}^{\text{c}}(1)$ & $\text{Hg}^{\text{c}}(2)^{\text{b}}$	-295 ± 20	-295 ± 20	-2995 ± 80	-1195 ± 2	2700 ± 100	+1
$\text{Hg}^{\text{c}}(3)$	-416 ± 20	-416 ± 20	-2696 ± 90	-1176 ± 2	2300 ± 100	+1

^aDue to insufficient signal-to-noise, only estimates of the span and skew could be obtained from the overall shape.

^bSpectrum appeared as two manifolds (2:1 intensity). Assignment based on structural similarity of sites 2 and 3

6.2.2 Structural Investigation of a Poorly-Crystalline Lead-Gold Cyanide

A luminescent lead-gold cyanide coordination polymer, $\text{Pb}(\text{H}_2\text{O})[\text{Au}(\text{CN})_2]_2$, was found to exhibit a large birefringence of 7.0×10^{-2} , nearly 3 times that of $\gamma\text{-Al}_2\text{O}_3$ which is commonly used for birefringent coatings.¹⁶⁵ The availability of single-crystals of high quality allowed structural analysis via diffraction methods, and the large birefringence of the compound could be correlated with the anisotropy of the 2D slabs in the structure. Upon dehydration (170 °C for 10-16 h) a new compound with formula $\text{Pb}[\text{Au}(\text{CN})_2]_2$ was formed. In addition to changes in the colour of the crystals (pale yellow to bright yellow upon dehydration), a loss of luminescence of the crystals was observed. The dehydration of the material resulted in crystals of poor quality obviating analysis by single-crystal diffraction techniques. A powder x-ray diffraction pattern could be obtained, but a unique structure could not be determined. In order to provide constraints for the asymmetric unit and thus possible structural models, a multinuclear magnetic resonance approach was undertaken.

^1H NMR of the hydrate and dehydrate was used to confirm the loss of the water ligand. The disappearance of signals is clear from Figure 6.3a and b. A spectrum of an empty rotor (Figure 6.3c) shows that the remaining signal in Figure 6.3b arises solely from the rotor. The slow spinning rate (9 kHz) available on the 5 mm probe is insufficient to eliminate the strong homonuclear (i.e., $^1\text{H}\text{-}^1\text{H}$) dipolar couplings and thus no in-depth analysis of the ^1H spectra was attempted.

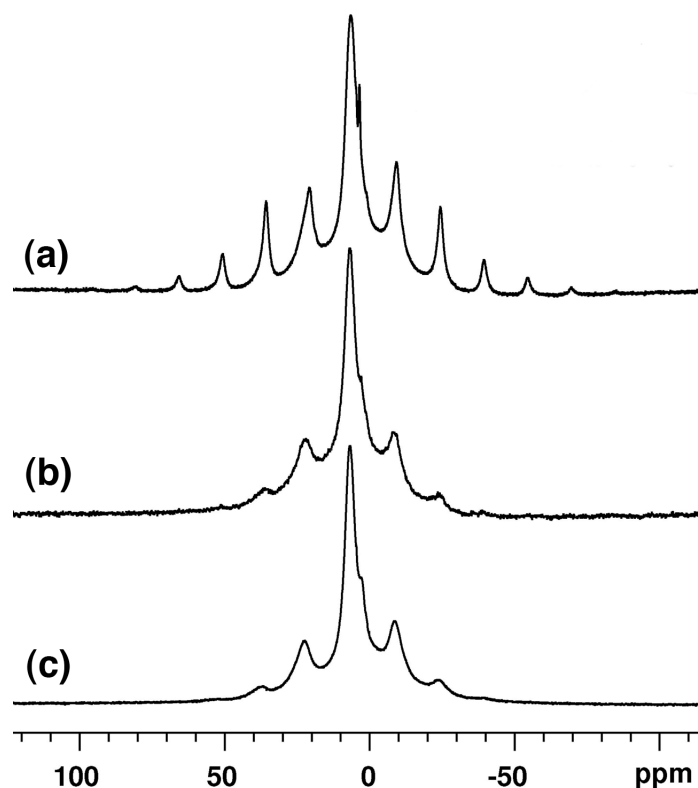


Figure 6.3: ^1H MAS spectra of (a) the hydrated sample (b) after dehydration and (c) the empty rotor. The loss of signals arising from the sample upon dehydration is clearly evident.

^{207}Pb MAS and non-spinning NMR of both compounds provided the shielding tensor principal components (δ_{11} , δ_{22} and δ_{33}). Both compounds were found to have surprisingly small spans (342 and 91 ppm) compared to other lead compounds.¹⁹³⁻¹⁹⁵ The hydrated compound possesses a skew which deviates significantly from axial symmetry ($\kappa = -0.16$). The dehydrated compound shielding tensor is nearly axially symmetric ($\kappa = +0.9$). From analysis of the tensor components, it appears that the δ_{33} and δ_{22} components are essentially unchanged, while the δ_{11} component (of the hydrate) becomes more shielded and very similar to the δ_{22} (Figure 6.4) upon dehydration.

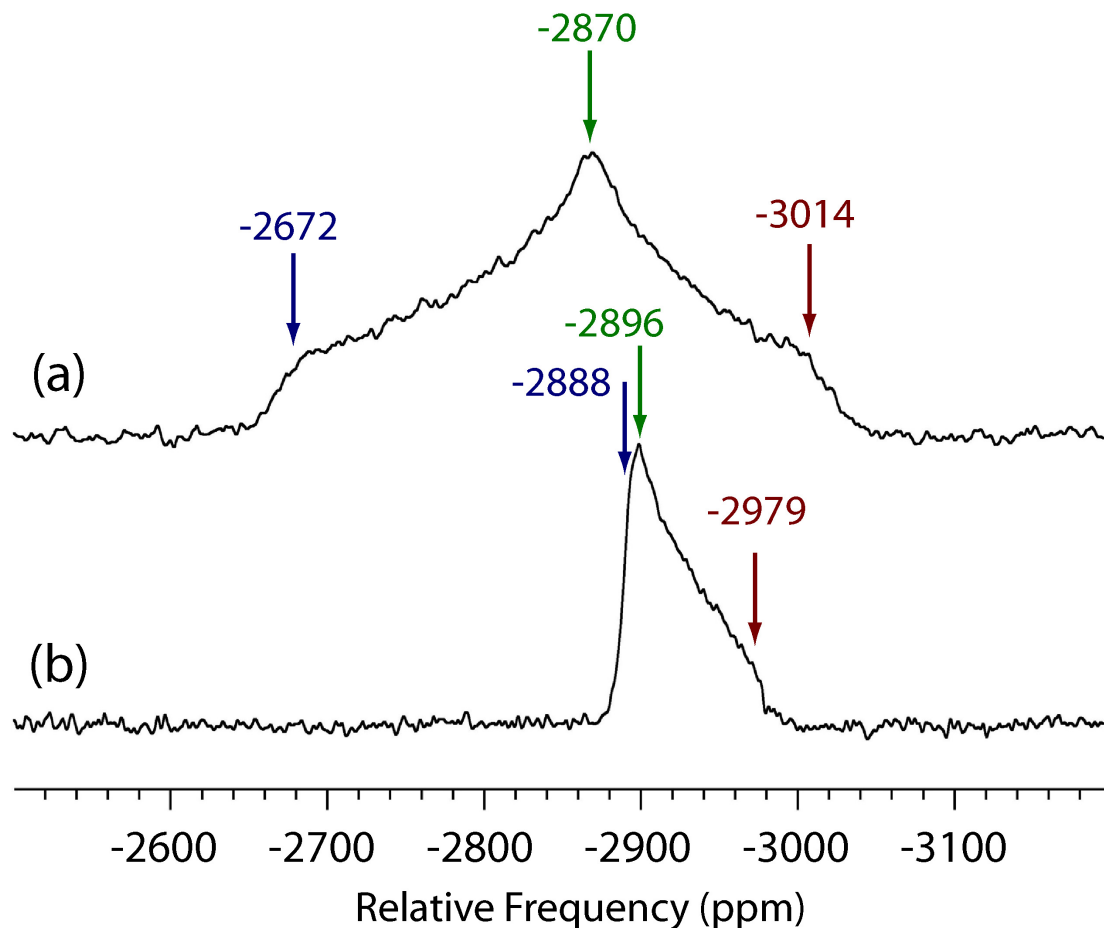


Figure 6.4: ^{207}Pb non-spinning NMR spectra for (a) PbAu1 and (b) PbAu2 showing the principal components ($\delta_{11} \geq \delta_{22} \geq \delta_{33}$) of the chemical shift tensors.

^{15}N MAS spectra of the two compounds are shown in Figure 6.5. The presence of two crystallographically distinct cyanide sites in PbAu1 is reflected by the presence of two signals (259 and 266 ppm). The distinct cyanides exhibit different Pb-N bond lengths (2.59 and 2.65 Å) and fairly different Pb-N-C bond angles of 132 and 138°. Slower spinning spectra (4 kHz) allowed extraction of all the principal components (see Table 6.3). Upon dehydration, only a single nitrogen signal is observed. The much longer

relaxation times necessary for the directly polarized ^{15}N spectrum of PbAu2 did not allow acquisition of a slow-spinning spectrum in a timely fashion.

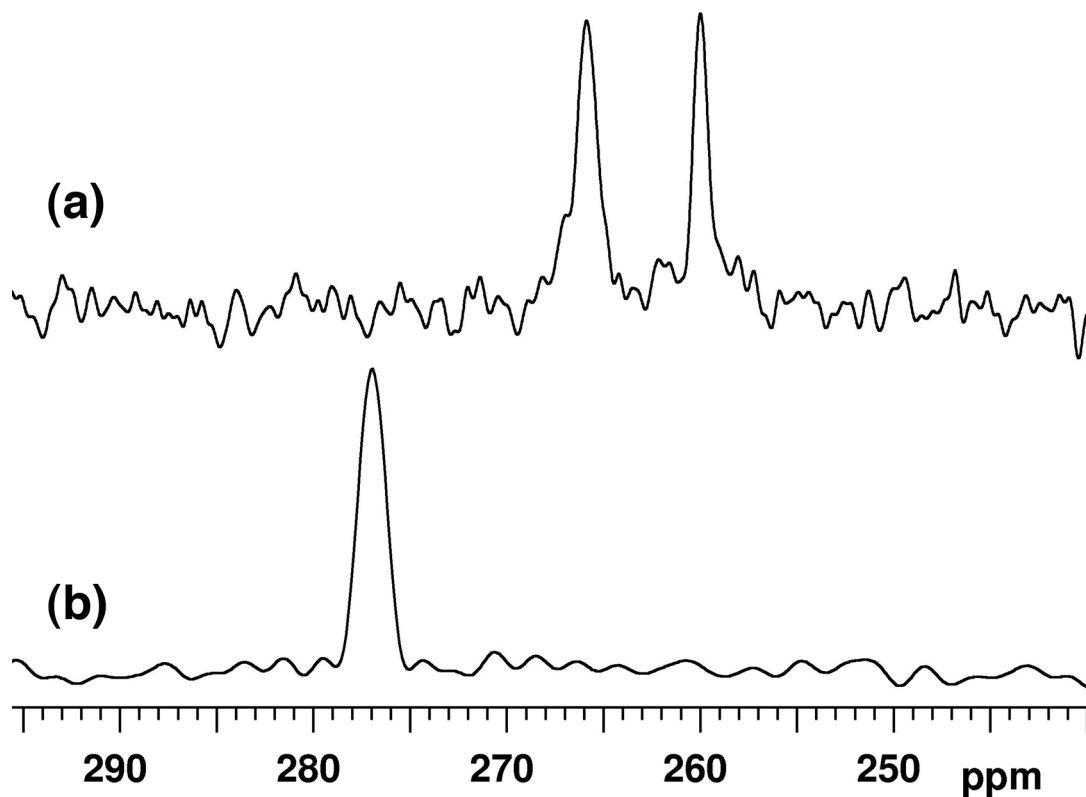


Figure 6.5: ^{15}N MAS NMR of (a) PbAu1 and (b) PbAu2 spinning at 18 and 17 kHz respectively.

The presence of protons in the hydrated PbAu1 allowed the use of cross-polarization, which made feasible (in combination with isotopic labeling) the acquisition of non-spinning ^{13}C and ^{15}N spectra. The use of doubly labeled cyanide ligands ($^{13}\text{C}^{15}\text{N}$) provides an ideal two-spin system for dipolar coupling measurements as greater than 98% of the observed signal will be from nuclei directly bonded to ^{15}N (for ^{13}C observation) or ^{13}C (for ^{15}N observation). A non-spinning spectrum will thus be subject to both the

chemical shift and dipolar coupling (sometimes referred to as dipolar-chemical shift spectra).^{196,197} The resultant spectrum in such cases is effectively that of multiple overlapping CSA patterns (multiplet # = $2NI + 1$), where the overall shape is dependent on the CSA principal components, the dipolar coupling and the orientation of the dipolar tensor (internuclear vector) within the chemical shielding principal axis system (see Figure 6.6). It is worth mentioning that for dipolar recoupling experiments such as REDOR, both complete CSA tensors and the orientation of the dipolar tensor would be required to extract accurate distances, whereas for dipolar-chemical shift spectra only the shielding anisotropy of the observed nucleus is required to extract accurate distance information.

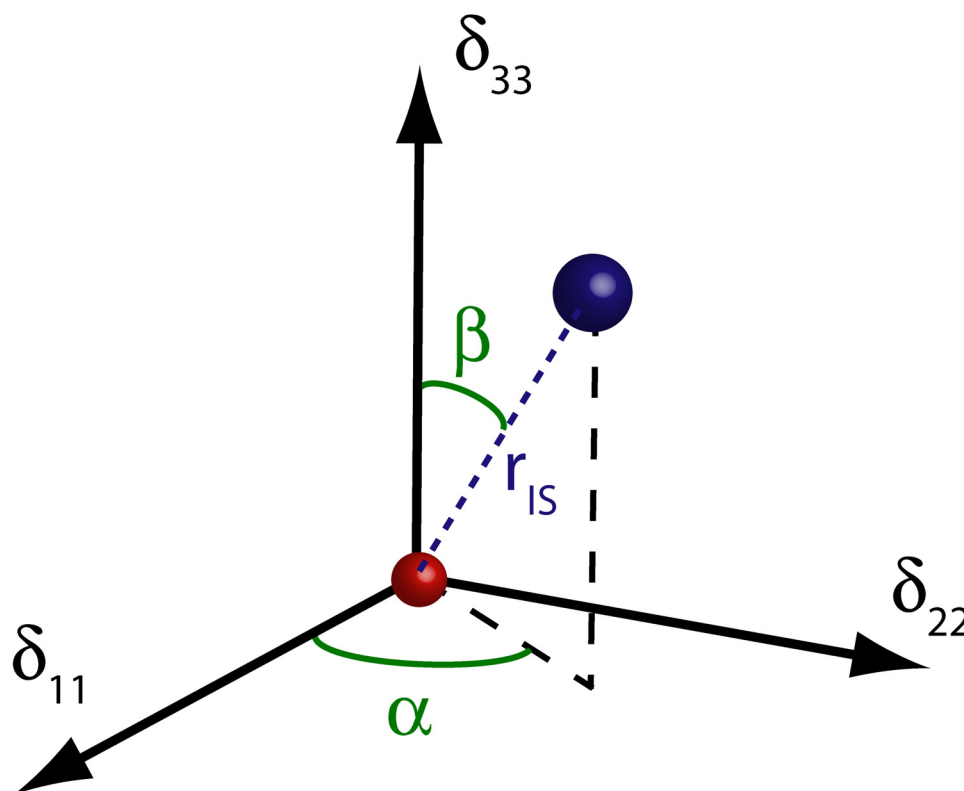


Figure 6.6: Relative orientation of a dipolar coupled spin system (separated by a distance, r_{IS}) with respect to the shielding tensor of the observed spin.

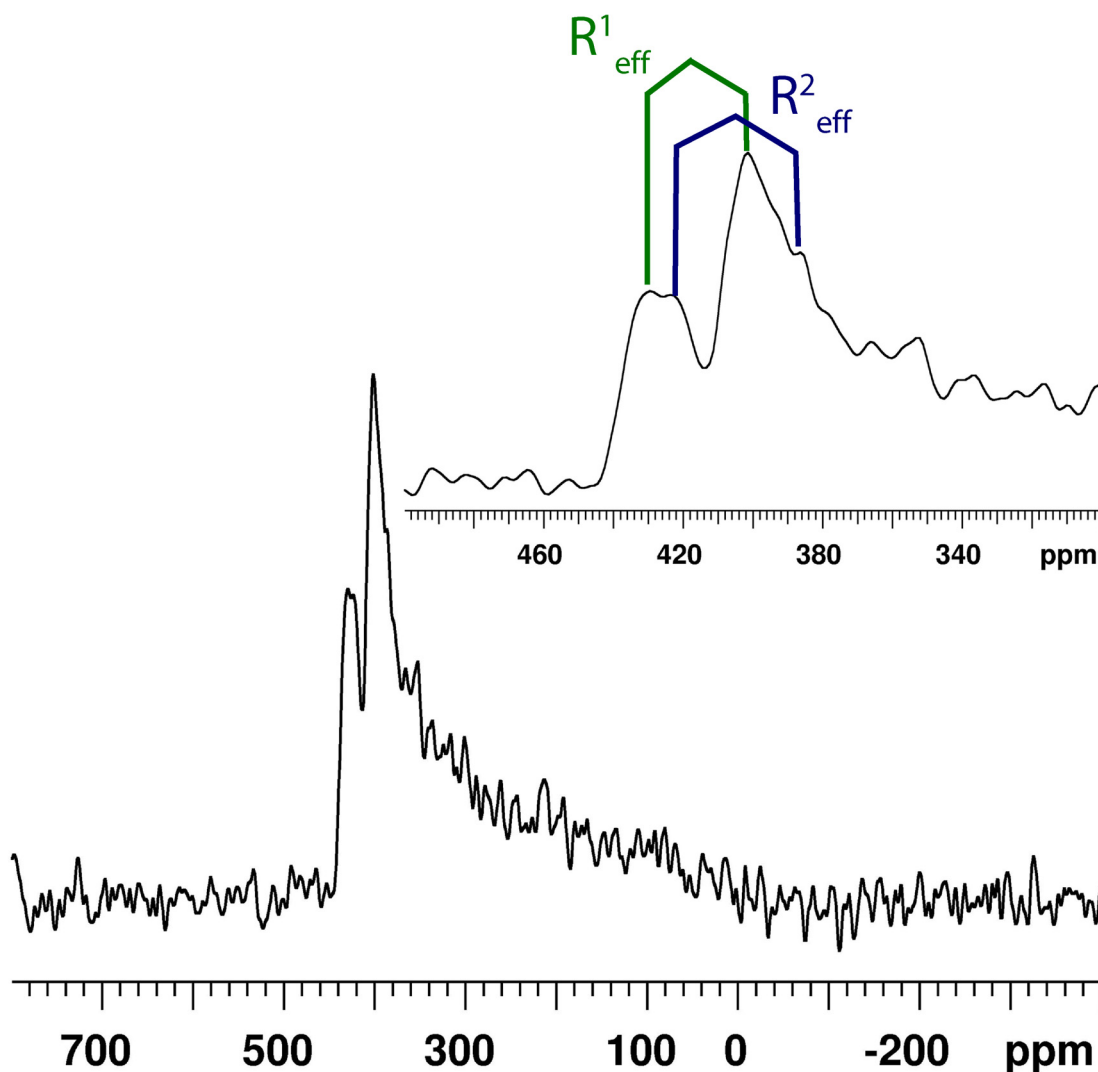


Figure 6.7: $^{15}\text{N}\{^1\text{H}\}$ CP non-spinning spectrum of PbAu1. The high-frequency edge of the pattern is shown inset, and the splittings due to the effective dipolar couplings for sites one and two (R^1_{eff} and R^2_{eff} , respectively) are designated.

The non-spinning ^{15}N spectrum of PbAu1 (Figure 6.7) is characteristic of a spin possessing axial symmetry (as determined by slow MAS, see Table 6.3). The effective dipolar couplings, R_{eff} , taken from the ^{15}N non-spinning spectrum are 1850 ± 50 Hz and 1950 ± 80 Hz for CN1 and CN2, respectively. These correspond to distances of $1.18 \pm$

0.01 Å and 1.16 ± 0.02 Å, respectively. These distances are slightly longer than the x-ray diffraction data, which yield distances of 1.166 and 1.137 Å. However, it should be noted that the spectrum reflects the *effective* dipole-dipole coupling. Included in this term is the true dipole-dipole coupling, R , and the anisotropic part of the \mathcal{J} -coupling, $\Delta\mathcal{J}$. From experimental and theoretical investigations of cyanide systems, it has been shown that the anisotropy in the \mathcal{J} -coupling for the cyanide group ranges from -42 to -64 Hz.^{101,158,198} If the median value of 50 Hz is taken as a rough estimate, $R_{\text{eff}} = R - \Delta\mathcal{J}/3$ predicts that the contribution from $\Delta\mathcal{J}$ is *ca.* 16 Hz, which is well within the errors of the measurement. Analysis of the non-spinning ^{13}C spectrum of PbAu1 provided a coupling of 1950 ± 100 Hz (1.16 ± 0.04 Å).

The ^{13}C MAS spectra (Figure 6.8 and Figure 6.9) of both PbAu1 and PbAu2 exhibit isotropic chemical shifts toward the highest range observed for diamagnetic metal cyanides (167 and 173 ppm, respectively). Interestingly, the ^{13}C MAS spectrum of PbAu1 consists of only a single resonance, despite the presence of two cyanides in the crystal structure, and as revealed by the ^{15}N MAS data. This lack of resolution is attributed to the very similar coordination geometry at the carbon: both are bonded to gold with similar bond lengths and angles. PbAu2 shows only a single signal, consistent with the observation of a single nitrogen signal. The ^{13}C MAS spectra for each could be fit to a single site (see Figure 6.8, Figure 6.9 and Table 6.3)

Table 6.3: NMR parameters for the hydrated (PbAu1) and dehydrated (PbAu2) samples.

		δ_{iso} (ppm)	Ω (ppm)	κ^a
^{13}C	PbAu1	167 ± 1	346 ± 4	> 0.95
	PbAu2	173 ± 1	353 ± 4	> 0.95
^{15}N	PbAu1 CN1	266 ± 1	480 ± 10	> 0.8
	PbAu1 CN2	259 ± 1	450 ± 30	> 0.7
	PbAu2	276 ± 1	n.d.	n.d.
^{207}Pb	PbAu1	-2850 ± 1	342 ± 5^a	-0.16 ± 0.07^a
	PbAu2	-2921 ± 1	91 ± 4^a	$> 0.9 \pm 0.1^a$

^a Obtained from non-spinning spectrum.

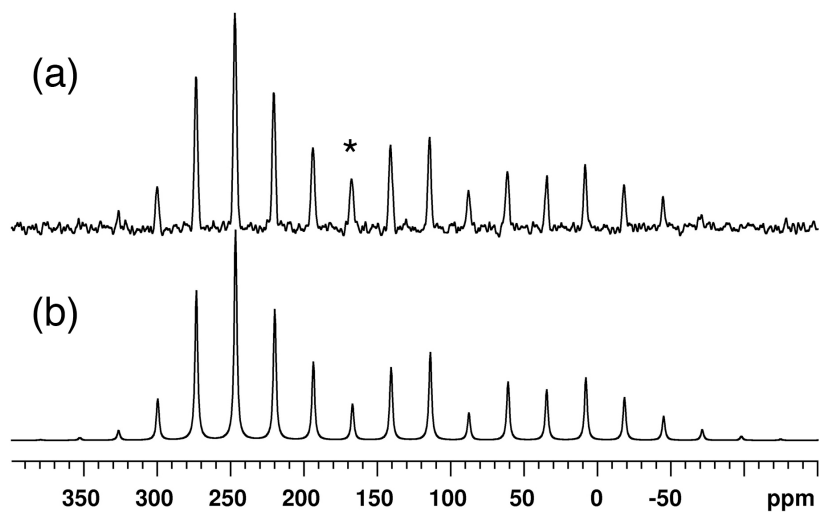


Figure 6.8: ^{13}C MAS (a) and simulation (b) of the hydrated compound. The isotropic chemical shift is marked by an asterisk.

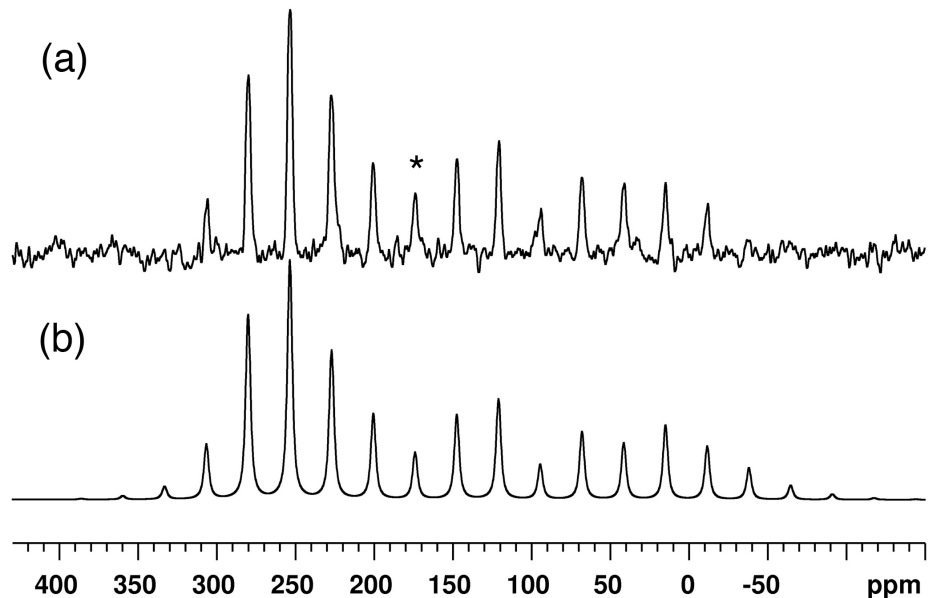


Figure 6.9: ^{13}C MAS (a) and simulation (b) of the dehydrated compound. The isotropic chemical shift is marked by an asterisk.

In terms of the structure, the local symmetry of the lead centre provides some constraints on possible tensor orientations. The presence of a mirror-plane orthogonal to the $\text{Au}(\text{CN})_2$ chains requires that one of the tensor components is orthogonal to it and thus parallel to the cyanide chains. The drastic change of the δ_{11} component of the ^{207}Pb CSA tensor upon the loss of water indicates that in the hydrated compound, δ_{11} is most likely along (or nearly along) the Pb-O bond (see Figure 6.10). The loss of the water would thus make that direction structurally more similar to the other directions in that mirror-plane, and one might expect these two tensor components then to be very similar. This is also consistent with the ^{207}Pb spectrum of the dehydrated compound, which possesses near-axial symmetry (i.e., $\delta_{11} \approx \delta_{22}$). From the ^{15}N MAS spectrum, the presence of a single cyanide in the asymmetric unit was established. As a result, the simplest solution to

the structure would be a trigonal prism, with a six-coordinated lead, and all cyanides related by symmetry. However, a decrease in the coordination number of lead from 8 to 6 would be expected to be accompanied by an increase in the isotropic chemical shift.¹⁹³ In fact, the ^{207}Pb isotropic shift decreases slightly (from -2850 to -2921 ppm) upon dehydration. Taking this into consideration, a model was developed in which adjacent slabs join to form lead centres which are square prismatic (see Figure 6.10). Analysis of the powder x-ray diffraction data (Michael Katz, Department of Chemistry, Simon Fraser University) shows that the arrangement of the lead and gold atoms (the lighter C and N contribute negligible intensity to the diffractogram) supports such an arrangement. The proposed structure (with idealized carbon and nitrogen bond lengths) is shown in Figure 6.11, and is in fairly good agreement with the proposal based solely on the NMR data of Figure 6.10. This illustrates the advantage of combining the long-range structural information available from powder diffraction techniques, with the short-range information available from NMR.

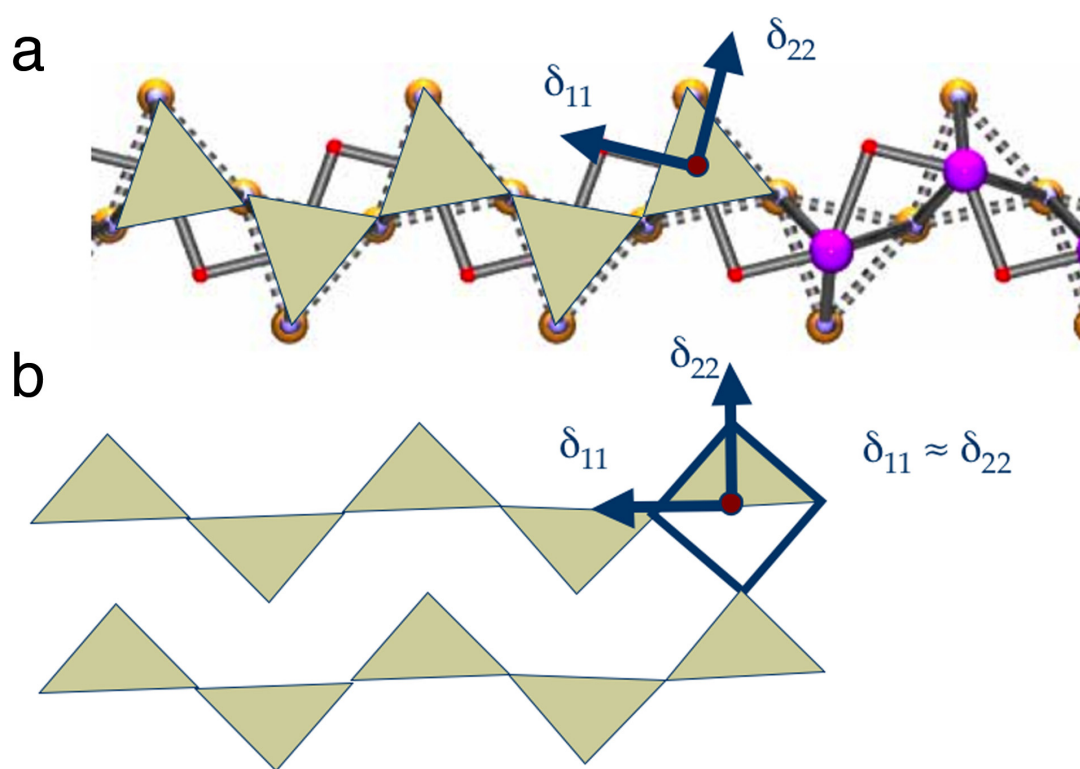


Figure 6.10: Formation of square prisms in PbAu₂ (b) upon dehydration of PbAu₁ (a) via adjacent slabs, including proposed chemical shift tensor orientations. View down b-axis, with δ_{33} directed out of the plane of the page. Lead in purple, oxygen in red, gold in yellow.

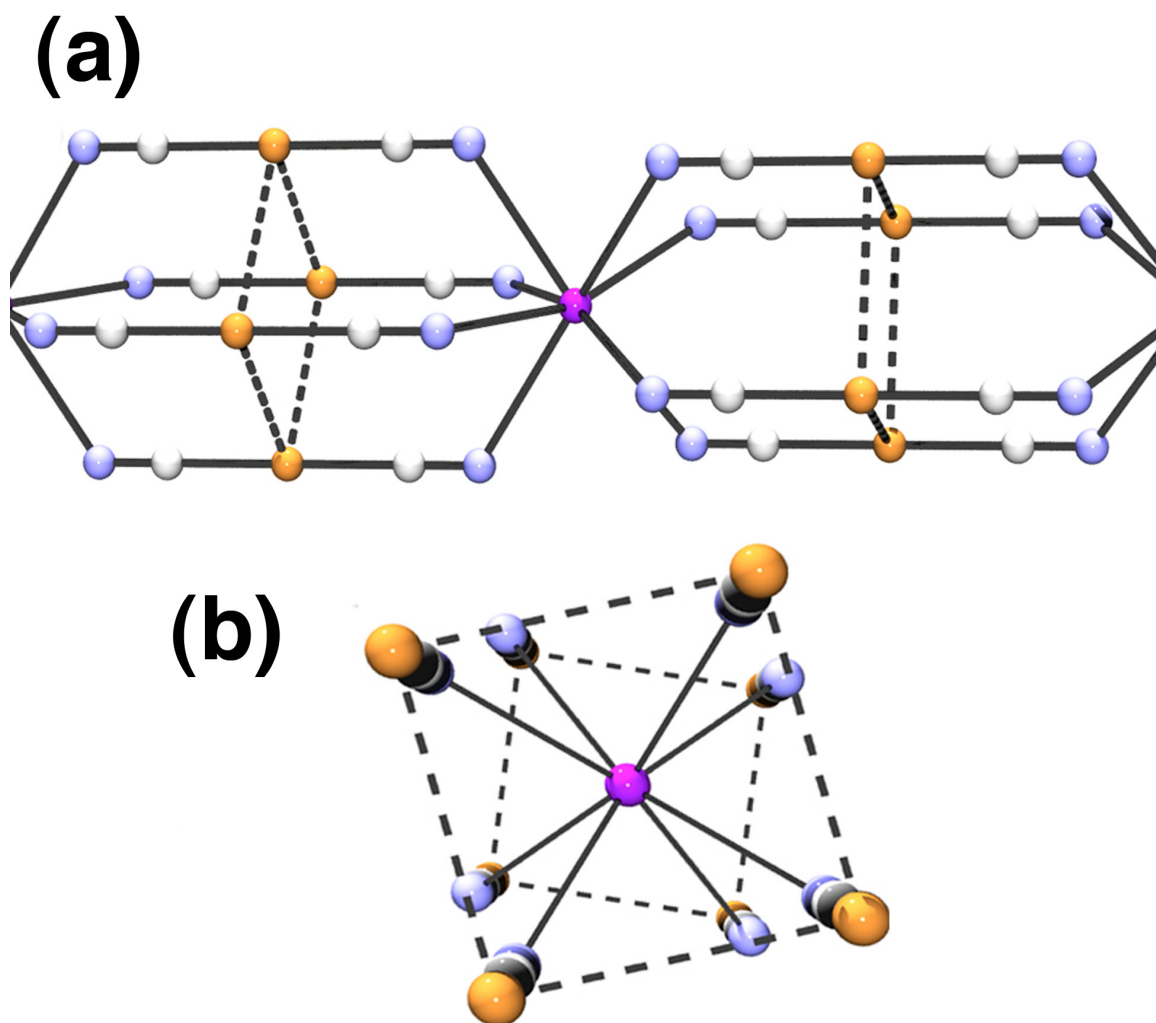


Figure 6.11: The proposed structure based on the combination of solid-state NMR and powder x-ray diffraction. The “square” arrangement of the gold atoms can be seen in (a), and in (b) the distortion from square anti-prismatic geometry can be seen. Lead in purple, gold in yellow, nitrogen in blue and carbon in white.

6.2.3 Variable Temperature ^{207}Pb NMR of $\text{Pb}[\text{Au}(\text{CN})_2]_2$

The temperature variation of the isotropic shifts, observed under MAS, provides only an average value, thus possibly masking more subtle effects (i.e., changes in individual components). The small span of the shielding tensor for PbAu_2 allowed for the acquisition of spectra in a reasonably short time and thus some simple variable-temperature experiments were undertaken in order to further examine changes in the full shielding tensor.

The ^{207}Pb spectra (Figure 6.12) show a shift to higher frequency and a narrowing of the peak. Approximating the shielding tensor as being axially symmetric with $\kappa = +1$, then $\delta_{11} = \delta_{22}$ and this component may be redefined as δ_{\perp} , and δ_{33} becomes δ_{\parallel} . Using these principal components, the isotropic shift is found to vary by $\sim 0.6 \pm 0.3$ ppm/K. This is similar to the temperature dependence observed for the lead in lead nitrate.^{175,176} However, it should be noted that the uncertainty is very large due to simplification of axial symmetry invoked, and the difficulty in extracting the isotropic shift from non-spinning spectra. In addition, the presence of ^{14}N nuclei directly bonded to the lead will obscure the simple extraction of the principal components. Equally interesting is that the span decreases, and thus the different components of the shielding tensor exhibit different temperature dependences. A similar observation has been made for non-spinning spectra of lead titanate.¹⁹⁴ Harbison associated this change in the lead shielding anisotropy with changes in the Pb-O bond distance. However, no experiments directly probing the Pb-O bond length as a function of temperature (by either NMR or other methods) were done.

Other re-arrangements, besides Pb-O bond lengths, could lead to higher symmetry at the lead in that system, and thus smaller shielding spans. In this case, where the proposed structure of PbAu₂ is a distorted square anti-prism (or distorted square-prism) one could envision a re-orientation towards either of these geometries. The square prism or the square anti-prism are both of higher symmetry (D_{4h} and D_{4d} , respectively), although neither of these would require a completely isotropic shielding tensor.¹⁹⁹ Variable-temperature x-ray diffraction should reveal the change in d-spacing(s) required by such movement of the heavy atoms.

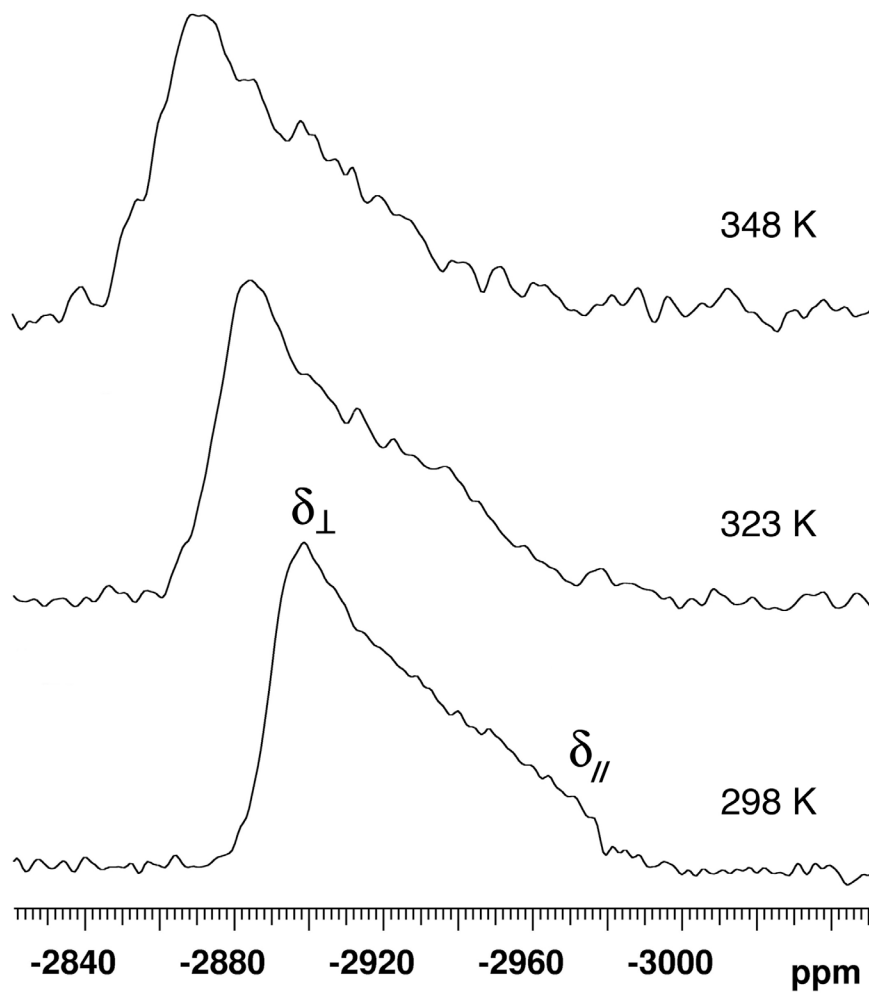


Figure 6.12: Variable-temperature non-spinning ^{207}Pb NMR of PbAu_2 . The positions of the perpendicular and parallel components are denoted on the 298 K spectrum.

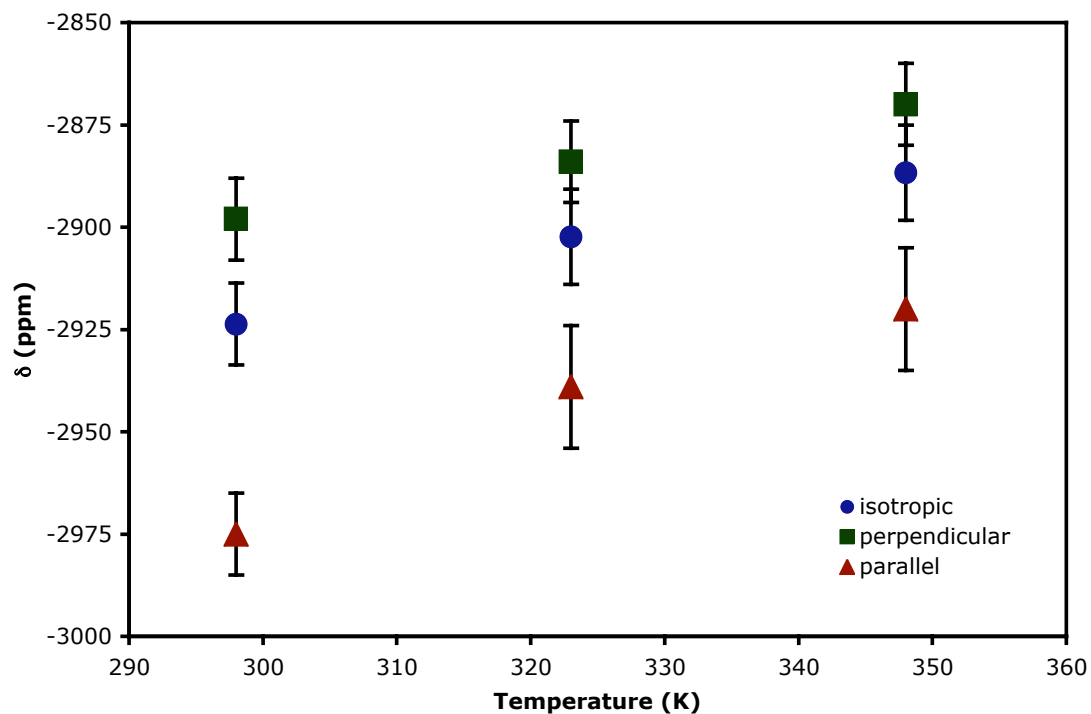


Figure 6.13: A plot of the temperature dependence of the ^{207}Pb shielding tensor principal components (and isotropic shifts calculated from them) for PbAu_2 reveals a decreased shielding with increasing temperature. The rate of change of the parallel component is greater than that of the perpendicular component, resulting in a decrease in the observed span.

6.3 *Paramagnetic Systems*

The application of NMR methods to paramagnetic materials is fraught with difficulties arising from the very strong electron-nucleus interactions. There is a significant body of work on the NMR of paramagnetic species in solution.^{21,200} However, the application of solid-state NMR to paramagnetic materials has generally been considered either very difficult or impossible, due to severe broadening arising from the electron-nucleus interactions, and much less has been done in this area. Previous studies on inorganic and organometallic paramagnetic systems have shown that ^1H resonances can exhibit extensive anisotropic broadening.^{201,202} This makes heteronuclear decoupling extremely inefficient, and has previously required isotopic dilution with ^2H , significantly reducing the magnitude of the dipolar interactions ($\gamma_{\text{H2}}/\gamma_{\text{H1}} \approx 0.15$).^{201,203,204} Recently, Ishii and co-workers have shown that the application of *fast* MAS ($\nu_{\text{r}} \geq 20$ kHz) allows for the acquisition of spectra of spin-half nuclides in paramagnetic systems.^{205,206} They find that with fast spinning, the application of high-power broadband heteronuclear (^1H) decoupling is generally unnecessary to achieve adequate resolution of ^{13}C resonances.

A similar approach is employed here for a series of well-characterized crystalline paramagnetic metal-cyanide systems in order to investigate the feasibility of solid-state NMR for the extraction of structural information. A set of systems with varying degrees of structural complexity were chosen, with the paramagnetic centre both outside and within the cyanide framework. Finally, using the observations of the well-characterized systems, a compound of unknown structure (but known to our collaborators) was probed to test the limits of the information which can be obtained.

6.3.1 $[\text{Cu}(\text{en})_2][\text{Hg}(\text{CN})_2\text{Cl}]_2$, (1)

Compound (1) has a ladder-type structure composed of $\text{Hg}(\text{CN})_2\text{Cl}$ units (see Figure 6.14). The structure possesses two crystallographically distinct terminal cyanides, carbon bound to mercury.¹⁶³ The paramagnetic $\text{Cu}(\text{en})_2$ moiety lies outside the mercury cyanide framework (i.e., no bonds to atoms within the mercury cyanide/chloride chains), and no evidence of structural re-orientation was observed by x-ray. The structure reveals that the nitrogen of CN1 has a much shorter $\text{N}-\text{Cu}^{2+}$ length (2.77 Å) than the nitrogen of CN2 (4.37 Å). This distance for CN1 falls within the van der Waals radii, indicating the presence of a small interaction and explaining the absence of re-orientation of the $\text{Cu}(\text{en})_2$ group. The CN1 nitrogen lies in an axial position of the Jahn-Teller distorted pseudo square-planar copper centre.

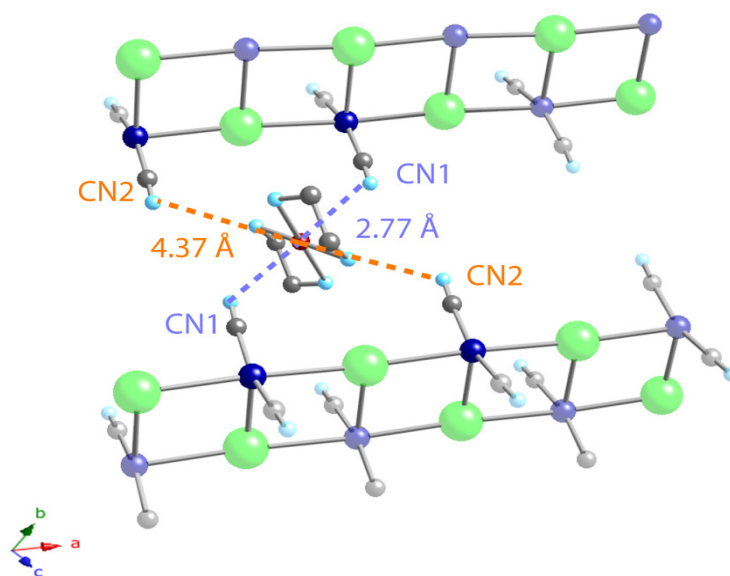


Figure 6.14: Structure of compound (1). The CN1-Cu distance is the shortest contact (2.77 Å). Mercury shown dark blue, carbon grey, nitrogen light blue, chlorine in green and hydrogen atoms have been omitted.

Two resonances are observed in the ^{13}C MAS spectrum of (1), as expected from the crystal structure, at 153 ppm and 137 ppm (Figure 6.15). The less shielded resonance (153 ppm) is at a frequency typical of transition-metal cyanides. The other resonance (137 ppm) is more shielded than typical C-bound mercury cyanides. The isotropic shift observed for HgCN is 149.5 ppm,²⁰⁷ and recent work on a series of diamagnetic mercury cyanides exhibited chemical shifts in the range of 144.4-169.0 ppm.¹⁶³ Using a Bloch-decay sequence, the methylene ^{13}C signal of the ethylenediamine ligand was also observed at -303 ppm. Assignments of the resonances are based on the observed shifts, along with the temperature sensitivity of the shifts, allowing for differentiation based on the relative proximity to the paramagnetic centre.

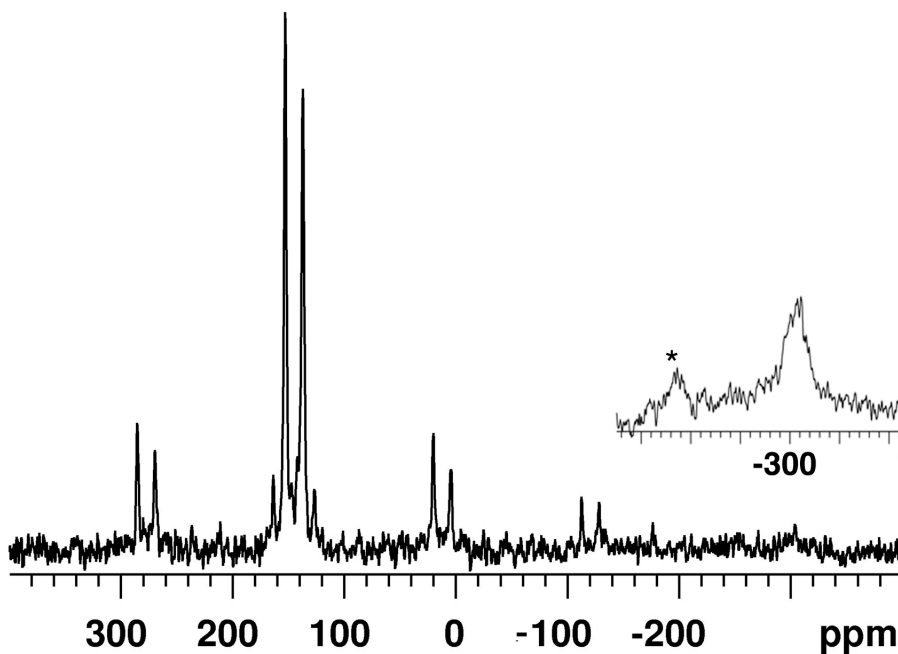


Figure 6.15: ^{13}C MAS spectrum of $[\text{Cu}(\text{en})_2][\text{Hg}(\text{CN})_2\text{Cl}]_2$, with the inset figure showing the region around -300 ppm as acquired using a single-pulse experiment. Two cyanide signals are present, and the presence of satellite peaks are observed at the base of the peaks arising from the $1J(^{199}\text{Hg},^{13}\text{C})$ coupling.

The methylene resonance at *ca.* -300 ppm displays the greatest temperature sensitivity, and possesses the shortest T_2 , being so short as to render it unobservable in the rotor-synchronized echo experiments, even at spinning rates of 20 kHz ($\tau_r = 50$ μ s). The large shift from typical frequencies (of 30-40 ppm)¹⁸⁶ for the methylene carbons, high temperature sensitivity, and very short T_2 s are all indicative of a nucleus subject to a large Fermi contact interaction, as expected for nuclei with connectivity to the paramagnetic metal.

On the basis of the N1-Cu interaction present in the crystal structure, and the absence of any evidence for such an interaction for N2, it is expected that cyanide-1 will experience a larger paramagnetic interaction (both Fermi and dipolar) than cyanide-2. This is consistent with what is observed in the NMR. In addition to the vital information about the proximity of the cyanide to the paramagnetic centre allowing assignment of the cyanides, the presence of satellite peaks due to the $^1J(^{13}\text{C}, ^{199}\text{Hg})$ with couplings of 3140 ± 50 and 3250 ± 50 Hz provides the crucial information that the cyanide is C-bound to the mercury. Moreover, the slightly larger J -coupling observed for CN2 is consistent with its greater linearity (Hg-C-N angle of 178.9°) than that of CN1 (Hg-C-N angle of 176.4°). The magnitude of the couplings are consistent with linear $\text{Hg}(\text{CN})_2^-$ units,^{163,188,207} and with single-crystal x-ray diffraction. However, the bonding mode of cyanide ligands may not always be discernable from x-ray diffraction due to the similar electron densities of carbon and nitrogen.^{151,153,179}

The N-15 spectrum consists of two resonances, with isotropic chemical shifts of 325 and 148 ppm. Typical ^{15}N chemical shifts for metal cyanides are in the range 230-290 ppm, with terminal C-bound cyanides generally to the higher

frequencies.^{157,158,184,185,208} Assignments are based on the vastly different chemical shifts, with the 325 ppm signal assigned to N2, due to its greater resemblance to those observed in diamagnetic systems. The more highly shielded resonance at 148 ppm is thus assigned to N1.

6.3.2 [Cu(en)₂][Ag₂(CN)₃][Ag(CN)₂], (2)

The structure of compound (2) consists of Ag₂(CN)₃ and Ag(CN)₂ units connected via Ag-Ag bonds, creating a zigzagging one-dimensional chain structure with the copper(II) ethylenediamine cations in between the chains (Figure 6.16). There are three types of cyanides in the structure. Cyanide CN21 has the closest contacts with the Cu²⁺ centre (2.66 Å), with the nitrogen atoms falling in the *axial* positions of the pseudo-D_{4h} Cu(en)₂. Although 2.66 Å is longer than typical Cu-N bonds (for example the Cu-N bonds to the en ligands are 1.9 to 2.0 Å), the absence of motion of the Cu(en)₂ cation indicates that there must be some interaction present. In addition to this closest contact, the nitrogen of CN21 also has a N-Cu contact to the next-nearest copper of 4.76 Å. The single-crystal x-ray diffraction data suggested the presence of head-to-tail disorder of CN20. The metal-carbon and metal-nitrogen distances for CN20 and for the third cyanide (CN11) are all greater than 4.3 Å.

The presence of head-to-tail cyanide orientational disorder of the bridging cyanide (CN20) is clearly evident in the nitrogen-15 MAS spectrum, as it consists of four (not three) resonances with chemical shifts of 172, 256, 288 and 316 ppm. Variable-temperature experiments show the largest temperature dependence for the signal at 172 ppm, allowing its assignment as CN21 due to its close copper(II) contacts.

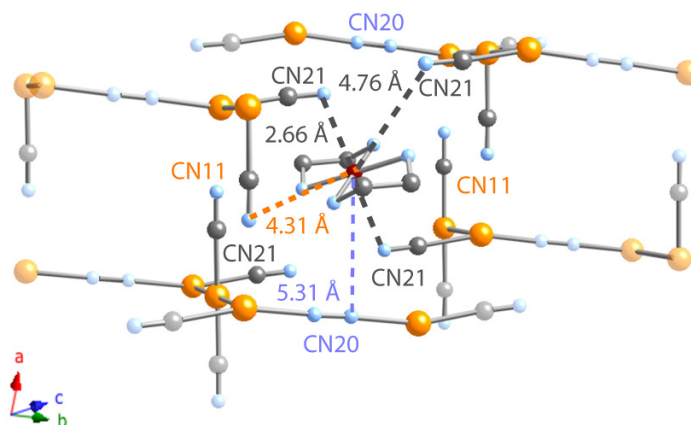


Figure 6.16: The structure of compound (2), exhibiting a Jahn-Teller distorted geometry about the copper with contacts to the “axial” CN21 ligands of 2.66 Å. The copper atom is shown in red, carbon in grey, nitrogen in blue, silver in yellow and hydrogen atoms have been omitted.

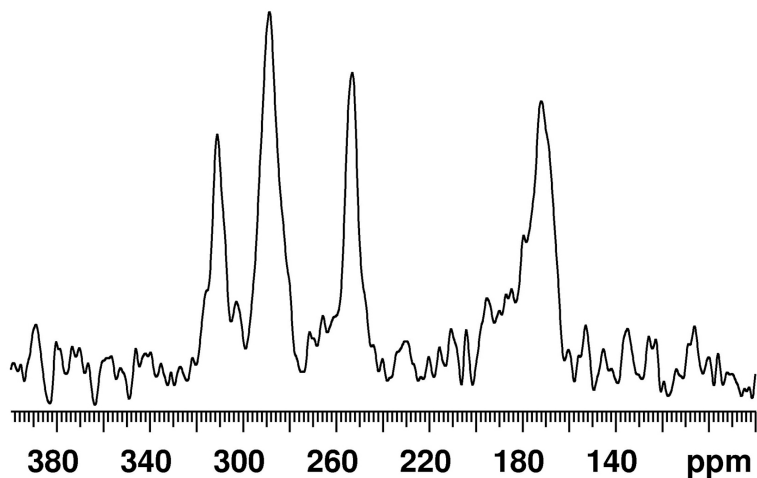


Figure 6.17: ^{15}N MAS spectrum of sample (2). The observation of four resonances confirms the presence of head-to-tail cyanide orientational disorder in the structure.

In agreement with the nitrogen NMR, the carbon-13 spectrum possesses four cyanide resonances confirming, the presence of orientational disorder of the bridging cyanide. The four cyanide resonances are observed at 162, 151, 146 and 116 ppm. As with compound (1) there is a Cu(en)_2 cation present external to the silver cyanide framework, and the methylene carbons are observed at a chemical shift of -300 ppm, exhibiting an extremely high sensitivity to temperature as expected from a centre experiencing a large Fermi contact interaction.

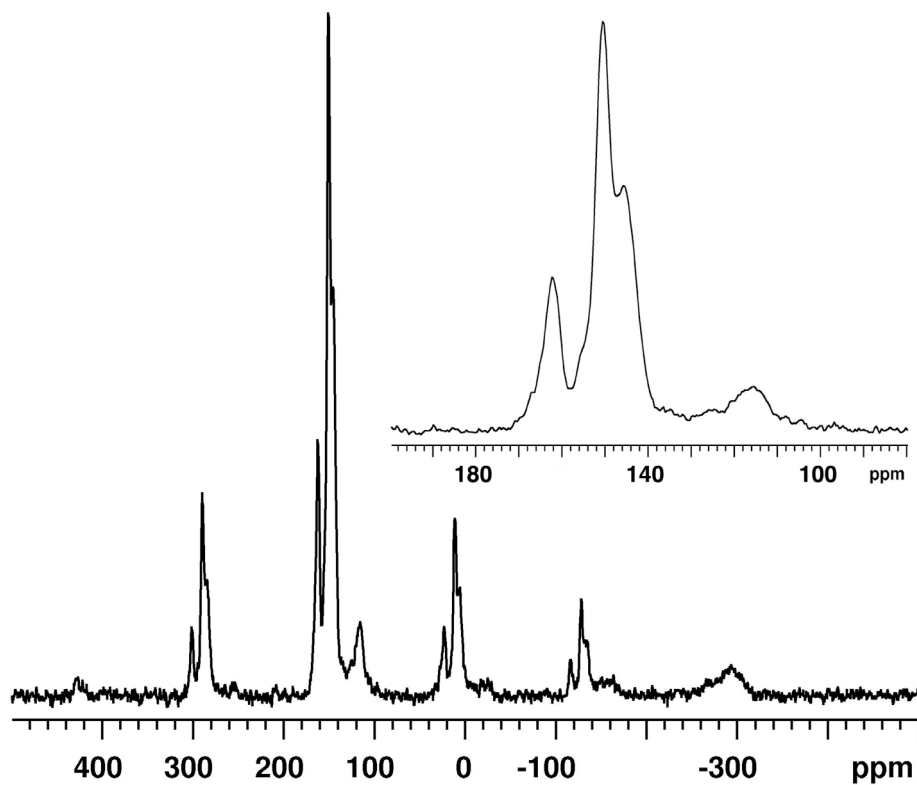


Figure 6.18: ^{13}C MAS spectrum of compound (2) with inset showing the presence of four cyanide signals in the isotropic region.

Assignment of resonances is based on the relative temperature sensitivities and the proximity/connectivity to the Cu^{2+} centre. A typical plot of the observed chemical shift (δ_{iso}) dependence on the inverse of temperature ($1000/T$ in this case) is shown in Figure 6.19. The high sensitivity of the methylene signal (from the en ligand) is quite clear.

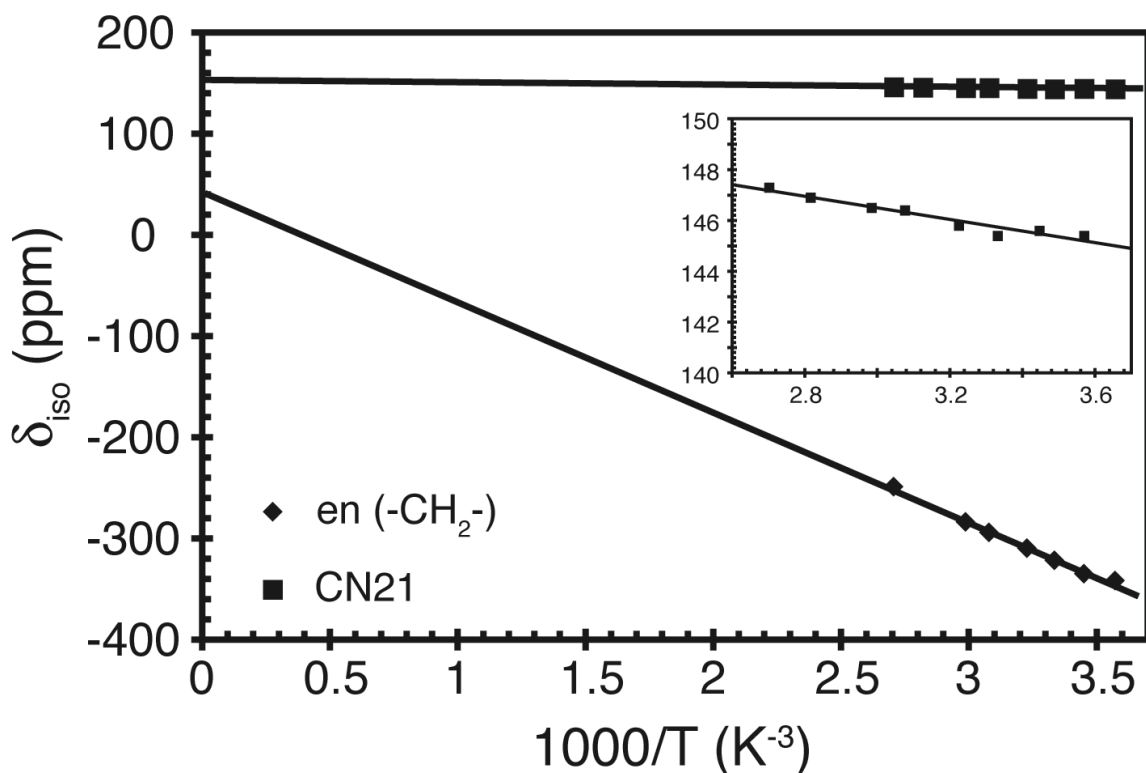


Figure 6.19: Observed chemical shifts for the ethylenediamine (-CH₂-) and for CN21 of compound (2). An expansion of CN21 region (shown inset) reveals the temperature dependence more clearly.

The methylene carbon varies by over 90 ppm in total over the temperature range of -10 to $+80^\circ\text{C}$. The linear correlation of the shift with inverse temperature allows extraction of the Fermi-contact coupling from the slope, from which the unpaired spin density at the nucleus, $\rho_{\alpha\beta}$ can be calculated²⁰⁹⁻²¹¹ as -0.003083 . The sign of the coupling

indicates that the unpaired electron density on the carbons of the ethylenediamine is likely a result of spin-polarization.^{200,212} In contrast, that for CN21 was only -0.000065.

6.3.3 [Cu(dmeda)₂Au(CN)₄][Au(CN)₄], (3)

The structure of this compound consists of two separate cyanide polymer chains, one of which possesses within it the paramagnetic copper(II) centres while the other consists solely of gold-cyanide.¹⁶⁸ The copper-bearing chain possesses two distinct cyanides (2:2). The first (CN21) lies at the axial positions of the Cu coordination sphere (see Figure 6.20a) with Cu-N distances of 2.72 Å. The second is terminal and has no short contacts to the copper. The second chain consists solely of gold-cyanide with three types of cyanide: two terminal (N11 and N13) and one bridging adjacent gold atoms (N12). The relative multiplicity of these sites is 2:1:1. Thus in total, five distinct cyanides are present within the structure with relative multiplicities of 2:2:2:1:1.

The ¹³C MAS NMR of compound (3) consists of four resonances at 80, 103, 111 and 115 ppm. These shifts are consistent with those observed for cyanides bound to Au(III) (AuCN₄¹⁻, $\delta_{\text{iso}} = 105.2$ ppm).²¹³ As the structure of (3) consists of two independent chains, one containing the paramagnetic Cu²⁺ center, and one without a paramagnetic center in the chain, the three resonances from 103 to 115 ppm may simply arise from the cyanides within the latter.

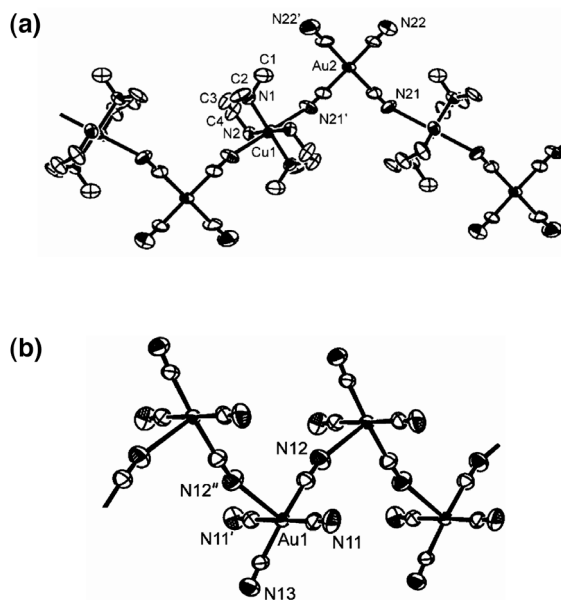


Figure 6.20: The structure of compound (3). In (a) the copper-bearing chain, in (b) the copper-free chain. Reprinted with permission from Shorrocks *et al.*¹⁶⁸ Copyright (2003) American Chemical Society.

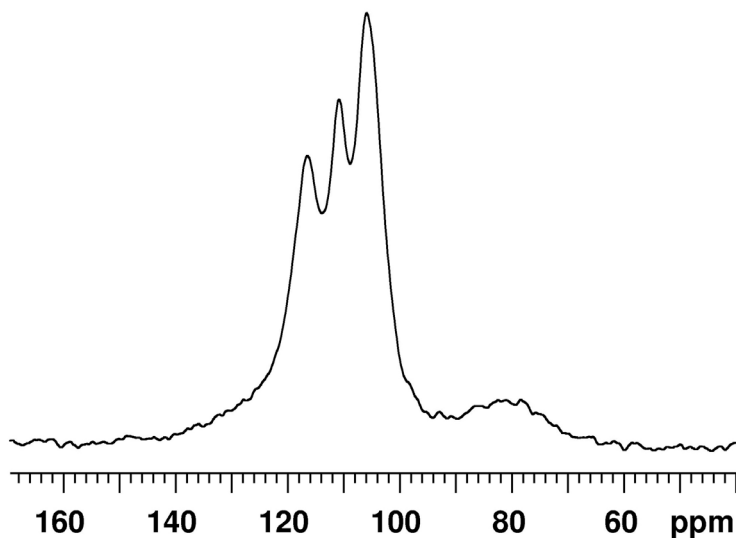


Figure 6.21: Isotropic region of the ¹³C MAS spectrum of compound (3).

As the only ^1H nuclei within the structure are part of the N,N-dimethylethylenediamine (dmeda) ligand, $^{13}\text{C}\{^1\text{H}\}$ rotational-echo double-resonance (REDOR) experiments were attempted as a potential method to assign the observed signals. The results were initially surprising. Dephasing of only a single signal (at 80 ppm) was observed, with no measurable dephasing of the other signals, even at total dephasing times ($N_c \cdot \tau_r$) of 440 μs . The implementation of significantly longer dephasing times was hindered by the very fast spin-spin (T_2) relaxation, and resulted in very poor signal-to-noise. The strong ^{13}C - ^1H dipolar interaction led to an initial assignment of the 80 ppm site as belonging to the methyl groups of the dmeda ligand. Further support for this assignment comes from the lack of spinning sidebands associated with this signal. Typical spans for the ^{13}C of a methylene range from 25 to 50 parts-per-million. This corresponds to less than 8000 Hz at 14.1 T; thus the spinning rates employed (*ca.* 20 kHz) for this sample should yield a nearly isotropic spectrum. The anisotropy typical for a cyanide signal (the only other carbon containing species) is much larger (300-400 ppm or 45,000-60,000 Hz at 14.1 T) and is not *spun-out* by MAS at these rates, resulting in significant intensity in sidebands. A series of Bloch-decay spectra over a ± 8000 ppm range were collected in order to search for any peaks which may have been significantly shifted from typical cyanide frequencies due to paramagnetic interactions. No additional resonances were observed. While it is uncertain whether all the cyanide resonances in compound (3) are accounted for within the group of signals between 120 and 130 ppm, the relative intensities of the three cyanide resonances are *ca.* 1:1:2 which corresponds well with the AuCN chain which contains no paramagnetic centre. Based on the intensities, the peak at

115 ppm may be tentatively assigned as the terminal N13, leaving the terminal N11 and bridging N12 to account for the 111 and 103 ppm resonances.

6.3.4 $[\text{Cu}(\text{en})_2[\text{Zn}(\text{NC})_4(\text{CuCN})_2]$, (4)

The cyanide ligand may exist in numerous bonding modes, the most common being terminal (C- or N-bonded to a single metal) and bridging (C- and N-bonded to two metals). These and some other common cyanide bonding modes are depicted in Figure 6.22.

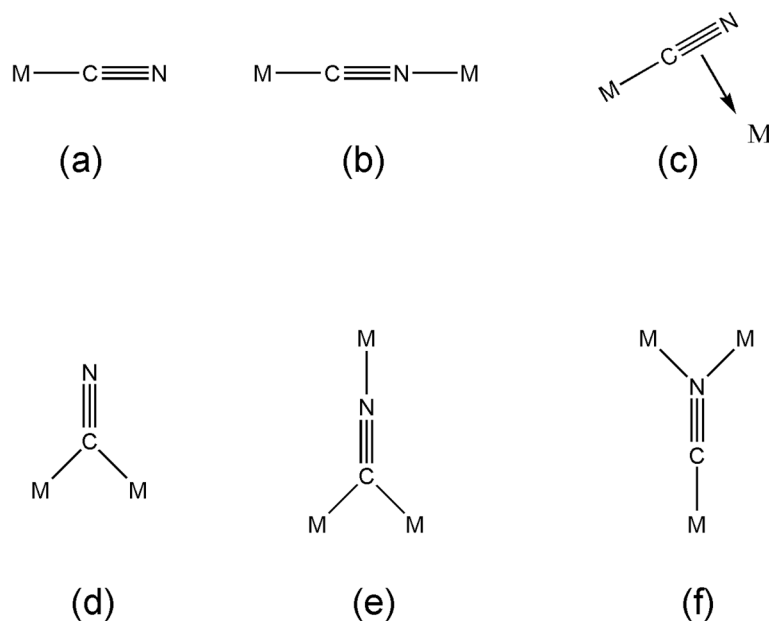


Figure 6.22: Depiction of known cyanide coordination modes. For cases with multiple metals, M, it need not be the same metal.

The mixed-metal cyanide (Zn/Cu(I)/Cu(II)) system $[\text{Cu}(\text{en})_2[\text{Zn}(\text{NC})_4(\text{CuCN})_2]$, (4) possesses six distinct cyanides (see Figure 6.23b). These six cyanides exist in 4 different coordination modes. Although none of these modes on its own is novel (they are all depicted in Figure 6.22), the presence of so many different bonding modes within the

same complex is atypical. The structural diversity mentioned can be seen in Figure 6.23b: CN6, CN7 and CN8 are all typical bridging cyanides, bridging Zn and the diamagnetic Cu(I). CN5 is μ_3 -bridging (as in Figure 6.22e or f). CN9 is μ_2 -bridging (as in Figure 6.22d) and CN10 is a typical terminal cyanide.

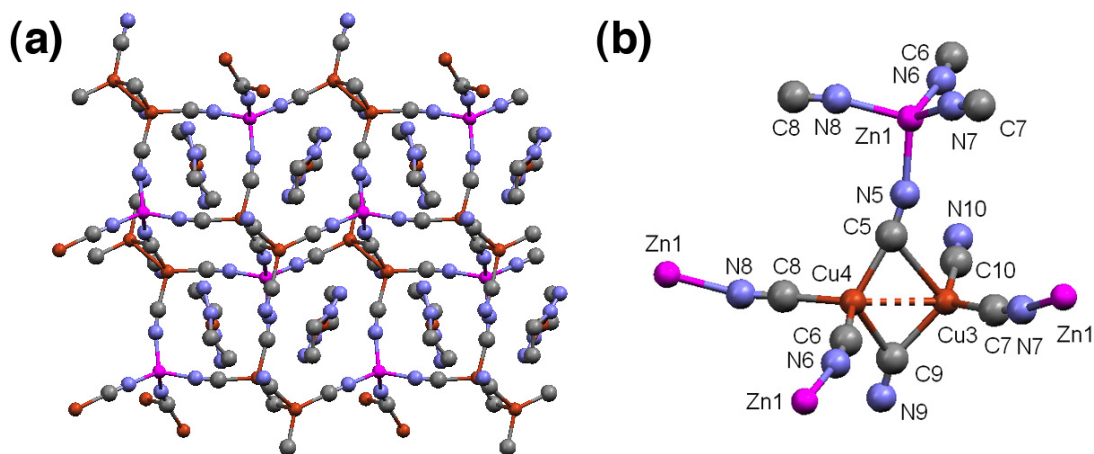


Figure 6.23: The structure of compound (4). The overall network structure (a) with the $\text{Cu}(\text{en})_2$ outside the cyanide framework. In (b), a more detailed view of the Zn/Cu(I) cyanide bonding is shown.

This diversity in cyanide-coordination environments is reflected in the NMR spectra. The ^{15}N MAS spectrum consists of four signals (231, 243, 246 and 255 ppm) in a *ca.* 1:2:2:1 ratio (Figure 6.24). This is consistent with the six crystallographically distinct cyanides observed in the crystal structure. The width of the ^{15}N resonances (120-160 Hz) are too narrow to allow for $^1J(^{15}\text{N}, ^{63/65}\text{Cu})$ couplings, which would be expected to be on the order of 120-250 Hz.^{157,208} The ^{13}C linewidths are much broader (1200-2000 Hz) and could be accounted for by the presence of $^1J(^{13}\text{C}, ^{63/65}\text{Cu})$, which are expected to be on the order of 200 to 700 Hz.^{157,184,208} ^{67}Zn is spin 5/2 and only 4% naturally abundant. Thus, any one-bond couplings would result in a sextet with each transition comprising

only 0.67% of the intensity of the ^{15}N or ^{13}C resonance bound to one of the NMR inactive zinc isotopes, making detection very difficult. This allows the conclusion that the cyanides are all C-bound to the copper(I) centres.

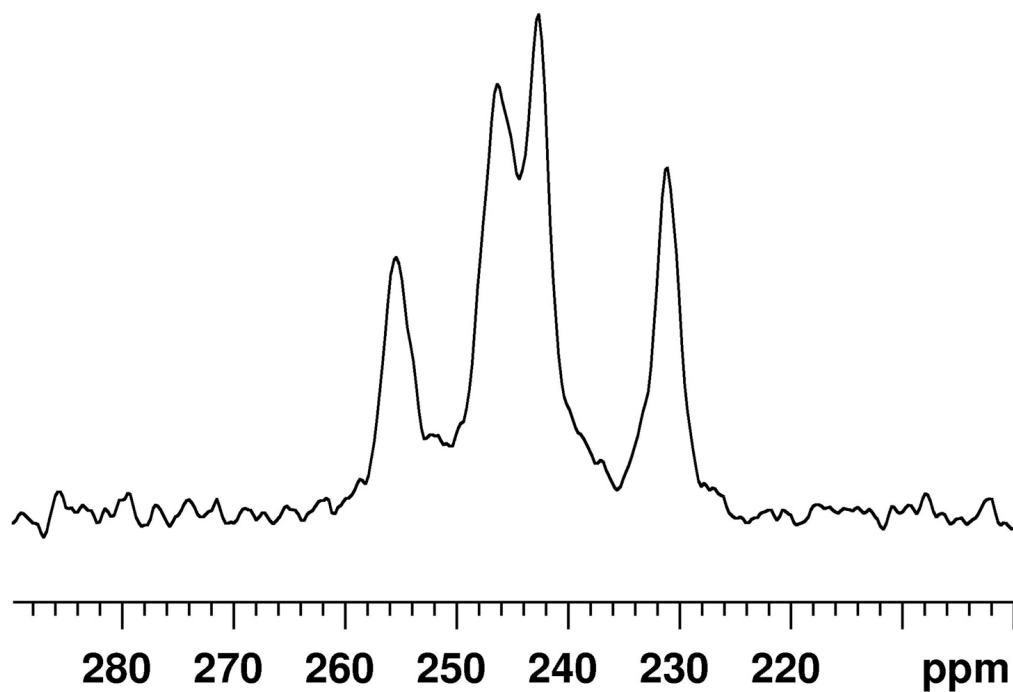


Figure 6.24: ^{15}N MAS spectrum of sample (4). Four signals in *ca.* 1:2:2:1 intensity are observed.

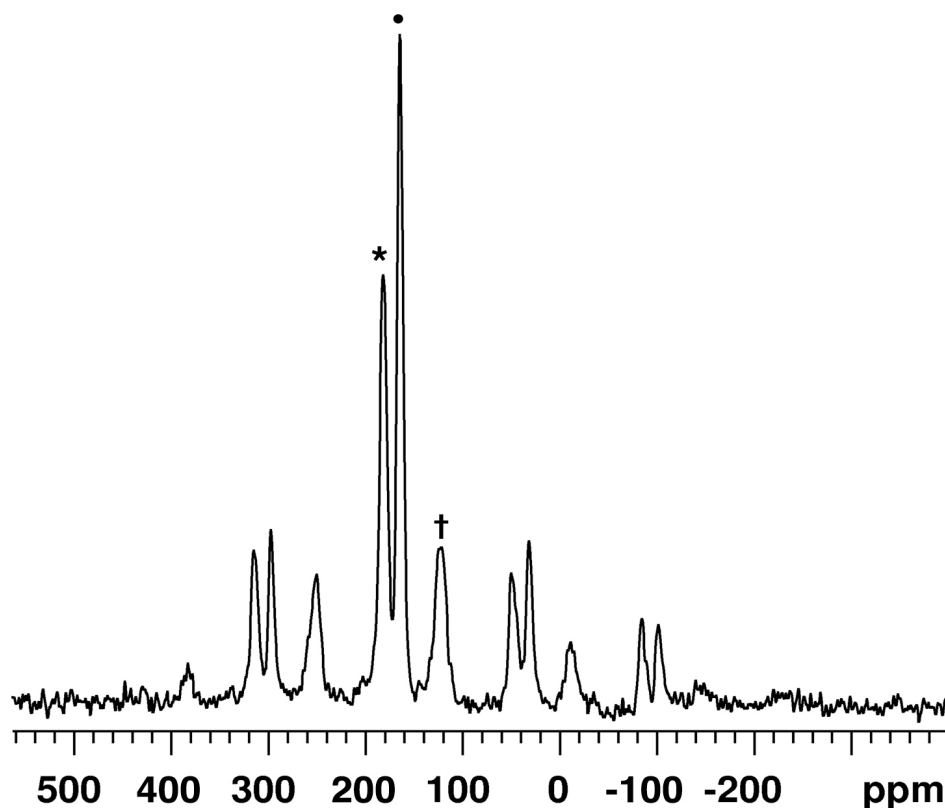


Figure 6.25: ^{13}C MAS spectrum of compound (4). The isotropic shifts are marked and other peaks are spinning sidebands.

In an attempt to verify that the copper T_1 relaxation times are not so short as to result in decoupling of the J -couplings, Cu-63 MAS experiments were attempted. No signal attributable to Cu-63 from within the sample was observed. However, two curious signals were observed. The first is a very broad peak at a resonance frequency of 2000 ppm and is assigned to the copper metal within the outer edge of the silver-plated copper coil used to detect the NMR signal.²¹⁴ The second signal was also quite strange, with a resonance frequency of -2400 ppm on the copper scale. However, it became clear that this signal was in fact due to a small amount of sodium present within the zirconia rotor-sleeve material. The difference in resonance frequency between ^{63}Cu and ^{23}Na is *ca.* 381

kHz (at 14.1 T), which is ca. 2400 ppm. The absence of a signal from the sample, although not satisfying, is not unexpected as ^{63}Cu in copper cyanides is known to potentially possess very large quadrupole couplings. CuCN has C_Q 's of roughly 80 MHz,¹⁵⁷ and the distorted tetrahedral copper centre in $\text{CuCN}\cdot\text{N}_2\text{H}_4$ has a C_Q of 26 MHz.²⁰⁸ These values are much larger than those observed for boron-11 (previous chapter) in the borate glasses (~ 2.5 MHz) and copper-63 has a smaller magnetogyric ratio ($\sim 20\%$ lower). The result is extremely broad peaks, which can be impossible to observe, and may be made even worse by MAS at typical frequencies.

The observed relative intensities of the ^{13}C signals at 182, 165 and 122 ppm are 3:4:1. These intensities do not, however, properly reflect the ratios expected from the known structure, which has 6 cyanides. As mentioned previously, sites subject to larger electron-nucleus interactions (eg., the $-\text{CH}_2-$ of the en ligands) are not always observed because they possess short T_{2s} , which can allow full relaxation (decrease) of the signal during the echo delay times. Spin-spin relaxation-time measurements were undertaken, to investigate what impact they may have on the relative intensities obtained from the ^{13}C Hahn-echo MAS spectrum.

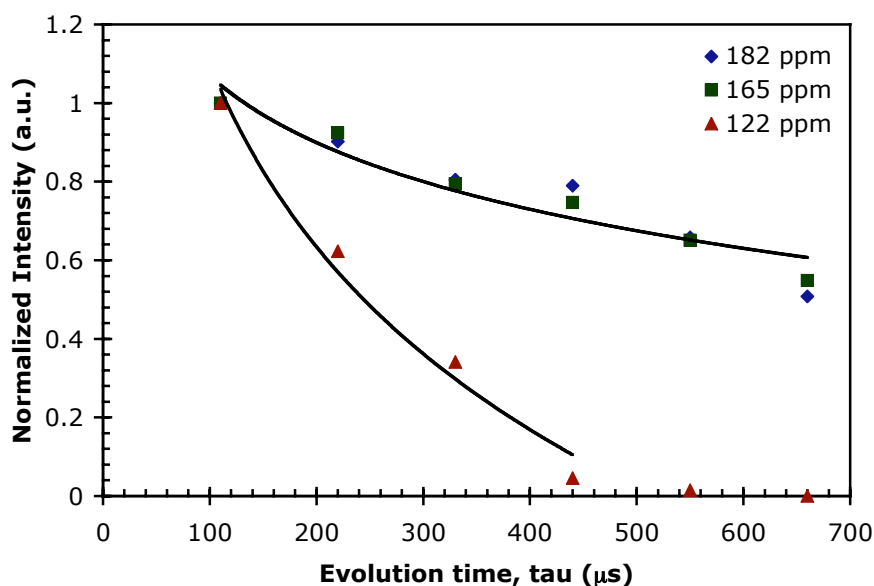


Figure 6.26: ^{13}C spin-spin relaxation data for compound (4), along with single-exponential fits. The fit to the 122 ppm signal was performed using only the first four points due to poor S/N at long evolution times.

The ^{13}C spin-spin relaxation data are shown in Figure 6.26. The two signals at higher frequency have very similar spin-spin relaxation time constants, T_2 of 0.88 and 0.93 ms. The signal at lowest frequency, however, relaxes much faster. As can be seen in Figure 6.26, beyond evolution times of 450 μs , the signal has decayed to zero intensity, whereas the other two signals still possess >50% of the signal acquired with a delay time of 110 μs . This limits the accuracy of the T_2 measurement, which was fit using only the first four points to give a value of 0.11 ms. Taking this into account, the intensity of the signals at an evolution time of *zero* (where no relaxation of the signal has occurred) approaches 1:1:0.7 (or 2:2:1.4), which is in reasonable accord with the six distinct cyanides within the structure. Additional confidence for these intensity estimates comes from variable-temperature and variable-spinning rate (effectively VT, due to change in

frictional heating) results, which shows a splitting of this peak into two peaks (see Figure 6.27), thus it (they) must arise from two distinct cyanide carbons.

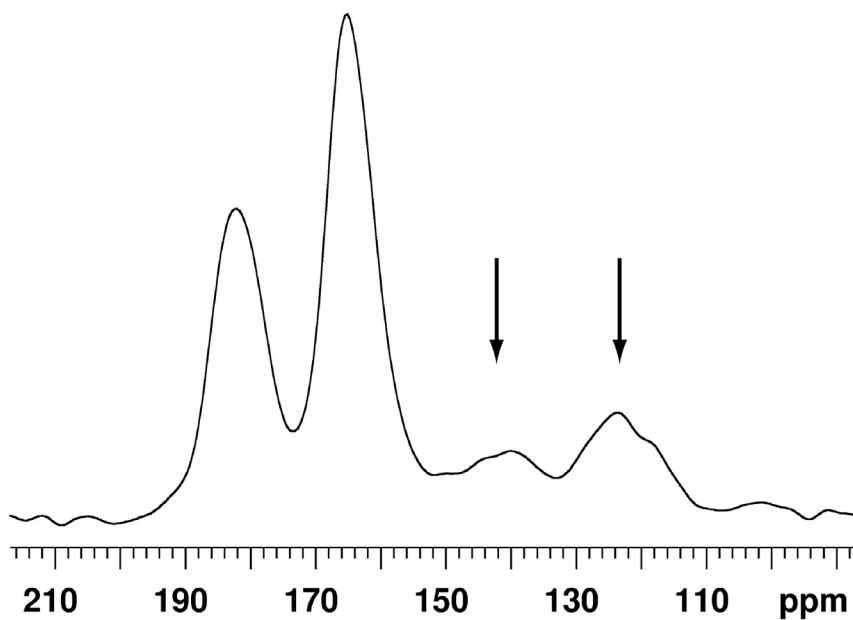


Figure 6.27: Isotropic region of ^{13}C MAS spectrum of (4), acquired at 12.5 kHz spinning.

6.3.5 $\{(\text{tmeda})\text{NiHg}(\text{CN})_2\}\text{HgBr}_4$, (5) and $\{(\text{tmeda})\text{CuHg}(\text{CN})_2\}\text{HgBr}_4$, (6)

Samples 5 and 6 are isostructural and are composed of nearly linear $\text{Hg}(\text{CN})_2$ moieties with the both nitrogens bound to a six-coordinate paramagnetic centre (either Cu or Ni), forming a 3D network (see Figure 6.28).¹⁵² There are two cyanides in the asymmetric unit (CN3 and CN4).

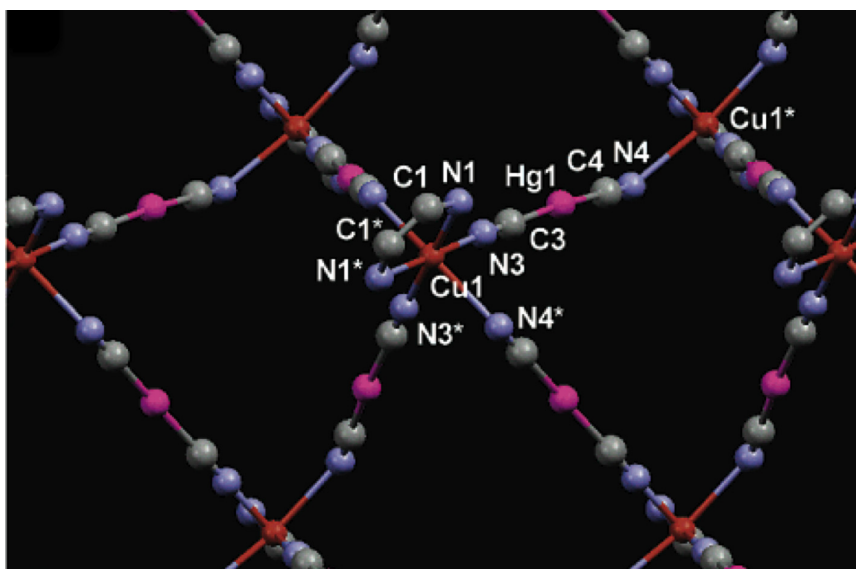


Figure 6.28: The structure of compound (6). That of compound (5) is identical, but with nickel replacing the copper. Reprinted in part, with permission, from Draper *et al.*¹⁵² Copyright (2003) American Chemical Society.

The carbon-13 MAS spectrum of sample 5 is shown in Figure 6.29. The cyanide signal has an isotropic shift of -205 ppm, a span in excess of 600 ppm, and peak widths of *ca.* 4500 Hz (30 ppm). The observed span is nearly twice that generally observed for metal cyanides, and the linewidths are nearly 5 times those observed in the other paramagnetic samples, and easily 10-20 times the linewidths observed in diamagnetic systems. No clear evidence for two resonances is observed; most likely, both resonances are within the

observed broad peak due to their structural similarity. No spectrum for sample 6 could be obtained. This is likely due to longer electron relaxation times for Cu^{2+} than Ni^{2+} .^{21,200} The observation of the signal relies on there being sufficient decoupling of the electron from the nucleus to observe a single resonance (recall section 2.6). The mechanism for this decoupling is the relaxation of the electron itself; if the relaxation time is short with respect to the inverse of the magnitude of the coupling interaction, the electron will be self-decoupled and an NMR spectrum of the nucleus should be observable. However, if the relaxation time is long compared to the inverse of the interaction, then it will not be decoupled and NMR of the nucleus may not be observable. Obviously, spectra with Cu^{2+} species have been observed (compounds 1-4), and thus it is more likely that the magnitude of the Fermi contact for the cyanides in (6) are much larger than in previous systems. The much larger span of the resonance arises from the dipole-dipole interaction of the nucleus and the net unpaired spin,^{21,202,215} and is sometimes termed the paramagnetic shielding anisotropy.²¹⁶⁻²¹⁸ Converting the span in ppm to Hz, we obtain a value of *ca.* 90 kHz. Given that Ni^{2+} has two unpaired electrons, and these are completely localized at the nickel, we can calculate the distance which would give rise to such a dipolar coupling using the following relation:^{202,218,219}

$$R_{DD} = \left(\frac{\mu_0}{4\pi} \right) \frac{\mu_{\text{eff}} \gamma_I}{r^{-3}} \quad \text{Equation 6.1}$$

where μ_0 is the permeability of vacuum, γ_I is the magnetogyric ratio of the observed nucleus, I , r is the distance between I , and the metal centre and μ_{eff} is the effective moment of the electron

$$\mu_{eff} = \frac{[\mu_B^2 S(S+1)]}{3k_B T} g^2 B_0 \quad \text{Equation 6.2}$$

where μ_B , is the Bohr magneton, S is the electron spin quantum number, g is the electron g -factor (-2.0023), k_B is the Boltzmann constant, T the temperature and B_0 the field. Using this relation and the measured anisotropy of 90 kHz, a metal carbon distance of 3.8 Å is obtained. This is longer than the known metal-carbon distance of *ca.* 3.1 Å. The most likely reason for this discrepancy is the assumption that all of the unpaired spin-density, $\rho_{\alpha\beta}$, is located at the metal centre. As has been shown with the other samples, the ligands directly bonded to the paramagnetic centre are displaced from their typical diamagnetic shifts (e.g., -CH₂- of en ligands) via the Fermi-contact mechanism. As this mechanism requires the presence of unpaired spin-density $\rho_{\alpha\beta}$ at the nucleus in question, the metal can only have that which is left over. This is expected to be the large majority; however, the fact that it is less (in this case not quite 2 electrons) means that any calculated distance will always be an overestimate.

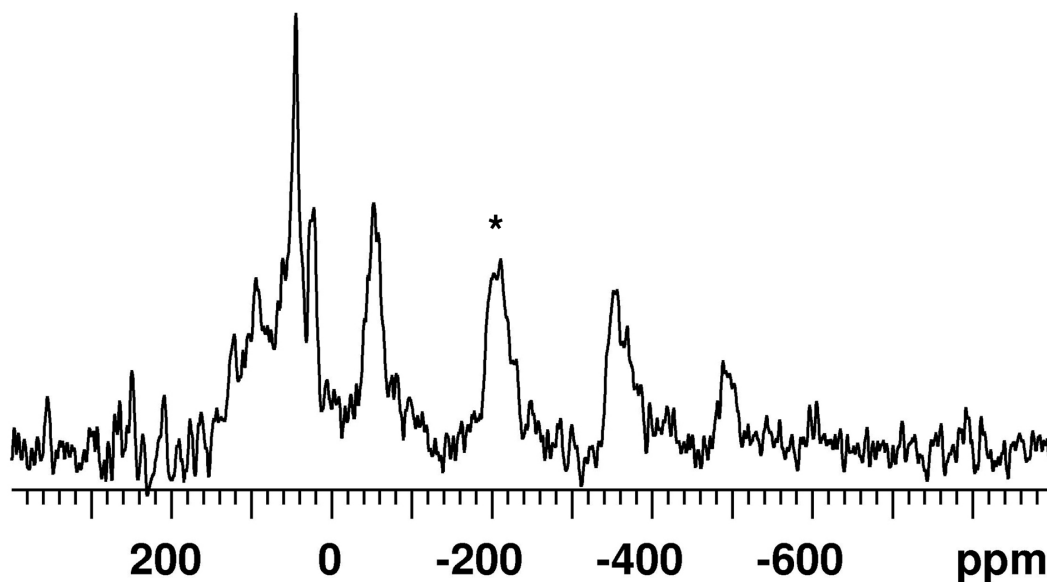


Figure 6.29: ^{13}C MAS spectrum of sample 5. The isotropic cyanide peak is denoted by an asterisk.

Figure 6.30 shows the ^1H MAS spectrum for compound (5), acquired using either a single-pulse (Bloch) or a Hahn-echo (Echo). The Hahn-echo spectrum consists of two signals at 7 and 2 ppm. The 7 ppm signal is known to belong to the Torlon® endcap and drive-tip from the rotor, as verified by the acquisition of spectra from an empty rotor. The peak at 2 ppm thus must arise from the sample. This peak exhibits a fairly small anisotropy, comparable to the rotor signals (which are diamagnetic). As a result this signal most likely arises from the methyl groups of the $\text{N,N,N}',\text{N}'$ -tetramethylethylenediamine (tmeda) ligand of the copper. These would be expected to be undergoing rapid rotation about the C-C bond, thus reducing the electron-nuclear dipolar interaction. The Bloch-decay spectrum has an additional signal with a very-large anisotropic broadening at *ca.* 80 ppm and this signal must be due to either the methylene or amine protons on the tmeda ligand.

The presence of hydrogen-containing materials in our probe hinders the acquisition of ^1H MAS spectra. In the paramagnetic systems, the lower S/N due to the larger anisotropic broadening has the potential to exacerbate this issue. However, if a significant shift of the resonance is present from the typical chemical shift range of -5 to $+15$ ppm for ^1H (as is the case here), enhanced resolution may actually occur. When large displacements of the isotropic shift are not present, this issue may be overcome somewhat by the use of a rotor-synchronized Hahn-echo experiment. However, in these and related systems, the strong electron-nuclear interaction can result in such small T_2 s that nearly complete signal-decay can occur before the receiver is turned on. This provides the ability to easily filter-out certain signals, allowing possible distinction of overlapping signals.

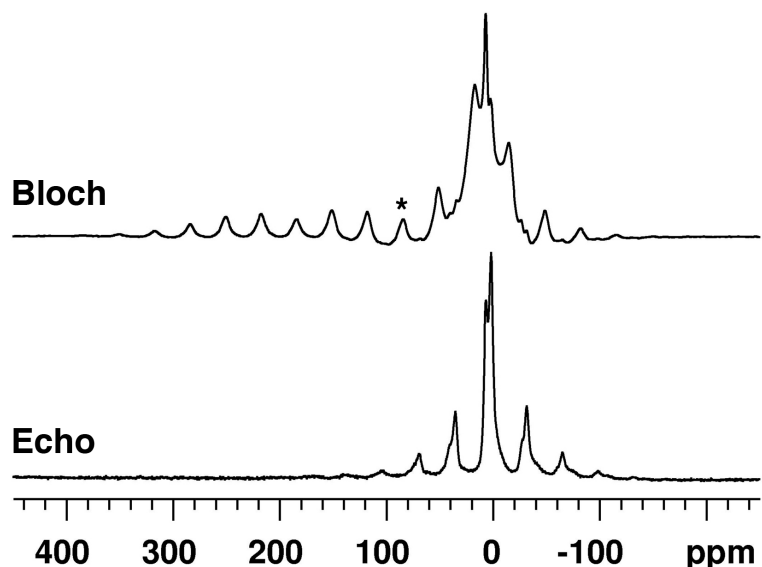


Figure 6.30: ^1H Bloch decay and Hahn-echo spectra of (5), showing the disappearance of the broad peak ($\delta_{\text{iso}} = 80$ ppm) due to short T_2 (marked with an asterisk).

6.3.6 Trends in ^{13}C NMR Peak Positions

Taking the chemical shifts observed and structurally assigned for compounds (1) through (6), an attempt is made to correlate the observed chemical shift with a particular structural environment. Not unlike that of different structural groups present in diamagnetic compounds (e.g., distinction of $-\text{CH}_3$ from $-\text{CH}_2-$ by their characteristic ^{13}C or ^1H shifts). However, in this case, not only would one potentially get information about the coordination environments (e.g., bridging versus terminal etc.), but also information about the location of cyanides with respect to the paramagnetic centre. This has been done for the $^6/7\text{Li}$ chemical shifts of paramagnetic metal-oxide systems.²¹² The chemical shift of $^6/7\text{Li}$ is generally rather small (~ 12 ppm).²²⁰ However, in paramagnetic materials,

it is much greater (~ 2700 ppm).²¹² A similar approach was attempted with these ^{13}C NMR results. A compilation of the ^{13}C MAS results for the six paramagnetic compounds is provided in Figure 6.31. The first trait observed for these paramagnetic cyanides is that the range of chemical shifts is greater than that for diamagnetic cyanides. This generally provides enhanced resolution over that in diamagnetic cyanides (recall the mercury and lead cyanides of sections 6.2 and 6.2.2). Secondly, some trends are beginning to emerge, despite the small number of species investigated. The chemical shifts seem to be based partially on the cyanide binding-mode, but they seem to generally dominated by the interaction with the paramagnetic centre. This may only be valid for systems of similar structure to those herein investigated, and with copper(II) as the paramagnetic centre. In order to get a more complete picture, the affect of other common paramagnetic metals in some of these polymeric cyanide systems, such as Fe(II)/Fe(II), Cr(II)/Cr(III) and Mn(III) should be investigated.

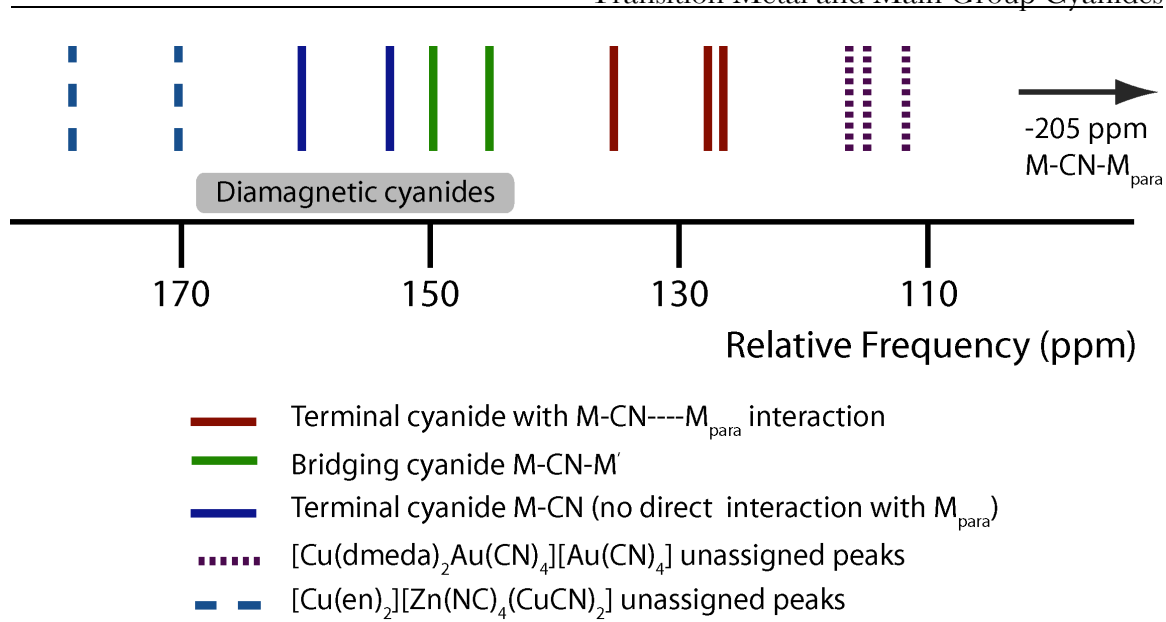


Figure 6.31: Observed trends in the ^{13}C NMR chemical shifts for a series of paramagnetic metal cyanides. Assigned (solid) and unassigned (dashed) peaks are included for completeness.

6.3.7 [Cu(en)₂][Au(CN)₂]₂, (7) & [Zn(en)₂][Au(CN)₂]₂, (8)

The two compounds [Cu(en)₂][Au(CN)₂]₂ and [Zn(en)₂][Au(CN)₂]₂ (referred to herein as (7) and (8), respectively), are known to be isostructural from x-ray crystal structure work performed by our collaborators (Daniel B. Leznoff, Department of Chemistry, Simon Fraser University). NMR analysis was performed without *a priori* knowledge of the structures using only the molecular formulas. This was done in order to test the limits of the structural information obtainable by NMR for these compounds. The zinc compound is diamagnetic, and thus the acquisition of spectra and their interpretation should be typical. The copper complex is paramagnetic, and thus subject to all of the challenges faced with the earlier compounds.

The ^{13}C MAS spectrum of the paramagnetic (7) exhibits two cyanide signals in a 1:1 ratio with chemical shifts of 172 and 119 ppm, respectively (FWHM = 500 Hz, for both) (Figure 6.32). However, the $^{13}\text{C}\{^1\text{H}\}$ CPMAS of the diamagnetic (8) consists of only a single peak at 148 ppm (FWHM = 500 Hz), despite being isostructural with (7). This must mean that the two signals overlap in the spectrum of (8). Spectra at additional spinning rates all exhibited a single manifold, ruling out the fortuitous overlap of the two signals by each other's spinning sidebands (i.e., that the difference in the chemical shifts was equal to an integer multiple of the rotation frequency). The linewidth and lineshape observed in the spectrum of (8) require that the signals from the two sites possess chemical shift differences ≤ 2 ppm. Also evident in the ^{13}C MAS spectra are the peaks due to the ethylenediamine ligand. In the paramagnetic complex, they appear at \sim -300 ppm, as observed previously. In the diamagnetic zinc compound, they appear at a more typical resonance frequency of 40 ppm and overlap with the cyanide signals. Thus the presence of the paramagnetic metal, shifting the resonances and effectively increasing the chemical shift range, allows acquisition of a better-resolved spectrum.

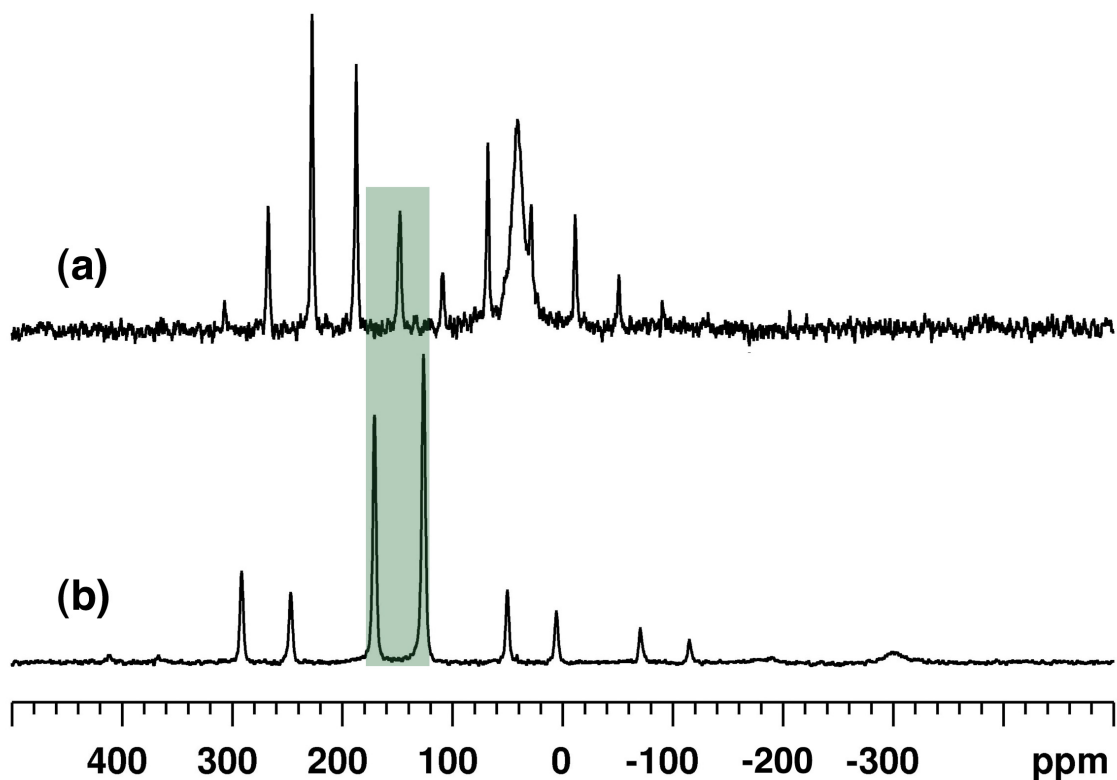


Figure 6.32: ^{13}C CPMAS (a) of sample (8), along with (b) the ^{13}C MAS of sample (7). The highlighted region denotes the isotropic cyanide shifts.

The temperature dependence of the ^{13}C chemical shifts for (8) are found to be of opposite sign (Figure 6.33). Thus, as the temperature is increased the two signals move towards one another. Linear fits of the shift versus T^{-1} have slopes of $+5.782$ and -8.154 1000Kppm for the 172 and 119 ppm signals, respectively. These slopes can be used to calculate the unpaired spin-density at the nuclei; 0.000164 and -0.000231, respectively. The larger unpaired spin density on the ^{13}C at 119 ppm suggests that it possesses a stronger interaction with the Cu(II) than the other ^{13}C (cyanide).

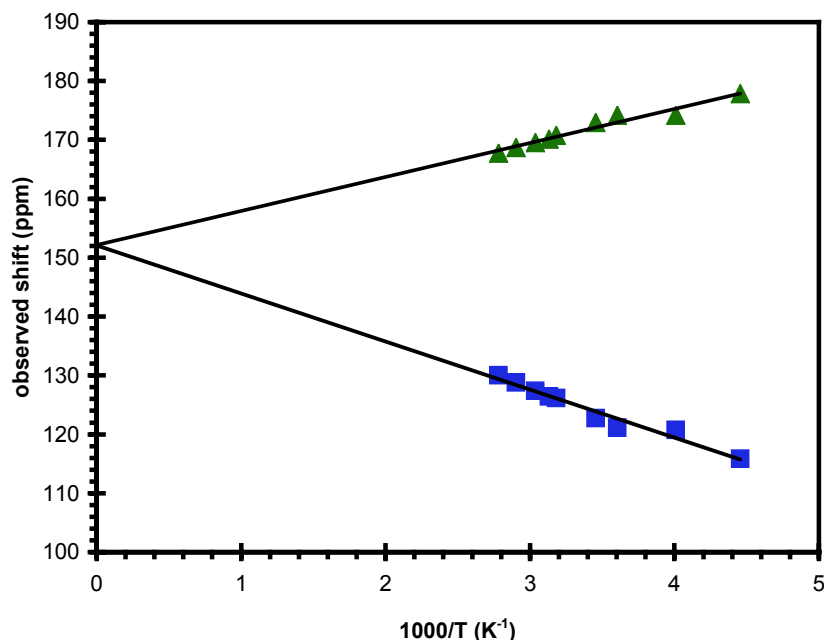


Figure 6.33: The observed temperature dependence of the two ^{13}C cyanide signals for sample 7. Extrapolation to infinite temperature provides diamagnetic shifts of 152 ppm for both signals.

In addition to the slopes, the intercepts (i.e., the shift at “infinite” temperature) provides an estimate of the diamagnetic shifts. The intercepts found for the 172 and 119 ppm peaks are both 152.1 ppm, in very good agreement with the observed isotropic shifts of the isostructural diamagnetic (8). The shielding tensors of the two sites in sample 7 have similar spans (330 ± 20 ppm), however, they have very different skews (0.6 ± 0.2 vs. 0.9 ± 0.1). This may indicate differences in the bond angles, in particular the Au-C-N bond angles. Despite the signal for the diamagnetic 6 containing responses from two sites, the spinning sideband pattern could be fit to a single shielding tensor.

The N-15 MAS spectrum of sample (7) consists of two signals at 311 and 92 ppm. Variable-temperature nitrogen-15 MAS spectra were acquired for (7). The 92 ppm signal

had the greater temperature dependence and is thus assigned to the nitrogen bound to the carbon exhibiting a ^{13}C signal at 119 ppm, because of its large temperature dependence.

In addition to the enhanced resolution of the signals from the two crystallographically distinct sites provided by the interaction with the paramagnetic centre, the reduction in the nuclear spin-lattice relaxation time constants allows for the acquisition of higher quality spectra for paramagnetic samples over their diamagnetic counterparts. This is simply a result of being able to co-add more transients per unit time. The carbon-13 spectrum of (7) (Figure 6.32) has better signal-to-noise than that of sample (8), despite being acquired on a much smaller sample size (32 mg *versus* 121 mg) and without cross-polarization. The ^{13}C MAS spectrum of (7) required the acquisition of 12,000 scans which were co-added, while the ^{13}C spectrum of (8) required only 128 scans. However, because less time was required for relaxation between co-added experiments (0.1 *versus* 60 seconds), thus the actual spectrometer time required was much shorter for the paramagnetic sample. This advantage is most convincingly demonstrated by the nitrogen-15 NMR spectra. Whereas natural abundance N-15 spectra could be acquired on the paramagnetic samples using 3.2 mm rotors, even with 5 mm rotors and cross-polarization, no signal was obtained for the diamagnetic sample (8).

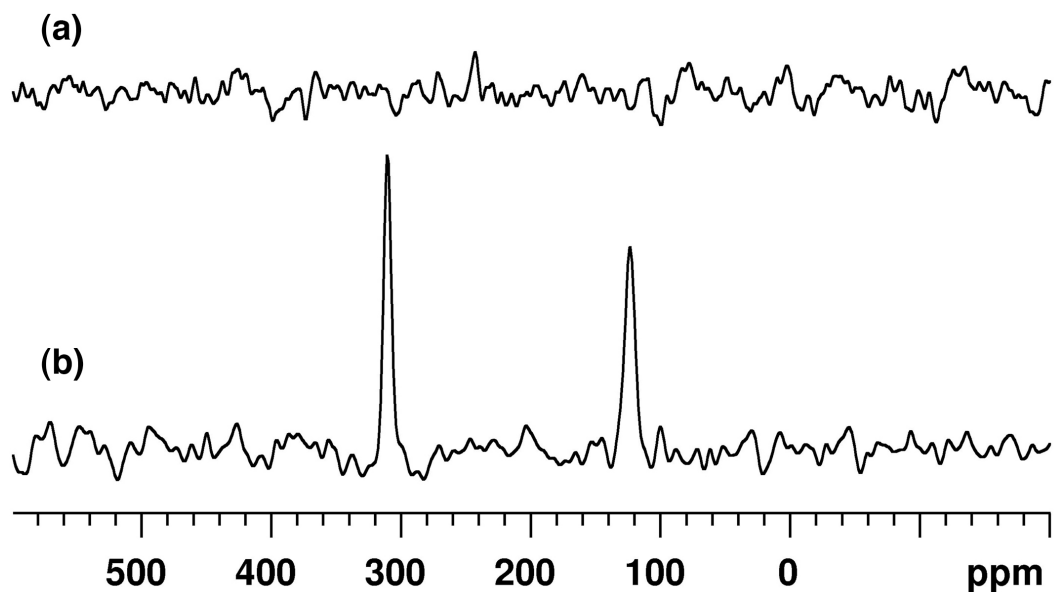


Figure 6.34: The $^{15}\text{N}\{^1\text{H}\}$ CPMAS spectrum of (8) (a) yields no signal after 50 hours of acquisition (121 mg). The ^{15}N MAS of (7) (b) exhibits two clear signals after 17 hours (32 mg).

From the ^{13}C and ^{15}N NMR results for samples (7) and (8), some constraints on the structure may be proposed. Both nuclei (^{13}C and ^{15}N) indicate the presence of two cyanides in the asymmetric unit. Based on the chemical shifts in comparison with those in Figure 6.31, and that in the diamagnetic complex they are so similar as to completely overlap, it is likely that both cyanides are terminal. The assumption that the cyanides are C-bound to the gold is made here, as this is the most common mode.²²¹ The cyanide giving rise to the ^{13}C chemical shift at 119 ppm has a significant (*ca.* 2.5-2.9 Å) interaction with the Cu(II) centre (i.e., a weak interaction, since direct bonding might result in no signal, as with compound (6)). In addition, this signal has greater deviation of the skew, κ , of this signal from axial symmetry ($\kappa = +1$), thus it likely possesses an Au-C-N bond angle

deviating from 180° . The other signal (172 ppm) exhibited a more axially symmetric shielding tensor, and thus should correspond to a cyanide with an Au-C-N bond angle closer to 180° .

The actual structure of these compounds is depicted below (Figure 6.35). It can be seen that the gold cyanides are in two-fold cyanide coordination, with gold-gold interactions (3.14 \AA) to create 1D gold-cyanide chains. One of the cyanides interacts with the metal (Cu or Zn), with a M-N distance of 2.58 \AA . The Au-C-N bond angle for this cyanide (CN1) is 176° , whereas the other has an Au-C-N angle of 180° .

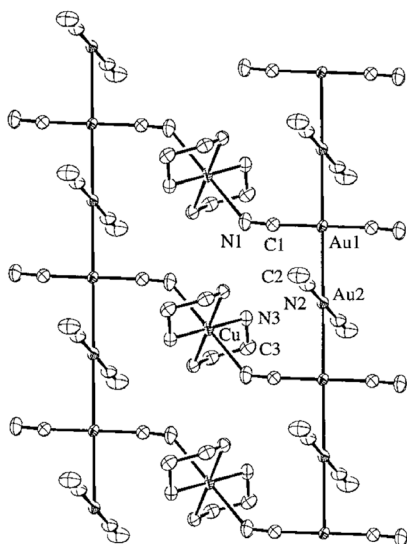


Figure 6.35: The structure of compound (7). That of (8) is identical, only with Zn replacing Cu. Reprinted with permission from Leznoff *et al.*²²² Copyright (2001) American Chemical Society.

Natural abundance ^{13}C and ^{15}N MAS NMR spectra of a series of paramagnetic metal-cyanide polymers could be acquired, and structurally assigned. This opens the door to analysis of a whole series of materials, which have not been characterized previously by solid-state NMR methods.

6.4 Conclusions

Given the recent resurgence in research involving metal-cyanide framework materials, this work shows that key structural (and potentially dynamical) information about these materials may be obtained through solid-state NMR.

The known ^{13}C NMR parameters for transition-metal cyanide systems have been extended, and a few systems have been encountered with isotropic chemical shifts greater than previously reported. Work on a series mercury cyanides indicates that the degree of covalent character of the ligands may play a greater role on the shielding tensor of the mercury (and potentially other metals) than simply the number of coordinating ligands. Despite the varying number of coordinating ligands about the mercury, both ^{199}Hg NMR and the $^1J(^{199}\text{Hg},^{13}\text{C})$ coupling constants reveal that the electronic environment is dominated by the cyanide ligands, with the chloride ligands playing a lesser role.

Powder x-ray diffraction can provide crucial long-range structural information, however identification of the asymmetric unit can be more challenging than single-crystal studies. The combination of powder x-ray diffraction and multinuclear solid-state NMR was employed to narrow down the possible long-range structural possibilities of a $\text{Pb}[\text{Au}(\text{CN})_2]_2$ compound, arriving at a single solution consistent with all experiments.

The reduced spin-lattice relaxation time of the paramagnetic systems allowed acquisition of ^{13}C and ^{15}N NMR spectra of a series of metal-cyanide polymer materials at natural isotopic abundances and without the aid of polarization-enhancement methods. The combination of variable-temperature and relaxation measurement experiments provides information which can be related to the proximity of the paramagnetic centre, and hence contribute to peak assignment. The use of these simple techniques should

allow for the characterization of a whole series of compounds not previously investigated by solid state NMR.

6.5 Future Work

The observed temperature dependence of the lead-207 shielding tensor for $\text{Pb}[\text{Au}(\text{CN})_2]_2$ may provide further confirmation for the proposed structure. Initial investigations extending the temperature range, as well as accompanying the NMR experiments with powder x-ray diffraction and/or other variable-temperature experiments (e.g., Raman or IR), could provide information about local bonding and any changes which are occurring.

Despite the application of fast MAS, many paramagnetic systems of interest possess large proton spin baths, making the application of some additional decoupling important to provide resolution of sites. It has been observed by the author and others in our group, and recently in the literature,²²³ that the application of “broadband” continuous-wave rf decoupling of ^1H under MAS in paramagnetic systems has a tendency to yield broader resonances than without rf decoupling. This implies that rather than decoupling these spins, the application of CW-decoupling results in a *recoupling* of spins. Examination of the rf-field-strength dependence for one sample (data not shown), indicates that it is not due solely to the well-known rotary-resonance condition(s) for recoupling of dipole-dipole interactions under MAS.^{224,225} In order to obtain further improvements in resolution without the need for spinning speeds in excess of 40 or 50 kHz (which severely limit sample size), a better understanding of the underlying

mechanism(s) giving rise to this recoupling is needed, and the development of enhanced “decoupling” techniques should be pursued.

It has been established that the directly unobservable zero-quantum (ZQ) transition between a coupled spin-pair is unaffected by inhomogeneous magnetic susceptibilities, which often lead to substantial broadening of the observed single-quantum transitions.^{226,227} It is also known that within a two-dimensional double-quantum/single-quantum correlation experiment, there exists a pseudo-ZQ axis at a characteristic angle with respect to the two orthogonal axes in such an experiment, which can yield high-resolution spectra of inhomogeneously broadened signals (in analogy to MQMAS).²²⁸ The demands imposed by the various pulse sequences to obtain such spectra are often limited by the spinning rates available due to numerous factors often encountered with paramagnetic samples. Recent advances in probe technology, spinning rates of 65 kHz available from commercial suppliers,^{229,230} and claims of MAS rates exceeding 90 kHz,^{231,232} may provide a simple way of making such experiments feasible for a greater variety of materials.

References

- (1) Abragam, A. *Principles of Nuclear Magnetism*; Oxford University Press: New York, 2004.
- (2) Bloch, F.; Hansen, W. W.; Packard, M. *Physics Reviews* **1946**, *70*, 474.
- (3) Purcell, E. M.; Torrey, H. C.; Pound, R. V. *Physics Reviews* **1946**, *69*, 37.
- (4) Dickinson, W. C. *Physical Review* **1950**, *77*, 736-737.
- (5) Knight, W. D.; Cohen, V. W. *Physical Review* **1949**, *76*, 1421.
- (6) Proctor, W. G.; Yu, F. C. *Physical Review* **1950**, *77*, 717.
- (7) Gutowsky, H. S.; McCall, D. W. *Physical Review* **1951**, *82*, 748-749.
- (8) Proctor, W. G.; Yu, F. C. *Physical Review* **1951**, *81*, 20-30.
- (9) Andrew, E. R.; Bradbury, A.; Eades, R. G. *Nature* **1958**, *182*, 1659.
- (10) Lowe, I. J. *Physics Reviews Letters* **1959**, *2*, 285-287.
- (11) Martin, R. W.; Zilm, K. W. *Journal of Magnetic Resonance* **2003**, *165*, 162-174.
- (12) Paulson, E. K.; Morcombe, C. R.; Gaponenko, V.; Dancheck, B.; Byrd, R. A.; Zilm, K. W. *Journal of the American Chemical Society* **2003**, *125*, 15831-15836.
- (13) Brevard, C.; Granger, P. *Handbook of High Resolution Multinuclear NMR*; John Wiley & Sons: New York, 1981.
- (14) MacKenzie, K. J. D.; Smith, M. E. *Multinuclear Solid-State NMR of Inorganic Materials*; Pergamon: New York, 2002.
- (15) Eichele, K.; Wasylishen, R. E. *WSOLIDS1 NMR simulation package, version 1.17.30* **2001**.
- (16) Amoureux, J. P.; Fernandez, C.; Granger, P. In *Multinuclear Magnetic Resonance in Liquids and Solids - Chemical Applications*; Harris, R. K., Granger, P., Eds.; Kluwer: Boston, 1988; Vol. 322.
- (17) Pake, G. E. *Journal of Chemical Physics* **1948**, *16*, 327-336.
- (18) McFarlane, W. *Journal of the Chemical Society D: Chemical Communications* **1971**, 609-610.

-
- (19) Schaefer, T.; Chum, K.; Marat, K.; Wasylishen, R. E. *Canadian Journal of Chemistry* **1976**, *54*, 800-804.
- (20) Wasylishen, R. E. In *Encyclopedia of Nuclear Magnetic Resonance*; Grant, D. M., Harris, R. K., Eds.; Wiley: New York, 2000; Vol. 9.
- (21) *NMR of Paramagnetic Molecules: Principles and Applications*; La Mar, G. N.; Horrocks, W. D.; Holm, R. H., Eds.; Academic Press: New York, 1973.
- (22) Hodgkinson, P.; Emsley, L. *Journal of Chemical Physics* **1997**, *107*, 4808-4816.
- (23) Maricq, M. M.; Waugh, J. S. *Journal of Chemical Physics* **1979**, *70*, 3300-3316.
- (24) Maudsley, A. A.; Wokaun, A.; Ernst, R. R. *Chemical Physics Letters* **1978**, *55*, 9-14.
- (25) Frydman, L.; Harwood, J. S. *Journal of the American Chemical Society* **1995**, *117*, 5367-5368.
- (26) Medek, A.; Harwood, J. S.; Frydman, L. *Journal of the American Chemical Society* **1995**, *117*, 12779-12787.
- (27) Brown, S. P.; Wimperis, S. *Journal of Magnetic Resonance* **1997**, *128*, 42-61.
- (28) Millot, Y.; Man, P. P. *Solid State Nuclear Magnetic Resonance* **2002**, *21*, 21-43.
- (29) Massiot, D.; Touzo, B.; Trumeau, D.; Coutures, J. P.; Virlet, J.; Florian, P.; Grandinetti, P. J. *Solid State Nuclear Magnetic Resonance* **1996**, *6*, 73-83.
- (30) Clark, T. M.; Grandinetti, P. J. *Journal of Physics: Condensed Matter* **2003**, *15*, S2387-S2395.
- (31) Clark, T. M.; Grandinetti, P. J.; Florian, P.; Stebbins, J. F. *Physical Review B: Condensed Matter and Materials Physics* **2004**, *70*, 064202/064201-064202/064208.
- (32) Bak, M.; Rasmussen, J. T.; Nielsen, N. C. *Journal of Magnetic Resonance* **2000**, *147*, 296-330.
- (33) Gullion, T.; Schaefer, J. *Journal of Magnetic Resonance* **1989**, *81*, 196-200.
- (34) Gullion, T. *Journal of Magnetic Resonance, Series A* **1995**, *117*, 326-329.
- (35) Grey, C. P.; Veeman, W. S.; Vega, A. J. *Journal of Chemical Physics* **1993**, *98*, 7711-7724.
- (36) Levitt, M. H. *Encyclopedia of Nuclear Magnetic Resonance* **2002**, *9*, 165-196.
- (37) Garbow, J. R.; Gullion, T. *Journal of Magnetic Resonance* **1991**, *95*, 442-445.

-
- (38) Amoureux, J.-P.; Pruski, M. In *Encyclopedia of Nuclear Magnetic Resonance*; Grant, D. M., Harris, R. K., Eds.; Wiley: New York, 2002; Vol. 9.
- (39) Frydman, L. In *Encyclopedia of Nuclear Magnetic Resonance*; Grant, D. M., Harris, R. K., Eds.; Wiley: New York, 2002; Vol. 9.
- (40) Rocha, J.; Morais, C. M.; Fernandez, C. *Topics in Current Chemistry* **2005**, *246*, 141-194.
- (41) Amoureux, J. P.; Trebosc, J. *Journal of Magnetic Resonance* **2006**, *179*, 311-316.
- (42) Vosegaard, T.; Florian, P.; Massiot, D.; Grandinetti, P. J. *Journal of Chemical Physics* **2001**, *114*, 4618-4624.
- (43) Hansen, M. R.; Vosegaard, T.; Jakobsen, H. J.; Skibsted, J. *Journal of Physical Chemistry A* **2004**, *108*, 586-594.
- (44) Nielsen, U. G.; Jakobsen, H. J.; Skibsted, J. *Solid State Nuclear Magnetic Resonance* **2003**, *23*, 107-115.
- (45) Nielsen, U. G.; Jakobsen, H. J.; Skibsted, J. *Solid State Nuclear Magnetic Resonance* **2001**, *20*, 23-34.
- (46) Medek, A.; Frydman, L. *Journal of Magnetic Resonance* **1999**, *138*, 298-307.
- (47) Derome, A. E. *Modern NMR Techniques for Chemistry Research*, 1987.
- (48) Madhu, P. K.; Goldbourt, A.; Frydman, L.; Vega, S. *Chemical Physics Letters* **1999**, *307*, 41-47.
- (49) Ashbrook, S. E.; Wimperis, S. *Progress in Nuclear Magnetic Resonance* **2004**, *45*, 53-108.
- (50) Grandinetti, P. J. RMN, versions 1.2.1, 1.2.5 and 1.3.0 (developmental version)
- (51) Skibsted, J.; Jakobsen, H. J. *Journal of Physical Chemistry A* **1999**, *103*, 7958-7971.
- (52) Vosegaard, T.; Skibsted, J.; Bildsoe, H.; Jakobsen, H. J. *Journal of Physical Chemistry* **1995**, *99*, 10731-10735.
- (53) Vosegaard, T.; Skibsted, J.; Bildsoe, H.; Jakobsen, H. J. *Journal of Magnetic Resonance, Series A* **1996**, *122*, 111-119.
- (54) Farrar, T. C.; Harriman, J. E. *Density Matrix Theory and its Applications in NMR Spectroscopy*; The Farrugut Press: Madison, 1995.

-
- (55) Kwak, H.-T.; Srinivasan, P.; Quine, J.; Massiot, D.; Gan, Z. *Chemical Physics Letters* **2003**, *376*, 75-82.
- (56) Schurko, R. W.; Wasylishen, R. E.; Foerster, H. *Journal of Physical Chemistry A* **1998**, *102*, 9750-9760.
- (57) Schurko, R. W.; Wasylishen, R. E.; Phillips, A. D. *Journal of Magnetic Resonance* **1998**, *133*, 388-394.
- (58) Vosegaard, T.; Jakobsen, H. J. *Journal of Magnetic Resonance* **1997**, *128*, 135-137.
- (59) Bryce, D. L.; Wasylishen, R. E.; Gee, M. *Journal of Physical Chemistry A* **2001**, *105*, 3633-3640.
- (60) Private Conversations with Dominique Massiot at the 90th Canadian Chemistry Conference and Exhibition, June, 2007 Winnipeg, MB, Canada.
- (61) Anderson, T. N.; Magnuson, J. K.; Lucht, R. P. *Applied Physics B: Lasers and Optics* **2007**, *87*, 341-353.
- (62) Mildren, R. P.; Ogilvy, H.; Piper, J. A. *Optics Letters* **2007**, *32*, 814-816.
- (63) Xue, D. F.; Zhang, S. Y. *Acta Crystallographica, Section B: Structural Science* **1998**, *B54*, 652-656.
- (64) Abdelouas, A.; Crovisier, J.-L.; Lutze, W.; Grambow, B.; Dran, J.-C.; Muller, R. *Journal of Nuclear Materials* **1997**, *240*, 100-111.
- (65) McKeown, D. A.; Muller, I. S.; Gan, H.; Pegg, I. L.; Stolte, W. C. *Journal of Non-Crystalline Solids* **2004**, *333*, 74-84.
- (66) Peugeot, S.; Broudic, V.; Jegou, C.; Frugier, P.; Roudil, D.; Deschanel, X.; Rabiller, H.; Noel, P. Y. *Journal of Nuclear Materials* **2007**, *362*, 474-479.
- (67) Peugeot, S.; Cachia, J.-N.; Jegou, C.; Deschanel, X.; Roudil, D.; Broudic, V.; Delaye, J. M.; Bart, J.-M. *Journal of Nuclear Materials* **2006**, *354*, 1-13.
- (68) Schaller, T.; Rong, C.; Toplis, M. J.; Cho, H. *Journal of Non-Crystalline Solids* **1999**, *248*, 19-27.
- (69) Rao, K. J. *Structural Chemistry of Glasses*; Elsevier: Kidlington, Oxford, 2002.
- (70) Shelby, J. E. *Introduction to Glass Science and Technology*; The Royal Society of Chemistry: Cornwall, UK, 2005.
- (71) Zachariasen, W. H. *Journal of the American Chemical Society* **1932**, *54*, 3841-3851.

- (72) Gilletpie, R. J.; Eaton, D. R.; Humphreys, D. A.; A., R. E. *Atoms, Molecules and Reactions: An Introduction to Chemistry*; Prentice-Hall: Englewood Cliffs, USA, 1994.
- (73) Stebbins, J. F. *Nature (London, United Kingdom)* **1987**, *330*, 465-467.
- (74) Stebbins, J. F. *Journal of Non-Crystalline Solids* **1988**, *106*, 359-369.
- (75) Zeyer, M.; Montagne, L.; Jaeger, C.; Palavit, G. *Phosphorus Research Bulletin* **2002**, *13*, 275-278.
- (76) Bray, P. J. *Inorganica Chimica Acta* **1999**, *289*, 158-173.
- (77) McLaughlin, J. C.; Tagg, S. L.; Zwanziger, J. W. *Journal of Physical Chemistry B* **2001**, *105*, 67-75.
- (78) McLaughlin, J. C.; Tagg, S. L.; Zwanziger, J. W.; Haeffner, D. R.; Shastri, S. D. *Journal of Non-Crystalline Solids* **2000**, *274*, 1-8.
- (79) Du, L.-S.; Stebbins, J. F. *Journal of Physical Chemistry B* **2006**, *110*, 12427-12437.
- (80) Lee, S. K.; Lee, B. H. *Journal of Physical Chemistry B* **2006**, *110*, 16408-16412.
- (81) Feller, S. A.; Dell, W. J.; Bray, P. J. *Journal of Non-Crystalline Solids* **1982**, *51*, 21-30.
- (82) Kroeker, S.; Aguiar, P. M.; Cerquiera, A.; Okoro, J.; Clarida, W.; Doerr, J.; Olesiuk, M.; Ongie, G.; Affatigato, M.; Feller, S. A. *Physics and Chemistry of Glasses: European Journal of Glass Science and Technology, Part B* **2006**, *47*, 393-396.
- (83) Clarida, W. J.; Berryman, J. R.; Affatigato, M.; Feller, S. A.; Kroeker, S.; Ash, J.; Zwanziger, J.; Meyer, B.; Borsa, F.; Martin, S. W. *Physics and Chemistry of Glasses* **2003**, *44*, 215-217.
- (84) Rao, K. J. *Structural Chemistry of Glasses*; Elsevier: New York, 2002.
- (85) Zarzycki, J. *Journal of Non-Crystalline Solids* **1982**, *52*, 31-43.
- (86) Hayes, T. M. *Journal of Non-Crystalline Solids* **1978**, *31*, 57-79.
- (87) Fleet, M. E.; Muthupari, S. *American Mineralogist* **2000**, *85*, 1009-1021.
- (88) Fleet, M. E. *American Mineralogist* **1992**, *77*, 76-84.
- (89) Kamitsos, E. I.; Patsis, A. P.; Karakassides, M. A.; Chryssikos, G. D. *Journal of Non-Crystalline Solids* **1990**, *126*, 52-67.
- (90) Kamitsos, E. I.; Chryssikos, G. D.; Karakassides, M. A. *Journal of Non-Crystalline Solids* **1990**, *123*, 283-285.

-
- (91) Chryssikos, G. D.; Kamitsos, E. I.; Karakassides, M. A. *Physics and Chemistry of Glasses* **1990**, *31*, 109-116.
- (92) Kamitsos, E. I.; Karakassides, M. A.; Chryssikos, G. D. *Physics and Chemistry of Glasses* **1989**, *30*, 229-234.
- (93) Moeller, A. R.; Olesiak, M. D.; Gao, J.; Giri, S. K.; Affatigato, M.; Feller, S. A.; Kodama, M. *Physics and Chemistry of Glasses* **2003**, *44*, 237-240.
- (94) Banerjee, J.; Ongie, G.; Harder, J.; Edwards, T.; Larson, C.; Sutton, S.; Moeller, A.; Basu, A.; Affatigato, M.; Feller, S.; Kodama, M.; Aguiar, P. M.; Krocker, S. *Journal of Non-Crystalline Solids* **2006**, *352*, 674-678.
- (95) Krogh-Moe, J. *Acta Crystallographica, Section B: Structural Crystallography and Crystal Chemistry* **1974**, *30*, 1178-1180.
- (96) Penin, N.; Seguin, L.; Toubol, M.; Nowogrocki, G. *Journal of Solid State Chemistry* **2001**, *161*, 205-213.
- (97) Rodriguez-Carvajal, J. FULLPROF: A Program for Rietveld Refinement and Pattern Matching Analysis Toulouse, France 1990
- (98) Kunwar, A. C.; Turner, G. L.; Oldfield, E. *Journal of Magnetic Resonance* **1986**, *69*, 124-127.
- (99) Chan, J. C. C.; Eckert, H. *Journal of Magnetic Resonance* **2000**, *147*, 170-178.
- (100) Marinelli, L.; Frydman, L. *Chemical Physics Letters* **1997**, *275*, 188-198.
- (101) Barszczewicz, A.; Helgaker, T.; Jaszunski, M.; Jorgensen, P.; Ruud, K. *Journal of Magnetic Resonance, Series A* **1995**, *114*, 212.
- (102) Silver, A. H.; Bray, P. J. *Journal of Chemical Physics* **1958**, *29*, 984-990.
- (103) Kriz, H. M.; Bray, P. J. *Journal of Magnetic Resonance* **1971**, *4*, 76-84.
- (104) Yun, Y. H.; Bray, P. J. *Journal of Non-Crystalline Solids* **1981**, *44*, 227-237.
- (105) Krocker, S.; Feller, S. A.; Affatigato, M.; O'Brien, C. P.; Clarida, W. J.; Kodama, M. *Physics and Chemistry of Glasses* **2003**, *44*, 54-58.
- (106) Ratai, E. M.; Janssen, M.; Epping, J. D.; Chan, J. C. C.; Eckert, H. *Physics and Chemistry of Glasses* **2003**, *44*, 45-53.
- (107) Youngman, R. E.; Zwanziger, J. W. *Journal of the American Chemical Society* **1995**, *117*, 1397-1402.

-
- (108) Vegiri, A.; Varsamis Cristos-Platon, E.; Kamitsos Efstratios, I. *The Journal of Chemical Physics* **2005**, *123*, 014508.
- (109) Borrelli, N. F.; McSwain, B. D.; Su, G.-J. *Physics and Chemistry of Glasses* **1963**, *4*, 11-12.
- (110) Krogh-Moe, J. *Arkiv foer Kemi* **1958**, *12*, 475-480.
- (111) Krogh-Moe, J. *Physics and Chemistry of Glasses* **1965**, *6*, 46-54.
- (112) Joo, C.; Werner-Zwanziger, U.; Zwanziger, J. W. *Journal of Non-Crystalline Solids* **2000**, *261*, 282-286.
- (113) Joo, C. G.; Werner-Zwanziger, U.; Zwanziger, J. W. *Physics and Chemistry of Glasses* **2000**, *41*, 317-320.
- (114) Zwanziger, J. W.; Tagg, S. L.; Huffman, J. C. *Science* **1995**, *268*, 1510.
- (115) Tossell, J. A.; Lazzeretti, P. *Journal of Physical Chemistry* **1990**, *94*, 1723-1724.
- (116) Zwanziger, J. W. *Solid State Nuclear Magnetic Resonance* **2005**, *27*, 5-9.
- (117) Tossell, J. A. *Journal of Non-Crystalline Solids* **1997**, *215*, 236-243.
- (118) Tossell, J. A. *Journal of Non-Crystalline Solids* **1995**, *183*, 307-314.
- (119) Burns, P. C.; Grice, J. D.; Hawthorne, F. C. *Canadian Mineralogist* **1995**, *33*, 1131-1151.
- (120) Grice, J. D.; Burns, P. C.; Hawthorne, F. C. *Canadian Mineralogist* **1999**, *37*, 731-762.
- (121) Michaelis, V.; Aguiar, P. M.; Kroeker, S. *Journal of Non-Crystalline Solids* **2007**, *In Press*.
- (122) Gullion, T. *Concepts in Magnetic Resonance* **1998**, *10*, 277-289.
- (123) Strojek, W.; Kalwei, M.; Eckert, H. *Journal of Physical Chemistry B* **2004**, *108*, 7061-7073.
- (124) Epping, J. D.; Strojek, W.; Eckert, H. *Physical Chemistry Chemical Physics* **2005**, *7*, 2384-2389.
- (125) Janssen, M.; Eckert, H. *Solid State Ionics* **2000**, *136-137*, 1007-1014.
- (126) Bertmer, M.; Eckert, H. *Solid State Nuclear Magnetic Resonance* **1999**, *15*, 139-152.
- (127) Rhee, C.; Bray, P. J. *Physics and Chemistry of Glasses* **1971**, *12*, 156-164.

- (128) Toubol, M.; Penin, N.; Nowogrocki, G. *Solid State Sciences* **2003**, *5*, 1327-1342.
- (129) Kroeker, S.; Eichele, K.; Wasylishen, R. E.; Britten, J. F. *Journal of Physical Chemistry B* **1997**, *101*, 3727-3733.
- (130) Duer, M. J.; Editor *Solid State NMR Spectroscopy: Principles and Applications*, 2002.
- (131) Kroeker, S.; Stebbins, J. F. *Inorganic Chemistry* **2001**, *40*, 6239-6246.
- (132) Lemaître, V.; Smith, M. E.; Watts, A. *Solid State Nuclear Magnetic Resonance* **2004**, *26*, 215-235.
- (133) Ashbrook, S. E.; Smith, M. E. *Chemical Society Reviews* **2006**, *35*, 718-735.
- (134) Grandinetti, P. J.; Baltisberger, J. H.; Farnan, I.; Stebbins, J. F.; Werner, U.; Pines, A. *Journal of Physical Chemistry* **1995**, *99*, 12341-12348.
- (135) Kroeker, S.; Rice, D.; Stebbins, J. F. *American Mineralogist* **2002**, *87*, 572-579.
- (136) Du, L.-S.; Stebbins, J. F. *Journal of Physical Chemistry B* **2003**, *107*, 10063-10076.
- (137) Du, L.-S.; Stebbins, J. F. *Journal of Non-Crystalline Solids* **2003**, *315*, 239-255.
- (138) Wang, S.; Stebbins, J. F. *Journal of the American Ceramic Society* **1999**, *82*, 1519-1528.
- (139) Ashbrook, S. E.; Berry, A. J.; Hibberson, W. O.; Steuernagel, S.; Wimperis, S. *American Mineralogist* **2005**, *90*, 1861-1870.
- (140) Ashbrook, S. E.; Berry, A. J.; Hibberson, W. O.; Steuernagel, S.; Wimperis, S. *Journal of the American Chemical Society* **2003**, *125*, 11824-11825.
- (141) Ashbrook, S. E.; Wimperis, S. *Journal of Magnetic Resonance* **2002**, *156*, 269-281.
- (142) Foit, F. F.; Philips, M. W.; Gibbs, G. V. *American Mineralogist* **1973**, *58*, 909-914.
- (143) Sherriff, B. L.; Grundy, H. D. *Nature* **1988**, *332*, 819-822.
- (144) Moulton, B.; Zaworotko, M. J. *Chemical Reviews* **2001**, *101*, 1629-1658.
- (145) Eddaoudi, M.; Moler, D. B.; Li, H.; Chen, B.; Reineke, T. M.; O'Keeffe, M.; Yaghi, O. M. *Accounts of Chemical Research* **2001**, *34*, 319-330.
- (146) Meng, X.; Song, Y.; Hou, H.; Fan, Y.; Li, G.; Zhu, Y. *Inorganic Chemistry* **2003**, *42*, 1306-1315.
- (147) Li, G.; Song, Y.; Hou, H.; Li, L.; Fan, Y.; Zhu, Y.; Meng, X.; Mi, L. *Inorganic Chemistry* **2003**, *42*, 913-920.

- (148) Kagan, C. R.; Mitzi, D. B.; Dimitrakopoulos, C. D. *Science* **1999**, *286*, 945-947.
- (149) Mitzi, D. B.; Wang, S.; Feild, C. A.; Chess, C. A.; Guloy, A. M. *Science* **1995**, *267*, 1473-1476.
- (150) Caulder, D. L.; Raymond, K. N. *Accounts of Chemical Research* **1999**, *32*, 975 -982.
- (151) Bowmaker, G. A.; Hartl, H.; Urban, V. *Inorganic Chemistry* **2000**, *39*, 4548-4554.
- (152) Draper, N. D.; Batchelor, R. J.; Sih, B. C.; Ye, Z.-G.; Leznoff, D. B. *Chemistry of Materials* **2003**, *15*, 1612-1616.
- (153) Stocker, F. B.; Staeva, T. P.; Rienstra, C. M.; Britton, D. *Inorganic Chemistry* **1999**, *38*, 984-991.
- (154) Chestnut, D. J.; Plewak, D.; Zubieta, J. *Journal of the Chemical Society, Dalton Transactions* **2001**, 2567-2580.
- (155) Hibble, S. J.; Cheyne, S. M.; Hannon, A. C.; Eversfield, S. G. *Inorganic Chemistry* **2002**, *41*, 4990-4992.
- (156) Hibble, S. J.; Hannon, A. C.; Cheyne, S. M. *Inorganic Chemistry* **2003**, *42*, 4724-4730.
- (157) Kroeker, S.; Wasylshen, R. E.; Hanna, J. V. *Journal of the American Chemical Society* **1999**, *121*, 1582-1590.
- (158) Bryce, D. L.; Wasylshen, R. E. *Inorganic Chemistry* **2002**, *41*, 4131-4138.
- (159) Harris, K. J.; Wasylshen, R. E. Rocky Mountain Conference on Analytical Chemistry, Breckeridge CO, USA, 2006.
- (160) Curtis, R. D.; Ratcliffe, C. I.; Ripmeester, J. A. *Journal of the Chemical Society, Chemical Communications* **1992**, 1800-1802.
- (161) Eddaoudi, M.; Moler, D. B.; Li, H.; Chen, B.; Reineke, T. M.; O'Keeffe, M.; Yaghi, O. M. *Acc Chem Res FIELD Full Journal Title:Accounts of chemical research* **2001**, *34*, 319-330.
- (162) Cernak, J.; Chomic, J.; Gravereau, P.; Orendacova, A.; Orendac, M.; Kovac, J.; Feher, A.; Kappenstein, C. *Inorganica Chimica Acta* **1998**, *281*, 134-140.
- (163) Draper, N. D.; Batchelor, R. J.; Aguiar, P. M.; Kroeker, S.; Leznoff, D. B. *Inorganic Chemistry* **2004**, *43*, 6557-6567.
- (164) Patterson, H. H.; Bourassa, J.; Shankle, G. *Inorganica Chimica Acta* **1994**, *226*, 345-348.

- (165) Katz, M. J.; Aguiar, P. M.; Batchelor, R. J.; Bokov, A. A.; Ye, Z.-G.; Kroeker, S.; Leznoff, D. B. *Journal of the American Chemical Society* **2006**, *128*, 3669-3676.
- (166) Ouyang, L.; Aguiar, P. M.; Batchelor, R. J.; Kroeker, S.; Leznoff, D. B. *Chemical Communications* **2006**, 744-746.
- (167) Shorrock, C. J.; Xue, B.-Y.; Kim, P. B.; Batchelor, R. J.; Patrick, B. O.; Leznoff, D. B. *Inorganic Chemistry* **2002**, *41*, 6743-6753.
- (168) Shorrock, C. J.; Jong, H.; Batchelor, R. J.; Leznoff, D. B. *Inorganic Chemistry* **2003**, *42*, 3917-3924.
- (169) Pines, A.; Gibby, M. G.; Waugh, J. S. *Journal of Chemical Physics* **1972**, *56*, 1776-1777.
- (170) Eichele, K.; Kroeker, S.; Wu, G.; Wasylshen, R. E. *Solid State Nuclear Magnetic Resonance* **1995**, *4*, 295-300.
- (171) Maciel, G. E.; Dallas, J. L. *J. Am. Chem. Soc.* **1973**, *95*, 3039.
- (172) van Gorkom, L. C. M.; Hook, J. M.; Logan, M. B.; Hanna, J. V.; Wasylshen, R. E. *Mag. Res. Chem.* **1995**, *33*, 791.
- (173) Bielecki, A.; Burum, D. P. *J. Magn. Reson. A* **1995**, *116*, 215.
- (174) Dybowski, C.; Neue, G. *Progress in Nuclear Magnetic Resonance Spectroscopy* **2002**, *41*, 153-170.
- (175) Neue, G.; Dybowski, C. *Solid State Nuclear Magnetic Resonance* **1997**, *7*, 333-336.
- (176) van Gorkum, L. C. M.; Hook, J. M.; Logan, M. B.; Hanna, J. V.; Wasylshen, R. E. *Magnetic Resonance in Chemistry* **1995**, *33*, 791-795.
- (177) Cromer, D. T.; Larson, A. C. *Acta Crystallographica* **1972**, *B28*, 1052-1058.
- (178) Cromer, D. T.; Larson, A. C.; Roof, R. B., Jr. *Acta Crystallographica* **1965**, *19*, 192-197.
- (179) Stocker, F. B. *Inorganic Chemistry* **1991**, *30*, 1472-1475.
- (180) Brodersen, K.; Frohring, H. M.; Thiele, G. *Zeitschrift fuer Anorganische und Allgemeine Chemie* **1981**, *483*, 86-94.
- (181) Thiele, G.; Brodersen, K.; Frohring, H. *Zeitschrift fuer Naturforschung, Teil B: Anorganische Chemie, Organische Chemie* **1981**, *36B*, 180-187.

- (182) Harris, R. K.; Becker, E. D.; Cabral de Menezes, S. M.; Goodfellow, R.; Granger, P. *Pure and Applied Chemistry* **2001**, *73*, 1795-1818.
- (183) Wu, G.; Wasylishen, R. E. *Magnetic Resonance in Chemistry* **1993**, *31*, 537-539.
- (184) Krocker, S.; Wasylishen, R. E. *Canadian Journal of Chemistry* **1999**, *77*, 1962-1972.
- (185) Wu, G.; Krocker, S.; Wasylishen, R. E. *Inorganic Chemistry* **1995**, *34*, 1595-1598.
- (186) Duncan, T. M. *Chemical Shift Tensors*; Second ed.; The Farragut Press: Ithaca, 1997.
- (187) Hexem, J. G.; Frey, M. H.; Opella, S. J. *Journal of the American Chemical Society* **1981**, *103*, 224-226.
- (188) Wasylishen, R. E.; Lenkinski, R. E.; Rodger, C. *Canadian Journal of Chemistry* **1982**, *60*, 2113-2117.
- (189) Wu, G.; Wasylishen, R. E. *Journal of Physical Chemistry* **1993**, *97*, 7863-7869.
- (190) Bowmaker, G. A.; Harris, R. K.; Oh, S.-W. *Coordination Chemistry Reviews* **1997**, *167*, 49-94.
- (191) Bowmaker, G. A.; Harris, R. K.; Apperley, D. C. *Inorganic Chemistry* **1999**, *38*, 4956-4962.
- (192) Han, M.; Peersen, O. B.; Bryson, J. W.; O'Halloran, T. V.; Smith, S. O. *Inorganic Chemistry* **1995**, *34*, 1187-1192.
- (193) Fayon, F.; Farnan, I.; Bessada, C.; Coutures, J.; Massiot, D.; Coutures, J. P. *Journal of the American Chemical Society* **1997**, *119*, 6837-6843.
- (194) Kye, Y.-S.; Connolly, S.; Herreros, B.; Harbison, G. S. *Main Group Metal Chemistry* **1999**, *22*, 373-383.
- (195) Sebald, A.; Harris, R. K. *Organometallics* **1990**, *9*, 2096-2100.
- (196) Eichele, K.; Lumsden, M. D.; Wasylishen, R. E. *Journal of Physical Chemistry* **1993**, *97*, 8909-8916.
- (197) Eichele, K.; Wasylishen, R. E. *Journal of Magnetic Resonance, Series A* **1994**, *106*, 46-56.
- (198) Hiltunen, Y.; Jokisaari, J.; Lounila, J.; Pulkkinen, A. *Journal of the American Chemical Society* **1989**, *111*, 3217-3220.
- (199) Buckingham, A. D.; Malm, S. M. *Molecular Physics* **1971**, *22*, 1127-1130.

-
- (200) Bertini, I.; Luchinat, C. *NMR of Paramagnetic Molecules in Biological Systems*; Benjamin/Cummings Publishing Company, 1986.
- (201) Liu, K.; Ryan, D.; Nakanishi, K.; McDermott, A. *Journal of the American Chemical Society* **1995**, *117*, 6897-6906.
- (202) Nayeem, A.; Yesinowski, J. P. *Journal of Chemical Physics* **1988**, *89*, 4600-4608.
- (203) Brough, A. R.; Grey, C. P.; Dobson, C. M. *Journal of the American Chemical Society* **1993**, *115*, 7318-7327.
- (204) Clayton, A. N.; Dobson, C. M.; Grey, C. P. *Journal of the Chemical Society, Chemical Communications* **1990**, 72-74.
- (205) Ishii, Y.; Wickramasinghe, N. P.; Chimon, S. *Journal of the American Chemical Society* **2003**, *125*, 3438-3439.
- (206) Wickramasinghe, N. P.; Shaibat, M.; Ishii, Y. *Journal of the American Chemical Society* **2005**, *127*, 5796-5797.
- (207) Bowmaker, G. A.; Churakov, A. V.; Harris, R. K.; Oh, S.-W. *Journal of Organometallic Chemistry* **1998**, *550*, 89-99.
- (208) Aguiar, P. M.; Kroeker, S. 39th IUPAC Congress and the 86th Conference of the Canadian Society for Chemistry, Ottawa, ON, 2003.
- (209) Jesson, J. P. In *NMR of Paramagnetic Molecules*; Mar, G. N. L., Jr., W. D. H., Holm, R. H., Eds.; Academic Press: New York, 1973.
- (210) Mao, J.; Zhang, Y.; Oldfield, E. *Journal of the American Chemical Society* **2002**, *124*, 13911-13920.
- (211) Zhang, Y.; Sun, H.; Oldfield, E. *Journal of the American Chemical Society* **2005**, *127*, 3652-3653.
- (212) Grey, C. P.; Dupre, N. *Chemical Reviews* **2004**, *104*, 4493-4512.
- (213) Pesek, J. J.; Mason, W. R. *Inorganic Chemistry* **1979**, *18*, 924-928.
- (214) Knight, W. D. *Physical Review* **1949**, *76*, 1259-1260.
- (215) Grey, C. P.; Dobson, C. M.; Cheetham, A. K. *Journal of Magnetic Resonance* **1992**, *98*, 414-420.
- (216) Antonijevic, S.; Wimperis, S. *Journal of Magnetic Resonance* **2003**, *164*, 343-350.

- (217) Antonijevic, S.; Wimperis, S. *Journal of Chemical Physics* **2005**, *122*, 044312/044311-044312/044314.
- (218) Siminovitch, D. J.; Rance, M.; Jeffrey, K. R.; Brown, M. F. *Journal of Magnetic Resonance* **1984**, *58*, 62-75.
- (219) Lee, H.; Polenova, T.; Beer, R. H.; McDermott, A. E. *Journal of the American Chemical Society* **1999**, *121*, 6884-6894.
- (220) Akitt, J. W. In *Multinuclear NMR*; Mason, J., Ed.; Plenum Press: New York, 1987.
- (221) Leznoff, D. B.; Lefebvre, J. *Gold Bulletin* **2005**, *38*, 47-54.
- (222) Leznoff, D. B.; Xue, B.-Y.; Batchelor, R. J.; Einstein, F. W. B.; Patrick, B. O. *Inorganic Chemistry* **2001**, *40*, 6026-6034.
- (223) Wickramasinghe, N. P.; Ishii, Y. *Journal of Magnetic Resonance* **2006**, *181*, 233-243.
- (224) Ernst, M.; Samoson, A.; Meier, B. H. *Journal of Chemical Physics* **2005**, *123*, 064102/064101-064102/064110.
- (225) Ernst, M. *Journal of Magnetic Resonance* **2003**, *162*, 1-34.
- (226) Spaniol, T. P.; Kubo, A.; Terao, T. *Molecular Physics* **1999**, *96*, 827-834.
- (227) Kubo, A.; Spaniol, T. P.; Terao, T. *Journal of Magnetic Resonance* **1998**, *133*, 330-340.
- (228) Sakellariou, D.; Brown, S. P.; Lesage, A.; Hediger, S.; Bardet, M.; Meriles, C. A.; Pines, A.; Emsley, L. *Journal of the American Chemical Society* **2003**, *125*, 4376-4380.
- (229) Palmer, A.; Comos, M.; Bronnimann, C. E.; Hafner, S. Experimental NMR Conference, Asilomar, CA, 2006.
- (230) Wiench, J. W.; Rice, D.; Palmer, A.; Comos, M.; Pruski, M. Experimental NMR Conference, Asilomar, CA, 2006.
- (231) Holmes, L.; Peng, L.; Grey, C. P.; Heinmaa, I.; Vannier, R.-N. Rocky Mountain Conference on Analytical Chemistry, Breckenridge, CO, 2006.
- (232) Samoson, A.; Tuherm, T.; Heinmaa, I. Rocky Mountain Conference on Analytical Chemistry, Breckenridge, CO, 2006.